POLITECNICO DI TORINO

Department of Mechanical and Aerospace Engineering

Politecnico di Torino

Master's Degree in Aerospace Engineering

Impact of AM-Induced Upscaled Surface Roughness on Flow Dynamics, Heat Transfer and Friction Properties: A Particle Image Velocimetry Study

Supervisor:

Prof. Gioacchino Cafiero
Dr.-Ing. Mats Kinell
Dr.-Ing. Alessio Bonaldo

Student:

Modesto Laguardia

Thesis in collaboration with
Siemens Energy

SIEMENS energy

Academic Year 2024/2025

Acknowledgments

Ai miei genitori, per avermi permesso di navigare in acque libere e meno sicure, lontano dalle rive che mi legano alla mia terra ma che mi hanno dato l'arbitrio di esprimere le mie idee. Senza il vostro sostegno nulla di tutto questo sarebbe stato realizzabile. Grazie di cuore.

Desidero esprimere un profondo ringraziamento al mio relatore, Prof. Gioacchino Cafiero, e a tutto il personale del Fluid Dynamic Laboratory presso Siemens Energy, in Svezia. Un grazie speciale va ad Alessio Bonaldo e al mio mentore in laboratorio, Mats Kinell. L'opportunità e le responsabilità affidatemi hanno arricchito il mio pensiero critico e il mio approccio ai problemi. La vostra professionalità è una continua fonte di ispirazione ed un modello concreto per la mia futura carriera.

Alla mia famiglia ed alla persona che mi ha costantemente atteso a braccia aperte, senza mai lamentarsi e senza mai limitare le mie ambizioni. Recupereremo insieme ogni momento sottratto ai nostri incontri, trasformando ogni saluto passato in un solido pilastro per il nostro domani. Grazie anche a coloro che hanno contribuito alla mia crescita personale, insegnandomi il valore dei sacrifici nella vita.

Un pensiero sentito va a tutte le ragazze ed i ragazzi che non hanno avuto la possibilità di raggiungere gli obiettivi per cui hanno tanto lavorato, come per me lo é stato questa laurea. Vittime di una societá narcisista, dove la normalità di un amore sano lascia un retrogusto amaro, contaminato da una realtá molto piú precaria, in cui é la malata ossessione ad essere spesso percepita come naturale. Auspico una maggiore sensibilizzazione su questi temi, che ponga l'accento sui carnefici e non su accuse mosse alle vittime rispetto a mancate azioni di prevenzione. Il dono alla vita non è mai una questione di opinioni ed il silenzio su questi argomenti non è mai stato così assordante.

Abstract

EN The increase in global energy demand has driven technological advancements aimed at improving the performance of machines used for energy production, particularly Land-Based Gas Turbines (LBGT). In the last decade, enhancements in compression ratio and Turbine Inlet Temperature (TIT) have led to a 40% improvement in efficiency, made possible by the adoption of Additive Manufacturing (AM), as opposed to traditional casting techniques. This study examined the flow dynamics under irregular texture typical of AM-produced products. Cooling channels were sectioned and up-scaled for testing on a rig, where PIV (Particle Image Velocimetry) technique was employed for the analysis. The validation of the setup and measurements enabled the examination of three multi-scale rough surfaces with irregular patterns. Mean and turbulence statistics were assessed using drag information, highlighting the variability in the turbulent nature of the flow across the three investigated rough surfaces as a function of roughness scale. Aerodynamic data were correlated with thermal data to determine flow characteristics in areas of high and low heat transmission. The analysis also explored how roughness parameters affect the friction coefficients of surfaces. It was found that, despite difference of up to 800% in certain roughness parameters, the friction coefficient was altered by only 5%. In stark contrast, the R_z roughness parameter demonstrated a significantly greater impact on the friction coefficients. These findings suggest that R_z may be the predominant influencing factor on the friction coefficient behavior of the examined surfaces.

IT L'incremento della domanda energetica globale ha spinto lo sviluppo tecnologico verso il miglioramento delle prestazioni delle macchine utilizzate per la produzione di energia, soprattutto riguardo le Land-Based Gas Turbines (LBGT). Negli ultimi dieci anni, aumenti nel rapporto di compressione e nella temperatura all'ingresso della turbina (Turbine Inlet Temperature - TIT) hanno comportato un miglioramento dell'efficienza del 40%, reso possibile dall'adozione dell'Additive Manufacturing (AM), in contrasto con le tecniche tradizionali di fusione. Questo studio ha esaminato la dinamica del flusso in contesti di irregolarità superficiali tipiche dei prodotti realizzati tramite AM. Canali di raffreddamento sono stati sezionati e replicati in versione up-scale per essere testati in un banco di prova, dove la tecnica PIV (Particle Image Velocimetry) é stata impiegata per l'analisi. La validazione dell'impianto e delle misure ha consentito l'analisi di tre superfici ruvide con pattern multi-scala ed irregolare. Sono state valutate le statistiche medie e di turbolenza utilizzando le informazioni sulla resistenza, evidenziando la diversità della natura turbolenta del flusso per le tre superfici ruvide indagate al variare delle scale di rugosità. I dati aerodinamici sono stati correlati con quelli termici per identificare le caratteristiche del flusso in aree di alta e bassa trasmissione di calore. L'analisi ha anche esplorato come i parametri di rugosità influenzino i coefficienti di attrito delle superfici. È emerso che, nonostante differenze fino all'800% in alcuni parametri di rugosità, i parametri di friction hanno subito una variazione limitata al 5%. In netto contrasto, il parametro di rugosità R_z ha mostrato un'influenza decisamente più marcata sui coefficienti di attrito facendo avanzare l'ipotesi che R_z potrebbe essere il fattore di dipendenza predominante sul comportamento del friction factor delle superfici esaminate.

Contents

1 Introduction **1**

1.1 Motivation 1
1.2 Literature Review 4
1.3 Research Objectives 7
1.4 Thesis Outline 8

2 Theoretical Background **9**

2.1 Additive Manufacturing 9
2.1.1 Additive Manufacturing Technologies 10
2.1.2 Roughness parameters 13
2.2 Gas turbine 15
2.2.1 The ideal cycle for Gas-Turbine engines 16
2.2.2 The Brayton Cycle with Intercooling, Reheating and Regeneration 19
2.2.3 Turbine Blade Cooling 20
2.2.4 AM Components for Gas Turbine Application 21
2.3 Fundamentals of Heat Transfer 23
2.3.1 Definition and governing law 23
2.3.2 Convection 25
2.3.3 Radiation 25
2.3.4 Conduction 27
2.4 Boundary Layer Theory 29
2.4.1 Laminar and Turbulent Flow 31
2.4.2 Fundamentals of Turbulent Flows 33
2.5 Internal Flows 35
2.5.1 Quantitative Descriptions of Fluid Behavior 36
2.5.2 Velocity Distribution and Friction Factor for Rough Surface 44
2.6 Particle Image Velocimetry 45
2.6.1 Equipment Selection 47

3 Research Methodology **51**

3.1 Research Approach 51
3.1.1 Dynamic Similarity 52
3.2 Experimental Framework 55
3.2.1 Wind Tunnel and Test Section 55
3.2.2 Analogue Rough Texture Modeling 59
3.2.3 PIV Measurement Systems 63
3.2.4 Data Analysis Methods 70
3.2.5 Image Evaluation 72

3.2.6 Image Pre-Processing . . . 74
3.2.7 Image Post-Processing . . . 75
3.2.8 Testing Campaigns . . . 77
3.2.9 Wall Friction Velocity Calculations . . . 78
3.3 Uncertainty Analysis . . . 80

4 Results **85**
4.1 Rig Validation - FULL FOV Test Smooth Plates . . . 85
4.2 Boundary Layer Test . . . 86
4.2.1 Smooth Plates . . . 86
4.2.2 Rough Plates . . . 90
4.3 Correlations with SRHT Rig . . . 97
4.3.1 Flow Behavior Near Roughness . . . 97
4.3.2 Skin-Friction Coefficient Estimation . . . 100
4.4 Correlations with QSSHT Rig . . . 105
4.4.1 Darcy Friction Factor Smooth . . . 105
4.4.2 Darcy Friction Factor Rough . . . 107

5 Conclusions and Future Works **117**

A Turbine Cooling Method **119**
A1 Rib Turbulated Cooling . . . 119
A2 Impingement Cooling . . . 119
A3 Pin-Fin Cooling . . . 121
A4 Dimple/Protrusion Cooling . . . 121
A5 Latticework cooling . . . 121
A6 Film Cooling . . . 123

B Dimensional Analysis **125**
B1 *Buckingham* π *− theorem* . . . 126
B1.1 Definition . . . 126
B1.2 Structure of the Generic Adimensional Group Π_i . . . 126
B1.3 Example 1. Aerodynamic resultant force F acting on an airfoil . . . 128
B1.4 Example 2. Conversion of the energy equation into its dimensionless form . . . 130

C Turbulence Scales and Energy Cascade **133**
C1 Turbulent scales . . . 134
C1.1 Integral Length Scale . . . 134
C1.2 Taylor Microscale . . . 135
C1.3 Kolmogorov Scales . . . 135

D Gamma Distribution **137**
D1 Implementing Gamma Distribution for Modeling Diameter Distribution . . . 137

List of Figures

1.1 Various types of roughness: (a) Erosion along the rudder of a ship; (b) Deposition on gas turbine blades, Bons[68] 2
1.2 World Energy Transitions Outlook, IRENA-International Renewable Energy Agency 3
1.3 Cooling system: (a) Schematic of a Turbine Vane Cross-Section with Impingement and Trailing Edge Pin-Fin Cooling[60]; (b) Modern cooling system, with complex internal channels 4

2.1 Overall AM Industry Revenues 1992–2022 [104] 10
2.2 Overall workflow of the additive manufacturing process [126] 10
2.3 Gas Turbine Blades made for Siemens by Material Soultions 12
2.4 Schematic of SLS 3D printers [106] 13
2.5 Schematic of directed energy deposition (DED) [126]: (a) Powder DED (laser source); (b) Wire DED (E-beam source) 13
2.6 Schematic of the profile texture parameters [123]: (a) R_a, R_q, R_p, R_v, R_z, (b) R_{sk} and the height probability distribution, (c) R_{ku} and the height probability distribution 14
2.7 A modern land-based gas turbine used for electric power production. This is a Siemens Energy SGT-800 gas turbine used for industrial power generation and oil and gas applications. It has a length of 20.8 m, it weighs 28.5×10^4 kg, and produces 62.5 MW at 6600 rpm with a gross efficiency of 41.1% and a NO_x emissions level of $15 - 25$ ppmvd [120] 16
2.8 Schematic representation of a gas turbine [75]: (a) An open-cycle gas-turbine engine; (b) A closed-cycle gas-turbine engine 17
2.9 Diagrams for the ideal Brayton cycle [75]: (a) T-s diagram; (b) P-v diagram; (c) T-s diagram with intercooling, reheating, and regeneration 17
2.10 A gas-turbine engine with two-stage compression with intercooling, two-stage expansion with reheating, and regeneration [75] 19
2.11 Typical surface heat flux distributions and cooling schemes for a turbine blade and vane [57] 20
2.12 Schematic of cooling technology in gas turbines [116] 21
2.13 AM parts shipping for gas turbine components by itsubishi Heavy Industries, Ltd. (MHI) Group over a period of six years [114] 22
2.14 (a) Vane 1, HS1 and vane 2 in SGT-800 turbine section [113]; (b) From impingement cooling in cast design to AM in-wall cooling for outer platform of vane 1 of SGT-800 [113] 23
2.15 Conduction, convection, and radiation heat transfer modes [58] 24
2.16 Boundary layer development in convection heat transfer [58] 25
2.17 Radiation exchange [58]: (a) at a surface and (b) between a surface and large surroundings. h is refereed to heat transfer coefficient, called h_{tc} in this work 26

2.18 Diffusion process [58]: (a) Association of conduction heat transfer with diffusion of energy due to molecular activity; (b) One-dimensional heat transfer by conduction (diffusion of energy) . . . 27
2.19 Velocity boundary layer on a flat plate [59] . . . 29
2.20 Thermal boundary layer on a flat plate [59] . . . 30
2.21 Velocity boundary layer development on a flat plate [58] . . . 31
2.22 Comparison of laminar and turbulent velocity boundary layer profiles for the same free stream velocity [58] . . . 32
2.23 (a) Fluctuations of the velocity component u with time at a specified location in turbulent flow [125]; (b) Momentum transfer due to the turbulent fluctuation velocity: fluid particle moving upward through a differential area dA as a result of the velocity fluctuation v' [125] . . . 34
2.24 (a) Entrance region and fully developed flow region of laminar flow through a tube [59]; (b) Turbulent flow in a pipe [59] . . . 37
2.25 Turbulent boundary layer multistrate . . . 39
2.26 Normalized mean velocity profile in a turbulent boundary layer in semi-log coordinates [47] . . . 40
2.27 (a) Defect law for a turbulent pipe flow [81]; (b) Normalized velocity profiles for different n when $m = 2$ [102] . . . 42
2.28 Friction factor for fully developed flow in a circular tube [58] . . . 43
2.29 Sand roughness height k_s [23] . . . 44
2.30 Overview of a PIV set up [90] . . . 46
2.31 (a) Discrepancy between particle and surrounding fluid velocity; (b) Theoretical time response of oil particles with different diameters in air [88] . . . 48
2.32 Discrete representation using a finite number of gray levels . . . 49
2.33 Not overlapping light sheets (top) and overlapping ones (bottom) . . . 50

3.1 Variation of the component of the velocity fluctuation along a nozzle [41] . . . 56
3.2 Wind Tunnel Schematic . . . 57
3.3 Arrangement of the test section for: (a) FULL FOV (Full Field of View) tests: Laser illuminating the plates parallel; (b) BL (Boundary Layer) tests: Laser illuminating the plates perpendicularly . . . 58
3.4 Test Section CAD . . . 59
3.5 Surface Roughness measurement of the test object [115]: (a) Profilometer Mitutoyo Surftest SJ-410 when measuring; (b) One measurement profile . . . 60
3.6 SEM pictures of the inner surfaces of the tested AM channel [107] . . . 61
3.7 Distributions of the spheres: (a) Histogram of the spheres captured from SEM pictures [112]; (b) Adapted gamma distribution and histograms of spheres [115] . . . 61
3.8 CAD design of the up-scaled prototype plate with AM-induced surface roughness. From left: Inconel939, Aluminum1, Aluminum2 . . . 62
3.9 From top, geometry of d-type and k-type slotted walls. Flow is from left to right [52] 63
3.10 Schematic of the testing set-up. Flow direction is perpendicular to the floor, from top to bottom . . . 64
3.11 Nano PIV Laser Head Internal Components . . . 65
3.12 Lenses configuration [65] . . . 66
3.13 Lenses used: (a) N-BK7 Plano-Concave Cylindrical Lens; (b) N-BK7 Plano-Convex Lens . . . 66

3.14 TINI CX seeding generator 67

3.15 (a) Chronos 2.1-HD High-Speed Monochromatic Camera; (b) Samyang 100 mm $f_{\#} = 2.8$ UMC MacroLens for Canon 67

3.16 Camera and Laser support structure on the Dantec Dynamics traverse System . . 68

3.17 Scheme of the Arduino connections 69

3.18 Timing Schematic [121] 69

3.19 Pictures showing the quality defects in images post the camera's black calibration process (with increased contrast for clarity) 70

3.20 Example of field of view for smooth plates tests 72

3.21 Example of field of view for Boundary Layer tests 72

3.22 Example of a cropped section (300×350 pixels of 1920×1080 pixel frame) from PIV images acquired during testing. In both images, an overexposure of 40% compared to the original is applied to make the differences in particle acquisition visible. (a) Image resulting from a 1.5 mm misalignment in the alignment-calibration stage; (b) Image with proper focus 73

3.23 Digital cross-correlation method [88] 73

3.24 Example of detection of a correlation peak, with analysis of an interrogation window localized at the center of Frame A. Illustration obtained using a MATLAB code that incorporates a (DCC) algorithm, using a 32×32 pixel interrogation window, with a 50% overlap and a 9 pixel displacement before finding the cross-correlation peak 74

3.25 Impact of various image pre-processing methods 75

3.26 Velocity Validation. On the x-axis, the u component of velocity, on the y-axis, the v component of velocity 76

3.27 Difference between two areas of the same zoomed PIV image where: (a) no validation was carried out, resulting in erroneous vectors (outliers); (b) a manual validation was performed, taking into account only the vectors aggregated in a single area, which determine the characteristics, presumed to be true, of the flow under examination . 76

3.28 Test campaign conducted on the test object that identifies the upscale roughness typical of Inconel 939. The green rectangles, measuring (1.336×13) mm, pinpoint the tests carried out with the aim of visualizing the flow in the immediate vicinity of the roughness ($FOV = (2.4 \times 1.2)$ cm). The section highlighted in red identifies the area from which the average characteristics of the plate were extrapolated (for example, the average motion field or friction characteristic). These tests were conducted with a wider field of view from (3.8×2.2) cm to (8.1×4) cm 77

3.29 Test campaign conducted on the test object that identifies the upscale roughness typical of Aluminium 1. For the legend, see the description of Figure 3.28 77

3.30 Test campaign conducted on the test object that identifies the upscale roughness typical of Aluminium 2. For the legend, see the description of Figure 3.28 78

3.31 Clauser chart 79

3.32 Clauser chart, interpolation area 80

3.33 Starting from the top left corner, clockwise: matched image I_1; matched image I_2; image intensity product Π; peaks' image ϕ 81

3.34 Particle images of I_1 (red circles) and I_2 (blue circles) and disparity vectors (black arrow). During the calculation phase of the disparity vectors and the peaks (ϕ), the pixels along the image borders were set to zero to avoid errors in the processing operations around each pixel using a search window. Therefore, if a peak is located along the edge of the image, operations attempting to examine the surrounding pixels might fail or yield incorrect results due to the absence of data beyond the border. This is the reason for the missing particles in the graph 82
3.35 Distribution of the disparity vector in the case study 83
3.36 Evaluation of the factors $\boldsymbol{\sigma}$ and $\boldsymbol{\mu}$ for the following case study 83
3.37 Error evaluation, as defined in Equation 3.8, for the current case study 84

4.1 Time averaged velocity magnitude at the center-channel position and point of maximum velocity for smooth plates at $Re = 2.30e + 04$. The point $y/R = 1$ represents the center of the duct 86
4.2 Velocity profile compared with the modified power law and resulting error [%] . . . 86
4.3 Time averaged velocity magnitude near the smooth wall at $Re = 2.48e + 04$. Visualization through streamlines for a illustration of the flow moving straight downward 87
4.4 Log law plots at $Re = 2.48e + 04$ with smooth walls 87
4.5 Non-dimensional velocity profile in wall unit for different Re and different interrogation windows 88
4.6 Dimensionless mean velocity profile u^+ as a function of the dimensionless wall distance y^+ for turbulent rectangular duct flow with Reynolds numbers between $7.56e + 03$ and $3.62e + 04$ 88
4.7 Mean velocity profiles in velocity-defect form for turbulent rectangular duct flow with Reynolds numbers between $7.56e + 03$ and $3.62e + 04$: inset in log-normal axes 89
4.8 Normal Reynolds stresses for $Re_{\tau_{Moser}} = 5.87e + 02$ and $Re_{\tau_{PIV}}$ between $4.55e + 02$ and $6.46e + 02$ 90
4.9 Inner scaling of the vertically averaged streamwise velocity profile for different rough surface, compared with the DNS Moser [39] turbulent boundary-layer profile for smooth surface, and with the experimental data for smooth plates from the current study. The value of the log-law slope κ and the smooth-wall intercept C used in the current investigation are 0.41 and 5, respectively. Considering the plate shown in Figure 3.28 as example, with the origin of the axes located in the bottom right corner, the tests reported in the graph pertain to the position $y = 0.045\,\text{m}$, $x = 0.120\,\text{m}$, with a thickness of the incident laser beam of $2e-3\,\text{m}$ and a field of view of $0.022\,\text{m}$. The x and y axes correspond respectively to the larger and smaller dimensions of the plate 91
4.10 (a) Indicator function Ξ; (b) Modified log-law function Ψ. Tests performed on Inconel 939 at $Re = 2.48e + 04$. The boundary-layer thickness δ was identified as the wall-normal distance at which the vertically-averaged streamwise velocity reached 99% of the free-stream speed $\overline{U}$ given by the volume flow 92
4.11 Mean velocity profiles in velocity-defect form for both smooth and rough walls . . 93
4.12 Topographic map for the three tested rough surfaces. The red rectangle represents the PIV captured area within which the parameter k is calculated 94
4.13 Reynolds stress for the tested rough surfaces at $Re_\tau = 950$ ($u_\tau = 0.311$). The test section is vertical with the x-axis following the streamwise direction of the flow. Consequently, the streamwise component is u, while the wall-normal component is v 95

4.14 Contour maps of Reynolds shear stress for $Re_\tau = 950$ ($u_\tau = 0.311$) 96
4.15 Turbulence production maps for $Re_\tau = 950$ ($u_\tau = 0.311$) 96
4.16 Nusselt map [127] for Inconel 939 at $Re = 2.48e + 04$ 97
4.17 Flow behavior in the vicinity of Inconel surface roughness at $Re = 2.48e + 04$. The images have been cropped to display only the area of interest 98
4.18 Nusselt map [127] for Aluminium 1 at $Re = 2.48e + 04$ 99
4.19 Flow behavior in the vicinity of Aluminum 1 surface roughness at $Re = 2.48e + 04$. The images have been cropped to display only the area of interest 99
4.20 Nusselt map [127] for Aluminium 2 at $Re = 2.48e + 04$ 100
4.21 Flow behavior in the vicinity of Aluminum 2 surface roughness at $Re = 2.48e + 04$. The images have been cropped to display only the area of interest 100
4.22 Analysis area of the SRHT rig [127]. These zones represent the final analysis window of the rig, where the flow is deemed to be fully developed. Highlighted in red is the PIV technique analysis area, measuring (50×1.36) mm. Tests conducted at $Re = 2.48e + 04$ 101
4.23 Skin-friction results for smooth surface. Results compared with the experimental values obtained by Schultz & Flack[79] 102
4.24 Skin-friction results for rough surface. The red stars highlight the skin-friction estimates corresponding to beginning of fully rough regime 102
4.25 Three surfaces comparison for all $Re = 1.0e + 04$ and $Re = 1.5e + 04$ [124] 104
4.26 Skin-friction results for aluminium surface. The red stars highlight the skin-friction estimates corresponding to beginning of fully rough regime, while the red circle represents the inversion point found experimentally 105
4.27 1:1 scale Test object TO2501-1, made of Inconel 939, with an internal diameter of 5 mm and a length of 90 mm. Images obtained using a Zeiss Stemi 2000-C stereomicroscope with Zeiss Axiocam 208 color camera 106
4.28 Darcy friction factor results for smooth surface 106
4.29 Darcy friction factor results for smooth surface compared with results from QSSHT rig in loglog plot 107
4.30 Zoomed-in image near the wall 107
4.31 Median line along which PIV and profilometer tests were conducted for the various roughnesses along this curve 108
4.32 Evaluation of parameters C_f and ΔU^+ for Inconel 939 along the median line for a total of 5 tests 109
4.33 Near wall velocity profile Inconel 939 for $Re = 2.31e + 04$ and $Re = 2.48e + 04$ . . 109
4.34 Evaluation of parameters C_f and ΔU^+ for Aluminium 1 along the median line for a total of 5 tests 110
4.35 Near wall velocity profile Aluminium 1 for $Re = 2.31e + 04$ and $Re = 2.48e + 04$. 110
4.36 Evaluation of parameters C_f and ΔU^+ for Aluminium 2 along the median line for a total of 5 tests 111
4.37 Near wall velocity profile Aluminium 2 for $Re = 2.31e + 04$ and $Re = 2.48e + 04$. 111
4.38 Moody diagram type chart related to the tests carried out on Inconel 939 using the PIV technique and the QSSHT rig. The highlighted area, also defined by the errorbar, shows the maximum measurement error determined by the parameter ζ . 112

4.39 Moody diagram type chart related to the tests carried out on aluminium surfaces using the PIV technique and the QSSHT rig. The highlighted area, also defined by the errorbar, shows the maximum measurement error determined by the parameter ζ. In the top left insert, a zoom of the area surrounded by the rectangle 113
4.40 Fully turbulent Darcy friction factor correlation in a rough channel. The larger markers represent the friction factor data obtained through the analysis performed using PIV technique 114

A.1 A Typical Test Model for Studies of Turbulent Cooling with Rib-Induced Secondary Flow [60] 120
A.2 Sketch of jet orientation relative to rotating axis [78] 120
A.3 (a) Secondary flow induced by pin fins [57]; (b) Conceptual View of Dimple Induced Secondary Flow [60] 121
A.4 Example of lattice cooled blade [30] and schematic of subchannel flow [77] 122
A.5 Gas turbine blade cooling schematic: (a) Path of the flow inside the blade [129]; (b) Typical techniques for turbine blade cooling [105] 122

B.1 Force vectors on an airfoil [101] 128

C.1 Energy Cascade [128] 133
C.2 Schematic Representation of Turbulence Energy Spectrum [128] 134

List of Tables

2.1 AM technology comparison [126] 11
2.2 Surface roughness parameters and their mathematical and discrete definitions . . . 15
2.3 Nomenclature for Types of Flows [38] 36
2.4 Values for the lower and upper bands of transitionally rough regime by Nikuradse [4] 45

3.1 Characteristic Dimensions of the Test Section 59
3.2 Surface Roughness Parameters Comparison. It should be noted the approach by which the roughness parameters for Aluminum 1 and Aluminum 2 correlate with real test object features in different ways: the optimization for the first is in terms of R_a, R_q, and R_z, whereas for the second, it refers to R_{sk} and R_{ku}. The R_z parameter demonstrates an adherence to real conditions for both models: directly for the first and indirectly for the second 62
3.3 Difference between FULL FOV and Boundary Layer tests for smooth plates 71
3.4 Difference between Boundary Layer tests for smooth plates and for rough plates . 72

4.1 Settings used for the tests related to the smooth plates presented. The evaluation of u_τ was carried out using both Relation 3.3 and the Clauser Chart Method (CCM) 89
4.2 Aerodynamic parameters of the turbulent boundary-layer flow over the different multiscale rough surfaces. The value of d is referenced with respect to the bed-plate, which is the region where roughness start to evolve on the plate. This point is the origin of the wall-normal distance y, or y^+ in wall units 93
4.3 Experimental parameters for determining Jiménez's threshold. The non-dimensional roughness height k^+ is evaluated using the friction velocity and the kinematic viscosity 94
4.4 PIV settings for correlation with SRHT rig across all three roughness surfaces . . . 97
4.5 Values of Re_τ and Re required for the different roughnesses to reach the fully rough regime condition (related to the red stars highlighted in Figure 4.24) 103
4.6 Values of k_s^+ and k_s for the three multiscale rough surfaces investigated 103
4.7 PIV settings for test along median line 108
4.8 Evaluation of roughness parameters on the real rough surface. Six tests were conducted to assess the parameters 113

B.1 Comparison between International System and Technical System 125
B.2 Commonly used dimensionless groups in fluid dynamics 128

Nomenclature

Abbreviations

Symbol	Description
2D	Two Dimensional
3D	Three Dimensional
AM	Additive Manufacturing
ASME	American Society of Mechanical Engineers
BL	Boundary Layers
CAD	Computer Aided Design
CCD	Charge-Coupled Device
CCM	Clauser Chart Method
CFD	Computational Fluid Dynamics
CLA	Center Line Average
CLAHE	Contrast Limited Adaptive Histogram Equalization
CMOS	Complementary Metal-Oxide-Semiconductor
CS	Cooling System
DCC	Direct Cross-Correlation
DED	Directed Energy Deposition
DFT	Discrete Fourier Transform
DNS	Direct Numerical Simulation
EBM	Electron Beam Melting
EDM	Electrical Discharge Machining
FFF	Fused Filament Fabrication
FFT	Fast Fourier Transform
FOV	Field Of View

FPS	Frame Per Second
GT	Gas Turbines
HGA	Harmonic Generation Assembly
HPT	Hight Pressure Turbine
HS1	Hight Stage 1
IGT	Industrial Gas Turbines
L-PBF	Laser Powder Bed Fusion
LBGT	Land-Based Gas Turbine
LOM	Laminated Object Manufacturing
LUCi	Litron Universal Control interface
PBF	Power Bed Fusion
PIV	Particle Image Velocimetry
QSSHT	Quasi-Steady State Heat Transfer
RMS	Root Mean Square
SEM	Scanning Electron Microscope
SGT	Small Gas Turbines
SLM	Selective Laser Melting
SLS	Selective Laser Sintering
SR	Surface Roughness
SRHT	Surface Roughness Heat Transfer
TBLs	Turbulent Boundary Layers
TIT	Turbine Inlet Temperature
TKE	Turbulent Kinetic Energy
TS	Test Section
ZPG	Zero Pressure Gradient

Roman and Greek Symbols

Symbol	**Description**	**Dimensions**	**Units**
δ	Momentum Boundary Layer Thickness	L	m
$\Delta\theta^+$	Shift of temperature in the logarithmic region of the flow	–	1
δ_t	Thermal Boundary Layer Thickness	L	m

ΔU^+	Shift of velocity in the logarithmic region of the flow	–	1
k	Height of roughness	L	m
k^+	Height of roughness in wall unit	–	1
k_s	Equivalent Sand Grain Roughness	L	m
k_s^+	Equivalent Sand Grain Roughness in wall unit	–	1
u^+	Mean Velocity in wall unit	–	1
y^+	Distance normal to the wall in wall unit	–	1
α	Absorptivity	–	1
α_{tc}	Molecular diffusivity of heat	$\mathrm{L^2T^{-1}}$	$\mathrm{m^2\,s^{-1}}$
$\dot{q}_x$	Heat Transfer rate in the x-direction per unit area perpendicular to the heat transfer direction	$\mathrm{MLT^{-3}\Theta^{-1}}$	$\mathrm{W\,m^2}$
$\dot{q}_{cond}$	Pure Conduction Heat Transfer rate per unit area	$\mathrm{MLT^{-3}\Theta^{-1}}$	$\mathrm{W\,m^2}$
$\dot{q}_{conv}$	Convection Heat Transfer rate per unit area	$\mathrm{MLT^{-3}\Theta^{-1}}$	$\mathrm{W\,m^2}$
$\dot{q}_{rad}$	Radiative Heat Transfer rate per unit area	$\mathrm{MLT^{-3}\Theta^{-1}}$	$\mathrm{W\,m^2}$
ϵ	Emissivity	–	1
η	Size of the Small Scales close to the Kolmogorov scale	L	m
η_{th}	Thermal Efficiency	–	1
γ	Specific Heat Ratio	–	1
κ	von Kármán constant	–	1
Λ_s	Roughness Parameter introduced by Van Rij	–	1
$\langle\Phi\rangle$	Time Averaged		
μ	Dynamic Viscosity	$\mathrm{ML^{-1}T^{-1}}$	$\mathrm{kg\,m^{-1}\,s^{-1}}$
ν	Kinematic Viscosity	$\mathrm{L^2T^{-1}}$	$\mathrm{m^2\,s^{-1}}$
$\overline{\Phi}$	Reynolds Averaged		
$\overline{U}$	Velocity from Volume Flow	$\mathrm{LT^{-1}}$	$\mathrm{m\,s^{-1}}$
Φ'	Fluctuating Quantities		
Φ	Example Variable	–	1
$\Pi(\frac{y}{\delta})$	Wake Function	–	1

Ψ	Modified Log-Wall Function	–	1
ρ	Fluid density	ML^{-3}	$\mathrm{kg\,m^{-3}}$
ρ_p	Seeding Particles Density	ML^{-3}	$\mathrm{kg\,m^{-3}}$
σ_B	Stefan Boltzmann constant	$\mathrm{MT}^{-3}\Theta^{-4}$	$\mathrm{W\,m^{-2}\,K^{-4}}$
τ_f	Characteristic Time Scale of the Flow	T	s
τ_s	Response Time	T	s
τ_w	Wall Shear Stress	$\mathrm{ML}^{-1}\mathrm{T}^{-2}$	Pa
ε	Real Surface Roughness	L	m
φ_t	Pulse Duration	–	1
Ξ	Indicator Function	–	1
ζ	Normalized Standard Deviation with respect to the average value in percentage %	–	1
A_f	Frontal Area Projected in the direction of the Flow	L^2	m^2
A_s	Square Surface Area	L^2	m^2
A_w	Wetted Area	L^2	m^2
C	Smooth Wall Intercept	–	1
C_f	Skin Friction Factor	–	1
C_K	Kolmogorov Constant	–	1
c_p	Specific heat capacity at constant pressure	$\mathrm{L}^2\mathrm{T}^{-2}\Theta^{-1}$	$\mathrm{J\,kg^{-1}\,K^{-1}}$
c_v	Specific heat capacity at constant volume	$\mathrm{L}^2\mathrm{T}^{-2}\Theta^{-1}$	$\mathrm{J\,kg^{-1}\,K^{-1}}$
D	Diameter	L	m
d	Zero-Plane Displacement	L	m
d^+	Zero-Plane Displacement in wall unit	–	1
D_h	Hydraulic Diameter	L	m
d_p	Particle Diameter	L	m
E	Surface Emissive Power	MT^{-3}	$\mathrm{W\,m^{-2}}$
f	Darcy Friction Factor	–	1
$f_\#$	f-stop	–	1
G	Irradiation	MT^{-3}	$\mathrm{W\,m^{-2}}$

H	Length Scale for Universal Velocity Defect Law	L	m
h	Enthalpy	ML^2T^{-2}	J
h_{tc}	Heat Transfer Coefficient	$MT^{-3}\Theta^{-1}$	$W\,m^{-2}\,K^{-1}$
j_H	Colburn Factor for heat transfer	–	1
k_{tc}	Thermal Conductivity of the Material	$MLT^{-3}\Theta^{-1}$	$W\,m^{-1}\,K^{-1}$
l_τ	Viscous length Scale	L	m
L_c	Characteristic Length	L	m
L_h	Hydrodynamic Entry Length	L	m
M	Magnification Factor	–	1
n_f	Refractive Index of the Fluid	–	1
n_p	Refractive Index of the Particles	–	1
Nu	Nusselt Number	–	1
P	Pressure	$ML^{-1}T^{-2}$	Pa
Pr	Prandtl Number	–	1
q	Dynamic Pressure	$ML^{-1}T^{-2}$	Pa
R	Pipe Radius	L	m
R_a	Arithmetic Mean Deviation	L	m
R_p	Maximum Peak Height	L	m
r_p	Pressure Ratio	–	1
R_q	Root Mean Square Roughness	L	m
R_v	Maximum Valley Depth	L	m
R_z	Maximum Peak to Valley Height	L	m
R_{ku}	Kurtosis	–	1
R_{sk}	Skewness	–	1
Re	Reynolds Number	–	1
s	Entropy	$ML^2T^{-2}\Theta^{-1}$	$J\,K^{-1}$
St	Stanton Number	–	1
Stk	Stokes Number	–	1
T	Temperature	Θ	K
T_∞	Fluid Temperature	Θ	K
T_s	Surface Temperature	Θ	K

U	Velocity at a given radial position r	LT^{-1}	$\mathrm{m\,s}^{-1}$
u	Stream-Wise velocity component	LT^{-1}	$\mathrm{m\,s}^{-1}$
u_∞	Free Stream Velocity	LT^{-1}	$\mathrm{m\,s}^{-1}$
u_τ	Friction Velocity	LT^{-1}	$\mathrm{m\,s}^{-1}$
$U_{\max}$	Maximum Velocity along the center-line of the pipe	LT^{-1}	$\mathrm{m\,s}^{-1}$
v	Wall Normal velocity component	LT^{-1}	$\mathrm{m\,s}^{-1}$
W	Work	$\mathrm{ML}^2\mathrm{T}^{-2}$	J
w	Span-Wise velocity component	LT^{-1}	$\mathrm{m\,s}^{-1}$
w_{net}	Net Work per unit mass	$\mathrm{L}^2\mathrm{T}^{-2}$	$\mathrm{J\,kg}^{-1}$
x	Stream-Wise direction	–	1
y	Wall Normal direction	–	1
z	Span-Wise direction	–	1

Chapter 1

Introduction

In this chapter, the motivations that inspired the conducted work will be presented, followed by an examination of the state of the art of research carried out in this field. It will conclude by outlining the main objectives of the research.

1.1 Motivation

The investigation into turbulent convective heat transfer in the presence of rough surfaces has established itself as an area of considerable interest in scientific research, particularly due to its direct implications in applied fields such as gas turbines and heat exchangers [98] [56] [117]. Such analyses have found a strong practical sector especially following the various studies in the literature conducted in this field: most of the treatises published before 1990 focused on the universal aspects of flows in the presence of rough walls [52]; however, more recent scientific inquiries have placed greater emphasis on distinguishing the peculiarities associated with different types of surface roughness.

Surface roughness manifests in engineering systems through a variety of mechanisms. Intrinsic factors such as material composition, along with manufacturing methods and finishing techniques employed, can lead to surface heterogeneity. In addition, phenomena related to the temporal degradation of the surface, as well as the accumulation of biofilms or other deposits, can exacerbate the condition of roughness. The implication of such morphological variations is significant, as they can greatly affect the fluid dynamic resistance. For example, it has been documented that the formation of fouling can result in an increase in frictional resistance of up to 217% in medium-sized naval units, such as merchant ships, frigates, or destroyers, depending on the type of surface treatment applied [54] . This figure significantly underscores the extent of the impact that surface roughness can exert on the operational efficiency of systems designed in the field of engineering. In the realm of contemporary research, the intellectual fervor towards the analysis of wall roughness manifests in two predominant directions of study. The first theme relates to the fluid dynamic resistance generated by surface roughness and its interactions with the specific geometry of the same. In order to synthesize the analysis of the turbulent boundary layer on rough walls with the established theory of the boundary layer on smooth walls, an approach is introduced where the influence of roughness is conceived as a translation of the mean velocity profile, accompanied by certain modifications [76]. This translation is related to the characteristic scales and morphology of the roughness, using empirical data. This methodology represents the current preferred strategy in the absence of a thorough understanding of the fundamental physical principles governing this phenomenon. The second theme of examination addresses Townsend's wall similarity hypothesis,

which postulates that the sphere of influence of roughness is confined to a domain equal to about five times the roughness height [55], defined as the roughness sublayer. Various empirical investigations and statistical analyses of flows have provided validation for this theory. However, some studies, such as those conducted by Wu et al. [64], suggest that the impact of roughness may propagate much further, also influencing the outer layer. According to the interpretation proposed by Jiménez [52], such discrepancy could arise from the use of experimental data collected at relatively low Reynolds numbers or with modest δ/k ratios (where δ indicates the thickness of the boundary layer and k the height of roughness), conditions that would not guarantee a clear and adequate distinction between the scales of motion, necessary for the wall similarity effect to manifest.

In practical terms, the effect of surface roughness plays a delicate role from a social perspective as well: improved predictions of aerodynamic resistance allow for better informed and more timely decisions. The correlation between cost and aerodynamic resistance is complex and involves socio-economic aspects, such as emissions. In terms of quantifying the economic implications associated with surface roughness, the study carried out by Chung et al.[98] provides a quantitative estimate of the uncertainty in hydrodynamic resistance attributable to roughness, which could result in a fluctuation in the annual operational costs of global naval fleets by approximately 67 billion dollars. This analysis extends beyond the maritime domain, highlighting how, in the aviation sector, uncertainties related to surface roughness can determine variations of up to 33% in total profits [98]. These figures underscore the economic significance of a detailed understanding and accurate control of finishing in engineering applications, to optimize performance and reduce operational costs in the strategic sectors of transport and energy. In this regard, the scientific literature has explored the implications of surface roughness on the performance of gas turbines for over fifty years. Numerous studies in this area have specifically investigated the consequences of the progressive deterioration of gas turbines throughout their operational life cycle. This area of research is particularly significant, as the degradation of surfaces can significantly affect thermal and mechanical efficiency, as well as the overall durability of the turbines. In analyzing the repercussions of pollutant deposition on gas turbines, Zwebek and Pilidis[48][49] assumed a decrease of 1% in the non-dimensional mass flow and a deviation of 0.5% in turbine efficiency. These parameters were incorporated into their component-level model, resulting in a predicted decrease of 1.2% in generated power and 1% in the operational efficiency of the gas turbine [48][49].

a b

Figure 1.1: Various types of roughness: (a) Erosion along the rudder of a ship; (b) Deposition on gas turbine blades, Bons[68]

The increasing demand for energy has acted as a catalyst for the intensification of research in this area, sparking renewed academic and industrial interest. This dynamism is reflected in a series of studies aimed at optimizing the performance and efficiency of systems and devices that

are crucial for the global energy production landscape. In this context, the proposed goal is to develop more sustainable and high-performing energy technologies, capable of effectively meeting the needs of a constantly evolving social fabric and a globalized economy that requires increasingly careful and rational energy resource management.

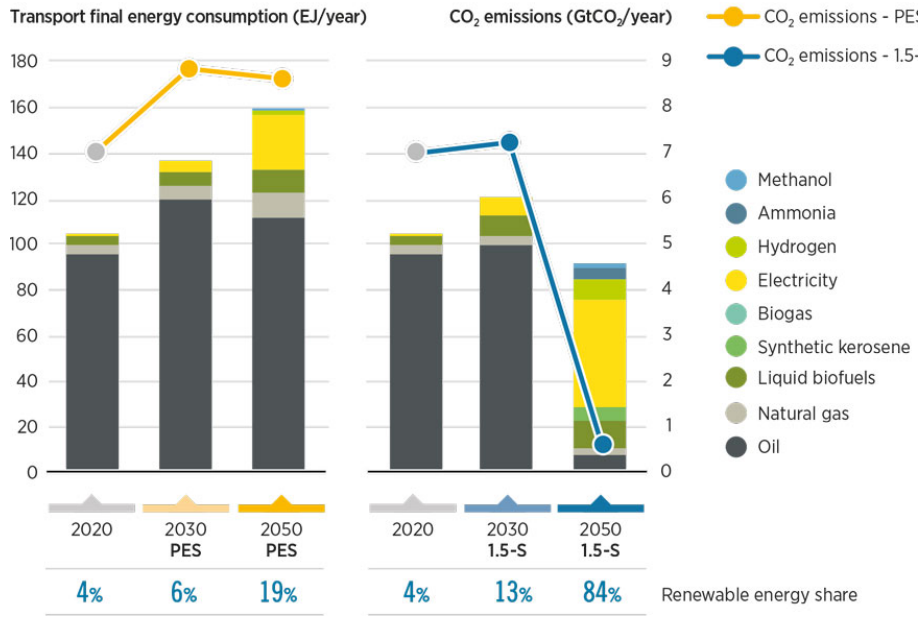

Figure 1.2: World Energy Transitions Outlook, IRENA-International Renewable Energy Agency

In wind still scenarios, wind turbines do not generate energy, while solar panels become less efficient in areas with low solar irradiation or high latitudes. Given the intermittency of these renewable sources, the development of hybrid systems that integrate renewable energies with fossil sources becomes imperative. In this landscape, Land-Based Gas Turbines (LBGT) play a crucial role, contributing to the energy supply both in meeting peak electrical demand and in ensuring a constant supply for base loads. Over the last decade, there has been a significant advancement in the performance of Industrial Gas Turbines (IGT), mitigating the pre-existing technological disparity. This development can be attributed to the adoption of next-generation coatings, advanced materials, and cutting-edge cooling solutions, which have led to a marked increase in both the pressure ratio and the Turbine Inlet Temperature (TIT). The key technology underpinning this engineering implementation is the use of Additive Manufacturing (AM), which allows for the design and construction of more complex internal cooling channels. In the current decade, an efficiency of about 40% has been achieved, compared to the 13% of 1940 [75], when traditional production methods such as casting were the norm.

The benefits of Additive Manufacturing for the advancement of Gas Turbines (GT) are evident. For instance, *Siemens Energy* has employed AM with metallic materials for the in-situ evolution of the *SGT-4000F* turbine blades, testing various cooling strategies and reducing the blade development period by over 75% [85], also allowing for the acceleration of burner development processes for their *SGT-600/700/800*.

The use of advanced AM methods, such as Laser Powder Bed Fusion (L-PBF) for the synthesis of components in metallic alloys, offers the possibility to significantly accelerate prototyping and validation processes. However, this approach is associated with an increase in the degree of Sur-

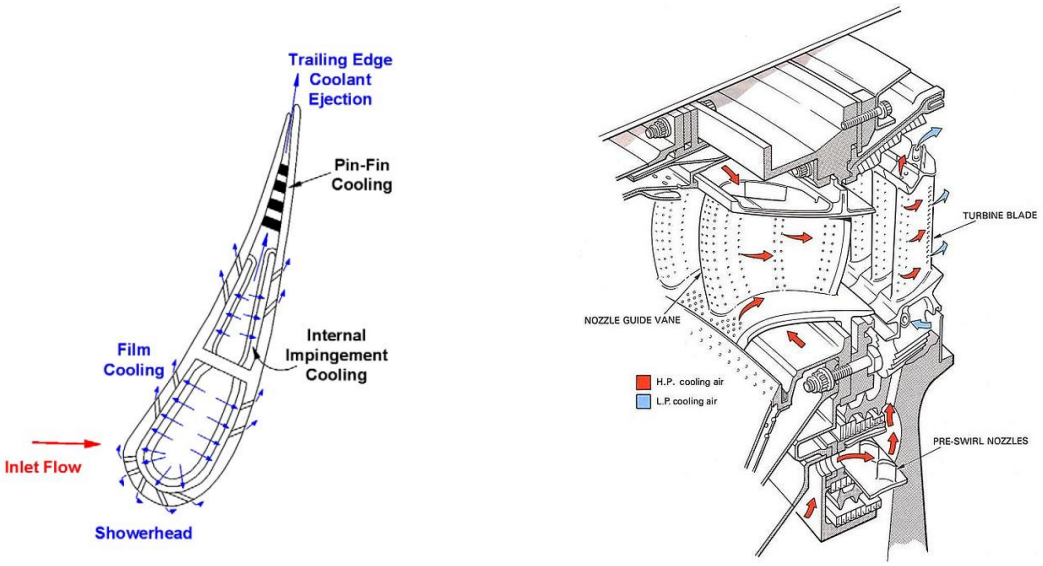

a b

Figure 1.3: Cooling system: (a) Schematic of a Turbine Vane Cross-Section with Impingement and Trailing Edge Pin-Fin Cooling[60]; (b) Modern cooling system, with complex internal channels

face Roughness (SR) of the manufactured parts. To mitigate this effect and maintain the desired aerodynamic properties, it is often necessary to resort to post-production surface treatments. Such treatments are aimed at optimizing the surface finishes, reducing the SR to acceptable levels, and thus ensuring the aerodynamic performance of the component meets the required technical specifications. It is, however, relevant to note that the roughness induced by Additive Manufacturing processes is not easily eliminable in the internal passages of components. The increase in such roughness is known to favor heat transfer, but this often comes at the price of a more pronounced increase in hydrodynamic resistance or a greater loss of load, thus adversely affecting the efficiency of heat transfer. The quantification of these effects remains insufficiently defined to date.

To address this issue, it is essential to develop dedicated infrastructures, as well as to refine measurement techniques and analytical correlation methodologies between aerodynamic and thermal behavior that allow for an accurate estimation of heat transfer in turbulent flow in the presence of rough surfaces.

1.2 Literature Review

Numerous academic studies have focused on investigating the correlation between surface roughness and the behavior of the flow in its immediate vicinity. The central issue to be addressed is correlating the characteristics of a surface's geometry with its aerodynamic behavior and heat transfer performance. Considering turbulent boundary layers (TBLs) developing over rough surfaces, these effects translate into shifts of velocity and temperature in the logarithmic region of the flow, respectively indicated with ΔU^+ and $\Delta\theta^+$, where the symbol $^+$ denotes variables normalized with respect to the inner layer [95]. Early investigations concerning the effects of roughness were primarily focused on examining two specific applications: on one hand, the investigation of the influence exerted by algae and shells on the hydrodynamic resistance of ship hulls [76]; on the other hand, the study of the impact of the internal finish of pipes on load losses, as documented by the pioneering works of Nikuradse [4][9]. His data on pressure losses, obtained by analyzing rough

pipe walls due to the presence of sand, showed different dependencies on the Reynolds number and roughness for various flow regimes. In particular, Nikuradse defined a dimensionless roughness parameter, ($k_s^+ = \frac{k_s u_\tau}{\nu}$), using the actual diameter of the sand grain (k_s), the shear or friction velocity (u_τ), and the kinematic viscosity (ν). Furthermore, Nikuradse [4] observed that for values of this parameter greater than 70 ($k_s^+ > 70$), the pipe loss coefficient is a function of k_s alone, whereas for $5 < k_s^+ < 70$, both Reynolds and k_s play a significant role. These regimes were termed *"completely"* or *"fully" rough* and *"transitionally" rough*, respectively. Schlichting [7], utilizing the empirical data gathered by Nikuradse, established correlations for a variety of roughness configurations atypical to sand, such as rivets, bulges, and protrusions. In this context, Schlichting [23] introduced the notion of "equivalent sand-grain roughness" to describe a roughness attribute (including spatial arrangement) that exerts an impact on frictional loss comparable to that of a homogeneous layer of real sand grains with diameter k_s.

As described by Bones [68], although the quantitative data provided by Schlichting has been subject to critical review by Coleman et al. [25], his approach to roughness based on the conceptualization of "equivalent sand grains" has gained global recognition. Until the recent past, almost every correlation model for determining surface friction, convective heat transfer, and even for the transition of the aerodynamic boundary layer, has employed the parameter k_s [23][45]. The concept of equivalent sand-grain height provides a standard reference point for assessing the dynamic impact of different rough surfaces in the fully turbulent regime. Several studies in the literature have attempted to propose models or correlations to estimate the values of k_s from specific morphological parameters of the surface, such as the spacing between elements, frontal areas, wetted surfaces, and gaps between elements. Van Rij et al. [44] proposed a relationship by analyzing hemispherical surface irregularities, identifying the roughness parameter Λ_s

$$\Lambda_s = \frac{A_s}{A_f}\left(\frac{A_w}{A_f}\right)^{1.6} \tag{1.1}$$

where each hemispherical element with radius r is centered on a square surface of area A_s; A_w refers to the wetted area of the element and A_f to the frontal area projected in the direction of the flow, distributing each element uniformly and staggered along the x axis. As discussed by Léon et al. [95], geometric roughness elements distributed in this way are known to induce increases in the friction coefficient as their density increases, up to a point where *sheltering* effects begin to play a significant role. For this purpose, the correlation proposed by Van Rij et al. [44] for a sparse roughness regime, characterized by $\Lambda_s > 28.12$, is articulated as follows: $k_s/k = 255.5\Lambda_s^{-1.454}$. This parameter, from a numerical standpoint, finds confirmation in the studies proposed by Dirling [19], as subsequently verified by Léon et al. [95]. These empirical relationships are commonly employed for any type of distributed geometric roughness element of height k, implicitly assuming that the flow developing over the studied rough surface can be considered as a turbulent boundary layer (TBL) in a fully-rough regime.

A necessary condition for this to occur is that the statistics and the structure of the turbulence in the boundary layer, beyond the region directly affected by the roughness elements (known as the roughness sublayer), are independent of the surface morphology when rescaled by the external velocity and length scales, respectively indicated with u_τ and δ. As described by Kim [53], Perry et al. [28] conducted experiments using three-dimensional (3D) diamond-shaped roughness with a height of 29 mm, equivalent to 0.35 times the boundary layer thickness δ characteristic of a turbulent boundary layer over a smooth wall. The mesh had dimensions in the streamwise and spanwise

directions of 10.5 mm (0.15δ) and 1.5 mm (0.015δ), respectively. In addition, they considered a two-dimensional (2D) wavy surface with a normalized peak-to-trough height of 17 mm (0.1δ) and a wavelength in the flow direction of 76 mm (0.85δ). In both cases, it was observed that the boundary layers associated with smooth and rough walls show substantially different structures and are subject to distinct length scales within the layer close to the wall. However, it was found that the lower-order statistics turn out to be similar at a sufficient distance from the surface, suggesting that the outer layer remains unchanged by the surface characteristics, regardless of whether it is smooth or rough. Raupach et al. [33] have provided further data, coming from both laboratory and atmospheric settings, that support the hypothesis of the similarity of the outer layer. This phenomenon is recognized in the literature as *wall-similarity* or *Townsend's outer-layer similarity* [20] among turbulent boundary layers of rough and smooth walls. Jimenez [52] has discussed how this wall similarity is expected to manifest only when there is a marked separation of scales between the roughness height k and the thickness of the turbulent boundary layer δ. This suggests that a ratio δ/k greater than $40 - 80$ must be respected. However, there is evidence to indicate that wall similarity can be observed even for significantly lower values of δ/k, especially in the presence of three-dimensional roughness configurations. For example, Castro [61] and later Amir and Castro [70] detected wall similarity with configurations of staggered cubes for values of δ/k higher than 5, while Flack and Schultz [55] observed such similarity for roughness composed of large sand grains with a ratio δ/k higher than 16. These discrepancies in the required thresholds are likely attributable to the fact that the roughness height k represents a geometric parameter that does not provide significant information regarding the aerodynamic behavior of a rough surface.

Léon et al. [95] further analyzed the influence of surface roughness on heat transfer, focusing their study on large hemispherical roughness elements. This study follows in the wake of past works centered on surface elements of the *packed spheres* [22][27] and *staggered hemispheres* [32][36] types. Interestingly, a direct link was suggested between $\Delta\theta^+$ and k_s^+ for these specific roughness geometries, referring to the earlier work of Dipprey and Sabersky [15]. The configuration with staggered and more widely spaced hemispheres, analyzed by Hosni et al. [32] and Hosni et al. [36], was examined from a more general perspective, with the intent of these authors to characterize the evolution of the Stanton number caused by such rough surfaces in relation to the Reynolds number. Dipprey and Sabersky [15] compared the results obtained with existing data in the literature, regarding both theoretical and experimental studies. Increases in the heat transfer coefficient h_{tc} of up to 270% were detected due to the effect of roughness. These increases are normally associated with even more significant increases in the friction coefficient C_f, observing an exception to this general trend only under conditions of high Prandtl numbers, in the transition region between the characteristics of C_f related to the *"smooth"* and *"fully rough"* regimes. It is therefore clear that the motivation behind the study of roughness is not only to associate the local statistics of turbulence with the geometric parameters of the rough surface but also to clarify the fundamental processes involved and to understand how these influence the zone of influence of the roughness. However, due to the characteristics of near-wall flow phenomena, current flow measurement techniques face inevitable challenges [71]. As found by Raupach [33], the accuracy of traditional point-measurement techniques, such as hot-wire probes, is negatively affected by the high intensity of turbulence as well as by the low mean velocity near and within the roughness.

Thanks to rapid advances in computing speed, *direct numerical simulation (DNS)* has been abundantly applied to study turbulence on smooth walls at increasingly high Reynolds numbers. However, adapting this tool to turbulence on rough walls requires much denser computational grids

to resolve the topography of three-dimensional roughness and the flow structures adjacent to it [71]. Consequently, DNS to study turbulence on rough walls has been predominantly implemented for two-dimensional roughness. Nonetheless, some recent studies on this type of roughness have provided valuable insights into the flow structures and turbulence statistics in the roughness layer. For instance, using DNS to assess turbulent flow in a channel over two-dimensional ribs, Ikeda and Durbin [62] observed that the disruption of the three-dimensional vortical streaks in the roughness layer is responsible for the high energy production just above the roughness itself. With a similar roughness configuration in a *ZPG (Zero Pressure Gradient)* boundary layer, Lee and Sung [63] report a significant effect of roughness on the redistribution of turbulent kinetic energy *(TKE)* near the wall. In summary, following the research conducted, none of the experimental or computational studies to date have resolved the turbulence in the roughness layer of a boundary layer, or a flow in a channel, well characterized on a three-dimensional and dense rough wall [71]. As a result, *Particle Image Velocimetry (PIV)* has developed as a non-intrusive measurement technique and has become an increasingly valued tool for studying boundary layers over rough walls [71]. However, many of the PIV measurements conducted do not meet the aforementioned conditions, and their spatial extension is limited by reflections from the wall [42]. Therefore, the primary goal of the present project is to carry out detailed flow measurements in the immediate vicinity of the wall, in order to use the collected datasets to clarify the predominant factors contributing to the generation of turbulence and, consequently, to heat transfer in that region. Through the use of an experimental apparatus equipped with an *NANO S65-15 PIV* class 4 Laser, in conjunction with the adoption of a *Chronos 2.1-HD High-Speed Monochromatic Camera*, it is intended to overcome the issues previously listed, in order to undertake measurements capable of resolving the flow behavior in the immediate vicinity of the roughness, for the purpose of extracting the relevant aerodynamic parameters.

1.3 Research Objectives

As can be deduced from the considerations set forth above, numerous questions remain open regarding the thermal characteristics and flow in conduits with irregular surfaces, especially following the introduction of roughness resulting from the use of Additive Manufacturing technologies. This aspect assumes critical importance and needs to be carefully evaluated during the design phase of various mechanical elements, such as turbine blades that incorporate internal cooling channels. The *Fluid Dynamics Laboratory* of *Siemens Energy AB*, located in Finspång, Sweden, has been engaged for some time in research concerning this field of study.

Throughout the years, various technological applications have been developed within the Swedish department. A *Quasi-Steady State Heat Transfer (QSSHT) rig* has been constructed to examine actual channels developed through AM and to attempt to construct correlations between the Nusselt number Nu, the Reynolds number Re, the Darcy friction factor f, and the Prandtl number Pr. The study involves micro-channels of various lengths and diameters, made of different materials including *Aluminum*, *Inconel 939*, and *Stainless Steel*, with various printing directions. For the study of thermofluid properties, both water (QSSHT Water) and air (QSSHT Air) have been used as heat transfer fluids. The details of the research are outlined in Lehmann [112], Venturi [111], Brugnera [119]. Although the QSSHT rig provides valuable data including thermal and fluid dynamic behavior, it has limitations regarding local heat transfer information. To overcome these constraints, a *Surface Roughness Heat Transfer (SRHT)* rig has been designed, focused on understanding the convective heat transfer coefficient and the Nusselt number in specific surface

areas, such as roughness elements and surface valleys [118]. For details and considerations regarding this test rig, please refer to Wen [115], Brogliato [118]. These research efforts are part of a context of systematic studies that have been ongoing for many years. Within these areas of study, however, there was a persistent knowledge gap regarding the behavior of flow in the presence of rough surfaces. To address this deficit, an experimental PIV facility was conceived and developed in 2023 [121][124], specifically designed to conduct detailed investigations aimed at analyzing the interactions between the boundary layer and up-scaled rough surfaces, used in the context of SRHT research. As a non-invasive measurement technique of the entire flow field, Particle Image Velocimetry has become an increasingly appreciated tool for the study of boundary layers in the presence of rough walls (for example, Nakagawa et al. [42], Hong et al [67], Andersson et al [84]). Therefore, the current research focuses on the analysis of the flow structure in a channel, into which an up-scaled model of surface roughness has been introduced. This model was developed based on images obtained by Scanning Electron Microscope (SEM) of an aluminum sample, with the intent to faithfully replicate the main statistical characteristics of the actual rough surface. Specifically, the three different modeled roughness plates (Aluminium 1, Aluminium 2 and Inconel 939) will be tested to extrapolate the main aerodynamic parameters. Considerations will be made regarding the propagation of turbulent activity linked to the Reynolds shear stress within the channel, and efforts will be made to establish connections with the other two rigs (QSSHT and SHRT) through a common friction parameter. A hypothesis on the roughness parameters that most significantly affect the friction factor f will be the final key to this thesis work.

1.4 Thesis Outline

Chapter 2 will focus on the theoretical background, emphasizing the theoretical aspects necessary for understanding the results and the adopted setup. Chapter 3 will address the adopted work methodology, design choices, settings, and software used and configured for the correct execution of the PIV tests, supported by the methods used for extracting certain adopted parameters. Chapter 4 encompasses the study's results, divided into the validation of the test section, the execution of tests to determine the aerodynamic parameters for smooth and rough plates and various thermal and hydraulic correlations with the other rigs. Chapter 5 defines the conclusions of the work and potential future directions for furthering or improving the analysis.

Chapter 2

Theoretical Background

The following chapter aims to meticulously examine the fundamental concepts that form the foundation of the motivations and objectives outlined in Chapter 1.3.

This analysis will focus on the operational dynamics of turbines in the energy sector, delving into the internal cooling systems and their progression alongside the advancement of cutting-edge Additive Manufacturing techniques. Moreover, the mechanisms governing the principles of heat transfer will be explored, with a specific focus on internal ducts and the behavior of the flow within them. Detailed attention will be given to turbulent structures and boundary layer behavior, including a critical assessment of the effects that surface roughness imparts.

Through this theoretical examination, the intention is to provide a solid foundation for a comprehensive understanding of the mechanisms and technologies that originate and continue to develop within the research field under study.

2.1 Additive Manufacturing

Structures designed for offshore renewable energy extraction face challenging conditions, enduring the constant stress from elements such as waves, wind, and tidal forces that can cause wear and tear over time. These conditions can lead to degradation through corrosion and erosion. To enhance the durability and fatigue life of such engineering structures, the application of Additive Manufacturing techniques has proven to be a beneficial strategy [122]. This innovative manufacturing process can significantly boost the mechanical robustness and resistance to fatigue of components exposed to the demanding offshore environment.

Similar to the renewables industry, the additive manufacturing field has experienced a remarkable uptick in attention over recent years, with a particularly sharp rise in growth beginning in the early 2010s [122]. This trend is illustrated in Figure 2.1, which showcases the increase in revenue generated from both the sale of products and the provision of services from 1992 to 2022. The growth can be attributed to technological advancements within the sector and the inherent benefits of AM. These benefits include the ability to fabricate intricate designs with ease and the reduction in the time required to produce these items when compared to conventional manufacturing techniques [122][114].

The process of 3D printing encompasses much more than just the printing itself, as briefly summarized in Figure 2.2. This technique functions similarly to how an inkjet printer operates, but instead of using ink, 3D printers build up layers of a specific material to transform a digital blueprint into a tangible item. Initially, the item is designed in three dimensions using specialized

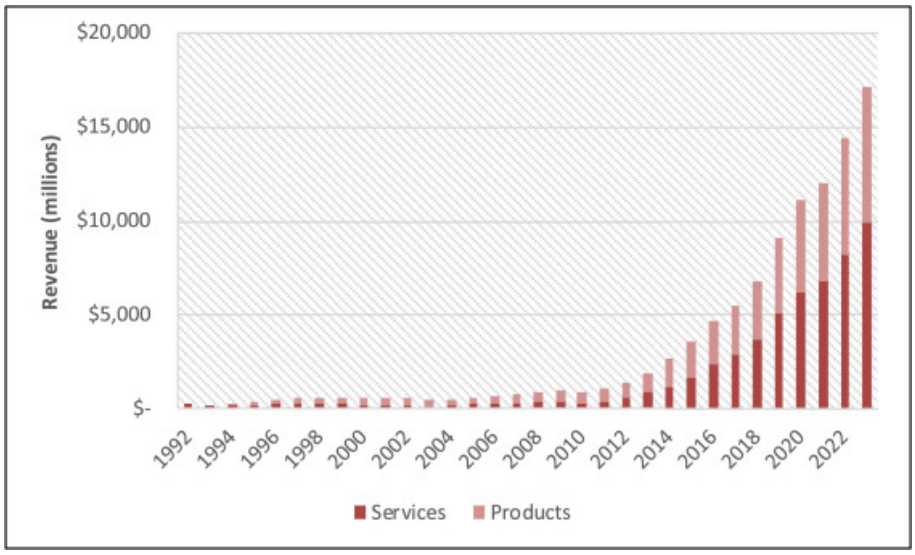

Figure 2.1: Overall AM Industry Revenues 1992–2022 [104]

Computer Aided Design (CAD) software, and the resulting design is saved in an STL format or another format compatible with 3D printers.
After the design phase, the 3D model is processed through a slicing program. This software converts the 3D design into executable commands by dissecting the model into horizontal layers and determining the path that the printing tool will follow (known as G-codes) within each of those layers [86]. These instructions can then be sent to the 3D printer using a USB drive, a direct USB connection, or through a local network.
Taking Fused Filament Fabrication (FFF) [86] systems as an example, the printer's extruder head heats and extrudes the print material, laying it down in precise, thin lines on the build platform to construct the object one layer at a time. After each layer is finished, the platform descends slightly to make room for the next layer. This process repeats until the entire object is fabricated. Once the printing is done, any surplus material, including the base raft and any support structures, is removed to unveil the final product.

2.1.1 Additive Manufacturing Technologies

The following segment explores principal additive manufacturing techniques employed within the offshore energy industry, along with a succinct presentation of other AM methods. For a compre-

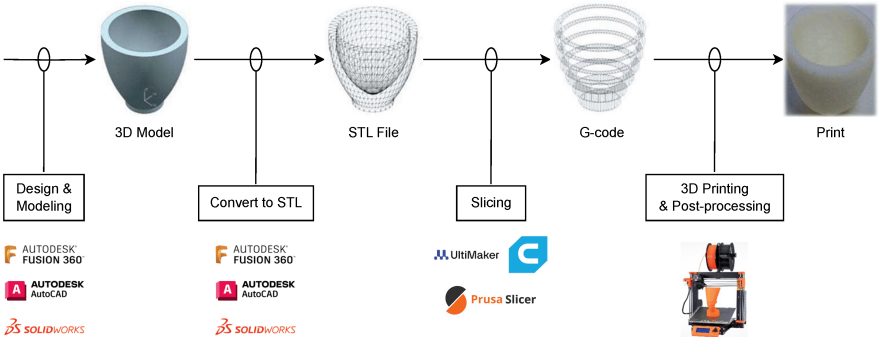

Figure 2.2: Overall workflow of the additive manufacturing process [126]

AM Tech.	Advantages	Limitations	Common Materials
FDM	Low price, Speed efficiency, Low maintenance	Requires high temperatures, Requires supports, Inability for certain geometries	PLA, ABS, PETG
VP	Exceptional details and surface, Ideal for intricate features	Limited build volume, Shrinkage and warping, Toxicity and environmental concerns	Photocurable resins, Waxes, Ceramics
MJ	Exceptional resolution and details, Multi-material and full color, Wide array of materials	High costs, Restricted build volume, Low printing speed	Photopolymers, Thermoplastic polymers, Metal powders
BJ	Full-color, Various materials	Labor-intensive, Complex post processing, Low-density parts	PVP, PVA, PAA
SLS	Support free, Isotropic final products, Complex geometries	Porosity, Shrinkage and impurities, Post-processing for final appearance	Plastics, Composites, Ceramics
SLM	Binder-free, Often faster than SLS, High powder recyclability	High costs, Less material flexibility, Support structures and inert gas	Titanium alloys, Stainless steels, Aluminum alloys
DMLS	Support-free, Various materials of metal alloy, High powder recyclability	High costs, High porosity, Limited build volume	Stainless steels, Titanium, Aluminum
EBM	Excellent material properties, Processing reactive metals, Fast and efficient process	High equipment costs, Additional post processing, Limited selection of materials	Titanium alloys, Niobium-based superalloys, Cobalt-chrome alloys
MJF	High speed and efficiency, Less post-processing, Multiple colors, High ductility	Material limitations, Specific use cases	Polyamides, Thermoplastic Polyurethane, Polypropylene
DED	Minimizes waste, Part repair and modification, Efficiency for larger components	Post-processing for a smooth finish, Low precision	Stainless steel, Titanium alloys, Nickel-based alloys
CFR	Strength and lightness, Customized fiber orientation	High costs, Limited material compatibility	Nylon + carbon fiber, PEEK + carbon fiber, ABS + carbon fiber
LOM	Cost-effectiveness and high speed, Environmental friendliness, Large part fabrication	Low dimensional accuracy and strength, Post-processing for surface finish, Limited material range for composites	Metal foils, Plastics, Paper

Table 2.1: AM technology comparison [126]

hensive understanding of the fundamental mechanisms, benefits, constraints, typical materials, key uses, and evolutionary patterns of these technologies, readers may consult Zhou et al. [126]. For thorough comparison, Table 2.1 delineates the merits, challenges, and frequently used materials across a diverse spectrum of AM technologies.

In the context of offshore applications, metal-based methods are expected to dominate the field of additive manufacturing. One particular technique, known as Sheet Lamination or Laminated Object Manufacturing (LOM), involves stacking and fusing cut sheets of material through methods such as rolling, ultrasonic welding, or adhesive bonding. However, this process is not anticipated to become widespread in offshore settings. This is primarily due to the extensive time required for post-processing, a narrow selection of materials that can be used, and challenges in achieving precise dimensions with the finished product [122]. Conversely, the two techniques that hold the most promise for fabricating components for offshore use are Powder Bed Fusion (PBF) and Directed Energy Deposition (DED). PBF exclusively utilizes a powdered substance as its building material, while DED is versatile, capable of employing both powdered and wire-based feedstocks

in its process.

2.1.1.1 Powder Bed Fusion (PBF)

Powder Bed Fusion (PBF) utilizes an energy source, such as a laser, heat, or electron beam, to melt and consolidate powdered materials into successive layers, building up the final part. Techniques that fall under this category include Selective Laser Sintering (SLS), Selective Laser Melting (SLM), and Electron Beam Melting (EBM). These methods are known for their ability to produce parts that are close to their final shape (near-net-shape) with intricate geometries and offer a broad selection of materials. Nonetheless, the intrinsic characteristics of PBF can result in challenges such as high levels of porosity, thermal stress, suboptimal density, and constraints on the size of the build, presenting potential drawbacks [122]. The energy industry has shown considerable interest in PBF, as exemplified by Siemens' achievement in receiving the Emerging Technology Award from the American Society of Mechanical Engineers (ASME) for their innovative production of gas turbine blades using additive manufacturing, which is illustrated in Figure 2.3.

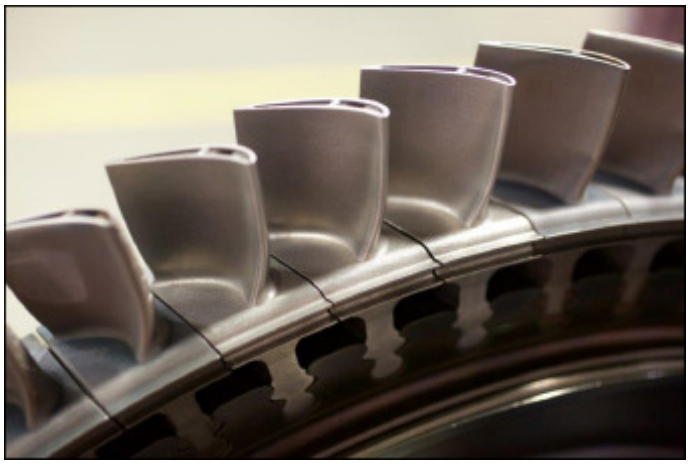

Figure 2.3: Gas Turbine Blades made for Siemens by Material Soultions

To provide an example, Selective Laser Sintering employs lasers as the heating mechanism and represents a variant of powder bed fusion. This technique is adept at facilitating swift prototyping and creates a denser material layer by directing a high-intensity laser onto the powder bed. A standard design for an SLS printer can be seen in a schematic form on Figure 2.4.

The procedure encompasses the following stages: initially, the powder is deposited and the feed container is linked to the build cylinder. Subsequently, an inert gas is introduced into the formation chamber to diminish the oxygen levels. A roller then proceeds to distribute a fine layer of powder across the build platform. In the concluding step, a laser traverses the surface of the powder, selectively melting it to create the designated layers [126].

2.1.1.2 Direct Energy Deposition

DED, or Directed Energy Deposition, involves melting materials using a concentrated energy beam, which could be an electric arc, electron beam, or laser. The molten material is then extruded onto a substrate to build up a structure. Typically, a robotic arm is employed to perform this task, although some systems feature an adjustable build platform that enhances the range of motion and facilitates the fabrication of large components [122].

The substance is dispensed via a nozzle that operates along several planes, enabling the creation of intricate shapes. Figure 2.5 illustrates the functional concept of two distinct DED methodologies

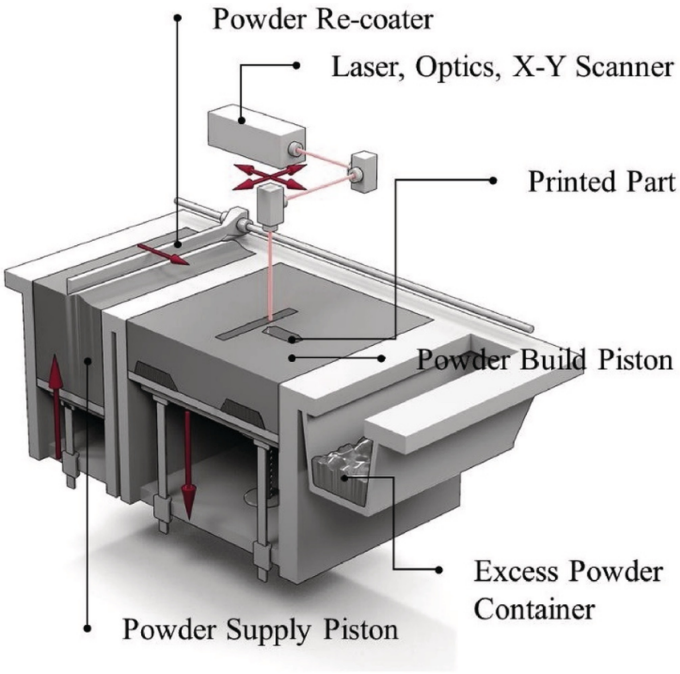

Figure 2.4: Schematic of SLS 3D printers [106]

[126].

Generally, a CAD file governs the process, directing the nozzle's trajectory to form the intended design in a sequential layering method. The meticulous deployment of both energy and substance leads to components that are compact and exhibit a robust adhesion to the base [97]. Recent progress in DED technology is consistently expanding its range of compatible materials, opening doors for its use in increasingly specialized domains [126]. Such advancements not only improve the versatility of DED but also highlight its capacity to transform manufacturing methods by handling a wide variety of materials for bespoke and complex productions.

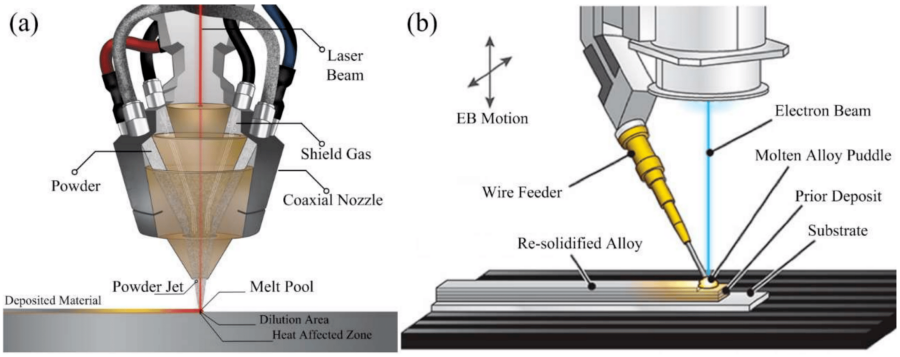

Figure 2.5: Schematic of directed energy deposition (DED) [126]: (a) Powder DED (laser source); (b) Wire DED (E-beam source)

2.1.2 Roughness parameters

The rapid advancement of additive manufacturing and its widespread adoption for the production and engineering of high-performance materials have necessitated the development of new validation and qualification protocols. These cutting-edge production technologies typically result in the formation and often enhancement of the surface texture of components, also referred to as Surface

Roughness (SR). Given the significance of these parameters in the realm of 3D fabrication and development, a reevaluation of traditional qualification methods is imperative [92]. Qualifying a component via non-destructive methods entails utilizing a comprehensive set of measurements that verify the material's quality integrity. Surface roughness is among these indicators. Although historically a specified requirement for components, it now serves an additional role as a marker of AM process efficiency, particularly in metal AM processes, such as laser powder bed fusion (L-PBF) [92].

The real surface geometry is so complicated that a finite number of parameters cannot provide a full description [43]. ASME B46.1 [91] and ISO 4287 [109] are the two commonly used standards for defining surface texture, including roughness, waviness, and lay. If the number of parameters used is increased, a more accurate description can be obtained. This is one of the reasons for introducing new parameters for surface evaluation. Surface roughness parameters are normally categorized into three groups according to their functionality. These groups are defined as *amplitude parameters*, *spacing parameters*, and *hybrid parameters* [43].

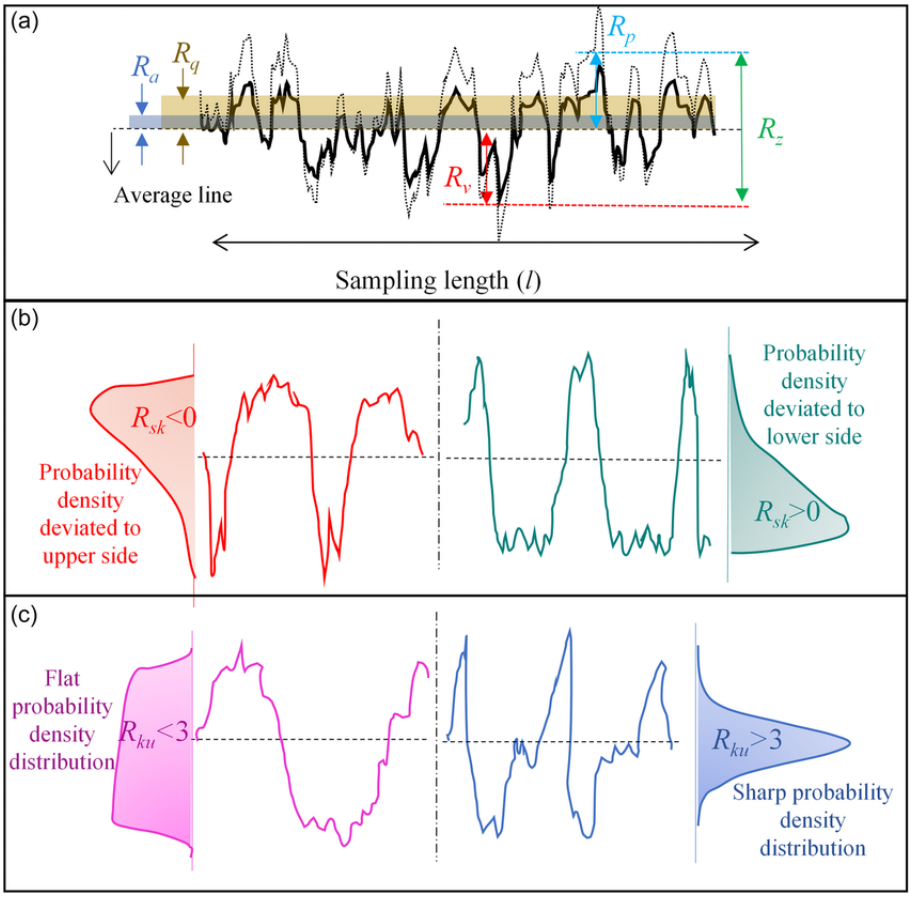

Figure 2.6: Schematic of the profile texture parameters [123]: (a) R_a, R_q, R_p, R_v, R_z, (b) R_{sk} and the height probability distribution, (c) R_{ku} and the height probability distribution

In the subsequent parts of this work, the parameters defined under the "amplitude parameters" category will be considered, as they more significantly characterize a random roughness, such as the one that will be introduced later in the work, and because they are the most important parameters for characterizing surface topography [43]. Amplitude parameters (R or S) can be defined using a height-map to characterize the surface based on the vertical deviations of the roughness profile from the mean line [99]. Commonly used amplitude parameters (based on the profile shown in Figure 2.6) are listed in Table 2.2.

Parameter	Description	Mathematical description	Discrete implementation
R_a	Arithmetic mean deviation	$\frac{1}{l}\int \lvert y\rvert dx$	$\frac{1}{n}\sum_{i=1}^{n} \lvert y_i\rvert$
R_q	Root-mean-square roughness	$\sqrt{\frac{1}{l}\int \lvert y\rvert dx}$	$\sqrt{\frac{1}{n}\sum_{i=1}^{n} y_i^2}$
R_v	Maximum valley depth below the mean line, within a single sampling length	$\lvert \min y(x)\rvert$	$\lvert \min y_i\rvert$
R_p	Maximum peak height above the mean line, within a single sampling length	$\max y(x)$	$\max y_i$
R_z	Maximum peak to valley height of the profile	$R_v + R_p$	
$R_{z(DIN)}$	Ten-point height based on the definition in DIN standard, within a five sampling length	$\frac{1}{10}(\sum_{j=1}^{5} R_{p_j} + \sum_{j=1}^{5} R_{v_j})$	
$R_{z(ISO)}$	Ten-point height based on the definition in ISO standard, within a five sampling length	$\frac{1}{5}(\sum_{j=1}^{5} R_{p_j} - \sum_{j=1}^{5} R_{v_j})$	
R_{sk}	Skewness	$\frac{1}{R_q^3}\frac{1}{l}\int \lvert y\rvert^3 dx$	$\frac{1}{nR_q^3}\sum_{i=1}^{n} y_i^3$
R_{ku}	Kurtosis	$\frac{1}{R_q^4}\frac{1}{l}\int y^4 dx$	$\frac{1}{nR_q^4}\sum_{i=1}^{n} y_i^4$

Table 2.2: Surface roughness parameters and their mathematical and discrete definitions

To provide a broad overview of these parameters, a brief discussion is presented to highlight their key features.

The *arithmetic mean roughness*, denoted as R_a and also referred to as the center line average (CLA), is the most widely adopted roughness parameter in routine quality assessment [43]. It quantifies the mean of the absolute deviations of surface irregularities from the central line across a single sampling interval. In comparison, the *root mean square roughness*, symbolized as R_q or RMS, quantifies the standard deviation of the surface height distribution, making it a crucial parameter for statistical analysis of surface textures. This measure tends to be more responsive to significant deviations from the central line compared to the arithmetic mean. Additionally, the RMS central line is characterized by its role in bisecting the profile in such a way that the total of the squared deviations of the profile's height relative to this line is minimized [43].

Other prevalent parameters for assessing surface roughness encompass *skewness* R_{sk} and *kurtosis* R_{ku}. Skewness offers a quantitative measure of the asymmetry of the surface texture relative to the mean line. Surfaces with a negative skewness predominantly consist of troughs, whereas surfaces with positive skewness are largely made up of peaks [92]. Kurtosis evaluates the pointedness of the surface's peaks. The establishment of these conventional definitions for surface roughness came before the emergence of additive manufacturing technologies [92].

The *ten-point height*, R_z, can be described by two distinct methodologies according to the defining system: the International ISO standard and the German DIN standard. In the current analysis, the ISO standard is utilized. This system defines R_z as the vertical distance between the average of the five highest peaks and the five deepest valleys within the measured length of the profile. This parameter is more sensitive to occasional high peaks or deep valleys than R_a [43]. Moreover, R_p represents the *maximum profile peak height* above the mean line, while R_v indicates the *maximum profile valley depth* below the mean line [43]. The parameters just described can be visually consulted in Figure 2.6.

For a more exhaustive description of these and other parameters belonging to different families, consult Gadelmawla et al [43].

2.2 Gas turbine

The inaugural installation of a gas turbine for an electric utility occurred in 1949 within a pioneering combined-cycle power plant in Oklahoma. Constructed by General Electric, this turbine had a production capacity of 3.5 MW [75]. Up until the mid-1970s, gas turbines grappled with issues of low efficiency and suboptimal reliability. Historically, the realm of base-load electric power generation was predominantly ruled by the more sizeable and established coal and nuclear power plants.

2.2.1 The ideal cycle for Gas-Turbine engines

In steam, gas, or hydroelectric power plants, the turbine is the device that drives the electric generator. As the fluid flows through the turbine, it performs work on the blades, which are connected to the shaft. Consequently, the shaft rotates, resulting in the production of work by the turbine. Compressors, as well as pumps and fans, are devices used to increase the pressure of a fluid. Work is delivered to these devices from an external source via a rotating shaft. It is important to distinguish that turbines generate power as an output, whereas compressors, pumps, and fans consume power as an input. Most *power-generating devices* operate on *cycles*, and the examination of these power cycles is a fascinating and crucial aspect of thermodynamics. When these cycles are abstracted by eliminating all internal irreversibilities and complexities, what remains is a cycle that closely mirrors the real-world cycle, yet is comprised entirely of internally reversible processes. Such a theoretical construct is known as an *ideal cycle*.

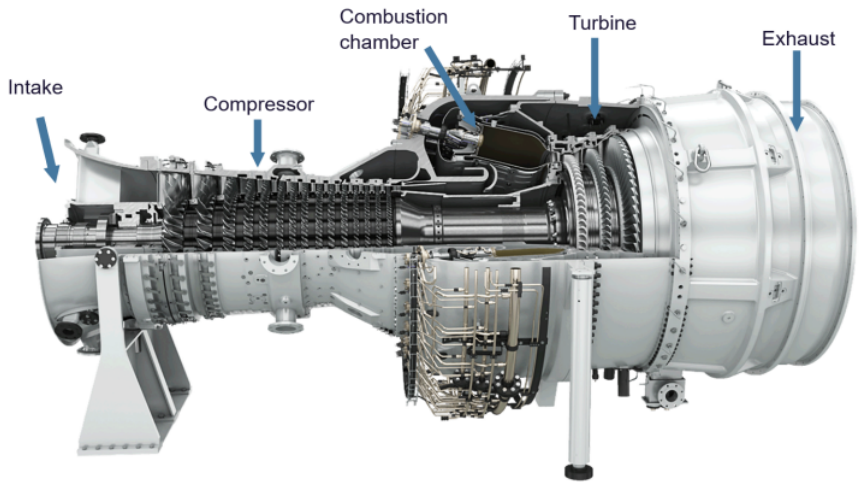

Figure 2.7: A modern land-based gas turbine used for electric power production. This is a Siemens Energy SGT-800 gas turbine used for industrial power generation and oil and gas applications. It has a length of 20.8 m, it weighs 28.5×10^4 kg, and produces 62.5 MW at 6600 rpm with a gross efficiency of 41.1% and a NO_x emissions level of $15 - 25$ ppmvd [120]

Examples of cycles that are important for engineering applications include: the *Carnot cycle*, composed of four totally reversible processes; the *Otto cycle*, which is the ideal cycle for spark-ignition reciprocating engines; the *Diesel cycle*, that is the ideal cycle for compression-ignition engines and the *Brayton cycle*, which is the ideal cycle for gas-turbine engines. It is clear that in this work, reference will be made to the latter.

The Brayton cycle was first proposed by George Brayton for use in the reciprocating oil-burning engine that he developed around 1870 [75]. Today, it is used only for gas turbines, where both the compression and expansion processes take place in rotating machinery. Gas turbines typically operate on an open cycle, as shown in Figure 2.8a. Fresh air at ambient conditions is drawn into the compressor, where its temperature and pressure are raised. The high-pressure air then proceeds to the combustion chamber, where fuel is burned at constant pressure. The resulting high-temperature gases enter the turbine, where they expand to atmospheric pressure while producing power. The exhaust gases leaving the turbine are discarded (not recirculated), which classifies the cycle as an open cycle.

The open gas-turbine cycle described above can be modeled as a closed cycle, as shown in

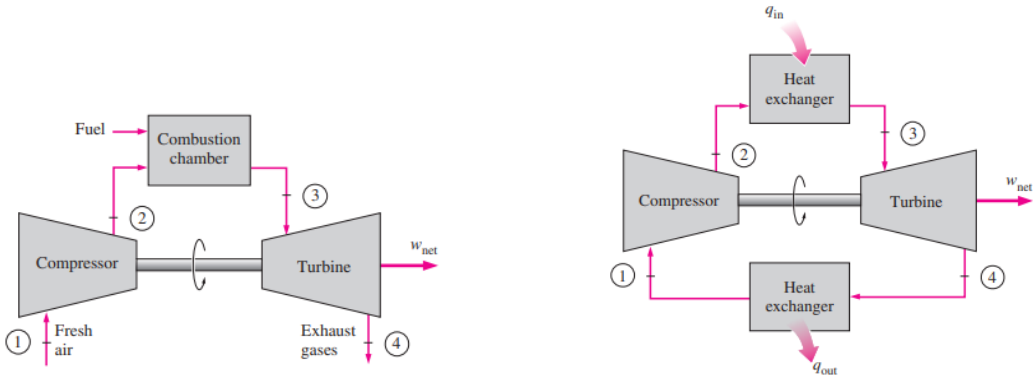

a b

Figure 2.8: Schematic representation of a gas turbine [75]: (a) An open-cycle gas-turbine engine; (b) A closed-cycle gas-turbine engine

Figure 2.8b, by utilizing air-standard assumptions. In this model, the compression and expansion processes remain the same, but the combustion process is replaced by a constant-pressure heat-addition process from an external source, and the exhaust process is replaced by a constant-pressure heat-rejection process to the ambient air. The ideal cycle that the working fluid undergoes in this closed loop is the Brayton cycle, which consists of four internally reversible processes:

1-2 Isentropic compression (in a compressor)

2-3 Constant-pressure heat addition

3-4 Isentropic expansion (in a turbine)

4-1 Constant-pressure heat rejection

It is important to acknowledge that the components of a steam power plant, such as turbines, compressors, heat exchangers, and pumps, typically operate continuously for extended periods, often spanning several months, before the system undergoes a shutdown for maintenance. Consequently, for the purposes of analysis, these components can be aptly treated as *steady-flow* devices [75].

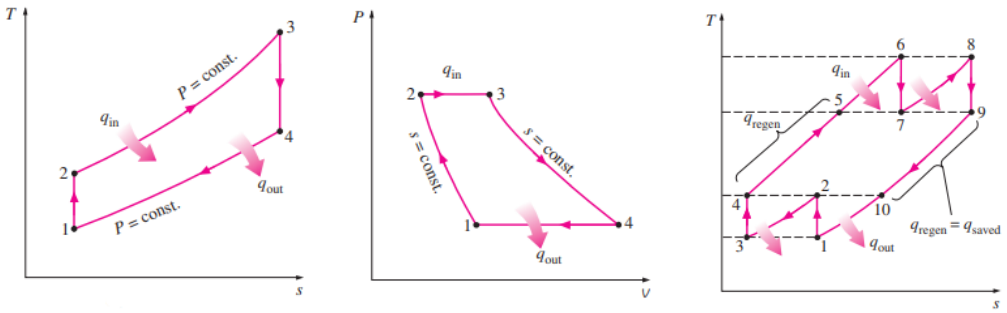

a b c

Figure 2.9: Diagrams for the ideal Brayton cycle [75]: (a) T-s diagram; (b) P-v diagram; (c) T-s diagram with intercooling, reheating, and regeneration

The temperature-entropy (T-s) and pressure-specific volume (P-v) diagrams for an ideal Brayton cycle are illustrated in Figure 2.9. Notice that all four processes of the Brayton cycle are

executed in steady-flow devices; consequently, these processes necessitate analysis as steady-flow processes. Assuming negligible changes in kinetic and potential energies, the energy balance for a steady-flow process, on a per unit mass basis, is given by:

$$\Delta h = h_{exit} - h_{inlet} = (q_{in} - q_{out}) + (w_{in} - w_{out})$$

where Δh represents the change in specific enthalpy, q is the heat transfer per unit mass, and w is the work per unit mass.

Heat transfers to and from the working fluid are described by the following equations:

$$q_{\text{in}} = h_3 - h_2 = c_p(T_3 - T_2),$$

and

$$q_{\text{out}} = h_4 - h_1 = c_p(T_4 - T_1).$$

Under the assumption of a cold-air-standard analysis, the thermal efficiency of the ideal Brayton cycle is:

$$\eta_{\text{th,Brayton}} = \frac{w_{net}}{q_{in}} = 1 - \frac{q_{\text{out}}}{q_{\text{in}}} = 1 - \frac{c_p(T_4 - T_1)}{c_p(T_3 - T_2)} = 1 - \frac{T_1(T_4/T_1 - 1)}{T_2(T_3/T_2 - 1)}$$

Given that processes 1-2 and 3-4 are isentropic, and considering the pressure relationships $P_2 = P_3$ and $P_4 = P_1$, can be defined:

$$\frac{T_2}{T_1} = \left(\frac{P_2}{P_1}\right)^{(\gamma-1)/\gamma} = \left(\frac{P_3}{P_4}\right)^{(\gamma-1)/\gamma} = \frac{T_3}{T_4}$$

By substituting the relevant equations into the expression for thermal efficiency and performing appropriate simplifications, one obtains:

$$\eta_{\text{th,Brayton}} = 1 - \left(\frac{P_1}{P_2}\right)^{(\gamma-1)/\gamma} = 1 - \frac{1}{r_p^{(\gamma-1)/\gamma}}$$

where

$$r_p = \frac{P_2}{P_1}$$

is the *pressure ratio* and γ is the *specific heat ratio* (c_p/c_v). From Equation 2.2.1 is clear that the thermal efficiency of an ideal Brayton cycle depends on the pressure ratio of the gas turbine and the specific heat ratio of the working fluid. The air in gas turbines performs two important functions: it supplies the oxidant necessary for fuel combustion and serves as a coolant to keep the temperature of various components within safe limits.

The primary application domains for gas turbine engines encompass *aircraft propulsion* and *electrical power generation*. In the context of aircraft propulsion, the gas turbine is engineered to produce just enough power to operate the compressor and a minor generator that supplies energy to the auxiliary systems. High-speed exhaust gases produce the necessary thrust to propel the aircraft forward. Gas turbines are also employed as stationary power plants for electricity generation, either as independent units or in combination with steam power plants in cogeneration systems. In such facilities, the exhaust gases from the gas turbine act as the heat source for steam production. In addition, the gas turbine cycle can be conducted in a closed-loop configuration,

which is particularly applicable in nuclear power plants. In this scenario, the working fluid is not restricted to air; instead, gases with more favorable properties, such as helium, may be utilized [75].

2.2.2 The Brayton Cycle with Intercooling, Reheating and Regeneration

Since its initial successful development in the 1930s, the gas turbine has undergone remarkable advancements and expansion. The early models of gas turbines constructed in the 1940s and 1950s achieved simple-cycle efficiencies of about 17% due to low compressor and turbine efficiencies and low turbine inlet temperatures due to the metallurgical limitations of those times.

In particular, various areas of interest have emerged where research has concentrated on enhancing the efficiency of cycle processes. A particularly effective strategy for increasing thermal efficiency has involved modifying the conventional thermodynamic cycle by adopting advanced systems such as intercooling, regeneration (or recuperation), and reheating. These measures aim to optimize the use of thermal energy in the process, reducing losses and maximizing the work output of the turbine. The result is a significant increase in overall efficiency, potentially doubling that achieved with a simple cycle.

The efficiency of a turbine's work output, operating across two different pressure levels, can be enhanced through a method known as multistage expansion with reheating. By expanding the gas in successive stages and applying reheating between these stages, the process can achieve greater output without the need to increase the cycle's maximum temperature. With an increase in the number of expansion stages, the process approaches an isothermal expansion.

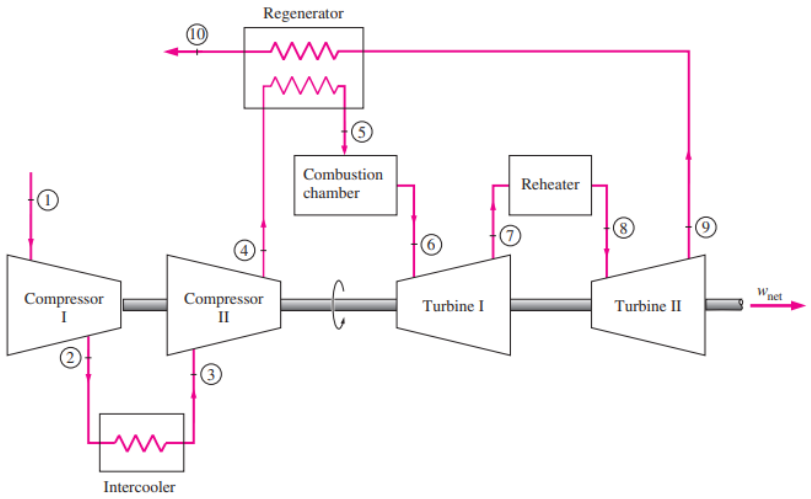

Figure 2.10: A gas-turbine engine with two-stage compression with intercooling, two-stage expansion with reheating, and regeneration [75]

This technique is grounded in a fundamental concept: the work done during steady-flow compression or expansion is directly related to the fluid's specific volume. Consequently, optimizing the work output involves minimizing the specific volume during compression and maximizing it during expansion, which is effectively achieved with intercooling and reheating. These methods result in the working fluid exiting the compressor at a cooler temperature and leaving the turbine at a warmer temperature, thus enhancing the potential for regeneration and making it a more viable process [75]. A schematic of the physical arrangement and the $T - s$ diagram of an ideal two-stage

gas-turbine cycle with intercooling, reheating, and regeneration are shown in Figures 2.9c and 2.10.

While intercooling and reheating contribute to an improved back work ratio for a gas-turbine cycle, it's important to note that they do not inherently increase thermal efficiency. In fact, without regeneration, these methods invariably reduce thermal efficiency. This is because intercooling lowers the average temperature at which heat is supplied, and reheating raises the average temperature at which heat is expelled, as also depicted in Figure 2.9c. Therefore, in gas turbine power plants, the strategy is to always pair intercooling and reheating with regeneration to achieve an efficient system.

2.2.3 Turbine Blade Cooling

The current state of the art and the field of application that offers the most room for development in enhancing turbine performance is related to increasing the Turbine Inlet Temperature (TIT). Turbine Inlet Temperatures have incrementally climbed from about 540°C in the 1940s to 1425°C [75] [110] [57] and even higher in modern applications. These increments have been made feasible by the introduction of novel materials and cutting-edge cooling techniques for vital components. This includes the application of ceramic coatings on turbine blades and employing the compressor's exhaust air for blade cooling. To sustain high turbine inlet temperatures when utilizing air-cooling methods, the combustion temperatures must be increased to offset the cooling impact of the air utilized for cooling: efficient use of cooling air becomes more important to achieve cycle efficiency gains. Therefore, sophisticated cooling schemes such as augmented internal cooling and external film cooling are two important issues that need to be addressed to ensure high-performance, high-power gas turbines for both aircraft and land-based applications [57]. Figure 2.11 shows a typical heat flux distribution on the surfaces of a turbine vane and blade and the associated internal and external cooling schemes.

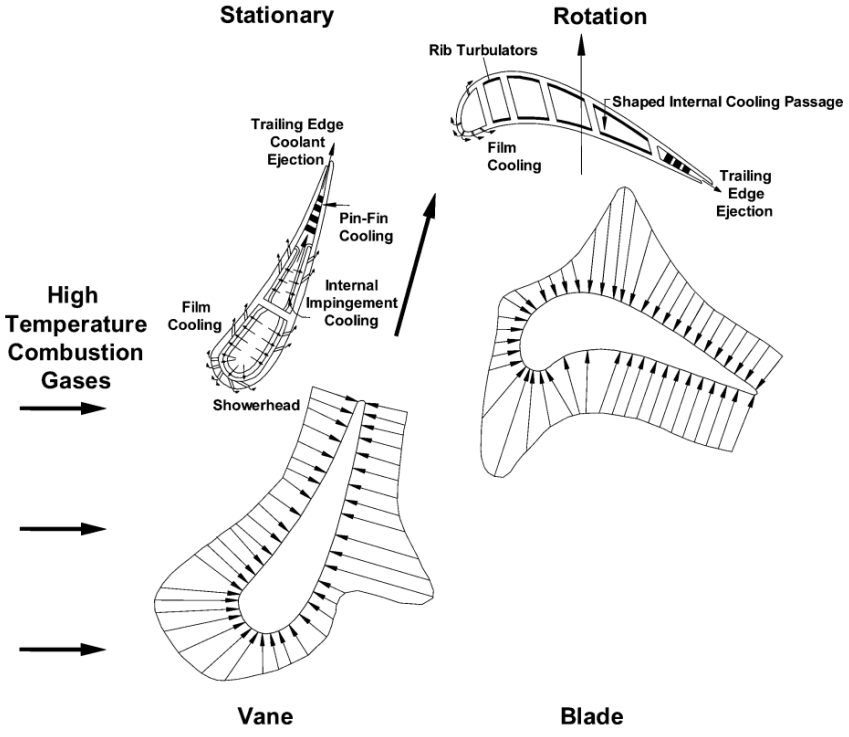

Figure 2.11: Typical surface heat flux distributions and cooling schemes for a turbine blade and vane [57]

The cooling of gas turbine blades is conducted through both internal and external mechanisms. Internal cooling is facilitated by channeling the cooling fluid through rib-turbulated serpentine channels within the blade. Techniques such as jet impingement and pin-fin configurations are also employed for internal cooling. External cooling, commonly referred to as film cooling, involves ejecting the internal cooling air through specific holes to create a protective coolant film over the blade's exterior surface against the hot combustion gases. The design of the turbine cooling system must aim to minimize the utilization of compressor discharge air for cooling purposes, as its extraction results in a decrease in the thermal efficiency and the power output of the gas turbine engine [57].

Figure 2.12 illustrates the typical cooling technology with three major internal cooling zones in a turbine rotor blade, featuring strategic film cooling on the leading edge, trailing edge, pressure surface, suction surface, and blade tip region.

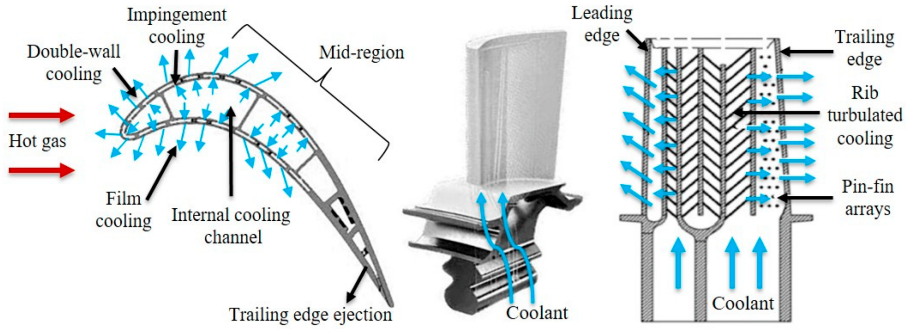

Figure 2.12: Schematic of cooling technology in gas turbines [116]

Internal cooling is achieved by passing coolant through several enhanced serpentine passages inside the blades, thereby extracting heat from the blade's external surface. Methods such as jet impingement cooling, rib turbulators, dimples, and pin-fin cooling are utilized for internal cooling. External cooling, also known as film cooling, involves ejecting the internal coolant air through discrete holes to form a protective coolant film over the external surface of the blade, shielding it from the hot combustion gases [87]. For a brief description of the most commonly used cooling techniques in the industrial field, the reader is referred to Appendix A.

2.2.4 AM Components for Gas Turbine Application

One of a gas turbine engine's main parameters is the turbine inlet temperature [80][57][75]. Elevated TIT correspond to increased engine efficiency. However, the values of TIT are constrained by the thermal resistance of the metal alloys used in turbine blades. Raising the TIT necessitates the adoption of superalloys, thermal barrier coatings, and advanced cooling systems (CS), posing one of the main challenges in blade manufacturing [80]. Blades equipped with intricate CS, film cooling holes, and technologies to enhance heat transfer are typically used in the initial stages of high-pressure turbines (HPT). Precision casting has been the traditionally favored method for producing such components, requiring specialized equipment [80]. Nonetheless, the limitations of this technology prevent the application of more effective and complex CS such as deflector systems, hindered by significant curvature along the chord line, or penetrating systems. With the rapid advancement of additive manufacturing, it is now possible to create blades with much more intricate geometries. To this end, it becomes imperative to move beyond current design experience and implement new optimization methods to maximize the benefits of using AM in blade production [114].

In recent times, the increase in machinery dimensions, the rapid construction rate using multi-laser technology, and the reduction of equipment costs have contributed to the anticipated increase in the number of components suitable for additive manufacturing processes [114]. The consideration of adopting a complex internal cooling structure for gas turbine components is driven by the potential to enhance performance through the reduction of cooling air requirements. Such structures cannot be fabricated using conventional manufacturing methods due to the issues outlined previously and are therefore exclusively producible through additive manufacturing techniques. This shift in production methodology reflects a strategic approach to optimize thermal management within gas turbine systems, leveraging the advanced capabilities of AM to achieve complex internal geometries that facilitate more efficient cooling. The Figure 2.13 depicts the quantity of gas turbine components produced using additive manufacturing technology and shipped by the Mitsubishi Heavy Industries, Ltd. (MHI) Group since the commencement of AM technology for mass production in 2017.

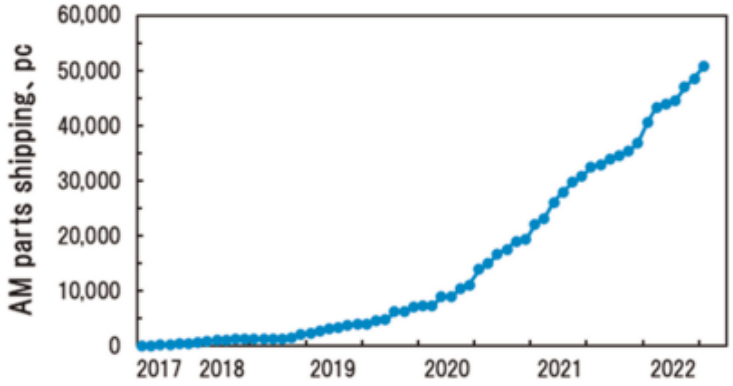

Figure 2.13: AM parts shipping for gas turbine components by itsubishi Heavy Industries, Ltd. (MHI) Group over a period of six years [114]

The integration of additive manufacturin techniques in the production of Land-Based Gas Turbine components, particularly within combustor sections, has been met with considerable success at Siemens Energy. To exemplify the progress, an initiative was launched to incorporate AM components into the high-temperature SGT-800 product [89][114][113]. Research efforts, including those by Lindbäck et al.[113] and Tanigawa et al.[114], have played a significant role in uncovering the advantages AM technology brings to this type of turbine. Notable benefits identified include [113]:

- *Enhanced Aerodynamic Performance:* AM enables the creation of more optimally shaped airfoils that are not limited by traditional casting methods, which often can't produce bowed shapes due to factors such as casting limitations and the need to incorporate cooling mechanisms within the mold. AM technology bypasses these constraints by integrating cooling features directly into the wall structure, allowing for improved aerodynamics. Additionally, AM allows for the production of much thinner trailing edges, facilitating advanced designs like centerline ejection or cut-back;
- *Cooling Efficiency Gains:* the design of cooling systems with AM focuses on minimizing temperature gradients and reducing the amount of coolant needed. By placing cooling channels closer to the surface in contact with hot gases, the cooling agent achieves higher exit temperatures, indicating a boost in cooling efficiency;

- *Extended Component Lifespan:* due to the innovative cooling mechanisms and temperature management facilitated by AM, components can sustain higher temperatures for extended periods, thereby increasing their operational lifespan.

To illustrate the advancements discussed, an example is provided in the Figure 2.14a showing the development of components such as vane 1, HS1, and vane 2 for the Siemens Energy-owned SGT-800 turbine. Figure 2.14b highlights the transition in cooling methods from impingement cooling in the outer platform of the cast vane 1 to the in-wall cooling scheme in the newly developed AM vane 1.

A critical consideration for this AM component lies in the area of heat transfer. The challenging aspect is to accurately predict the friction factor and heat transfer coefficients in AM channels. As previously mentioned, these channels typically exhibit greater surface roughness compared to those created through Electrical Discharge Machining (EDM) or precision casting processes. Siemens Energy, along with researchers at the Fluid Dynamics Laboratory, has invested considerable effort to comprehend the impact of various parameters, such as diameter, build angle, and build plate position, on the heat transfer characteristics. This thesis also endeavors to contribute to this understanding.

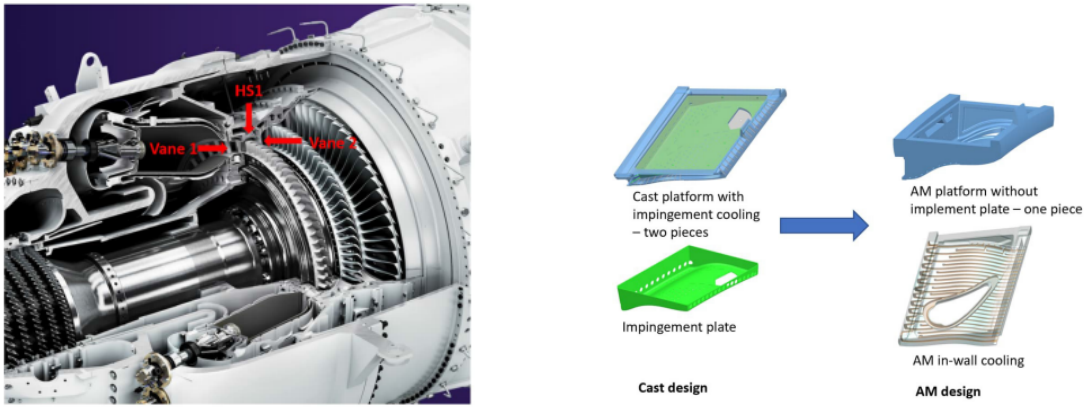

a b

Figure 2.14: (a) Vane 1, HS1 and vane 2 in SGT-800 turbine section [113]; (b) From impingement cooling in cast design to AM in-wall cooling for outer platform of vane 1 of SGT-800 [113]

2.3 Fundamentals of Heat Transfer

This section presents principles that underlie the fundamental mechanisms of heat exchange research. For a more detailed analysis of these and other mechanisms, the reader is referred to Kothandaraman[59], Incropera et al.[58], Yunus et al.[125] and Rohsenow et al.[38], from which the following paragraph is derived.

2.3.1 Definition and governing law

The investigation into heat transfer encompasses two primary objectives: first, to assess the energy flow rate as heat across a system's boundary in both stable and changing scenarios; second, to ascertain the temperature distribution within the system during both constant and fluctuating conditions. This investigation provides essential information on the changes in temperature gra-

dients and the rate at which temperature changes at various locations and over time. Hence, a definition can be offered:

Heat transfer (or heat) is the thermal energy in transit due to a spatial temperature difference [58]

Consequently, whenever there exists a temperature difference within a medium or between different media, heat transfer must occur.

The fundamental principles that govern heat transfer and their applications are as follows [59]:

1. The *First Law of Thermodynamics*, which postulates the principle of energy conservation: this law establishes the relationship between the heat transferred, the energy stored, and the energy produced within a given system. For a closed system, the relationship is as follows: The net heat flow across the system's boundary plus the heat generated inside the system equals the change in the system's internal energy. This principle is also valid for an open system with minor modifications;
2. The *Second Law of Thermodynamics*, which determines the direction of energy transport as heat: this law asserts that energy flow as heat through a system's boundary will invariably occur from a region of higher temperature to a region of lower temperature, or down the temperature gradient;
3. *Newton's Laws of Motion*, which are utilized in determining fluid flow parameters;
4. The *Law of Conservation of Mass*, which is employed in the assessment of flow parameters;
5. The *rate equations* relevant to the specific mode of heat transfer being considered.

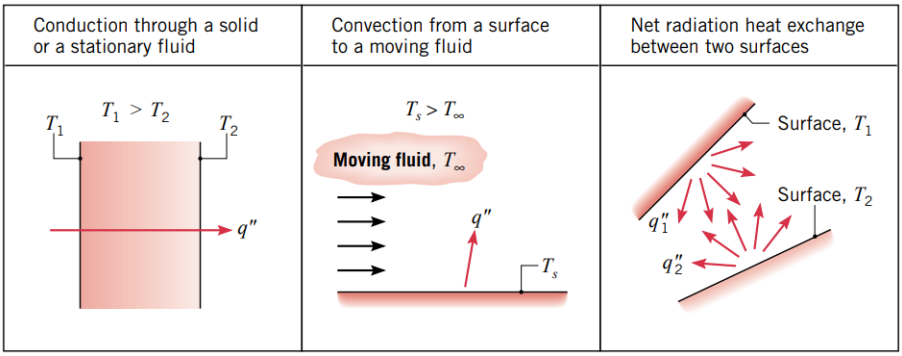

Figure 2.15: Conduction, convection, and radiation heat transfer modes [58]

Figure 2.15 illustrates various heat transfer processes, which are categorized into distinct modes. In the presence of a temperature differential within a static medium, either solid or fluid, the term "conduction" is used to describe the resultant heat transfer through the material. On the other hand, "convection" describes the heat transfer that occurs between a moving fluid and a surface when their temperatures are not the same. A third method of heat transfer, known as "thermal radiation", involves the emission of energy from all surfaces above absolute zero as electromagnetic waves. Consequently, even in the absence of a material medium, there is a net transfer of heat by radiation between two surfaces with differing temperatures.

The subsequent section provides a concise overview of the physical mechanisms underlying the modes of heat transfer delineated above.

2.3.2 Convection

Convection as a mode of heat transfer involves a dual mechanism [58]: the transfer of energy through the random motion of molecules, and the macroscopic transport of the fluid itself. Within a fluid subjected to a temperature gradient, the latter mechanism is characterized by the collective movement of numerous molecules in a coordinated way, which significantly influences the heat transfer process.

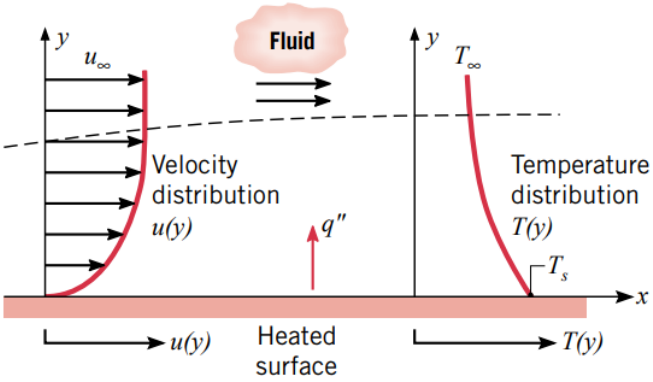

Figure 2.16: Boundary layer development in convection heat transfer [58]

The study of convection heat transfer is particularly relevant when considering the interaction between a fluid in motion and a surface at a contrasting temperature. Variations in temperature between the fluid flow and the surface lead to the formation of a thermal boundary layer, an area where the temperature of the fluid transitions from that of the surface to that within the bulk flow, as shown in Figure 2.16. The extent of this thermal boundary layer can be variable, potentially being smaller, larger, or similar in scale to the region where the fluid's velocity changes.

Within this boundary layer, convection heat transfer is driven by both *microscopic molecular motion* and the overall motion of the fluid. Near the surface, where fluid velocity is minimal, molecular diffusion is the primary mode of heat transfer. At the very interface between the fluid and the surface ($y = 0$), where the velocity of the fluid is zero, heat transfer is exclusively by diffusion.

The classification of convection heat transfer depends on the flow's driving force. *Forced convection* occurs when the flow is generated by external forces, such as pumps, fans, or natural winds. In the case of *free* or *natural convection*, the flow results from buoyancy forces, which arise due to density changes within the fluid caused by temperature differences.

The rate of convection heat transfer, regardless of its type, is described by the equation:

$$\dot{q}_{conv} = h_{tc}(T_s - T_\infty)$$

In this equation, $\dot{q}_{conv}$ denotes the convective heat flux (in $(\mathrm{W/m^2})$), proportional to the temperature difference between the surface (T_s) and the fluid (T_∞). This principle is recognized as *Newton's law of cooling* [58]. The coefficient (h_{tc}) is referred to as the convection heat transfer coefficient and is measured in $(\mathrm{W/m^2K})$.

2.3.3 Radiation

Thermal radiation is energy emitted by matter that is at a nonzero temperature [58]. This form of energy release is the result of changes in electron configurations within the atoms or molecules

of the material. The propagation of this energy takes place through electromagnetic waves or photon particles. In contrast to conduction or convection, which necessitate a material medium to transport energy, radiation can propagate in the absence of any material substance.

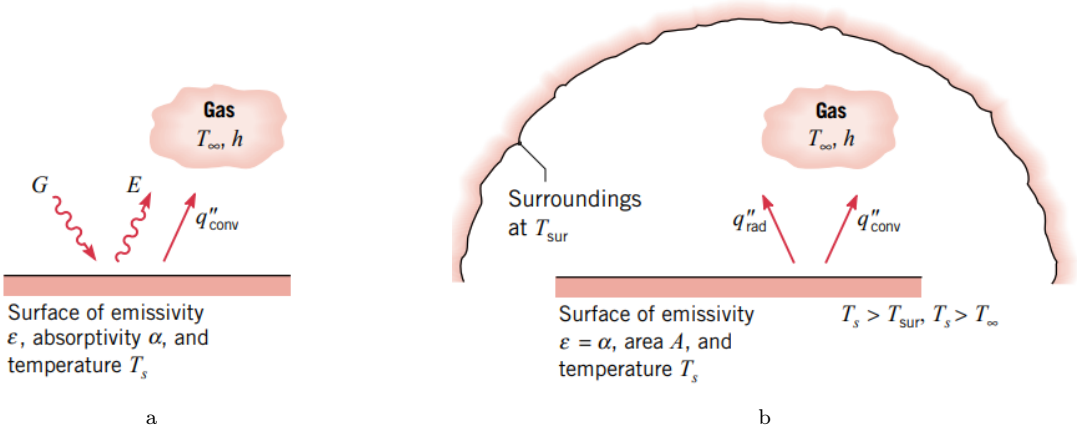

Figure 2.17: Radiation exchange [58]: (a) at a surface and (b) between a surface and large surroundings. h is refereed to heat transfer coefficient, called h_{tc} in this work

Consider radiation transfer processes for the surface of Figure 2.17a [58]. The energy emitted from the surface is derived from the thermal energy contained within the matter that the surface confines. The term *"surface emissive power"* (E) refers to the rate at which this energy is released per unit area, expressed in watts per square meter (W/m^2). The maximum emissive power is constrained by the *Stefan-Boltzmann law*, which is defined as:

$$E_b = \sigma_B T_s^4$$

Here, (T_s) represents the absolute temperature in Kelvin (K) of the emitting surface, and σ_B is the Stefan-Boltzmann constant ($\sigma_B = 5.67 \times 10^{-8} W/m^2K^4$). A surface that emits at this maximal rate is termed an ideal radiator or a *blackbody*.

For a real surface, the emitted heat flux is less than that of a blackbody at the same temperature. This is quantified by:

$$E = \epsilon \sigma_B T_s^4$$

In this context, ϵ is the emissivity, a radiative property of the surface. Emissivity values range between 0 and 1 and indicate the efficiency of a surface's energy emission as compared to a blackbody.

A common scenario involves the radiative heat exchange between a small surface at temperature T_s and a significantly larger isothermal surface that encompasses it (Figure 2.17b). The larger surface could be, for instance, the walls of a chamber or furnace at a different temperature [58]. For a surface considered a gray surface, where its emissivity ϵ is equal to its absorptivity α, the net radiative heat transfer rate per unit area is given by:

$$\dot{q}_{rad} = \frac{q}{A} = \epsilon E_b T_s - \alpha G = \epsilon \sigma (T_s^4 - T_{sur}^4)$$

In this equation, α represents the *absorptivity* of the surface, with values ranging from 0 to 1, and G represents the *irradiation*, which is the rate at which radiation is incident on a unit area of the surface.

2.3.4 Conduction

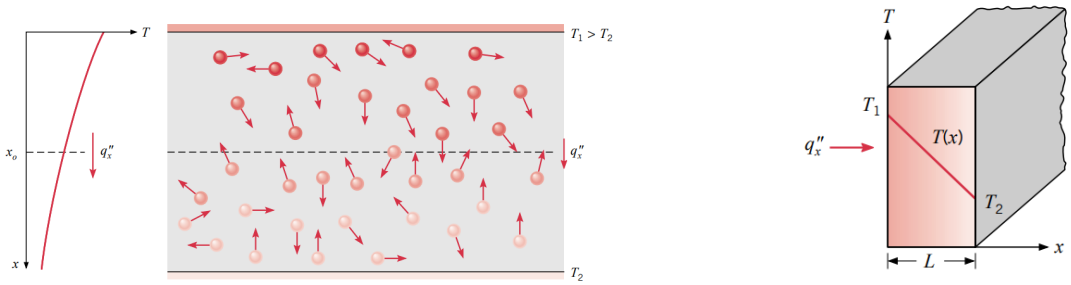

a b

Figure 2.18: Diffusion process [58]: (a) Association of conduction heat transfer with diffusion of energy due to molecular activity; (b) One-dimensional heat transfer by conduction (diffusion of energy)

Energy transfer through conduction can be conceptualized as the energy flow from particles with higher energy levels to those with lower energy within a substance, due to particle interactions. To elucidate the conduction mechanism, one may consider a gas exhibiting a thermal gradient, without any significant large-scale movement [58]. This scenario could be represented by a gas contained between two surfaces held at varying temperatures, as depicted in Figure 2.18a.

At any given point within this system, the temperature is correlated with the energy of the nearby gas molecules, energy that stems from their random translational movements, as well as their intrinsic rotational and vibrational motions. Regions of higher temperature correspond to increased molecular energy levels. Constant molecular collisions result in an energy shift from more energized molecules to those with less energy. Given a thermal gradient, this inevitably leads to energy migration from hotter to cooler areas, even in the hypothetical absence of molecular collisions.

Nevertheless, molecular interactions, particularly collisions, significantly bolster this energy migration. Molecules at higher elevations, which are warmer, will naturally transfer energy towards cooler, lower regions, culminating in a *net* energy flow in the upward direction. This process of energy movement via random molecular motion can be likened to a *diffusion process*.

Heat transfer processes can be quantified using specific rate equations that enable the calculation of the energy transfer rate. For conductive heat transfer, this rate equation is referred to as *Fourier's law*. In the scenario of a one-dimensional plane wall, as presented in Figure 2.18b, with a temperature profile $T(x)$, the rate of heat transfer can be mathematically articulated:

$$\dot{q}_x = -k_{tc}\frac{dT}{dx}$$

Here, $\dot{q}_x$ represents the heat *flux* in watts per square meter ($\mathrm{W/m^2}$), which is the rate of heat transfer in the x-direction per unit area that is perpendicular to the heat transfer direction. This rate is directly proportional to the temperature gradient, dT/dx, in the x-direction. The constant of proportionality, k_{tc}, represents the *thermal conductivity of the material* (measured in W/mK) and is an intrinsic property of the wall material. The negative sign indicates that heat naturally flows from regions of higher temperature to regions of lower temperature.

In a steady-state condition, as indicated in Figure 2.18b, the temperature profile is typically linear, and the temperature gradient can be determined by the change in temperature over the distance between two points:

$$\frac{dT}{dx} = \frac{T_2 - T_1}{L}$$

Under these conditions, the heat transfer rate per unit area can be calculated using the derived temperature gradient

$$\dot{q}_x = -k_{tc}\frac{T_2 - T_1}{L}$$

or

$$\dot{q}_x = -k_{tc}\frac{T_2 - T_1}{L} = k_{tc}\frac{\Delta T}{L}$$

The heat transfer results identified through the SRHT rig, which will be discussed in the following chapters, are the outcome of these physical principles.

2.3.4.1 Pure Conduction

As fluid layers glide past one another, a friction force develops between them and the slower layer tries to slow down the faster layer [125]. This frictional response is defined by a characteristic of the fluid known as viscosity, which is a measure of internal stickiness of the fluid. The origin of viscosity can be attributed to the cohesive interactions between molecules within liquids and the collisions occurring at a molecular level in gases. It is important to note that an absolute absence of viscosity is non-existent in any fluid; consequently, viscous influences are a factor in all types of fluid flow, although to a different extent. Considering all experimental observations in this field (the reader is referred to source [35][83] for an in-depth description of the phenomenon), viscosity is responsible for a fundamental principle in fluid dynamics, known as the *no-slip condition.*

Due to this no-slip condition, the mechanism of heat transfer from the solid interface to the fluid layer that is directly in contact with it is by *pure conduction* [125], because there is no relative motion in this fluid layer. This can be quantified as:

$$\dot{q}_{conv} = \dot{q}_{cond} = -k_{tc_{fluid}}\left.\frac{\partial T}{\partial y}\right|_{y=0}$$

In this equation, T is the spatial temperature variation within the fluid, and the term $\left.\frac{\partial T}{\partial y}\right|_{y=0}$ represents the rate of change of temperature at the boundary surface. Heat is then convected away from the surface as a result of fluid motion [125].

2.3.4.2 Nusselt Number

In the field of heat convection, a standard method involves transforming the governing equations into their nondimensional form and consolidating the variables into dimensionless groups [3][58][125][59][38], thereby simplifying the system by reducing the total number of variables. Similarly, the heat transfer coefficient h_{tc} is commonly rendered dimensionless through the use of the *Nusselt number*, which is expressed as:

$$Nu = \frac{h_{tc}L_c}{k_{tc}}$$

In this equation k_{tc}, as is known, represents the thermal conductivity of the fluid, and L_c represents the characteristic length. The Nusselt number, which bears the name of Wilhelm Nusselt as a tribute to his pivotal work in advancing the understanding of convective heat transfer [3] during

the early 20th century, essentially serves as a dimensionless indicator of the convection heat transfer coefficient.

2.4 Boundary Layer Theory

When a fluid comes into contact with a solid surface, it "adheres" to that surface because of viscous effects, resulting in the fluid coming to a complete stop at the boundary, with a relative velocity of zero with respect to the surface. The flow region adjacent to the wall in which the viscous effects (and thus the velocity gradients) are significant is called the *boundary layer*. To introduce the concept of a boundary layer, consider the flow over a flat plate as depicted in Figure 2.19.

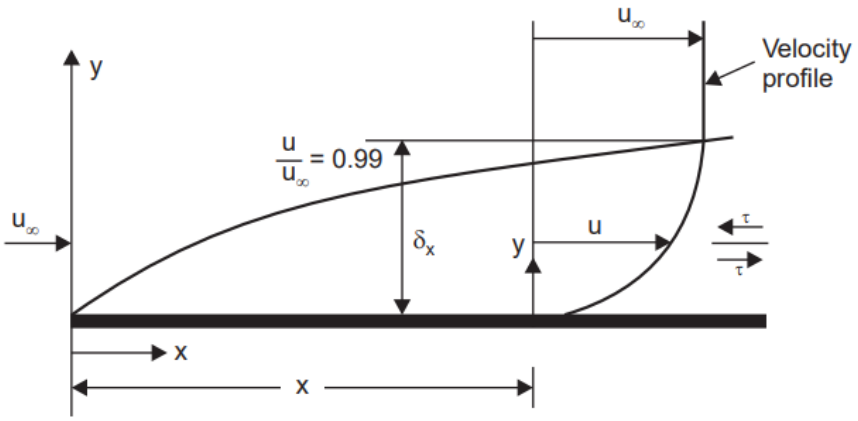

Figure 2.19: Velocity boundary layer on a flat plate [59]

As the fluid moves toward the plate in the x-direction, it does so at a velocity $V = u_\infty$, which closely resembles the free-stream velocity found at a distance from the plate's surface. Upon contact with the plate, the velocity of the fluid particles decreases to zero due to the effects of viscosity. These slowed particles then impede the flow of the adjacent layer. However, since these are layers of fluid, the reduction in velocity is not absolute in the subsequent layer. This process of velocity reduction propagates through the layers until, at a certain distance y from the surface, the impact of the reduction becomes minimal and the fluid's velocity closely approximates the free-stream velocity at that height. So, the thickness δ of this layer increases along the plate from front to back and it is conventionally defined as the distance y from the surface where the velocity u reaches 99% of the free-stream velocity u_∞. The demarcation line where $u = 0.99u_\infty$ separates the flow over a flat plate into two distinct zones: the boundary layer zone, where the influence of viscosity and the variations in velocity are pronounced, and the non-viscous flow zone, where the effects of friction are minimal and the velocity is almost uniform, often referred to as potential flow. It is generally understood that the boundary layer thickness corresponds to the distance over which the majority of the velocity transition occurs.

Within the boundary layer region, viscous forces are described in terms of shear stress (τ) among the fluid layers [38]. Experimental studies indicate that the shear stress for most fluids is proportional to the velocity gradient, and the shear stress at the wall surface is expressed as

$$\tau_w = \mu \left. \frac{du}{dy} \right|_{y=0} \tag{2.1}$$

The constant of proportionality μ is the *dynamic viscosity* of the fluid, with units of $\mathrm{kg}/(\mathrm{m} \cdot \mathrm{s})$, which is equivalent to $\mathrm{N} \cdot \mathrm{s}/\mathrm{m}^2$, or $\mathrm{Pa} \cdot \mathrm{s}$. One poise is equal to 0.1 $\mathrm{Pa} \cdot \mathrm{s}$.

Calculating the wall shear stress τ_w directly from Equation 2.1 can be impractical due to the necessity of understanding the velocity profile of the flow. An alternative method more commonly used in external flows involves associating τ_w with the volume flow velocity $\overline{U}$ using the following relationship:

$$\tau_w = C_f \frac{\rho \overline{U}^2}{2}$$

where C_f represents the dimensionless friction coefficient, also known as the skin friction coefficient, which often needs to be determined by experimental means, while the density of the fluid is represented by ρ.

In instances where heat or mass transfer occurs between the fluid and a surface, it is commonly observed that the most significant changes in temperature and concentration take place within a region very close to the surface [59]. This observation has led to the introduction of the concept known as the thermal boundary layer, where the thickness is denoted as δ_t.

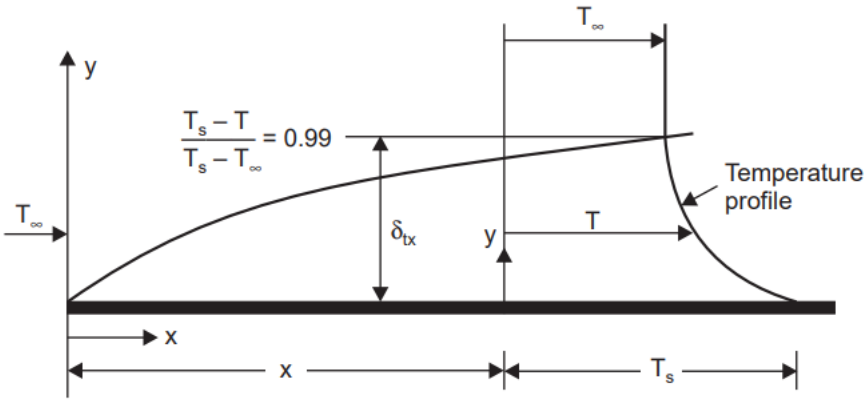

Figure 2.20: Thermal boundary layer on a flat plate [59]

Considering the flow over a flat plate where the fluid temperature is T_∞ and the surface temperature is T_s, the fluid maintains the temperature T_∞ throughout the flow until it arrives at the leading edge of the plate. Fluid particles that come into contact with the surface slow down to zero velocity, and the fluid layer achieves equilibrium with the surface, attaining the temperature T_s. Subsequently, these particles transfer heat to the layer above, creating a temperature gradient [59]. This gradient diminishes and becomes negligibly small at a certain distance y from the surface. The zone within the fluid characterized by these temperature gradients is known as the thermal boundary layer. Its thickness, denoted by δ_t, is conventionally determined by the distance y at which the ratio $[(T_s - T)/(T_s - T_\infty)]$ reaches or exceeds 0.99 [58]. Consequently, a velocity boundary layer automatically forms when a real fluid flows over a surface, but the thermal boundary layer develops only when the fluid temperature is different from the surface temperature [59]. The development of the thermal boundary layer is shown in Figure 2.20. It should be noted that the velocity of the fluid greatly influences the temperature profile. Therefore, the development of the velocity boundary layer in relation to the thermal boundary layer will significantly affect convective heat transfer [125].

The relative thickness of the velocity and the thermal boundary layers is best described by the dimensionless parameter Prandtl number [125]. This parameter is determined by the ratio of two quantities which characterize the transport properties of the fluid with respect to the momentum (kinematic viscosity) and with respect to the heat (thermal diffusivity) [23]:

$$Pr = \frac{\text{Molecular diffusivity of momentum}}{\text{Molecular diffusivity of heat}} = \frac{\nu}{\alpha_{tc}} = \frac{\mu c_p}{k_{tc}}$$

So, if the transport property related to momentum (viscosity) is particularly high, the momentum decreasing effect of the wall (no–slip condition) will extend well into the flow. This means that the thickness of the velocity boundary layer will be relatively large [23]. A similar principle applies to the thickness of the thermal boundary layer δ_t. Therefore, it is clear that the Prandtl number in forced convection serves as a direct indicator of the ratio between the thicknesses of these two boundary layers.

2.4.1 Laminar and Turbulent Flow

There are basically two different types of fluid motion, identified as laminar and turbulent flow. Boundary layer development on a flat plate and differences between laminar and turbulent flow conditions are illustrated in Figure 2.21.

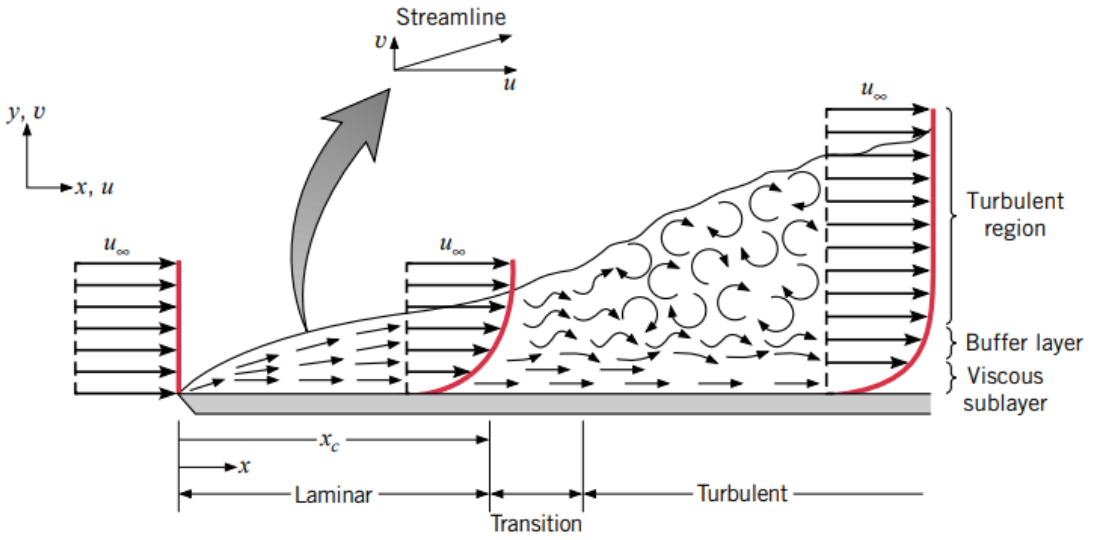

Figure 2.21: Velocity boundary layer development on a flat plate [58]

In the laminar boundary layer, the fluid flow is highly ordered and it is possible to identify streamlines along which fluid particles move. This orderly flow persists until it encounters a transitional area, wherein the flow switches between laminar and turbulent states. The behavior of the flow within this transitional area is dynamic, with the flow sometimes exhibiting laminar behavior and sometimes exhibiting the characteristics of turbulent flow [58].

Once the flow enters the fully developed turbulent boundary layer, the movement becomes substantially less predictable, characterized by chaotic and random three-dimensional displacements of fluid clusters. This chaotic mixing is often facilitated by longitudinal vortices, known as streaks, which form sporadically close to the flat plate surface and evolve rapidly [23].

The turbulent boundary layer can be segmented into three distinct zones based on the proximity to the boundary surface. Closest to the surface is the viscous sublayer, where molecular diffusion is the primary transport mechanism, and the velocity profile appears almost linear. Adjacent to this is the buffer layer, where both diffusion and turbulent mixing have significant roles. Beyond this lies the fully turbulent zone, where turbulent mixing predominates.

The contrasts between laminar and turbulent boundary layer velocity profiles, particularly for the velocity in the direction parallel to the surface (the x-component), are evident when compared [58]. For instance, the turbulent profile tends to be more uniform across most of the boundary layer due to the extensive mixing in both the buffer and turbulent zones. This results in steep velocity gradients near the viscous sublayer, which is clearly illustrated in the provided Figure 2.22.

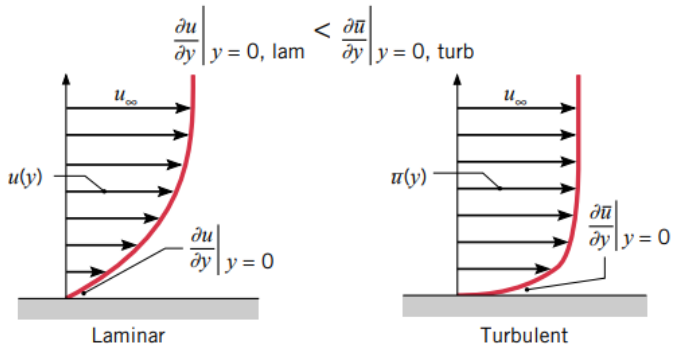

Figure 2.22: Comparison of laminar and turbulent velocity boundary layer profiles for the same free stream velocity [58]

The shift from laminar to turbulent flow is influenced by a variety of factors including the geometry of the surface, its roughness, the velocity of the flow, the temperature at the surface, and the properties of the fluid involved, among other variables. Osborn Reynolds, through comprehensive experiments conducted in the 1880s [1], established that the type of flow is primarily determined by the ratio of inertial forces to viscous forces within the fluid. This ratio is represented by the *Reynolds number*, a dimensionless value, which can be formulated for external flow as:

$$Re = \frac{\text{Inertial forces}}{\text{Viscous forces}} = \frac{u_\infty L_c}{\nu} = \frac{\rho u_\infty L_c}{\mu}$$

Here, u_∞ represents the velocity of the fluid approaching the object (analogous to the free-stream velocity over a flat plate), L_c is the characteristic length based on the object's geometry and ν is the kinematic viscosity.

The Reynolds number that delineates the boundary between laminar and turbulent flow is known as the *critical Reynolds number*. This threshold value varies depending on the shape of the object and the specific flow conditions involved.

In the field of forced convection analysis, the primary focus is on determining critical parameters such as the friction coefficient C_f (utilized to compute the shear stress at the boundary surface) and the Nusselt number Nu (which is essential for determining heat transfer rates). It is highly beneficial to establish a relationship between C_f and Nu, enabling the calculation of one from the other when available [125]. This interrelation is predicated upon the observed parallels between momentum and thermal transport within boundary layers. This conceptual linkage is commonly known as the *Reynolds analogy*. While the nondimensionalized momentum and energy equations that underpin this relationship are not discussed here to maintain brevity (readers are encouraged to refer to Reference [125] for a comprehensive analysis), the relationship can be concisely expressed as:

$$C_{f,x}\frac{Re_L}{2} = Nu_x \quad (\text{for } Pr = 1)$$

This analogy is significant as it facilitates the calculation of the heat transfer coefficient for fluids

with a Prandtl around 1, utilizing the more readily measurable friction coefficient. An alternative expression of the Reynolds analogy is:

$$\frac{C_{f,x}}{2} = St_x \quad (\text{for } Pr = 1)$$

where St represents the *Stanton number*, defined as:

$$St = \frac{h}{\rho c_p u_\infty} = \frac{Nu}{Re_L Pr}$$

The Stanton number serves as a dimensionless quantity relating to the heat transfer coefficient. It provides a measure that combines the effects of heat transfer, fluid properties, and flow velocity. It has been highlighted that by introducing appropriate adjustments, the use of the analogy can be extended to broad ranges of the Prandtl number. Specifically, the revised version of the Reynolds analogies, also known as *Chilton–Colburn analogies* [16][6], is presented in the following formula:

$$\frac{C_f}{2} = StPr^{\frac{2}{3}} = j_H \qquad 0.6 < Pr < 60 \tag{2.2}$$

Within this formulation, the term j_H denotes the Colburn j factor for heat transfer. In the context of laminar flow, Equation 2.2 is suitable only under conditions where dp^*/dx^* is zero[1] [58]. In contrast, within the turbulent flow regime, the influence of pressure gradients is less significant, and thus the previously mentioned equation retains an approximate validity. Should the analogy prove valid at every point on a surface, it could then be extended to the average coefficients calculated over the entire surface [58]. In the analysis performed, it is related with a duct ($dp/dx \neq 0$) and with air as the characteristic fluid ($Pr \neq 1$). Consequently, the application of the Reynolds analogy requires the use of correction factors.

In the following section, a more detailed examination of turbulent flow will be conducted, as it is pertinent to the study carried out in this work. Specifically, an in-depth investigation of flows in internal ducts, which are the center of analysis for the conducted research, will be undertaken. As will be discussed in subsequent chapters, the various tests within the rectangular test section under scrutiny were conducted at Reynolds numbers greater than 5×10^3. Therefore, the discussion will be confined to the study of the flow within the duct considered to be fully turbulent [23][38][58][125].

2.4.2 Fundamentals of Turbulent Flows

Most flows encountered in real-world applications are turbulent [23][38][58][125]. This term describes a flow pattern characterized by chaotic and random fluctuations, often manifesting as mixing or eddying motions, that are superimposed onto the primary flow direction. These irregular movements introduce an alternative method for the exchange of momentum and energy. In the case of laminar flow, fluid particles proceed in a structured pattern following specific paths and follows distinct trajectories, while the transfer of momentum and energy across these paths occurs through molecular diffusion. However, with turbulent flow, the chaotic eddies facilitates the swift relocation of mass, momentum, and energy across different areas of the flow, surpassing the effectiveness of molecular diffusion. This results in a pronounced increase in the rates of mass, momentum, and heat transfer, leading to higher coefficients in these domains when compared to laminar flow.

[1] The asterisk '$*$' denotes the dimensionless independent variables, used in the context of boundary layer theory to normalize the equations (the reader is referred to Appendix B for a more detailed description). In this context: $x^* = x/L$, where L is the characteristic length for the surface of interest, while $p^* = p_\infty/(\rho V^2)$.

Since the turbulent fluctuations are intricately linked with the average flow, when trying to derive the fundamental equations for the average motion by time-averaging the Navier-Stokes equations, additional terms emerge. These terms are influenced by the turbulent fluctuations themselves [23]. These extra terms introduce new unknowns into the calculation of the average motion. As a result, when the time average of the Navier-Stokes equations is taken, it leads to a situation in which there are more unknowns than equations.

In order to resolve the equation system for the motion, it's necessary to incorporate extra equations. These will need to link the additional terms arising from the fluctuating motion to the velocity field of the average motion [23]. These new equations can't be solely derived from the balances of mass, momentum, and energy, but instead take the form of models that represent the interactions between the fluctuations and the average motion [23]. The process of formulating these model equations to close the system of equations is known as turbulence modeling and presents the central challenge in simulating the average motion of turbulent flows. As the work progresses, this analysis will be omitted, but for a detailed description, the reader is encouraged to consult reference [23].

2.4.2.1 Mean Motion and Fluctuations

The most essential characteristic of turbulent flow is that, at any given point within the flow, a property X (such as a velocity component, pressure, temperature, or species concentration) is not constant over time. Instead, it displays highly irregular, high-frequency fluctuations, as depicted in Figure 2.23a. At any given moment, the property X can be described as the sum of a time-averaged value $\overline{X}$ and a fluctuating component X'. The average is calculated over a duration that is significantly longer than the typical fluctuation period [23]. When the property X does not vary with time, the time-averaged flow is considered to be steady.

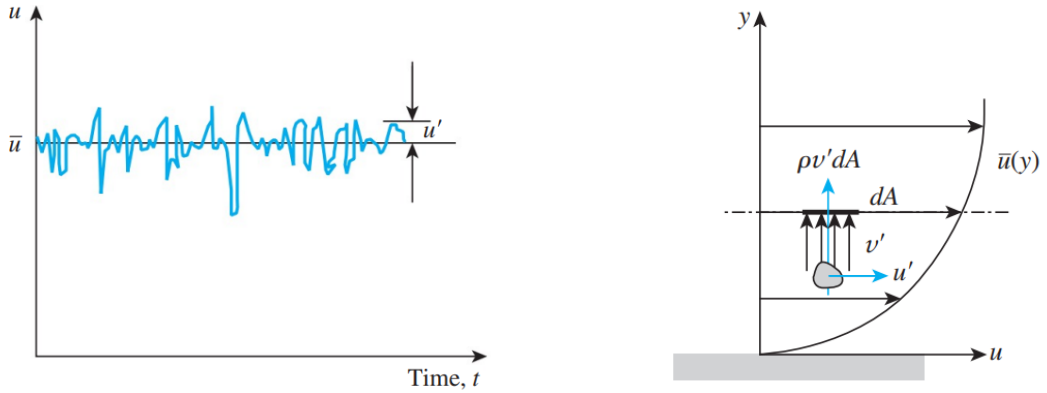

Figure 2.23: (a) Fluctuations of the velocity component u with time at a specified location in turbulent flow [125]; (b) Momentum transfer due to the turbulent fluctuation velocity: fluid particle moving upward through a differential area dA as a result of the velocity fluctuation v' [125]

The chaotic fluctuations of fluid particles play a dominant role in pressure drop, and these random motions must be considered in analyses together with the average velocity [125].

To give an example, the velocity components and the pressure may be written down as

$$u = \overline{u} + u', \qquad v = \overline{v} + v', \qquad w = \overline{w} + w', \qquad p = \overline{p} + p'$$

while the average is formed as the time average at a fixed point in space, thus for example

$$\overline{u} = \frac{1}{t_1}\int_{t_0}^{t_0+t_1} u\,dt$$

The time averages of the fluctuating quantities are then zero by definition:

$$\overline{u'} = 0, \qquad \overline{v'} = 0, \qquad \overline{w'} = 0, \qquad \overline{p'} = 0$$

Regarding shear stress, experimental studies indicate that it is significantly greater in this case due to the turbulent fluctuations. Consequently, it is useful to conceptualize it as being composed of two distinct elements: the first is the laminar portion, which is attributable to the friction encountered between layers in the flow direction [125] (represented by $\tau_{\text{lam}} = -\mu\frac{d\overline{u}}{dr}$), while the second is the turbulent portion. This latter component is a result of the interaction between the oscillating motion of fluid particles and the main body of the fluid, identified by τ_{turb} and is associated with the velocity's fluctuating components. This turbulent shear stress can be formulated as $\tau_{\text{turb}} = \rho\overline{u'v'}$, Where the product $\overline{uv}$ comes from the relationship that defines the time-averaged product between u and v:

$$\overline{uv} = \overline{u}\,\overline{v} + \overline{u'v'}$$

Such terms, like $\rho\overline{u'v'}$ or $\rho\overline{u'^2}$, are referred to as Reynolds stresses, or turbulent stresses, highlighting the contribution of turbulence to the overall stress within the fluid. It is important to note that the time average of $\overline{u'v'}$ indeed has a nonzero value. Considering the plane shear flow depicted in Figure 2.23b with $\overline{u} = \overline{u}(y)$, $\overline{v} = \overline{w} = 0$, and $d\overline{u}/dy > 0$, the transverse motion causes eddies to approach the layer y from below [23]. These eddies ($v' > 0$) originate from a region with a lower average velocity $\overline{u}$. Since they essentially retain their original velocity $\overline{u}$ during the transverse movement, they induce a negative u' within the layer y. Conversely, particles approaching from above ($v' < 0$) lead to a positive u' in the layer y. Therefore, in this flow, a positive v' is generally coupled to a negative u', and a negative v' to a positive u' [23]. Consequently, the time average of $\overline{u'v'}$ is expected to be nonzero and indeed negative.

It is possible to extend this reasoning to heat exchange as well, in order to provide a definition of heat exchange in a turbulent flow regime. Considering that $h_{tc} = c_pT$ represents the energy of the fluid and T' is the eddy temperature relative to the mean value, the rate of thermal energy transport by turbulent eddies is $\dot{q}_{turb} = \rho c_p v'T'$ [125].

2.5 Internal Flows

The current thesis work emphasizes the investigation of the flow within a rectangular duct (with dimensions $b \times l = 0.102\,\text{m} \times 0.0915\,\text{m}$), where the tests carried out fall within a region characterized by a turbulent and fully developed flow, as will be demonstrated in the following paragraphs. For the reasons mentioned above, it was decided to delve deeper into the study of turbulent flows in ducts under conditions of fully developed flow. The reader is invited to review References [58][125][23][59][38] to gain a more comprehensive insight into the physical field being examined.

The turbulent flow relations provided for circular tubes can also be applied to non-circular tubes with reasonable accuracy by substituting the diameter D with the hydraulic diameter $D_h = \frac{4A_c}{P}$ in the evaluation of the Reynolds number [38][125], where A_c represents the cross-sectional area

Flow type	**Hydrodynamic boundary layer**	**Velocity distribution in the flow direction**	**Friction factor**	**Thermal boundary layer**	**Temperature distribution / Nu number**
Fully developed flow	Developed	Invariant	Constant	Developed	Invariant / Constant
Hydrodynamically developing flow	Developing	Variant	Variant	–	–
Thermally developing flow	Developed	Invariant	Constant	Developing	Variant / Variant
Simultaneously developing flow	Developing	Variant	Variant	Developing	Variant / Variant

Table 2.3: Nomenclature for Types of Flows [38]

of the duct and P is the wetted perimeter. Therefore, the theoretical analysis will be conducted taking into account what has been stated above.

2.5.1 Quantitative Descriptions of Fluid Behavior

The internal flow configuration is the most convenient and popularly used geometry for heating or cooling of fluids in various thermal and chemical processes [59]. There are fundamental differences in the development of the boundary layer between external flow geometry and internal flow geometry. In the case of internal flow, the fluid is confined by a surface, and the boundary layer, after a certain distance, can no longer continue to develop. As a result, viscous effects affect the entire cross-section, and the velocity profile stops changing as the distance along the x-axis increases. This leads to a condition known as *fully developed flow*, and the distance from the inlet at which this condition occurs is defined as the *hydrodynamic entry length* L_h. The development of hydrodynamic boundary layer in a pipe, together with velocity distributions at various sections for laminar and turbulent flows are shown in Figures 2.24a and 2.24b. In the case of turbulent flow, the profile is flatter due to turbulent mixing in the radial direction [58].

In the analysis of internal flows, it is essential to take into account the extent of the entry region, which varies depending on whether the flow is laminar or turbulent. In the study of fluid dynamics within a conduit of hydraulic diameter D_h, the Reynolds number is expressed by the formula:

$$Re = \frac{\overline{U}\rho D_h}{\mu}$$

In this context, $\overline{U}$ represents the mean velocity of the fluid traversing the cross-sectional area of the tube, known also as velocity from volume flow. In practical applications, the flow regime within a tube is predominantly laminar when $Re < 2300$, transitions to fully turbulence as Re increases beyond around 4000, and exhibits transitional characteristics within this range.

The entry length depends on several factors. Varied correlations are available in literature. The hydrodynamic entry length is commonly defined by the distance from the entrance at which the wall shear stress, and consequently the friction factor, approximates the fully developed value within a margin of approximately 2% [125]. For laminar flow regimes, both hydrodynamic and thermal entry lengths are functions of the Reynolds number and the Prandtl number. Conversely, in turbulent flow, the pronounced mixing due to random fluctuations tends to dominate over molecular diffusion effects, resulting in hydrodynamic and thermal entry lengths that are roughly equivalent in magnitude and largely independent of the Prandtl number [125]. As a result, the

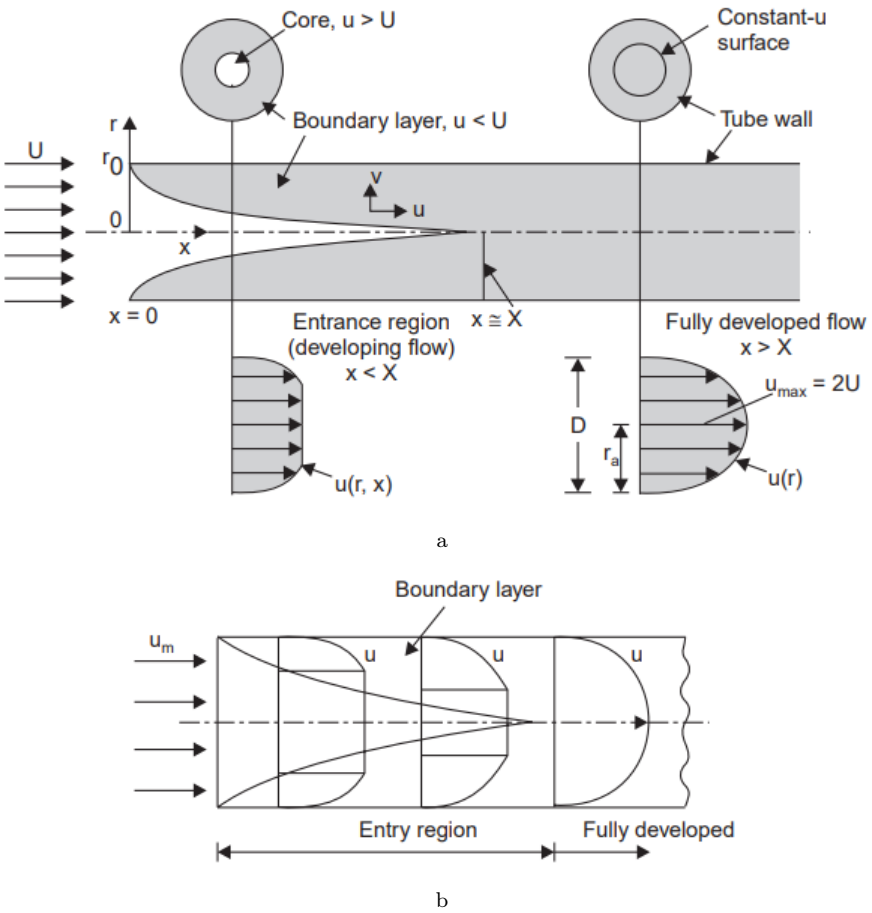

Figure 2.24: (a) Entrance region and fully developed flow region of laminar flow through a tube [59]; (b) Turbulent flow in a pipe [59]

entry length in turbulent flow is significantly reduced, exhibiting a weaker dependence on the Reynolds number.

As a preliminary estimation for turbulent flow, the hydrodynamic entry length L_h relative to the hydraulic diameter D_h can be approximated as follows:

$$10 \leq \left(\frac{L_h}{D_h}\right)_{\text{turb}} \leq 60$$

For the purposes of the current analysis, it is postulated that the flow is fully developed and turbulent when the ratio of the distance from the tube entrance (x) to the hydraulic diameter is greater than 10, in alignment with the methodology adopted by Incropera et al [58] and Yunus et al [125].

2.5.1.1 Turbulent Velocity Distribution

In the classical framework, turbulence is classified into two main types: *free-shear flows*, which include phenomena such as jets and wakes, and *wall-bounded flows*, such as those observed in channels, boundary layers, or pipes. Turbulence in free-shear flows originates from velocity differentials within the fluid medium. Conversely, in wall-bounded flows, turbulence is induced by the interaction of the fluid with a solid boundary. This interaction is further influenced by fluid viscosity and the no-slip condition at the wall, where the fluid velocity effectively becomes zero.

This dissertation concentrates on the dynamics of wall-bounded turbulence, with a specific

focus on pipe flow. The influence of the wall introduces distinctive characteristics and turbulent scales that require a detailed exploration. The principles discussed here are broadly applicable to wall-bounded turbulent flows. To achieve a solid theoretical understanding, it is strongly recommended to review Pope [41], from which the following considerations are derived.

According to the classical analysis, wall bounded turbulent flows can be divided into two regions: an inner region close to the wall and an outer region far away from it. Flow's behavior in the inner layer is predominantly governed by the effects of fluid viscosity, while the external geometry does not influence the flow field. Under this hypothesis, all turbulent flows should display a similar near-wall behavior, independent of varying external conditions. The dynamics within the inner layer are notably affected by viscous effects.

The mean velocity profile $\overline{U}$ is influenced by the wall shear stress τ_w, the distance from the wall y, the fluid's kinematic viscosity ν and the density of the fluid ρ:

$$\overline{U} = f(y, \mu, \rho, \tau_w)$$

To synthesize the flow dynamics in the inner layer, a characteristic velocity scale known as the friction velocity u_τ is defined by the relation:

$$u_\tau = \left(\frac{\tau_w}{\rho}\right)^{1/2} \tag{2.3}$$

Correspondingly, the characteristic length scale, called the *viscous length scale* l_τ, is given as:

$$l_\tau = \frac{\nu}{u_\tau}$$

These scaling parameters are essential for the dimensional analysis of the flow properties within the viscous region adjacent to the wall [41].

Upon conducting a dimensional analysis for the inner region, the non-dimensional relationship between the mean velocity and the friction velocity can be expressed as a function of the non-dimensional distance from the wall:

$$\frac{\overline{U}}{u_\tau} = f\left(\frac{y u_\tau}{\nu}\right) = f\left(\frac{y}{l_\tau}\right)$$

Defining u^+ and y^+

$$u^+ = \frac{\overline{U}}{u_\tau} \tag{2.4}$$
$$y^+ = \frac{y}{l_\tau} = \frac{y u_\tau}{\nu}$$

as the non-dimensional representations of mean velocity and the distance normal to the wall, where these are normalized by the inner variables u_τ and l_τ, respectively, the aforementioned equation can be transformed into:

$$u^+ = f(y^+)$$

This reformulated equation concisely represents the relationship between the normalized mean velocity and the normalized wall-normal distance within the viscous sublayer of the flow.

2.5.1.2 Law of the Wall

The turbulent boundary layer exhibits a multi-layered structure, each with distinct flow characteristics, as shown in Figure 2.25. Adjacent to the wall lies the *viscous sublayer*, a region where viscous stresses prevail and the velocity profile $u(y)$ is approximately linear. Expressed in wall units, using friction velocity u_τ and viscous length scale l_τ, the non-dimensional velocity u^+ within the sublayer, where $y^+ \leq 5$, is proportional to the non-dimensional wall distance y^+. The viscous sublayer is extremely thin, making measurements within this portion of the boundary layer highly challenging.

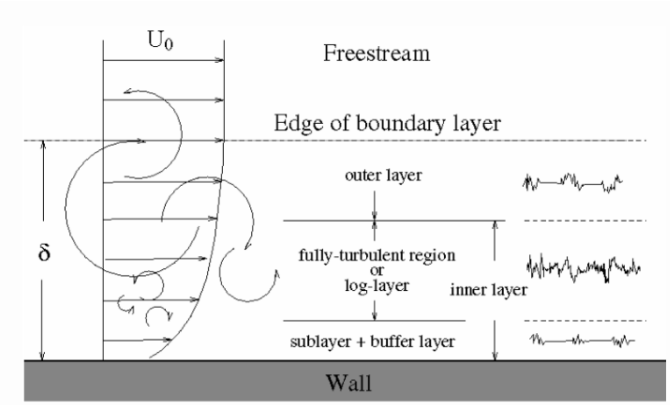

Figure 2.25: Turbulent boundary layer multistrate

Progressing away from the wall, the *buffer layer* serves as a transitional region leading up to the logarithmic layer. Within the buffer layer, significant turbulent activity occurs in relation to the production of turbulent kinetic energy. The velocity profile in the logarithmic region is described by the *logarithmic law*

$$u^+(y) = \frac{1}{\kappa} \ln y^+ + C \tag{2.5}$$

with the range typically spanning $30 \leq y^+ \leq 500 - 1000$. The constants $\kappa \approx 0.41$, known as the von Kármán constant, and $C \approx 5.1$, often referred to as the Coles' constant or smooth-wall intercept, are nearly universal.

The upper limit of y^+ in the logarithmic layer is a function of the Reynolds number and the pressure gradient. The entirety of the region extending from the upper limit of the logarithmic layer to the wall is known as the inner layer. Geometrically, the inner layer encompasses about $(0.1 - 0.2)\delta$ of the boundary layer thickness.

Finally, the *outer layer*, which constitutes approximately $(0.9 - 0.8)\delta$ of the boundary layer, covers the remainder of the flow field up to the edge of the boundary layer. In this region, the logarithmic law expressed in Equation 2.5 loses its applicability, as the observed turbulent velocities in this region exceed those predicted by the law. In this part of the flow, the velocity profile is influenced by the free shear layer dynamics and deviates significantly from the logarithmic distribution [99]. This region is also termed the "*defect layer*" due to the noticeable velocity deficit relative to the free-stream velocity.

To capture the velocity profile within this layer accurately, Coles [14] proposed a composite model that amends the foundational equation by incorporating an additional wake function. This function progressively becomes relevant as one approaches the boundary layer's outer edge. Accordingly, the revised velocity profile equation is expressed as:

$$u^+(y) = \frac{1}{\kappa} \log y^+ + C + \Pi\left(\frac{y}{\delta}\right)$$

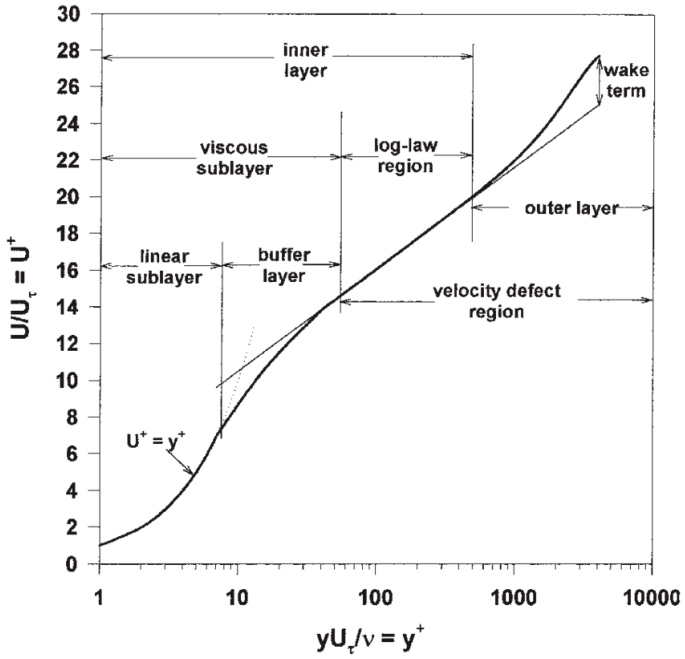

Figure 2.26: Normalized mean velocity profile in a turbulent boundary layer in semi-log coordinates [47]

In this equation, $\Pi(\frac{y}{\delta})$ denotes the wake function, which is generally normalized such that $\Pi(1) = 2$ at the boundary layer's furthest extent. The coefficient $\frac{2\Pi}{\kappa}$ signifies the influence of the outer-layer structures on the mean velocity profile, similar to how the constant C characterizes the effects of the near-wall layer [52].

In Figure 2.26, a normalized mean velocity profile within a typical turbulent boundary layer is presented, expressed in wall units.

2.5.1.3 The Modified Power Law Velocity Distribution

For flow within pipes under laminar conditions, the velocity distribution is characterized by a well-defined analytical model. The *Hagen-Poiseuille* equation describes the parabolic nature of the velocity profile across the pipe's radius:

$$\frac{U}{U_{\max}} = 1 - \left(\frac{r}{R}\right)^2$$

where U is the fluid velocity at a given radial position r, $U_{\max}$ is the maximum velocity occurring along the centerline of the pipe, and R is the pipe's radius.

The maximum velocity, $U_{\max}$, can be deduced from the following relationship, which is a consequence of the balance between the pressure gradient and viscous forces [38]:

$$U_{\max} = -\frac{1}{8\mu}\left(\frac{dp}{dx}\right)R^2$$

Here $\frac{dp}{dx}$ is the pressure gradient along the pipe's axis. From this formulation, it can be deduced that the mean fluid velocity, $\overline{U}$, is half of the centerline velocity. Thus, it is established that $\overline{U} = U_{\max}/2$.

For turbulent flow, it is not possible to derive such an equation; however, some successful models have been established by fitting curves to experiment or numerical data, like the *power law model*. The solution for the power law velocity distribution is introduced in Prandtl [66] in the following

form:

$$\frac{U}{U_{\max}} = \left(\frac{y}{R}\right)^{\frac{1}{n}}$$

where $y = R - r$ represents the radial distance measured from the wall and the exponent n is, generally, a function of the Re. In many cases, it is found that a value of $n = 7$ fits many of the cases of turbulent flows over smooth surfaces [102]. Despite its utility, the specified law exhibits certain limitations. Firstly, the law lacks a continuous derivative at the pipe's centerline, as evidenced by the non-zero value of $\frac{du}{dr}$. Secondly, the law fails to converge to the expected laminar flow profile in scenarios where the Reynolds number is relatively small. For this reason, Salama [102] developed a *new modified model*:

$$\frac{U}{U_{max}} = \left[1 - \left(\frac{r}{R}\right)^{m}\right]^{\frac{1}{n}}$$

where m and n are exponents that are utilized to adjust the theoretical profile so that it aligns with the profiles observed through experimental measurements.

In the referenced study, the theoretical model was compared with CFD simulations to determine optimal values for the parameters m and n. Analysis revealed that for the entire range of Reynolds numbers from 10^4 to 10^7, setting m to a constant value of 2 was justified. Regarding the parameter n, it was established that the following logarithmic relationship provided the best fit:

$$n = 0.77 \ln(Re) - 3.47 \tag{2.6}$$

This formulation has served as a benchmark for the validation of velocity profiles in wind-tunnel experiments. Nevertheless, caution is advised when applying this model [102], as it was originally derived for flow in circular pipes. While the study in Salama [102] suggests that the model could be adapted for non-circular cross-sections, such as a square duct, evidence of a fully developed model for such geometries has not been located.

2.5.1.4 Universal Velocity-Defect Law

Figure 2.27b illustrates the effect of varying the exponent n on the normalized velocity profile, while keeping m constant at a value of 2. As n changes, a trend towards a more uniform velocity distribution across the majority of the duct's cross-section is evident. Furthermore, the inverse relationship between the exponent n and the Reynolds number (as indicated in Equation 2.6) results in the reduction of the exponent $1/n$ in the power law of the velocity distribution, with an increase in Re. This pattern has contributed to the proposal of an alternative expression for the velocity distribution, known as the *universal velocity-defect law* that describes a universal scaling behavior for the outer region, which is attributed to the seminal work of Theodore von Kármán in the early 20th century [5].

The characterization of velocity profiles within pipe flows can be addressed through dimensional analysis. The scale of external velocity is typically represented by the friction velocity, denoted as u_τ, while length scale is symbolized by H, that is a characteristic length scale of the flow geometry: for example the diameter of a pipe or the thickness of a boundary layer. Considering a pipe of radius R, the analysis yields the following dimensionless relationship for the velocity deficit in the outer region:

$$\frac{U_{max} - U}{u_\tau} = f\left(\frac{y}{H}\right)$$

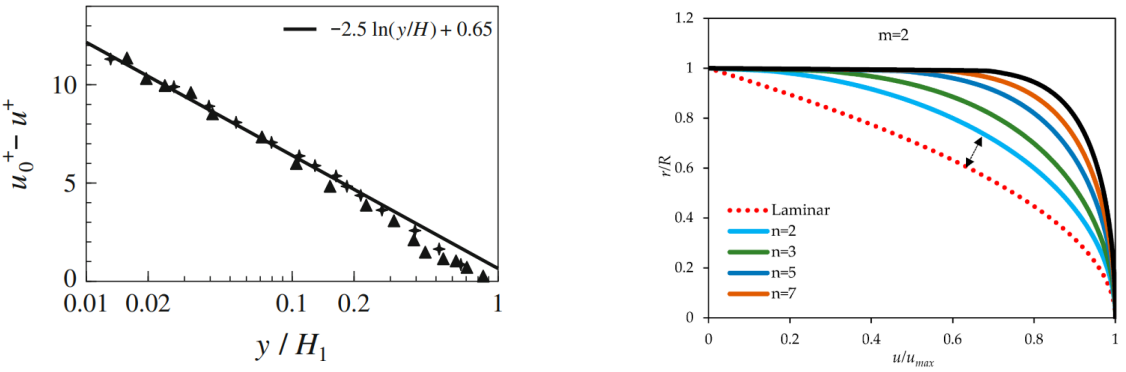

a b

Figure 2.27: (a) Defect law for a turbulent pipe flow [81]; (b) Normalized velocity profiles for different n when $m = 2$ [102]

where

$$u_\tau = \sqrt{\frac{\tau_w}{\rho}}$$

denotes the friction velocity. In the case under examination, the radius R of the pipe will be adopted as the length scale, which is equivalent to half of the hydraulic diameter D_h; therefore, it is set that $(H = R)$.

Following the derivation from Millikan [10] and integrating the relevant equations (details are omitted, but for a more in-depth background the reader is directed to Fiorini [82] and Nieuwstadt et al. [81] for a detailed discussion), the following relationship is derived:

$$\frac{U_{max} - U}{u_\tau} = -\frac{1}{\kappa} \ln\left(\frac{y}{R}\right) + C$$

Figure 2.27a demonstrates the law of velocity defect for rectangular duct. In this case, as the boundary is approached, the law reveals a uniform gradient characterized by a value of (-2.5), indicative of the inverse of the von Kármán constant. In the context of a rectangular duct, the specific constant C calculated is 0.65, which is determined by the definition for the outer region length scale [81], thus resulting in the following expression:

$$\frac{U_{\max} - U}{u_\tau} = -2.5 \ln\left(\frac{y}{R}\right) + 0.65 \tag{2.7}$$

2.5.1.5 Friction Factor

An important factor in evaluating pipe flow is the pressure differential ΔP, as it directly influences the energy needed by a fan or pump to maintain flow.

For a comprehensive range of fully developed internal flows, which may include laminar or turbulent movements, span various pipe shapes from circular to noncircular, and incorporate different surface textures as well as orientations such as horizontal or inclined positions, the representation of pressure loss is standardized [125]. It is expressed as:

$$\Delta P = f \frac{L}{D} \frac{\rho \overline{U}^2}{2}$$

Here, $\frac{\rho \overline{U}^2}{2}$ represents the dynamic pressure and f denotes the *Darcy friction factor*, which is

calculated as:

$$f = \frac{8\tau_w}{\rho \overline{U}^2} \tag{2.8}$$

This coefficient is also known as the *Darcy–Weisbach friction factor*.

This quantity is not to be confused with the friction coefficient, sometimes called the Fanning friction factor, which is defined as [58]:

$$C_f = \frac{2\tau_w}{\rho \overline{U}^2} = \frac{f}{4} \tag{2.9}$$

In the case of laminar flow within a circular tube that has reached a fully developed state, the friction factor can be determined by the formula:

$$f = \frac{64\mu}{\rho D \overline{U}} = \frac{64}{Re}$$

This expression indicates that for laminar flow, the friction factor solely depends on the Reynolds number and remains unaffected by the surface roughness of the pipe.

Most correlations for friction and heat transfer coefficients in turbulent flow are based on experimental studies because of the difficulty in theoretically dealing with turbulent flow [125].

Figure 2.28 features the Moody chart, which illustrates friction factors across an extensive range of Reynolds numbers for fully developed turbulent flow. Additionally, the friction factor varies not only with the Reynolds number but also with the condition of the tube's surface. The factor reaches its lowest value for tubes with smooth surfaces and increases as the surface roughness (ε) increases.

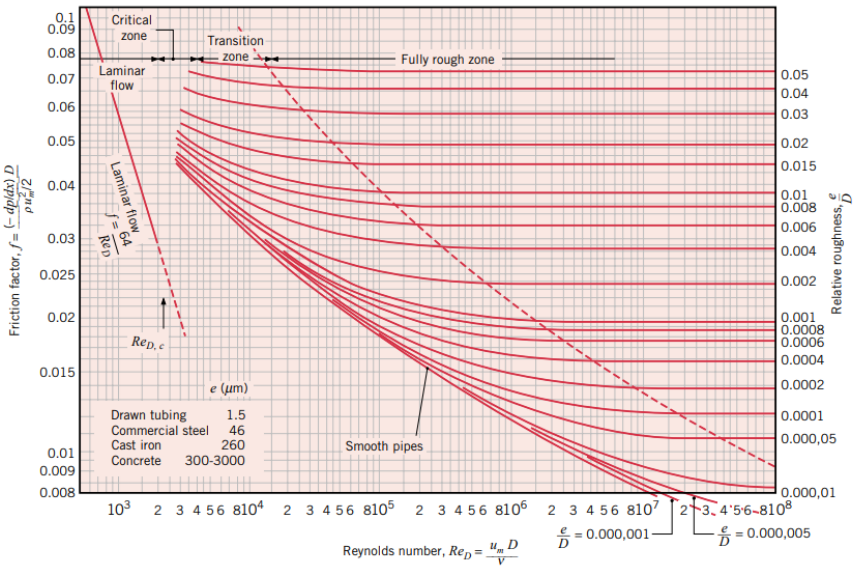

Figure 2.28: Friction factor for fully developed flow in a circular tube [58]

For smooth tubes, the friction factor within the turbulent regime is characterized by the explicit first Petukhov equation [18], applicable within the Reynolds number range of 3000 to 5×10^6:

$$f = (0.790 \ln(\mathrm{Re}) - 1.64)^{-2}$$

Regarding the evaluation of the Nusselt number in turbulent flow, it is correlated with the friction

factor through the *Chilton–Colburn analogy* (Equation 2.2), expressed as:

$$\mathrm{Nu} = 0.125 f \mathrm{RePr}^{1/3}$$

Using the friction factor obtained, this equation facilitates the calculation of the Nusselt number for smooth and rough tubes [125].

2.5.2 Velocity Distribution and Friction Factor for Rough Surface

To characterize the influence of surface texture on flow dynamics, a conventional roughness concept is employed by Nikuradse [4][9] and Schlichting [7]. This approach conceptualizes the wall as being uniformly coated with a layer of spheres packed together as densely as possible [23]. Such an arrangement is depicted in Figure 2.29, where the diameter of the particles is called the *sand roughness height*, denoted by k_s. This parameter serves as an index for quantifying the wall's surface roughness.

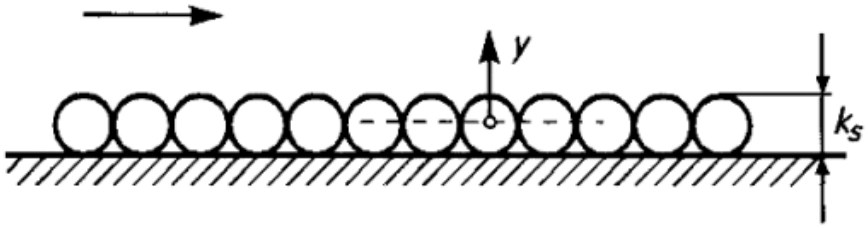

Figure 2.29: Sand roughness height k_s [23]

By applying the characteristic length of the wall layer, a non-dimensional characteristic number is derived to quantitatively express the sand roughness. This roughness parameter is given by:

$$k_s^+ = \frac{k_s}{l_\tau} = \frac{k_s u_\tau}{\nu}$$

Surface roughness alters the traditional law-of-the-wall pertinent to the viscous sublayer. The turbulent boundary layer's interaction with the wall can be categorized into three distinct regimes, each defined by the roughness Reynolds number, denoted as k_s^+. These regimes are delineated by two critical thresholds: k^+_{Smooth} and k^+_{Rough} [99]. The regimes are as follows:

- *Hydraulically Smooth Regime:* characterized by $k_s^+ < k^+_{\mathrm{Smooth}}$, this regime indicates that the roughness elements are fully immersed within the viscous sublayer;
- *Transitionally Rough Regime:* defined by $k^+_{\mathrm{Smooth}} < k_s^+ < k^+_{\mathrm{Rough}}$, the impact of surface roughness is multifaceted. Here, both the Reynolds number and relative roughness contribute to variations in skin friction and drag coefficients, implying that the interaction between viscous and pressure forces governs these coefficients;
- *Fully Rough Regime:* in instances where $k_s^+ > k^+_{\mathrm{Rough}}$, the roughness elements extend into the fully turbulent region, causing a *downward shift* of the logarithmic velocity profile.

Different values for k^+_{Smooth} and k^+_{Rough} are reported in the literature, but for the following work, the values defined by the pioneering studies of Nikuradse [4] have been chosen as a theoretical reference, as presented in Table 2.4. Throughout the present study, an experimental analysis of the k_s^+ values for the considered roughness will be conducted.

Roughness type	k^+_{Smooth}	k^+_{Rough}
Uniform sand-grain	5	70

Table 2.4: Values for the lower and upper bands of transitionally rough regime by Nikuradse [4]

The velocity deficit due to roughness has been represented in various ways; for the current thesis work, the formulation presented in the research by Flack et al. [69] has been adopted.

The influence of surface roughness on the velocity profile is captured through a roughness function, denoted as ΔU^+, defined independently by Clauser [12] and Hama [13]. This function accounts for the downward shift observed in the logarithmic law of the wall, capturing the momentum deficit resulting from surface roughness, and thus can be interpreted as a measure of the drag penalty relative to a smooth wall: drag increases for $\Delta U^+ > 0$ and drag reduces for $\Delta U^+ < 0$. Therefore, Equation 2.5 can be expressed as:

$$u^+ = \frac{1}{\kappa}\ln(y^+) + C - \Delta U^+ \tag{2.10}$$

for turbulent flows over rough-walls, where κ represents the von Kármán constant and C is the smooth wall intercept. This can also be recast into a relative roughness form, Equation 2.11, where k is a measure of the roughness height,

$$u^+ = \frac{1}{\kappa}\ln\left(\frac{y^+}{k^+}\right) + C - \Delta U^+ + \frac{1}{\kappa}\ln(k^+) \tag{2.11}$$

In this context, a common roughness scale in literature is the equivalent sandgrain roughness height k_s [69], indeed Nikuradse[4] showed that ΔU^+ could be estimated from the size of the mono-dispersed sand grains that roughened the walls of their pipe flow experiment. Using the logarithmic intercept for a uniform sand grain surface in relative roughness form ~ 8.5 [4], one can deduce the value of k_s for a specified roughness profile from the roughness function ΔU^+ in the fully rough flow regime. The relationship is given by:

$$C - \Delta U^+ + \frac{1}{\kappa}\ln(k_s^+) = 8.5 \tag{2.12}$$

This value is widely used and accepted in the literature, as demonstrated in the research of Jiménez [52], Mohammadreza et al. [99] and Nieuwstadt et al. [81].

2.6 Particle Image Velocimetry

The investigative methodology used in the following thesis work was the *Particle Image Velocimetry (PIV)* technique, a non-intrusive and whole filed optical method providing instantaneous velocity information in fluids.

The setup for conducting an experiment using PIV typically requires one digital camera, a lighting source (often a dual-cavity pulsed laser), sheet-light optics consisting of a combination of cylindrical and spherical lenses, and a unit for synchronization. The fluid being examined is mixed with tracer particles, which are then illuminated in the measurement plane by the light source, multiple times in quick succession within a brief time frame. Figure 2.30 illustrates a flow chart that describes the entire process involved in a flow-field measurement using PIV. The principle of PIV is based on the measurement of the displacement of this small tracer particles that are carried

by the fluid during a short time interval.

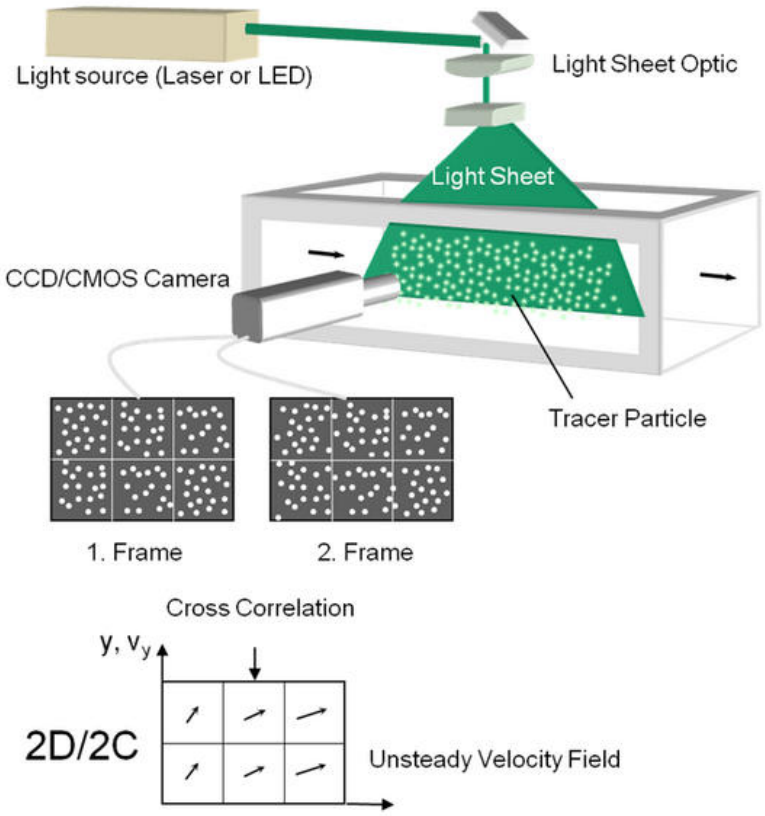

Figure 2.30: Overview of a PIV set up [90]

Specifically, the process consists of the following major steps [73]:

1. *Set-up:* the necessary PIV apparatus is meticulously put together according to the required optical layout and its operational status is confirmed. In particular, the optical plane for the light sheet is carefully aligned, ensuring the lenses are adjusted to capture high-quality images. Calibration for PIV is then carried out carefully;

2. *Data Capture:* the digital cameras capture the scattered light from tracer particles that have been introduced into the fluid. The flow is made visible using a minimum of two laser pulses, which are captured by the cameras in a very brief interval. Captured images are broken down into numerous pixels, with the brightness of each pixel quantified at discrete levels. This transformation of a smooth gradation of light into a grid of pixels is termed pixelization [73], followed by a process known as quantization [73], where the magnitude of the signal is digitized;

3. *Analysis:* the captured images are divided into numerous sections for analysis, known as interrogation areas. Within these zones, correlation methods are employed to compute a map of displacement vectors. These displacements are translated into velocity figures, utilizing the time span between laser pulses and the spatial calibration from the imaging plane to the physical measurement area. The resulting velocity map is then evaluated and any outlying vectors removed and replaced in a process called validation [73]. Finally, post-processing is performed to refine the data before it is produced.

2.6.1 Equipment Selection

In the following section, the main devices used for PIV measurements will be analyzed. To prevent making the discussion too heavy, many demonstrations will be left out. For a complete and more in-depth review of the topic, consulting the work of Raffel et al. [88] and Ronald [31] is advised, from which the forthcoming considerations and theoretical bases are derived.

2.6.1.1 Flow Seeding

When selecting tracer particles for flow visualization, certain characteristics are essential to ensure their effectiveness.

Firstly, the particles must be capable of generating clearly visible images when subjected to the specific lighting conditions employed during observation [73]. The scattering capacity of these tracers, which is crucial for their visibility, is largely influenced by two parameters: the particle diameter, often denoted as d_p, and the refractive index of the particles in relation to the surrounding fluid, expressed as n_p/n_f.

Furthermore, it is vital that these particles exhibit minimal inertia to accurately track the fluid's movement. This characteristic is very important because any significant inertia could alter the flow, leading to inaccurate representations of the fluid dynamics being studied.

Lastly, the concentration of tracer particles within the fluid is a critical factor. An optimal concentration ensures that a sufficient number of points in the spatial domain are marked, thereby providing an effective resolution of the flow pattern. This allows for a detailed and accurate mapping of the fluid's behavior, which is essential for thorough analysis and understanding of the flow dynamics.

In gas flows, the density of the particles is typically much higher than that of the fluid. Therefore, the particle diameter must be chosen sufficiently small in order to minimize the settling velocity of the particles [88]. For very small particle tracers as used in PIV the particle motion is predominantly governed by the quasi-steady viscous force, known as Stokes drag. As a result, the discrepancy in velocity between the particles (V) and the ambient fluid (U) can be approximated as [88]:

$$\mathbf{V} - \mathbf{U} = d_p^2 \frac{(\rho_p - \rho)}{18\mu}\mathbf{a}$$

In the given context, $\mathbf{V}$ and $\mathbf{U}$ represent the velocities of the tracer particle and the surrounding fluid, respectively. The term $a = \frac{1}{2}d_p$ defines the radius of the tracer particle, where d_p is the diameter of the particle. The symbol μ denotes the dynamic viscosity of the fluid, while ρ_p and ρ correspond to the densities of the seeding particles and the fluid, respectively. The velocity difference $\mathbf{V} - \mathbf{U}$ is also referred to as slip velocity or settling velocity in analogy to the case of a heavy sphere settling in a fluid, as shown in Figure 2.31a.

When the density of the tracer particles significantly exceeds that of the fluid, the particle velocity $\mathbf{V}(t)$ can be expressed as [88]:

$$\mathbf{V}(t) = \mathbf{U}\left(1 - \exp\left(-\frac{t}{\tau_s}\right)\right) \tag{2.13}$$

where the response time τ_s is defined by:

$$\tau_s = d_p^2 \frac{\rho_p}{18\mu}$$

This response time serves as an indicator of the particles' ability to reach velocity equilibrium with the fluid. The behavior described by Equation 2.13 is depicted in Figure 2.31b, which illustrates the response time for particles of various diameters subjected to a sudden deceleration within an airflow.

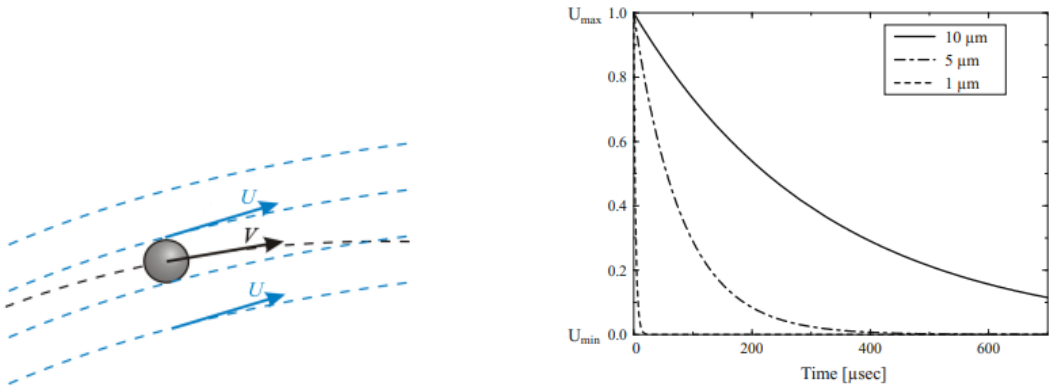

a b

Figure 2.31: (a) Discrepancy between particle and surrounding fluid velocity; (b) Theoretical time response of oil particles with different diameters in air [88]

To assess whether a particle tracer can accurately follow the flow dynamics, one must consider more than just the response time. The *Stokes number Stk* is a dimensionless parameter introduced for this purpose [88][31]:

$$Stk = \frac{\tau_s}{\tau_f}$$

Here, τ_f denotes the characteristic time scale of the flow, related to the velocity fluctuations encountered by the particle along its path. A Stokes number less than 10^{-1} is generally considered indicative of sufficient accuracy for flow tracing [34].

2.6.1.2 Image Recording System

For PIV, the process of capturing images often employs advanced digital imaging technology, specifically cameras outfitted with *CCD (Charge-Coupled Device)* or *CMOS (Complementary Metal-Oxide-Semiconductor)* sensors. These cameras are adept at quickly recording a pair of images in quick succession, with the interval between shots being just a few hundred nanoseconds.

When choosing a camera for PIV, it's essential to consider several critical factors that will affect the quality of the measurements [73]. One of the most important features is the *camera's sensor spatial resolution*. This determines the level of detail with which the continuous light intensity field is mapped into discrete units on the sensor array. A higher spatial resolution allows for more detailed visualization of the flow patterns. More specifically, this feature, referring to the camera's resolution, determines the number of pixels with which the physical image is depicted. Each pixel is an element of the sensor array that forms the image on the camera's focal plane, and their number is indicative of the image quality in depicting the flow's details. These elements respond differently to light intensity, which is represented by a function that defines the *gray level* on the $x - y$ plane:

$$I = f(x, y)$$

Therefore, the image seen by the human eye is characterized by a continuum of color shades that describe the object's details, while a digitized image involves a discrete representation, through a

limited number of gray levels. The ability to represent gray levels is determined by the *number of bits* related to the resolution of the sensor under consideration, which is related to the number of gray levels via powers of two. A sensor with 8-bit depth can achieve a resolution of $2^8 = 256$ gray levels (ranging from 0 to 255). These levels are encoded in binary language using combinations of 0 and 1 for each pixel, with the maximum value being assigned to white (in this case, 255 [11111111]) and the minimum to black (0 [00000000]). As a result, the *map of gray levels* is viewed as an array of numbers that can be processed from a computational perspective.

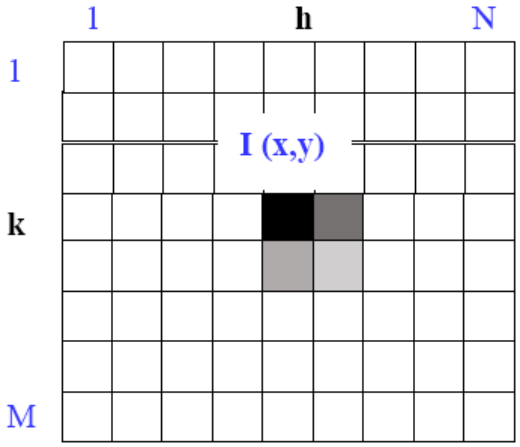

Figure 2.32: Discrete representation using a finite number of gray levels

Equally important is the *sensor's sensitivity*. This characteristic is crucial because it defines the minimal level of light that the camera can reliably detect as a signal, above the level of the background noise. The higher the sensitivity, the better the camera can capture images in low-light conditions or detect little differences in light intensity, which is necessary for accurate velocity measurements in PIV applications.

Moreover the imaging system is characterized by the focal length (denoted as f), the f-number which is expressed as [31] $f\# = \frac{f}{D}$ (where D represents the diameter of the lens aperture), and the image magnification factor M. This magnification factor is calculated as the ratio of the image size (sensor size) and the imaged object size (knowed as *field of view* or FOV):

$$M = \frac{\text{sensor size}}{\text{imaged object size}} = \frac{\text{pixel size} \times \text{number of pixels in the sensor}}{FOV} \tag{2.14}$$

2.6.1.3 Light Source

PIV requires the use of a high energy laser to illuminate small tracer particles within the fluid. The light source should exhibit several key requirements. The first is the necessity for the illumination to be of short duration, known as the pulse duration φ_t. For accurate imaging, it's essential that the particles do not appear elongated or streaked across the image; instead, they should be depicted as compact, round spots. This effect is achieved when the distance that the particles travel during the pulse (or during the exposure time of the imager for continuous illumination) is substantially less than the diameter of the particle image itself:

$$\varphi_t \ll \frac{d_p}{VM} \tag{2.15}$$

where V is the particle velocity and M the magnification factor.

The second critical factor is the selective illumination of particles within a specific narrow plane, so that they are all sharply in focus. This precision is accomplished by carefully positioning the light sheet to coincide with the focal plane of the imager.

The third consideration involves the *intensity of the light source*. It must be powerful enough to ensure that the light scattered by the seeding particles is detectable by digital imaging devices. The energy required from the pulse is directly related to the size of the area being observed [73]. For instance, a pulse energy of around 100 millijoules is typically adequate for illuminating a $(10 \times 10)\text{cm}^2$ area in air flow experiments.

The most commonly-used laser system for PIV applications is a *dual-cavity pulsed Nd:Yag laser*, currently available in a wide range of pulse energy from 100 to 800 mJ, and with a repetition rate up to around 30 Hz [73].

2.6.1.4 Light Sheet Formation Optics

In the context of PIV technique, it is essential to use a lens system to tailor the laser beam for the test area. Specifically, it is necessary to create a very thin laser beam at the measurement zone. A cylindrical lens is a crucial component for generating a light sheet.

When employing light sources such as Nd:YAG lasers, a combination of different lenses is often required to produce thin, high-intensity light sheets. At least one additional lens is needed to focus the light to the desired thickness. The initial use of a diverging lens is to prevent the ionization of air near the focal point, which can occur with high-power pulse lasers. Although focal lines typically do not ionize the air, dust particles might burn if the surrounding area is not shielded or evacuated. In both scenarios, acoustic radiation would be emitted, and the beam's properties would be significantly altered [88]. To minimize variations in the light sheet properties within the area of interest, it is advisable to design the light sheet optics so that the beam waist, or point of minimal divergence, does not coincide with the measurement region.

The quality of illumination in PIV experiments is significantly influenced by the degree of overlap between the dual thin light sheets, particularly when using dual-head Nd:YAG lasers. Insufficient overlap of the light sheets is a primary cause of unsuccessful experimental outcomes. Consequently, precise alignment of the two laser sheets is essential to ensure an adequate overlap, which should ideally reach around 80%. Figure 2.33 depicts this feature.

Figure 2.33: Not overlapping light sheets (top) and overlapping ones (bottom)

Chapter 3

Research Methodology

This chapter will discuss the research methodology adopted for this thesis work. In particular, the research approach, which is based on fluid dynamic analogy and the correlation of experimental results, will be examined. The experimental setup is described in detail, with a focus on the key instruments of the study. The data analysis method is presented with an emphasis on the various processes implemented for a thorough analysis of the results. Finally, an estimate of the error associated with the use of the PIV technique is presented; moreover, the uncertainty analysis related to the technique and the software used for data acquisition and analysis is detailed.

3.1 Research Approach

Over the years, the advent of increasingly high-performance computers and the development of *advanced fluid dynamics simulation techniques* have led to significant success and continuous evolution of numerical techniques in the field of fluid-thermal dynamics. This progress has been made possible by extensive research over time. Among the advantages offered by these techniques is the ease of configuring and modifying simulation parameters, as well as the adaptability of the method to the analysis of different applications of interest, such as fluid dynamics simulations for environmental purposes, external and internal aerodynamics, and the automotive and aeronautical sectors, among others. However, there are also disadvantages in using these simulations, such as the difficulty in reproducing high Reynolds numbers, especially in the presence of turbulent flows, which involve wide ranges of spatio-temporal turbulent scales:

$$\frac{L}{\eta} = Re^{\frac{3}{4}}$$

Where L is the size of the large scales, while η represents the small scales close to the Kolmogorov scale (the reader is referred to Appendix C for a better understanding of the phenomenon). It thus becomes clear that as the Reynolds number increases, the ratio L/η must also increase, leading to a decrease in the size of η and consequently in the fineness of the computational grid to be used. As a result, numerical analysis requires the creation of a particularly dense grid in areas where gradients are more pronounced, with the effect of limiting the analysis to an accurate reproduction of the flow only in a portion of the entire computational grid.

In parallel, the *experimental approach* continues to garner significant interest among researchers as a fundamental tool for the faithful characterization of a physical phenomenon. Reference is made here to physical experiments that are conducted under actual or similar conditions, during

which measurements of relevant fluid dynamic quantities are collected for the study of the specific problem. This experimental methodology requires specialized facilities and equipment, as well as sensors, instruments, and data acquisition technologies. Experimental investigation is relatively simple to carry out even for very high Reynolds numbers, on the order of 10^6, which are much higher than those achievable with numerical simulation. Naturally, this methodology also involves complexity, including the difficulty of varying the experimental parameters related to geometry, boundary conditions (for example, wall interference), and initial conditions (such as the turbulence of the upstream flow).

Consequently, it is clear that adopting a single approach can limit the accuracy of the results obtained. For this reason, it is generally preferable to adopt an integrated Numerical-Experimental methodology, in which measurements aim to understand the physical phenomenon and validate numerical simulation codes, which in turn guide the experimental investigation. From this perspective, the approaches adopted in experimental aerodynamics are illustrated to correlate experiments to real conditions and to integrate experimental results with numerical predictions.

The goal of such integration is to exploit the strengths of both approaches, namely the precision and flexibility of numerical simulation and the reliability and concreteness of the experimental research.

3.1.1 Dynamic Similarity

Correct experimentation in a wind tunnel requires adherence to fluid dynamic similarity when working with a scaled model. Maintaining this similarity implies that the conditions for dynamic similarity are met for both the scaled model and the actual prototype. This means that:

- Both bodies, as well as any other solid boundaries, must be *geometrically similar* and positioned at the *same angle*, which is particularly important when analyzing an aerodynamic profile inclined relative to the flow lines;
- The similarity parameters, represented by the dimensionless groups Π_i, must match in both systems, ensuring that the physical phenomena are analogous. For further details on dimensionless groups and their application, the reader is referred to Appendix B.

To accurately simulate the impact of fluid viscosity in experiments, maintaining the same Reynolds number is crucial [93]. Typically, the reference values for these variables are taken from the conditions of the undisturbed flow far upstream, labeled with u_∞, ρ_∞, and μ_∞ respectively. The Reynolds number is pivotal in characterizing viscous phenomena, encompassing boundary layer behavior and the broader scope of dissipative flow features such as wakes, mixing layers, transitions from laminar to turbulent flow, flow separation, and related dynamics. In the thesis work, the scale ratio is approximately 70 : 1, necessitating careful adjustment of the parameters that define the Reynolds number to uphold the principle of dynamic similarity.

In the studied scenario, the influence of the Reynolds number on flow transition (from laminar to turbulent) does not pose an issue, as the tests are carried out in a regime where the flow is already turbulent and fully developed. Furthermore, the typical Reynolds numbers for industrial-scale turbines are quite large, often spanning two orders of magnitude (from 10^4 to 10^6) [68]. The current study will focus on scaled-up models of geometries originating from the cooling ducts of turbines. Specifically, recent research conducted by Siemens Energy on the cooling zones in the *SGT600-700* and *800* series turbines has revealed a flow pattern within the ducts characterized by a Reynolds number that significantly varies depending on the geometry and operating conditions,

typically settling in a range from 10^4 to 10^5. Consequently, it was decided to target Reynolds numbers in the same range as those found in actual gas turbine cooling channels. It is understood that there will be a need to contextualize the results if they are to be extrapolated to the real system in the future. This is because more precise correlations are required, rather than extrapolations within a range, as is currently the case.

In the context of fluid dynamic similarity and heat transfer similarity, the following parameters are identified as correlation variables, which are utilized to derive the desired non-dimensional relationships. Below is illustrated how to derive such independent variables by dividing the problem into the context of hydrodynamic similarity, for the study of flow in the duct, and heat transfer similarity.

1. Momentum transfer: in this scenario, the primary focus is on analyzing the variation in pressure from the entry to the exit of a conduit. The conduit is specified by its length L_c, hydraulic diameter D_h, and a roughness typically denoted by k; the flow is characterized by the fluid's density ρ, its dynamic viscosity μ, and the mean velocity U. Consequently, the pressure drop is influenced by all these factors, yet the exact form of this relationship needs to be ascertained.

$$\Delta p = f(L_c, D_h, k, \rho, \mu, U)$$

To simplify the problem, Buckingham's Pi Theorem is employed (for a detailed explanation of the procedure, refer to the Appendix B), revealing that the total number of variables to be identified is $N(=7) - K(=3)$, hence indicating the calculation of four dimensionless groups. These are:

$$\Pi_1 = \frac{\Delta p}{\frac{1}{2}\rho U^2}$$

$$\Pi_2 = \frac{L_c}{D_h}$$

$$\Pi_3 = \frac{k}{D_h}$$

$$\Pi_4 = \frac{U\rho D_h}{\mu}$$

As a result, the functional relationship can be converted into a dimensionless form:

$$g(\Pi_1, \Pi_2, \Pi_3, \Pi_4) = \text{const}$$

By solving for the dimensionless pressure drop Π_1 and recognizing Π_4 as the Reynolds number:

$$\frac{\Delta p}{\frac{1}{2}\rho U^2} = F\left(\frac{L_c}{D_h}, \frac{k}{D_h}, Re\right)$$

In cases of fully developed pipe flow, F must be a linear function of $\Pi_2 = \frac{L_c}{D_h}$, leading to the well-established friction factor parameter λ, which is solely dependent on the Reynolds number and relative roughness.

$$\lambda = \frac{\Delta p / L_c}{\frac{1}{2}\rho U^2 / D_h} = \lambda\left(\frac{k}{D_h}, Re\right)$$

Therefore, maintaining geometric and hydrodynamic similarity is crucial when comparing experimental data from a prototype to the actual full-scale object.

2. Heat transfer: in the study of convective heat transfer, emphasis is typically placed on the convective heat flux $\dot{q}$ rather than the total heat $\dot{Q}$. The influential variables in forced convection heat flux include the hydraulic diameter D_h representing the geometry of the duct; the heat transfer surface area A; the temperature distribution over the interface surface T_s; the bulk main flow temperature distribution T_∞; the velocity field u; and the fluid's properties such as thermal conductivity k_{th}, specific heat at constant pressure c_p, density ρ, and dynamic viscosity μ.

   Considering the Equation 2.3.2, the convective heat transfer coefficient h is defined as a function of these parameters:

$$h = f(D_h, k_{th}, c_p, \rho, \mu, u)$$

   Application of Buckingham's Pi theorem allows for the identification of the following dimensionless groups:

$$\Pi_1 = \frac{hD_h}{k_{th}}$$
$$\Pi_2 = \frac{c_p\mu}{k_{th}}$$
$$\Pi_3 = \frac{\rho u D_h}{\mu}$$

   These dimensionless groups are identified as the Nusselt number Nu, the Prandtl number Pr, and the Reynolds number Re, respectively:

$$Nu = \frac{hD_h}{k_{th}}$$
$$Pr = \frac{c_p\mu}{k_{th}}$$
$$Re = \frac{\rho u D_h}{\mu}$$

   The correlation for forced convection is thus formulated as a function of these dimensionless numbers:

$$f(Nu, Pr, Re) = 0$$

   From the interpretation of the experimental findings, correlations are established in the form:

$$Nu = f(Pr, Re)$$

   If the friction factor and geometric parameters are also found to substantially influence the outcome:

$$Nu = f(Pr, Re, \lambda, \frac{L_c}{D_h})$$

3.2 Experimental Framework

The following will present the design and experimental setup of the *rig* used for the thesis work. The structure and preliminary design of the wind tunnel were the subjects of another thesis [121], as well as the test section [124]. In the present thesis, instead, modifications have been implemented to the experimental setup, including alterations to the system responsible for the motor-driven movement of the workbench along the $y - z$ plane. Additionally, the arrangement of the optical lenses has been reconfigured, and novel testing procedures for the flow measurement campaign have been introduced, incorporating image representation on a plane parallel to the surface roughness.

3.2.1 Wind Tunnel and Test Section

For the execution of experiments, a dedicated room was set up within the Fluid Dynamic Lab at Siemens Energy, sealed with an interlock on the door as a safety device for the laser. This room allows for work in a dark environment, which is crucial for the proper conduct of tests using the PIV technique. Specifically, a vertical closed-circuit wind tunnel was developed and constructed. The design of this tunnel has been one of the main works of Pedreño Marin [121]. It operates at ambient pressure and functions within a velocity range of approximately 0.9 m/s to 8.33 m/s, with a Reynolds number ranging from about 5500 to 53000. It is equipped with an *83W SystemAir K 100 EC Sileo fan.* The current prototype of this tunnel does not feature any cross-sectional changes for pressure recovery, except for a convergent section followed by a divergent near the fan. This configuration is justified by the absence of a stator component (a system of fixed blades) in the motor assembly, which would serve to straighten the flow downstream of the fan, eliminating the swirling component of the flow; in other words, downstream of the propeller, the flow would have rotational kinetic energy that, without stators, would be lost, increasing losses. Proper orientation of the stator blades downstream of the rotor blades would allow for the reorientation of the flow by eliminating the tangential motion component, thereby converting rotational kinetic energy into longitudinal kinetic energy. The convergent section before the fan aims to compensate for this absence (justified by the limited space available), ensuring that the flow is uniform, aligned with the fan housing axis, and with a low level of turbulence before interacting with the rotor blades. In fact, the presence of the convergent section helps to reduce longitudinal velocity fluctuations, u'. Indeed, by applying Bernoulli's equation and neglecting pressure fluctuations and head losses, the following is obtained:

$$p_i + \frac{1}{2}\rho\left(\overline{U}_i + u'_i\right)^2 = p_u + \frac{1}{2}\rho\left(\overline{U}_u + u'_u\right)^2 \Rightarrow$$
$$p_i + \frac{1}{2}\rho\left(\overline{U}_i^2 + 2\overline{U}_i u'_i + u'^2_i\right) = p_u + \frac{1}{2}\rho\left(\overline{U}_u^2 + 2\overline{U}_u u'_u + u'^2_u\right)$$

By averaging and neglecting all fluctuations, one gets:

$$p_i + \frac{1}{2}\rho\overline{U}_i^2 = p_u + \frac{1}{2}\rho\overline{U}_u^2$$

Comparing the relations, for equality, the terms containing the fluctuations must also be equal:

$$2\overline{U}_i u'_i + u'^2_i = 2\overline{U}_u u'_u + u'^2_u$$

Dividing by $\overline{U}_i^2 \cdot \overline{U}_u^2$ yields:

$$\frac{u'^2}{\overline{U}_i^2 \overline{U}_u^2} + \frac{2\overline{U}_i u'_i}{\overline{U}_i^2 \overline{U}_u^2} = \frac{u'^2_u}{\overline{U}_i^2 \overline{U}_u^2} + \frac{2\overline{U}_u u'_u}{\overline{U}_i^2 \overline{U}_u^2}$$

Neglecting the term $u_i'^2$ (squared fluctuations) compared to $2u'U$, one arrives at:

$$\frac{u'_i}{\overline{U}_i \overline{U}_u^2} = \frac{u'_u}{\overline{U}_i^2 \overline{U}_u}$$

In terms of turbulence levels ($I = u'/U$) between the outlet and the inlet, it follows that:

$$\frac{u'_u}{\overline{U}_u} = \frac{u'_i}{\overline{U}_i} \cdot \left(\frac{\overline{U}_i}{\overline{U}_u}\right)^2 = \frac{u'_i}{\overline{U}_i} \cdot \left(\frac{A_u}{A_i}\right)^2 = \frac{u'i}{\overline{U}i} \cdot \frac{1}{n^2}$$

Since the geometric parameter characterizing a convergent is the ratio n between the inlet area A_i and the outlet area A_u, referred to as the contraction ratio:

$$n = \frac{A_i}{A_u}$$

To give an example, for $n = 5$, the turbulence level I_u at the outlet is reduced by a factor of 25. Alternatively, in terms of the ratio of the standard deviations of the velocity fluctuations between the outlet and the inlet, one obtains:

$$\frac{u_{\mathrm{rms}_u}}{u_{\mathrm{rms}_i}} = \left(\frac{\overline{U}_u}{\overline{U}_i}\right) \cdot \frac{1}{n^2} = \left(\frac{A_i}{A_u}\right) \cdot \frac{1}{n^2} = \frac{1}{n}$$

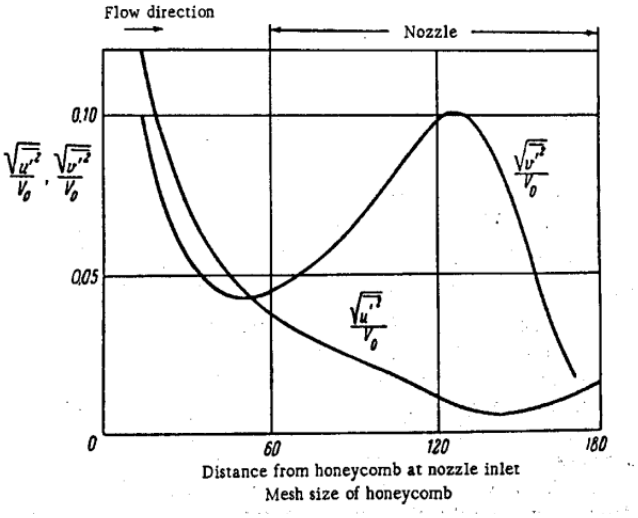

Figure 3.1: Variation of the component of the velocity fluctuation along a nozzle [41]

As an associated effect, there is a decrease in the longitudinal fluctuations u' and an increase in the transverse fluctuations v', which reach a peak roughly at the midpoint of the convergent and then decrease until the exit, as shown in Figure 3.1.

To mitigate the effects of model blockage in the wind tunnel, it is imperative to implement sophisticated methodologies for the measurement of dynamic pressure in the test chamber. One option involves the use of a *Pitot tube ring*, strategically placed at the entrance of the test chamber. This device allows for the computation of average values of total pressure P_{tot} and static

pressure P_{stat}. By correlating the dynamic pressure measurements obtained from the reference Pitot tube, located at the center of the test chamber, with those acquired from the Pitot ring, a linear relationship is established for various operating conditions, expressed as:

$$q_{\text{TS}} = K \cdot q_{\text{Ring}}$$

where q_{TS} represents the dynamic pressure measured by the single Pitot tube, and q_{Ring} is that measured by the Pitot ring. The coefficient K is an empirical correction factor.

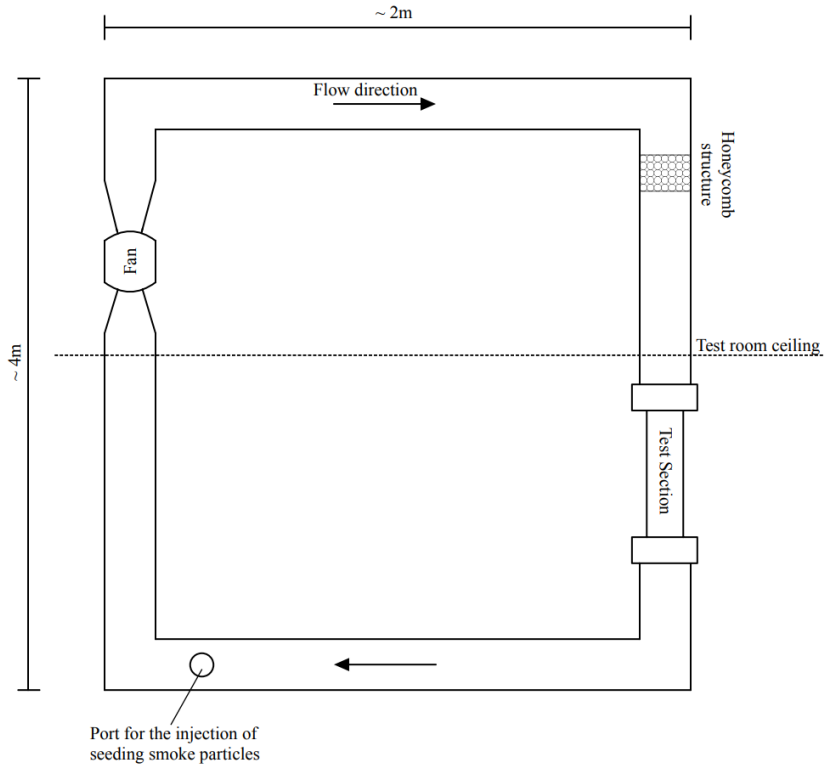

Figure 3.2: Wind Tunnel Schematic

In the absence of such advanced measurement systems, the determination of air velocity is performed through a direct correlation between the rotational speed of the fan (expressed in revolutions per minute, RPM) and the volumetric flow rate. The latter can be measured using a flow control device, located near the operator's station. The calculation of the volume flow rate and velocity is as follows:

$$v = K_m \sqrt{\Delta p}$$

$$Q_v = A K_m \sqrt{\Delta p}$$

where the probe flow rate constant is $K_m = 7.93$. The measurement error is $\pm 3\%$ [124]. A schematic representation of the wind tunnel used is illustrated in Figure 3.2.

To reduce the effect of pressure loss at the edges, straightening vanes are not used; instead, a honeycomb structure has been placed just after the corner before the test section. The structure and design of this honeycomb are discussed in the work of Tamagnini & Agostino [124].

The structurally complex part of the wind tunnel is the region where tests are conducted. Specifically, this area consists of a structure that houses the plates to be tested (testing bed)

a b

Figure 3.3: Arrangement of the test section for: (a) FULL FOV (Full Field of View) tests: Laser illuminating the plates parallel; (b) BL (Boundary Layer) tests: Laser illuminating the plates perpendicularly

and two adapters to connect the test section to the rest of the wind tunnel. The choice of such structural adapters is justified by the need to conduct two types of tests:

1. Tests in which the laser is parallel to the plates, allowing the camera to capture images perpendicular to the Test Section (TS). These measurements are identified in the thesis as FULL Field Of View (FULL FOV) tests, which are useful for validating the wind tunnel and ensuring that theoretical physical principles are respected, such as demonstrating that the maximum velocity is at the center of the duct using smooth plates.

2. Tests in which the laser is perpendicular to the plates, with the camera recording the thickness of the plates and thus their roughness. These tests will be referred to in the following work as Boundary Layer (BL) tests, necessary to categorize the flow behavior in the presence of roughness.

It is evident, therefore, that the operator must change the orientation of the test section by rotating it 90 degrees. An example of how the section is positioned for the two different tests is presented in Figure 3.3.

Figure 3.4 illustrates a representation of the test section with an adapter; the second extremity is intentionally depicted without an adapter to highlight the presence of a plate blank short, which is used for easier plate removal. These are fixed and held in position through the holes visible at the bottom of the test bed. All components, with the exception of the Plexiglas, were 3D printed in plastic. Table 3.1 summarizes the characteristic dimensions of the section, accounting for approximately ± 1 mm of tolerance for each measurement. The Plexiglas has been carefully fixed into its housing using epoxy glue: the accurate and precise execution of this operation ensured

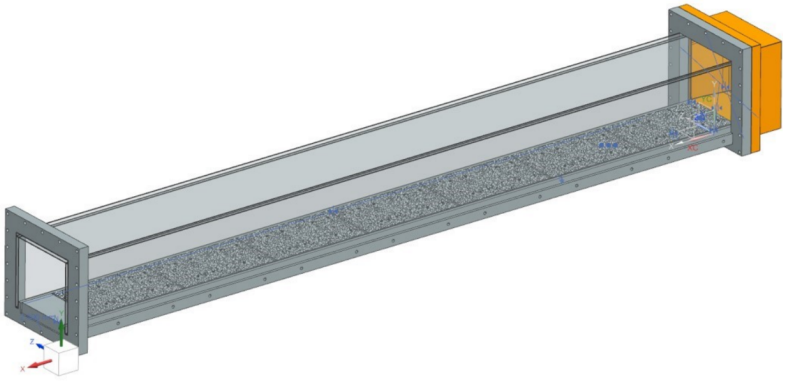

Figure 3.4: Test Section CAD

that no excess glue was present on the lateral walls, which require transparency and cleanliness to minimize reflections during tests and imaging.

Parameter	Dimension
Length of the test bed	1100 mm
Width of the test bed	91 mm
Height of the section	111 mm
Thickness of the channel for Plexiglas housing	6 mm
Number of plates that can be inserted	7

Table 3.1: Characteristic Dimensions of the Test Section

3.2.2 Analogue Rough Texture Modeling

In the current state of research conducted by previous thesis students, three possible up-scale roughness configurations with different characteristics for various tests have been identified. In this work, for the sake of completeness, only the research methods and identification of the first recreated up-scale artificial roughness model, *Inconel939*, are reported, as well as the texture that has been most extensively tested in the thesis in the field of flow visualization, because it has characteristics particularly suitable for visualizing fluid through surface roughness. The following discussion is the result of a broader and more complex work within the research conducted by Wen [115]. For further research details, the reader is referred to the aforementioned reference. Regarding the two most recent Analogous Rough Surfaces, named *Aluminium1* and *Aluminium2*, only the characteristic parameters are reported below. It is sufficient to know that these plates come from the same test object and have been obtained by optimizing different roughness parameters, as compared to the reference samples; this topic will be further discussed in the continuation of the work. For a more detailed description of the modeling and identification process of the textures, the reader is referred to the works of Brogliato [118] and Tamagnini & Agostino [124].

The method employed involves a stochastic distribution of spheres with varying sizes on a flat surface, which serves as a simulation for the textural properties of an actual additive manufacturing surface. This particular surface was derived from a mini-channel fabricated through Laser Powder Bed Fusion of Inconel 939 at a vertical orientation and with a channel diameter of 1.25 mm. The

hydraulic and thermal performance of the AM channel was evaluated using the quasi-steady state hydraulic thermal rig, as described by Pagani [108]. Subsequently, a section of the channel was cut to facilitate a detailed examination of its surface roughness.

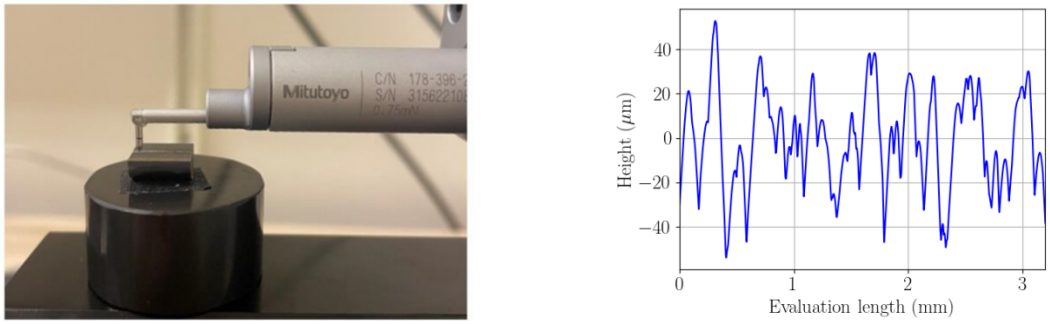

a b

Figure 3.5: Surface Roughness measurement of the test object [115]: (a) Profilometer Mitutoyo Surftest SJ-410 when measuring; (b) One measurement profile

The investigation of roughness was conducted in another Master's thesis by Björnram and Ljunggren [107]. The channel specimen was cut in half, and a non-contact profilometer was utilized to capture the surface's profile data. As depicted in Figure 3.5a, one half of the bisected channel was positioned under the profilometer's stylus, which traversed the length of the channel to record variations in height. Figure 3.5b presents one such profile that was recorded. To ensure the accuracy of the representation, Wen conducted a total of ten measurements on the sample [115].

To construct an analogous rough surface, it is crucial to accurately replicate the up-scaled surface parameters. Wen's investigation into the original test surface revealed that the test rig has a rectangular cross-section, measuring 0.09 m in height and 0.1 m in width, and each corner has a circular blend with a radius of 5 mm [115]. Excluding roughness considerations, the hydraulic diameter D_h of the up-scaled model was calculated to be 96.7 mm. In comparison, the hydraulic diameter of the actual Inconel 939 AM channel, without accounting for roughness, is 1.25 mm. To align the hydraulic diameters of the actual channel and the up-scaled model, the roughness parameters are scaled by a factor of $s = \frac{96.7}{1.25}$, which is approximately 77.4.

Subsequent to scaling, detailed micrographs were captured using a *Jeol JSM-IT500* scanning electron microscope (*SEM*), as illustrated in Figure 3.6. The micrographs revealed a heterogeneous distribution of spherical entities interspersed with more pronounced ridges and valleys. To fabricate a comparable surface, it was necessary to quantify this distribution. Lehmann [112] performed this quantification manually by examining the two SEM images, selecting discernible spheres, and noting their diameters. The resulting distribution is depicted in Figure 3.7a. Moreover, Wen [115] observed that by adjusting the coefficients of a gamma probability function, the resulting distribution closely mirrored that of a gamma distribution. Further details of this analysis can be found in the Appendix D.

The identified diameters were scaled by the factor s and compiled into a single dataset to determine the appropriate statistical distribution.

Figure 3.7b showcases the actual measured distribution alongside the theoretical gamma function and the simulated sphere diameter distribution. The sphere density, derived from the aforementioned manual selection procedure, was established at 372 spheres per square millimeter over an area of 2.28 mm^2, totaling 848 spheres. To account for situations where one sphere might be completely obscured by another, a slightly higher density of 380 spheres per square millimeter was

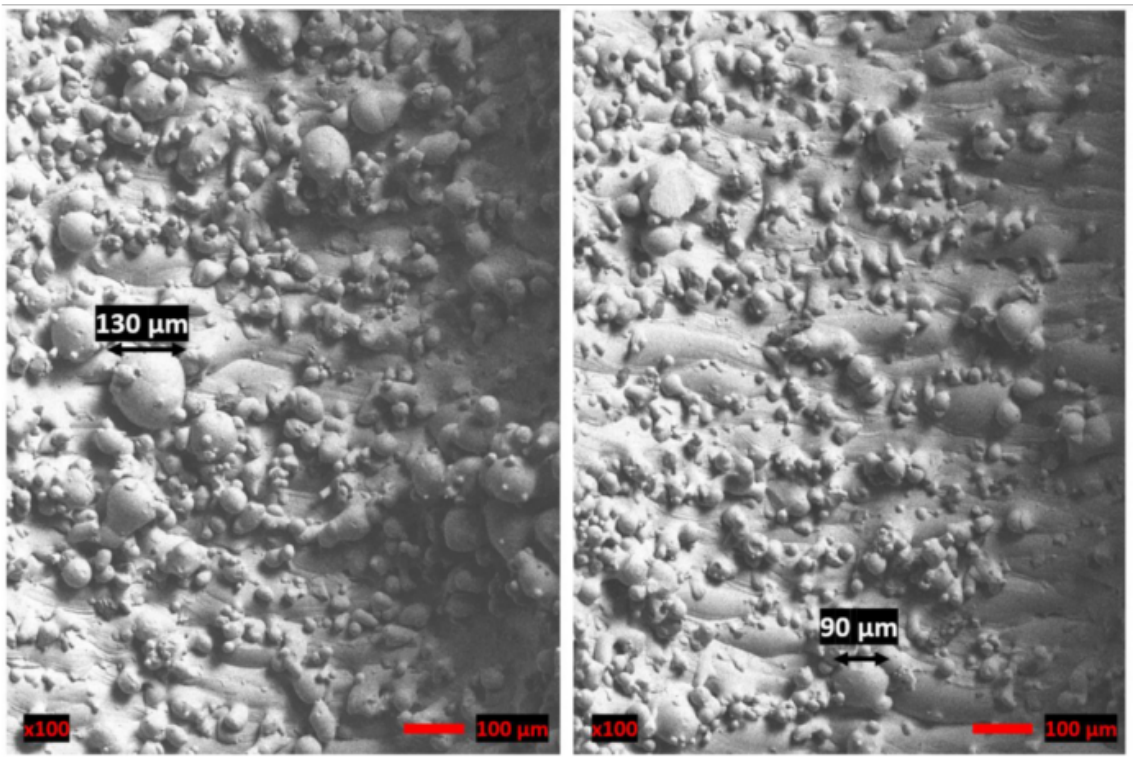

Figure 3.6: SEM pictures of the inner surfaces of the tested AM channel [107]

utilized [115].

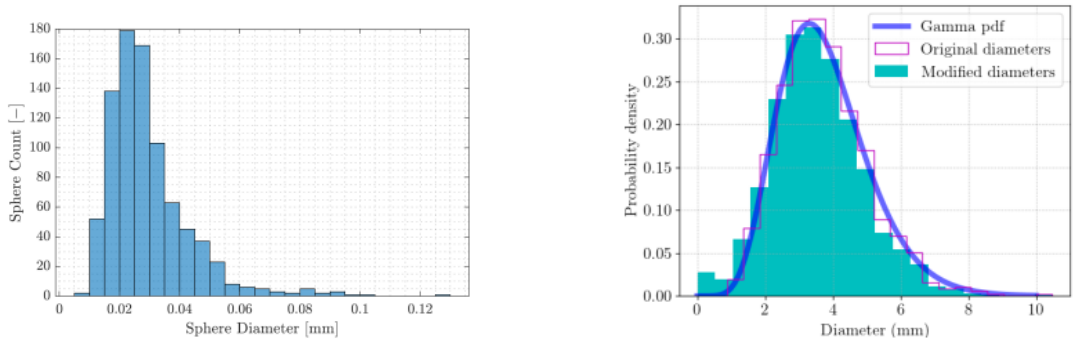

a b

Figure 3.7: Distributions of the spheres: (a) Histogram of the spheres captured from SEM pictures [112]; (b) Adapted gamma distribution and histograms of spheres [115]

The coordinates for the x and y positions of each sphere are determined using a uniform random distribution.

As specified by Wen [115], the depth of a sphere is represented by the ratio $\frac{z}{D}$, where z is the vertical position of the sphere's center. This ratio is derived from a normal distribution $\frac{z}{D} \sim \mathcal{N}(0, 0.04)$, with a mean μ of 0 and a standard deviation σ of 0.2. The selection of these parameters was refined through a systematic process of trial and error. To ensure that the spheres are attached to the plate without being fully submerged, the values are restricted within the interval $[-0.45, 0.45]$[1].

The roughness parameters related to both the analog rough surface and the real one (upscaled

[1] In this context, a $\frac{z}{D}$ value of 0 implies that the center of the sphere is precisely aligned with the surface level of the plate.

Material	Parameter	R_a [mm]	R_q [mm]	R_z [mm]	R_{sk} -	R_{ku} -
Inconel939	Real SR	1.077	1.325	5.689	0.46	2.79
[115]	Analogue SR	1.103	1.304	5.741	0.944	3.157
	Percent Error	2.41%	1.58%	0.91%	105.2%	13.62%
Aluminium1	Real SR	0.37	0.47	2.32	0.22	3.47
[118]	Analogue SR	0.37	0.49	2.35	2.00	5.80
	Percent Error	0%	4.25%	0.8%	814%	67.27%
Aluminium2	Real SR	0.37	0.47	2.32	0.22	3.47
[118]	Analogue SR	0.62	0.69	2.48	0.29	3.50
	Percent Error	66.7%	44.81%	7.27%	1.36%	0.94%

Table 3.2: Surface Roughness Parameters Comparison. It should be noted the approach by which the roughness parameters for Aluminum 1 and Aluminum 2 correlate with real test object features in different ways: the optimization for the first is in terms of R_a, R_q, and R_z, whereas for the second, it refers to R_{sk} and R_{ku}. The R_z parameter demonstrates an adherence to real conditions for both models: directly for the first and indirectly for the second

model) are presented in Table 3.2. This table also includes the parameters for the other two textures.

Figure 3.8 shows the three models of the generated analog rough surface. The printing process employs *Stereolithography* (*SLA*) with *Accura Xtreme Grey* material for all plates. To ensure a smooth surface quality, the printing process is carefully calibrated to maintain a layer resolution of 0.1 mm.

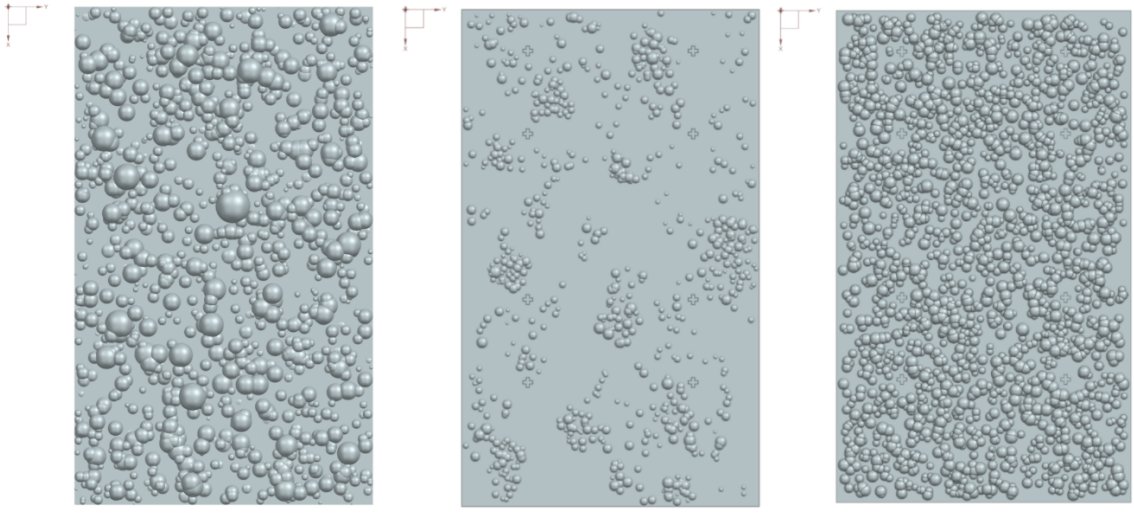

Figure 3.8: CAD design of the up-scaled prototype plate with AM-induced surface roughness. From left: Inconel939, Aluminum1, Aluminum2

As previously mentioned, the majority of the tests were carried out on the first model of artificial roughness, as it features a texture with larger, more pronounced spheres that are more easily observed with the available PIV facility.

Subsequent models were designed to examine heat transfer behavior by altering the sphere size and, most notably, the surface density of these spheres. The intention was to characterize the distinction between "k-type" and "d-type" roughness, initially proposed by Perry et al.[17] In fact, the primary characteristic used to differentiate the two models is the surface density [52], which Schlichting [7] quantified using the solidity parameter λ, defined as the ratio of the total projected

frontal area of the roughness elements to the wall-parallel projected area. These findings led to the identification of two distinct regimes: the sparse regime with a solidity below 0.15, where roughness effects intensify with increasing solidity, and the dense regime, where they diminish due to the roughness elements providing mutual shelter. In the sparse regime, the incremental drag from roughness is logically expected to be proportional to the frontal surface of the roughness elements, as stated by λ [52].

Presenting only the core findings (readers are encouraged to refer to Jimenez [52] for a detailed discussion), various experimental studies attempted to describe flow behavior over a surface after altering the λ factor. The prevailing explanation for this behavior, considering the roughness for the d-type regime, asserts that they maintain stable recirculation vortices that shield the outer flow from the roughness elements, as depicted in Figure 3.9. Surfaces with grooves wider than $(3:4)k$ act like k-type surfaces and also keep recirculation bubbles that reattach before the subsequent rib, exposing it to the outer flow.

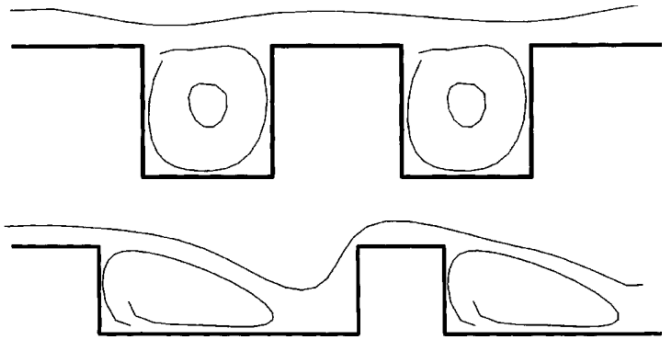

Figure 3.9: From top, geometry of d-type and k-type slotted walls. Flow is from left to right [52]

As observed by Perry et al.[17], across several boundary layers over plates roughened with narrow spanwise square grooves, the effective roughness k_s was not proportional to the roughness height k, but rather to the boundary-layer thickness δ. Jimenez [52] provides a clear analysis of this behavior, interpreting how this model explains how the flow becomes insulated from the grooves' interiors, rendering k_s independent of their depth. While the influence of the boundary-layer thickness is more elusive, in the case of ideally stable groove vortices, the outer flow encounters an alternating boundary condition of no-slip at the rib tops and partial slip over the cavities. Here, the pertinent length scales seem to be the groove width and pitch, both of which scale with k.

3.2.3 PIV Measurement Systems

The PIV measurement system was the primary data collection method used in this thesis. Prior to its use, an analysis was conducted to clarify the actual usefulness of this measurement technique for the tests of interest. However, the turbulent nature of the flow and the need to measure dynamic instantaneous characteristics of it (such as the presence of eddies or recirculation zones to correlate with the actual heat exchange in those areas) quickly reduced the array of available usage techniques to those "*multi-point*", ultimately leading to the selection of the planar PIV technique.

A schematic representation of the setup in the PIV room is presented in Figure 3.10.

3.2.3.1 Laser

The laser used in the experiments was the *NANO S65-15 PIV Laser*, manufactured by Litron Lasers UK. The system uses two pulsed and Q-switched Nd:YAG lasers producing infrared laser light at

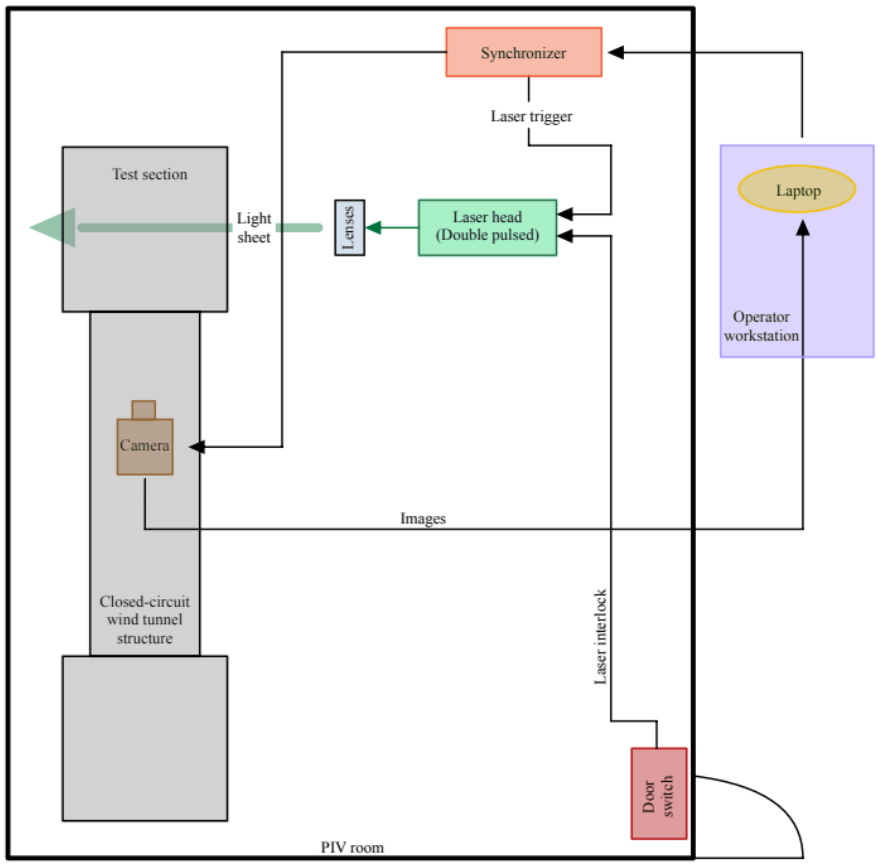

Figure 3.10: Schematic of the testing set-up. Flow direction is perpendicular to the floor, from top to bottom

1064 nm, which is converted to visible 532 nm laser light by a Harmonic Generation Assembly (HGA); the outgoing laser beam is of a Gaussian nature. To ensure that both laser outputs can be used with a single set of external optics, the 1064 nm laser beams are combined using polarizers before the HGA. The two beams are factory-aligned to be co-axial and exit the laser orthogonal to the output front plate. The output front plate for the Nano PIV series is supplied with the correct holes and screw threads to allow easy fitting of laser light sheet optics from all the main PIV system manufacturers. The 532 nm HGA is actively heated and thermally stabilized at approximately 100 $°C$. The active temperature stabilization ensures consistent tuning of the 532 nm crystal regardless of the local ambient temperature.

A motorized attenuator is fitted onto the base plate after the beam-combining optics and before the HGA. This allows for fine control of the laser output energy, without changing any of the lamp or Q-switch drive settings. This ensures the highest fidelity of the beam spatial profile at all pulse energies, as reported in the manufacturer's manual. An overview of the internal components of the laser is illustrated in Figure 3.11. The Nano PIV series utilizes an integrated PIV power supply (LPU450), with the lower part of this unit dedicated to the thermal management process: deionized water is used to cool the lamps and the laser rod during operation.

The laser functionality is controlled via an RS232 serial interface. The RS232 interface allows for the option of using the supplied software running on a PC or the touchscreen remote Litron Universal Control interface – LUCi. Setting the system parameters related to the laser is a key element for the correct execution of PIV tests; indeed, the main parameters studied and varied during laboratory tests are reported below.

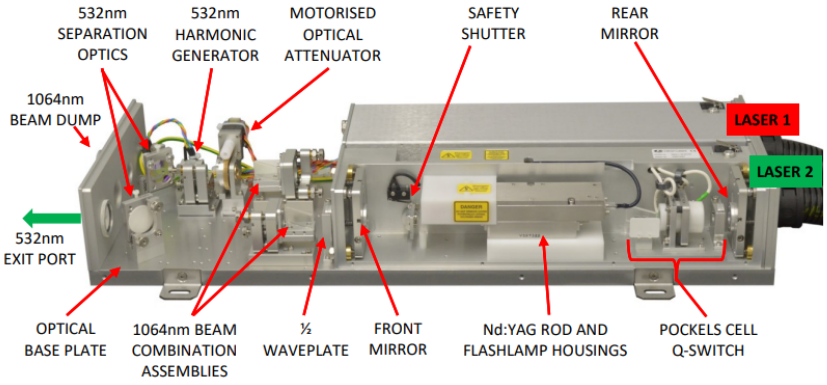

Figure 3.11: Nano PIV Laser Head Internal Components

Drive: This changes the amount of energy delivered to the flashlamps for each pulse, and can be adjusted for Laser 1 and Laser 2 independently. For all experiments, a value of 100% was set for both Laser 1 and Laser 2.

Attenuator: it uses a rotating waveplate to vary the polarization of the combined 1064 nm beam, thereby achieving different levels of 532 nm harmonic generation efficiency. When the attenuator is set to a low value, only a small portion of the laser output is converted to 532 nm and exits the laser head, while the residual 1064 nm is absorbed by a beam dump. This value was carefully managed during the tests, as too high a value could create reflections dangerous for the camera sensor, with the possibility of damaging it. For this reason, the value was maintained in the $15\% - 45\%$ range depending on whether the tests were conducted very close to a wall or farther from it. For the alignment and calibration phase, a value of 2% was used.

Q-Switch Delay: this is the delay between triggering the flashlamps and triggering the Q-switch. The optimum delay time will be recorded in the Laser Test Results supplement, and for the current laser, the values are set at: 120 μs for Laser 1 and 125 μs for Laser 2.

Repetition Rate: the duration of the pulse is 4 ns, and the system is capable of reaching a peak repetition frequency of 100 Hz. Nonetheless, operations have been conducted at a frequency of 15 Hz. This operational choice is informed by the manufacturer's tests, which have established this frequency as the one at which the laser system's performance is optimized, particularly with respect to the timing of the Q-switch.

3.2.3.2 Optics and Lenses

A dual-lens configuration, comprising a cylindrical lens coupled with a spherical lens, is employed to form the laser sheet. Figure 3.12 illustrates this arrangement. Within this system, the initial lens is responsible for the vertical expansion of the beam, while the subsequent lens narrows the light sheet. This effectively counteracts the initial expansion, thereby preserving a uniform width of the sheet. The determination of the laser sheet's height is facilitated by a direct calculation, utilizing the relationship [65]:

$$D = \frac{f_2}{f_1} \cdot d$$

Within the actual experimental framework, the lenses are characterized by focal lengths of

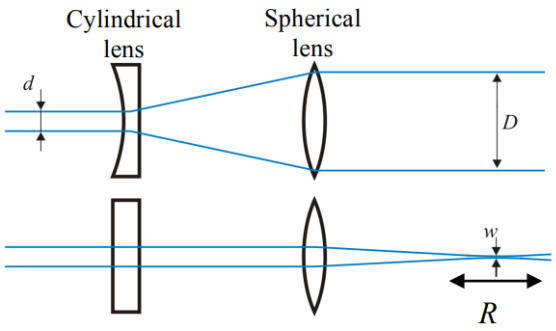

Figure 3.12: Lenses configuration [65]

40 mm and 500 mm, respectively, and the diameter of the laser beam is 4 mm. Therefore, the calculation yields:

$$D = \frac{f_2}{f_1} \cdot d = \frac{500\ \text{mm}}{40\ \text{mm}} \cdot 4\,\text{mm} = 50\,\text{mm}$$

In general terms, the thickness of the actual laser sheet upon impact with the plates was determined by assessing the divergence angle of the laser beam, which is considered to have a Gaussian profile. This was achieved by first calculating the divergence angle θ_0 using the formula [65]:

$$\theta_0 = \arctan\left(\frac{d/2}{f_1}\right)$$

Subsequently, trigonometric relations were applied after evaluating the distance from the plates to the focal point of the second lens, which is 225 mm:

$$\frac{x}{2} = l\sin(\theta_0)$$
$$225\,\text{mm} = l\cos(\theta_0)$$

From which it follows that:

$$x = 2\tan(\theta_0) \cdot 225\,\text{mm} = 1.798\,\text{m}$$

It is therefore reasonable to consider that the thickness of the actual laser sheet upon impact with the plates is less than 2 mm.

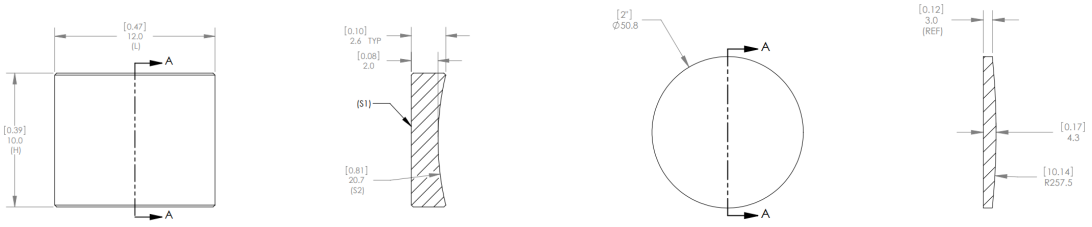

a b

Figure 3.13: Lenses used: (a) N-BK7 Plano-Concave Cylindrical Lens; (b) N-BK7 Plano-Convex Lens

3.2.3.3 Seeding Generator

For the generation of tracer particles within the airflow, a portable fog device, the *TINI CX fogger*, is employed as shown in Figure 3.14. The device operates with a proprietary solution known as

Tiny Fluid, which is a mixture mainly consisting of glycol and water, yielding a harmless, non-toxic fog. Despite thorough investigation, precise information on the fog particles' size distribution has not been obtained. Therefore, it is hypothesized that the mean droplet diameter (d_p) is in the vicinity of 1 μm.

Figure 3.14: TINI CX seeding generator

As described in Section 2.6.1.1, the size of these droplets is pivotal for achieving a Stokes number below one. Utilizing the formula $\tau_p = \frac{d_p^2 \rho_p}{18\mu}$, the response time of the particles is inferred to be approximately 3.0×10^{-6} s.

Conversely, given a wind speed in the wind tunnel of 2.5 m/s, the fluid's characteristic time is computed to be 0.0379 s [121]. The considerably low Stokes number, being well below 1, suggests that the particles are expected to closely mimic the airflow, exhibiting negligible slip [34].

3.2.3.4 Camera and Camera Lens

In the conducted experimental studies, a *Chronos 2.1-HD High-Speed Monochromatic Camera* was utilized, as illustrated in Figure 3.15a. The deployment of such a camera in conjunction with a dual pulse laser system is atypical due to its lack of an inherent double shutter capability. To address this limitation, a specialized synchronization apparatus was engineered, building upon the groundwork laid by Pedreño Marin [121], with further elaboration provided in the subsequent section.

a b

Figure 3.15: (a) Chronos 2.1-HD High-Speed Monochromatic Camera; (b) Samyang 100 mm $f_\# = 2.8$ UMC MacroLens for Canon

The camera's sensor is CMOS type and it is capable of capturing imagery at a rate of 1000

frames per second (FPS) when operated at its highest resolution setting of 1920×1080. With a pixel size of $10\,\mu$m, the sensor's physical dimensions amount to 19.2 by 10.8 mm. The operational mechanism selected for the camera was the shutter gating trigger mode, which permits an external signal to dictate the exposure duration and frame rate, a feature that will be expounded upon in a forthcoming discussion.

For the purpose of image acquisition, the lens chosen was a *Samyang* 100 mm $f_{\#} = 2.8$ *UMC Macro Lens* designed for Canon EF mounts. It is equipped with a manual ring for adjusting the aperture, offering a wide range from an f-stop (f-number) of 32 to its widest setting at 2.8, as shown in Figure 3.15b. The manual control of the aperture was a critical feature because the camera lacks the capability to adjust the aperture settings electronically. The ability to manually widen the aperture becomes essential when dealing with small seed particles or in scenarios with low light intensity, as it enables the camera to maximize light sensitivity.

3.2.3.5 Laser and Camera Support Structure

In the experimental environment of the PIV chamber, a dedicated structure has been integrated to support both the camera and the laser, while also enabling the positional adjustment of the laser. The assembly features a mechanical bridge with an equipped motor, which can be remotely operated via a laptop. This mechanism facilitates vertical movement of the entire apparatus. Lateral movements (left and right) are manually controlled through the use of knobs. Furthermore, the camera's position in relation to the test section is manually adjusted to ensure the correct focal distance.

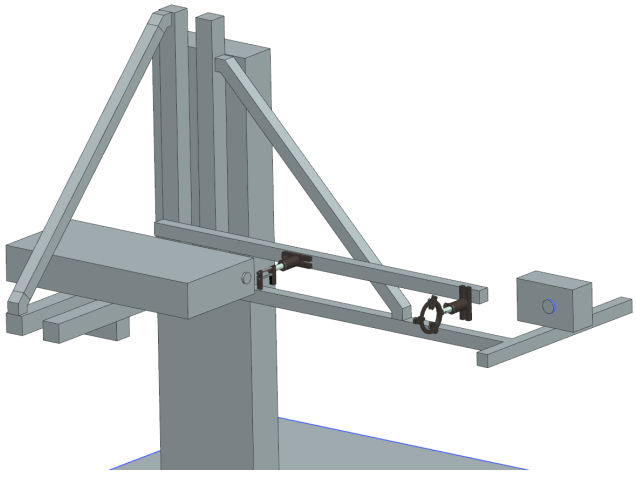

Figure 3.16: Camera and Laser support structure on the Dantec Dynamics traverse System

3.2.3.6 Synchronizer

The synchronization of laser and camera activation is managed by custom-developed software [121] running on an Arduino Uno R4 board. Within this configuration, the laser operates as the "master" unit, while the Arduino intermediates to activate the camera. Equipped with a 32-bit microprocessor clocked at 48 MHz, the Arduino begins the sequence by responding to the internal flash-lamp trigger from laser-head 1. This trigger prompts the Arduino to signal the camera to commence the exposure. Following a delay, the Q-switch triggers, issuing the first laser pulse. The Arduino monitors the Q-switch signal and, after a designated delay period, stops the "shutter open" signal to the camera, prompting shutter closure. Almost immediately, the Arduino reissues the

"shutter open" signal, but only for a negligible duration, on the millisecond scale. This completes a single cycle, successfully producing a pair of images. A schematic of the Arduino circuitry is shown in Figure 3.17.

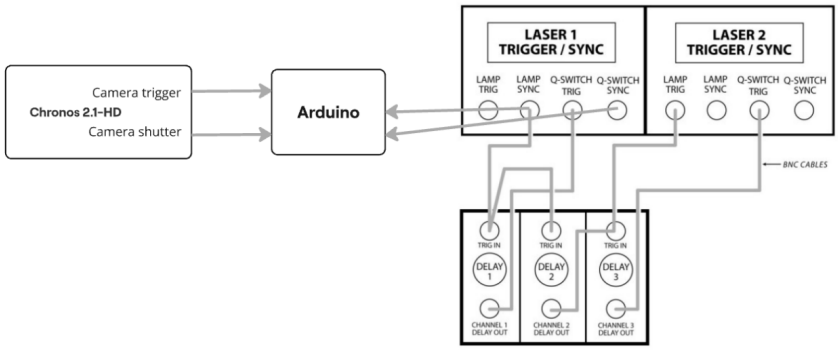

Figure 3.17: Scheme of the Arduino connections

The method employed to control the camera shutter poses complications during the black calibration phase. This calibration is critical for the camera's functionality, as it subtracts a reference black image from all captured frames to refine image clarity. Nonetheless, the following issues have arisen with this approach:

- Initially, horizontal lines appear in the images, suggesting a malfunction in certain pixels;
- Moreover, there is sporadic evidence of superfluous white noise in one image of each pair, either image A or B. This anomaly is likely attributed to a disparity in the shutter's open times for the respective frames, which is confirmed by the "camera exposure" signal in the timing schematic illustrated in Figure 3.18, highlighting a longer duration for frame B. An example is shown in Figure 3.19.

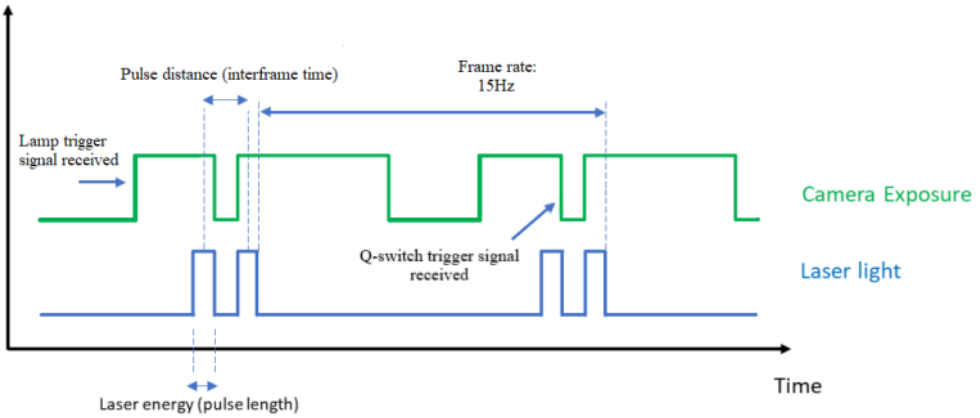

Figure 3.18: Timing Schematic [121]

3.2.3.7 Software

The control of image recording was achieved through Arduino software, and camera parameter adjustments were facilitated via the Chronos website interface. Concurrently, settings for laser timing

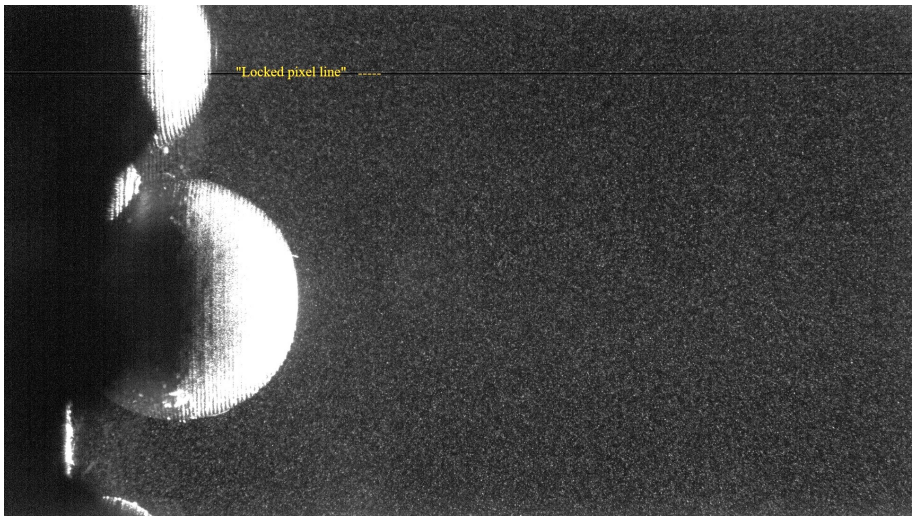

Frame A depicting the line of "locked" pixels and white noise

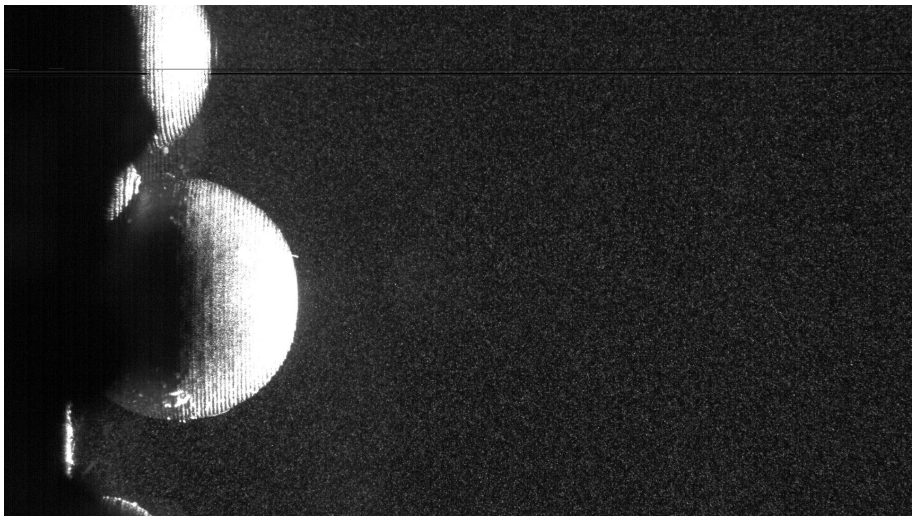

Frame B with no white noise

Figure 3.19: Pictures showing the quality defects in images post the camera's black calibration process (with increased contrast for clarity)

and illumination were configured using the provided LUCi Controller. This configuration permitted the alteration of the interval between successive images by employing the Arduino Synchronizer.

For the purposes of image post-processing, the open-source software *PIVlab* for Matlab [103] was utilized. PIVlab employs a cross-correlation algorithm to extract the velocity field from the PIV images. Subsequent post-processing of the velocity field data was predominantly executed in Matlab.

3.2.4 Data Analysis Methods

For the effective execution of PIV experiments, an Excel spreadsheet was devised. This spreadsheet requires input of specific test parameters such as the tunnel's mass flow rate, the desired field of view for the camera, and the dimensions of the interrogation windows. Based on these inputs, the spreadsheet calculates the appropriate f-stop setting, which must then be manually entered into the camera according to the magnification factor. Additionally, the spreadsheet provides a value for Δt (pulse separation time), which is to be configured in PIVlab and also serves as a crucial parameter for the laser settings. More specifically, within the LUCi laser control system,

it is necessary to input a FLASHLAMP DELAY value, calculated as $\Delta t - 5\,\mu$s. This deduction accounts for the inherent delay between the firing of the two Q-Switches, which activate with a $120\,\mu$s and $125\,\mu$s delay respectively.

Regarding the evaluation of Δt, it is important to consider some factors. Above all is the consideration of particle displacement between frames, which depends precisely on Δt. It is typically recommended to keep the in-plane particle displacement below one quarter of the interrogation window size [65]. Therefore, regarding to Equation 2.15:

$$d_{\text{particle}} = V_{\text{particle}} \cdot M \cdot \Delta t$$

where M is the magnification factor and is calculated as shown in Equation 2.14. Hence:

$$\Delta t = \frac{d_{\text{particle}}}{V_{\text{particle}} \cdot M} = \frac{\frac{1}{4} \cdot \text{Interrogation window pixel size} \cdot \text{pixel pitch}}{\text{Wind tunnel speed} \cdot M} \tag{3.1}$$

By varying the inputs, which turn out to be the magnification factor (as it depends on the desired length of view of the camera), the wind tunnel speed and the size of the interrogation window, the value of Δt is known. This parameter has some limitations: the minimum achievable value for Δt is limited to $20\,\mu$s, due to the intrinsic delay associated with the Arduino system. Consequently, if the input parameters result in a Δt value that falls below the established minimum threshold, adjustments to these parameters will be required. This threshold has been empirically established, drawing upon accumulated experience.

3.2.4.1 PIV Settings

The experiments conducted, as stated in Section 3.2.1, can be categorized into two types: FULL FOV tests and Boundary Layer tests, depending on whether the laser beam is parallel or perpendicular to the plates, respectively. This distinction necessitates two different settings, depending on the type of test to be conducted. The following tables illustrate some differences in the settings; specifically, Table 3.3 displays the differences between the FULL FOV and BL tests conducted with smooth plates, while Table 3.4 shows the variation in parameters when setting up the BL tests, comparing smooth and rough plates. Initially, tests were conducted on smooth plates to validate the test section and to compare the results with those found in the literature, in order to ascertain the accuracy of the PIV experiments.

Smoot plates test	FULL FOV	Boundary layer
Field of view	(6.3×3.5) cm	From (3.1×1.75) cm To (8.1×4) cm
Laser power	25%	From 15% to 45%
Interrogation windows [px]	16×16	From 18×18 To 34×34
Reynolds	$2.35e+04$	From $7.56e+03$ To $4.48e+04$

Table 3.3: Difference between FULL FOV and Boundary Layer tests for smooth plates

It is clear that the substantial difference when operating in these two different modes is the camera's field of view, which becomes a critical parameter when conducting tests with plates featuring artificial roughness. Being very close to the wall is an essential requirement to obtain high-quality PIV images with high validation. This requirement must also take into account the Reynolds number in the tunnel and the size of the interrogation windows, which depend on the size of the field of view. These factors must be considered when setting the parameters, due to the

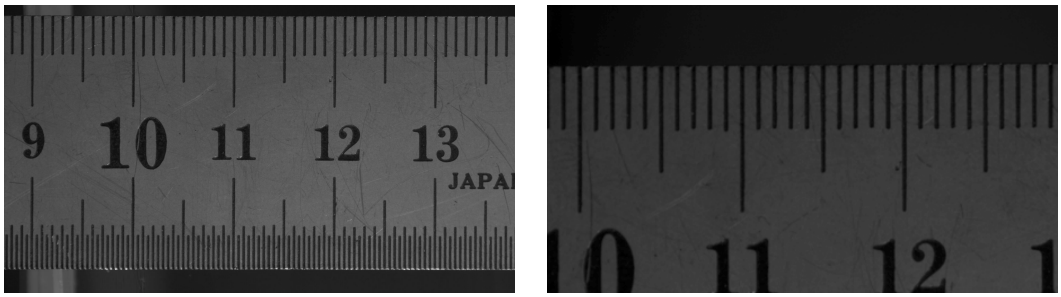

FULL FOV Boundary Layer

Figure 3.20: Example of field of view for smooth plates tests

limitations previously explained.

Boundary layer tests	**Smooth plates**	**Rough plates**
Field of view	From (3.1×1.75) cm	From (2.4×1.2) cm
	To (8.1×4) cm	To (8.1×4) cm
Laser power	From 15% to 45%	From 15% to 45%
Interrogation windows [px]	From 12×12	From 12×12
	To 34×34	To 28×28
Reynolds	From $7.56e + 03$	From $5.78e + 03$
	To $4.48e + 04$	To $4.46e + 04$

Table 3.4: Difference between Boundary Layer tests for smooth plates and for rough plates

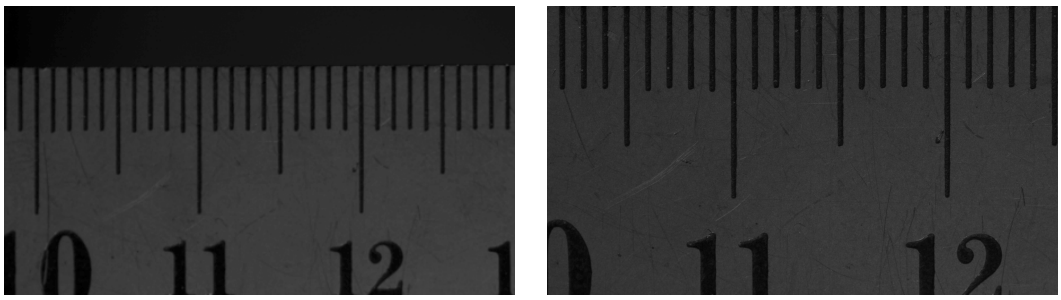

Smooth plates Rough plates

Figure 3.21: Example of field of view for Boundary Layer tests

The PIV technique is highly susceptible to errors that arise from misalignment and miscalibration. Consequently, it is imperative for the operator to execute these procedures with the highest precision. To facilitate accurate alignment, the laser should be positioned so that its beam closely parallels the edge nearest to the camera. By placing a ruler along the side designated for laser alignment, the camera can be meticulously focused to ensure that the ruler's image appears sharp and is not overexposed. A deviation as minor as 1 mm in alignment can introduce significant errors, as depicted in Figure 3.22.

3.2.5 Image Evaluation

To obtain the displacement data from a PIV recording, it is necessary to employ a specific method of examination. The PIV technique used generates individually exposed images, meaning the flow field is illuminated and captured at the same instant by the camera thanks to the synchronization system, so that each pair of images contains the same particles, but at different time instants.

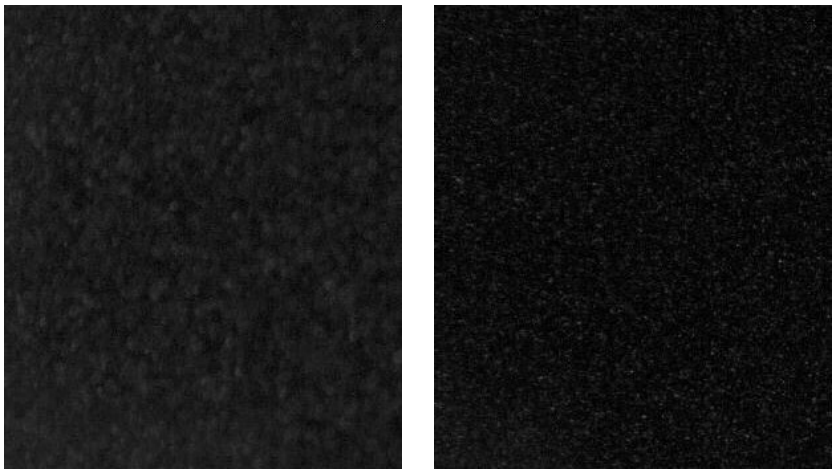

a b

Figure 3.22: Example of a cropped section (300×350 pixels of 1920×1080 pixel frame) from PIV images acquired during testing. In both images, an overexposure of 40% compared to the original is applied to make the differences in particle acquisition visible. (a) Image resulting from a 1.5 mm misalignment in the alignment-calibration stage; (b) Image with proper focus

Subsequently, an instantaneous velocity field is extrapolated from these image pairs by implementing a statistical algorithm called cross-correlation (see Figure 3.23). The calculation of the cross-correlation function is generally performed numerically using efficient FFT algorithms [88], as in the case of the implementation in PIVlab.

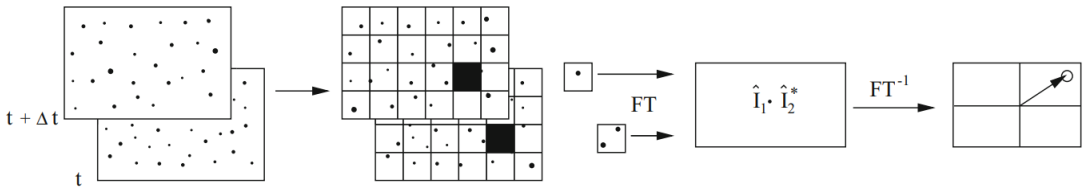

Figure 3.23: Digital cross-correlation method [88]

3.2.5.1 Correlation

Interrogation windows are analyzed using cross-correlation to figure out the likely movement of particles in these areas. Cross-correlation is a way of comparing patterns to match the particle arrangements from one section (Zone A) to another (Zone B) [74]. The discrete cross-correlation function is defined as:

$$C = \sum_i \sum_j A(i,j)B(i-m, j-n) \tag{3.2}$$

where A and B are corresponding interrogation areas from image A and image B, while m and n represent the displacement along the x-axis and y-axis, respectively. The location of the intensity peak in the resulting correlation matrix C gives the most probable displacement of the particles from A to B [74], as shown in Figure 3.24.

There are two common approaches to solve Equation 3.2: compute the correlation matrix in the spatial domain using direct cross-correlation (DCC), or compute the correlation matrix in the frequency domain (discrete Fourier transform, DFT). The analysis method used is related to frequency analysis using an FFT window deformation, with 4 passes and 50% overlap: the analysis

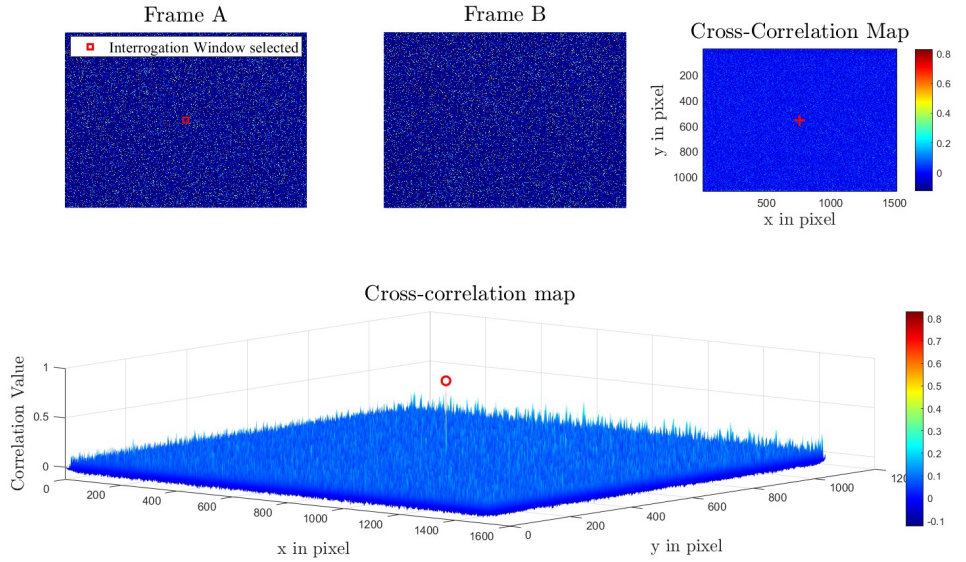

Figure 3.24: Example of detection of a correlation peak, with analysis of an interrogation window localized at the center of Frame A. Illustration obtained using a MATLAB code that incorporates a (DCC) algorithm, using a 32×32 pixel interrogation window, with a 50% overlap and a 9 pixel displacement before finding the cross-correlation peak

starts from a larger interrogation area (ranging from 64×64 to 96×96 pixels), ensuring that the displacement information is at the center of each interrogation area. When the areas overlap, additional displacement data is present at the periphery and vertices of each interrogation zone. In this way, after a few passes, the displacement information accumulates, making the analysis of movement more accurate. The correlation peak is located using a Gaussian function, which fits the intensity distributions. Although the analysis method using a Gaussian function fit through 3 points is widely used in literature (see Thielicke[74] for more details), the analysis conducted was adopted through a 9-point fitting method (two-dimensional Gaussian function implemented in PIVlab) to avoid errors due to excessive motion blur to which the images are subject.

3.2.6 Image Pre-Processing

The PIV measurement method is a technique whose effectiveness is strongly influenced by the quality of the captured images. In particular, the correlation signal is easily distorted under conditions of non-uniform particle illumination, irregular sizes and shapes of particles, and by a non-uniform laser beam. These factors, related to light intensity, affect the peak of the cross-correlation function, as the latter coincides with the point where the light intensity of the particle at time t_0 matches the light intensity of the same particle captured in the interrogation area at time $t_0 + \Delta t$. Subsequently, the distance between the origin and the centroid of the most intense peak corresponds to the most probable displacement within the interrogation area under analysis. The close dependence that exists between these parameters, which conditions the validity of the results, necessitates the use of *pre-processing* techniques for PIV images in order to enhance the contrast of the particle images and to bring the intensities of the particle images to a similar signal level, so that all particle images have a uniform contribution to the correlation function. As reported by Raffael et al.[88], among the methods for image enhancement, *background subtraction* from PIV recordings reduces the effects of laser glare and other stationary image features. The background

image that will subsequently be subtracted from the raw PIV images is calculated by defining an average intensity image from the set of input images evaluated for the test under analysis. This operation is directly performed in PIVlab using the "subtract mean intensity" command. Moreover, in the analysis of PIV images, the software PIVlab utilizes the CLAHE (*Contrast Limited Adaptive Histogram Equalization*) approach to enhance the probability of detecting valid vectors in experimental images. Unlike standard histogram equalization, which spreads the most frequent intensities across the entire data range, CLAHE improves contrast in a localized manner by operating on small regions of the image, known as tiles. This technique is particularly suitable for PIV, where uniform exposure across the entire image cannot be guaranteed due to the Gaussian nature of the laser beam's intensity distribution [74]. As implemented in PIVlab, CLAHE allows for the independent optimization of areas with low and high exposure. The final image, produced after the application of CLAHE, exhibits a seamless transition between tiles through the use of bilinear interpolation, thereby removing any visible borders between them. To remove spurious information due to low-frequency background reflections, a *high-pass filter* is applied that mostly preserves the high-frequency information coming from the particle illumination. This high-pass effect is achieved by applying a low-pass filter to the image (blurring the image) and then subtracting the result from the original image. The implementation of this method in PIVlab ensures an emphasis on the particle information in the image and suppresses any low-frequency information. It is necessary that the width of the filter Kernel be greater than the diameter of the particles captured in the image [88]:

$$k_{smooth} > d_p$$

This condition is sufficiently met by setting a Kernel size of 15 px, taking into account that the estimated particle diameter is around $(1 \pm 0.5)\,\mu$m and that, in the testing condition with the smallest interrogation window in the data campaign (12×12) px, the size of one pixel is about $9\,\mu$m.

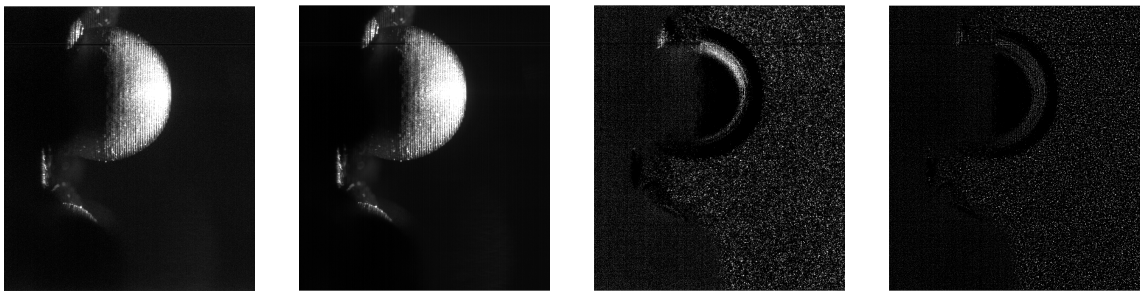

Original | Background Subtract | CLAHE | High-pass filter

Figure 3.25: Impact of various image pre-processing methods

3.2.7 Image Post-Processing

After examining the PIV recordings, a number of velocity vectors that appear to be incorrect, known as outliers, are often found. These outliers are typically identified through an initial visual evaluation of the preliminary data. To accurately identify these anomalies, the raw flow field data must undergo a validation process. This requires the development of sophisticated algorithms capable of performing the validation autonomously, which are already implemented in PIVlab [74]. The validation process is carried out by selecting only the vectors that are relevant for the evaluation of the results. Specifically, these vectors are identified by selecting the area where they tend to concentrate. This type of validation falls under the category of *manual* analyses, performed

in PIVlab (see Figure 3.26). It is important to exercise discretion when utilizing this approach, as it is contingent upon the experimenter's judgment, thus introducing a considerable subjective element. For all the analyses performed, a validation threshold greater than 95% was chosen.

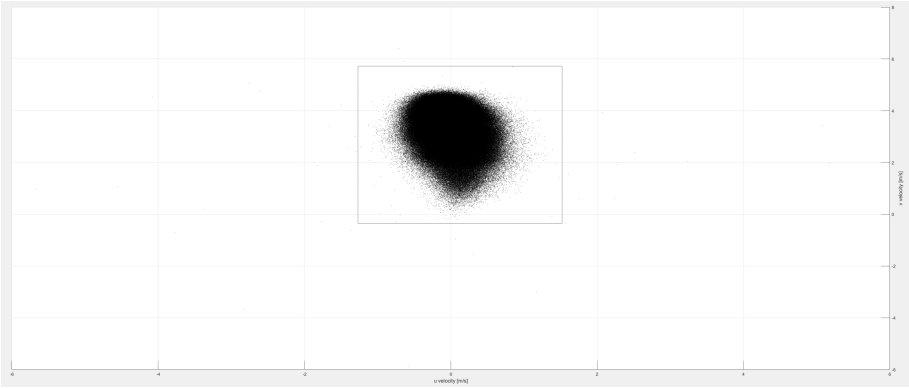

Figure 3.26: Velocity Validation. On the x-axis, the u component of velocity, on the y-axis, the v component of velocity

Semi-automatic estimations have also been conducted, developing a MATLAB code where each velocity component can be compared with a lower threshold and an upper threshold (t_{lower} and t_{upper}):

$$t_{lower} = u - n \cdot \sigma_u$$

$$t_{upper} = u + n \cdot \sigma_u$$

where u is the mean velocity; σ_u is the standard deviation of u. The user-defined constant n determines the strictness of this filter. As a result, velocities that do not fall within these thresholds will be discarded. This simple filter is very effective in practice [74], as it adapts to some extent to the nature of the flow: in highly turbulent flow, the standard deviation will be large, and the filter will be less strict. In laminar flow conditions, the standard deviation is likely to be small, and the filter will tend to reject vectors that deviate slightly from the mean velocity. Figure 3.27 displays an example of such a validation.

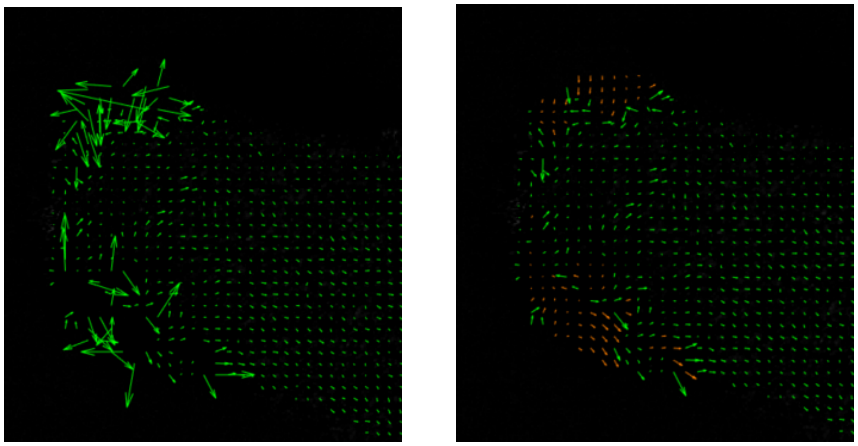

a b

Figure 3.27: Difference between two areas of the same zoomed PIV image where: (a) no validation was carried out, resulting in erroneous vectors (outliers); (b) a manual validation was performed, taking into account only the vectors aggregated in a single area, which determine the characteristics, presumed to be true, of the flow under examination

3.2.8 Testing Campaigns

The measurement campaign covered all three up-scale roughness profiles developed over the years by previous thesis students: Inconel 939, Aluminium 1, and Aluminium 2. Specifically, the aim was to compile a comprehensive database for future use. The tests conducted focused on both the visualization of flow in the immediate vicinity of the roughness and a wider visual window, so as to also identify the average properties of the plates by observing the behavior of these properties in relation to the constitutive roughness parameters of the test objects.

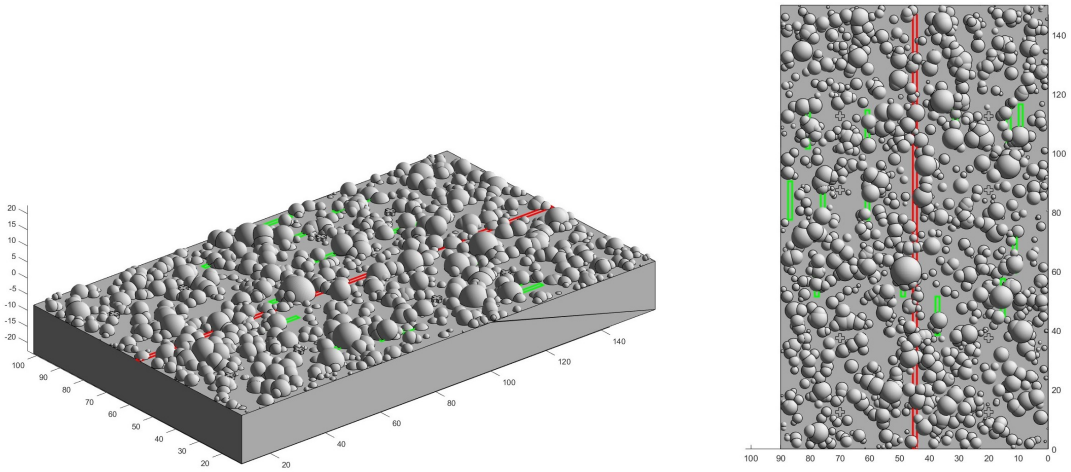

Orthographic view Top view

Figure 3.28: Test campaign conducted on the test object that identifies the upscale roughness typical of Inconel 939. The green rectangles, measuring (1.336×13) mm, pinpoint the tests carried out with the aim of visualizing the flow in the immediate vicinity of the roughness ($FOV = (2.4 \times 1.2)$ cm). The section highlighted in red identifies the area from which the average characteristics of the plate were extrapolated (for example, the average motion field or friction characteristic). These tests were conducted with a wider field of view from (3.8×2.2) cm to (8.1×4) cm

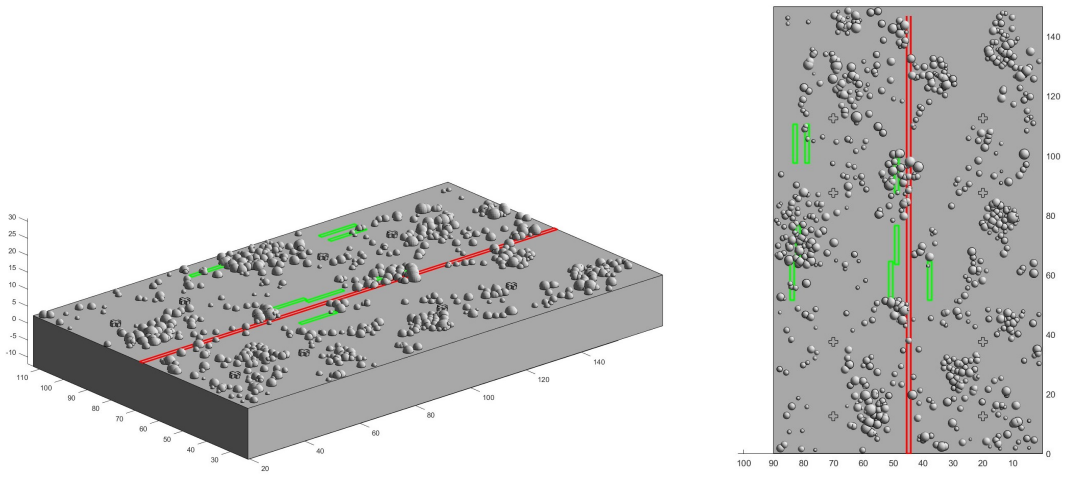

Orthographic view Top view

Figure 3.29: Test campaign conducted on the test object that identifies the upscale roughness typical of Aluminium 1. For the legend, see the description of Figure 3.28

It is clearly evident from Figures 3.28, 3.29, and 3.30 that the majority of tests were conducted on Inconel 939. This is because there was an intention to emphasize areas where the geometric characteristics of the roughness were different, and the test object representing Inconel 939 turned

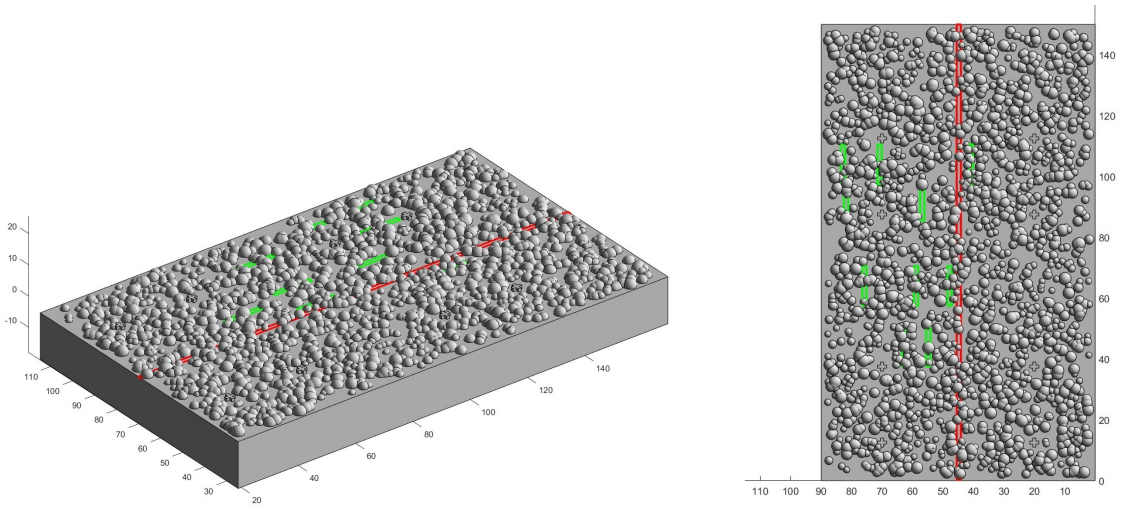

Orthographic view

Top view

Figure 3.30: Test campaign conducted on the test object that identifies the upscale roughness typical of Aluminium 2. For the legend, see the description of Figure 3.28

out to have the least homogeneous pattern possible. Furthermore, this plate also differs from the other two in terms of the roughness height profile, which shows significant variation in the peaks within the same plate under examination: generally, the two test objects representing aluminum differ in roughness density but have very similar peak heights, so much so that they exhibit a very close R_z value (maximum peak to valley height of the profile). However, the R_{sk} factor, which offers a quantitative measure of the asymmetry of the surface texture relative to the mean line, is quite different, as one side shows a predominance of valleys (Aluminum 1), while the other side has peaks (Aluminum 2).

In terms of identifying the captured zones and virtually displaying them (using software like MATLAB or *NX*), a precise method for transmitting results from the physical model to the CAD has been developed. Specifically, the identification of the incident beam on the plate, the thickness of the laser when it strikes the plates (development of calculations in Section 3.2.3.2), and the various offsets related to the movement of the test bench with respect to the test section were analyzed.

3.2.9 Wall Friction Velocity Calculations

The assessment of the Darcy friction factor can be carried out using Equation 2.8, by employing the wall shear stress. By introducing the correlation that exists between the wall shear stress and the friction velocity:

$$u_\tau = \sqrt{\frac{\tau_w}{\rho}}$$

It is possible to explicitly express the term representing the friction velocity by introducing it into Equation 2.8, thus obtaining:

$$u_\tau = \overline{U}\sqrt{\frac{f}{8}} \tag{3.3}$$

The measurement setup used allows for a system in which the flow, within the test section, can be considered fully developed, as it satisfies the condition defined by Equation 2.5.1. Taking into account what is explained in Section 3.1.1 regarding the Reynolds numbers adopted in the test campaign, it is sufficiently above the $Re = 4000$ threshold required to use the *Colebrook-White*

relation as the evaluation method for the friction factor, which is presented in the form [8]:

$$\frac{1}{\sqrt{f}} = -2\log_{10}\left[\left(\frac{\varepsilon}{3.7D_h}\right) + \left(\frac{2.51}{Re\sqrt{f}}\right)\right] \tag{3.4}$$

where the calculation of f is carried out iteratively by introducing an initial guess. The ε factor that defines the absolute pipe roughness is assessed by the roughness parameter R_z (*maximum peak to valley height of the profile*). The convergence value of the function is defined after about $3-4$ iterations with an initial guess of 0.042.

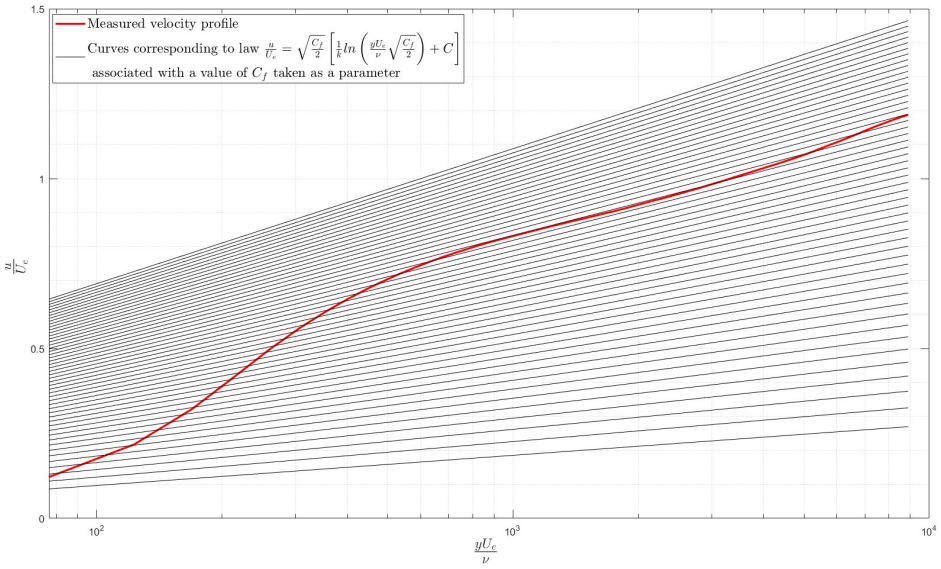

Figure 3.31: Clauser chart

In cases involving smooth surfaces, an additional method known as "*Clauser's Method*" has been considered. This method proves applicable to the examined case as it utilizes the logarithmic wall law for turbulent boundary layers, which is defined by Relationship 2.5. By multiplying and dividing by the external velocity U_e, the following is obtained:

$$\frac{u}{u_\tau}\frac{U_e}{U_e} = \frac{1}{\kappa}\ln\left(\frac{yu_\tau}{\nu}\frac{U_e}{U_e}\right) + C$$

from which follows:

$$\frac{u}{U_e} = \frac{u_\tau}{U_e}\left[\frac{1}{\kappa}\ln\left(\frac{yU_e}{\nu}\frac{u_\tau}{U_e}\right) + C\right] \tag{3.5}$$

Considering Equation 3.5 and expressing the wall shear stress τ_w in terms of the skin friction factor C_f (Equation 2.9), the following is derived:

$$u_\tau^2 = \frac{\tau_w}{\rho} = \frac{C_f\frac{1}{2}\rho U_e^2}{\rho} \quad \Rightarrow \quad \frac{u_\tau}{U_e} = \sqrt{\frac{C_f}{2}} \tag{3.6}$$

By making explicit the term u/U_e, the dependent relationship becomes:

$$\frac{u}{U_e} = \sqrt{\frac{C_f}{2}}\left[\frac{1}{\kappa}\ln\left(\frac{yU_e}{\nu}\sqrt{\frac{C_f}{2}}\right) + C\right] \tag{3.7}$$

Data are plotted in semi-logarithmic form; specifically, the ratio yU_e/ν is plotted on a logarithmic axis, and the dimensionless velocity u/U_e is plotted on the ordinate with a linear axis. Numerous curves are plotted, each corresponding to the velocity profiles defined by the aforementioned law and each representing a value of C_f as a parameter, as shown in Figure 3.31.

Thus, the *Clauser chart* is generated. On the same chart, the measured velocity profile is plotted using Equation 3.7. The C_f value characterizing the measured profile is ascertained by interpolating between the C_f values corresponding to the two curves which bracket the experimental data on the chart, as shown in Figure 3.32. A measured profile belonging to a turbulent boundary layer in equilibrium, featuring a sufficiently extended logarithmic region, will be indicated by a linear segment. It is observed that this method provides a more precise data fitting compared to the aforementioned method.

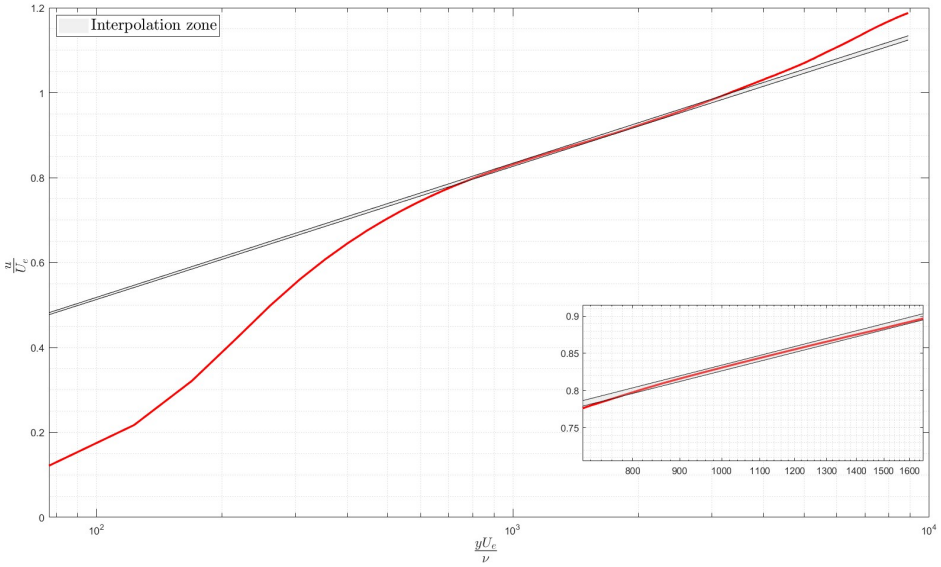

Figure 3.32: Clauser chart, interpolation area

3.3 Uncertainty Analysis

The overall measurement error in PIV is a combination of various factors ranging from the setup and recording process to the evaluation methods [88]. Consequently, errors are introduced through multiple ways. Generally, the first errors to consider for a comprehensive overview should be those associated with inaccuracies in the setup of the measurement apparatus, such as alignment, laser characteristics, suboptimal positioning of lenses, and seeding, which in the current work is introduced manually rather than through an automated system. Consequently, the duration during which particles are injected into the wind tunnel, and thus their density, is not perfectly consistent from one test to another. Efforts were made to minimize errors related to alignment by conducting verification tests after each alignment procedure, examining the cross-correlation function, the magnitude of its peak, and the displacement of particles between two consecutive images, to ensure they were within the acceptable limits cited in literature (a typical displacement of 5-10 pixels [88]). These operational errors, arising from the installation of the rig, are very difficult to quantify as they introduce uncertainties in many phases of the experiment's execution. The reader is encouraged to consult Raffel et al.[88] for a general overview of this field. In the

following work, however, only the errors due to the uncertainty of the PIV technique itself and those related to the identification of displacement vectors by the PIVlab software will be considered.

The method adopted in the following work is derived from an Image Matching methodology, developed by Sciacchitano et al.[72], in which the uncertainty related to a PIV measurement is evaluated by matching individual particle images from a given interrogation window at time t to the same window at time $t + \Delta t$, where Δt signifies the time between the laser pulse. The degree of matching will depend on various factors, including the dimensions of the interrogation window, the scale of flow structures, motion perpendicular to the imaging plane, and the specific algorithm implemented [72].
The analysis method focuses on pairs of single particle images that are detected within an interrogation window after a pairing process has been performed. To identify these image pairs, the product of the intensity of two consecutive images, I_1 and I_2, is considered. This product is symbolized as Π, and defined as $\Pi = I_1 \cdot I_2$. Within Π, the peaks correspond to paired particle images. These peaks contribute to the creation of the correlation peak. To clearly identify these peaks, a binary image ϕ is introduced, which takes a value of 1 at the points corresponding to the peaks of Π and 0 elsewhere. In mathematical terms, ϕ is defined as follows:

$$\phi(i,j) = \begin{cases} 1 & \text{if } \Pi(i,j) \text{ is a relative maximum} \\ 0 & \text{otherwise} \end{cases}$$

where each point (i, j) where ϕ is non-zero signals the presence of a pair of particle images.

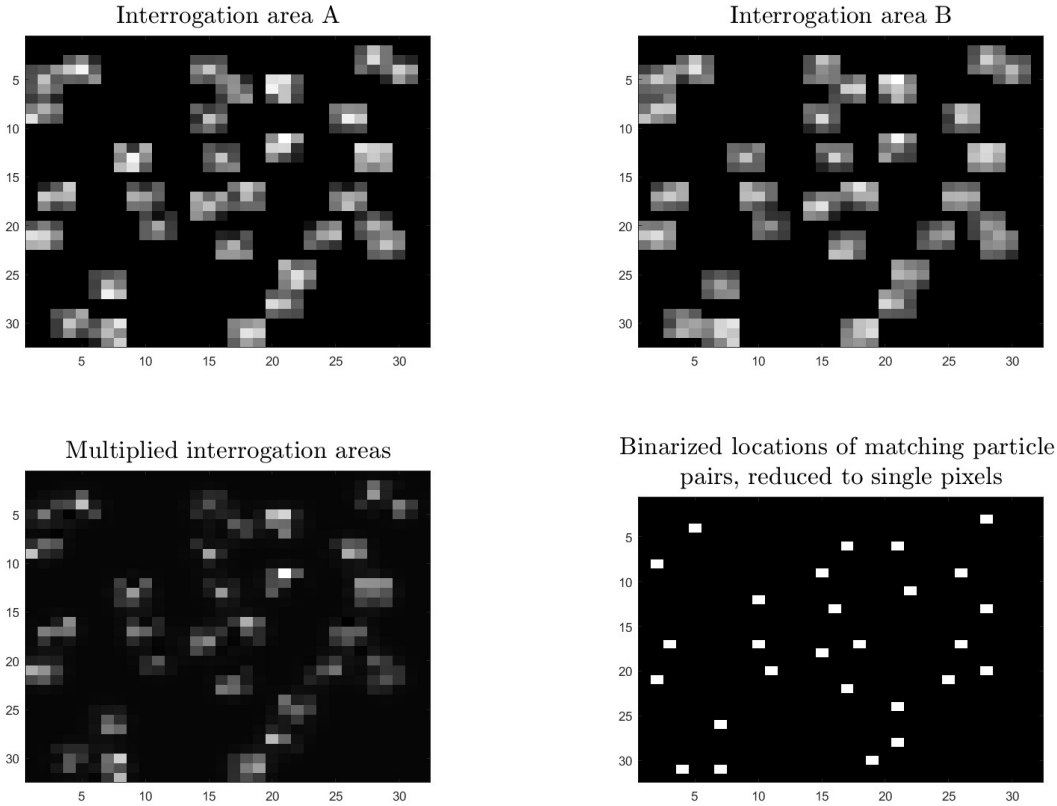

Figure 3.33: Starting from the top left corner, clockwise: matched image I_1; matched image I_2; image intensity product Π; peaks' image ϕ

The corresponding peaks of these particle images are then detected in the images I_1 and I_2 within a search area of radius r, which is typically 1 or 2 pixels, and centered at the point (i, j). The particle displacement between image 1 and 2 is determined by applying a subpixel estimation algorithm, through which the mismatch between particle images contains information about the measure of uncertainty. The fit returns sets of particle positions at times t_1 and t_2, respectively, $X_1 = \{x_{1_1}, x_{1_2}, \ldots, x_{1_N}\}$ and $X_2 = \{x_{2_1}, x_{2_2}, \ldots, x_{2_N}\}$, where x_{j_i} is the position occupied by the i-th particle in the matched image j and N is the number of particle pairs in the interrogation window [72]. Furthermore, in practical applications, the positions of the particle images at times t_1 and t_2 do not correspond exactly [72], as shown in Figure 3.34. The mismatch is taken into account by introducing disparity vectors $\mathbf{d}_i$, where:

$$\mathbf{D} = \{\mathbf{d}_1, \mathbf{d}_2, ..., \mathbf{d}_N\} = \mathbf{X}_2 - \mathbf{X}_1$$

is the disparity set.

Using PIVlab as the PIV analysis software, the Sciacchitano et al.[72] code has been modified to adapt it to the previously mentioned software thanks to Thielicke's[103] code, such that the initial inputs were those related to the intermediate results of the `piv_FFTmulti.m` function, generated during the cross-correlation, applied to images resulting from a laboratory test. The outputs are depicted in Figure 3.33.

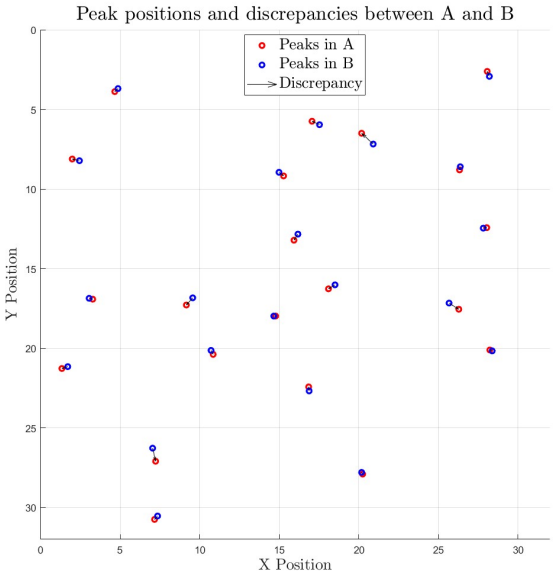

Figure 3.34: Particle images of I_1 (red circles) and I_2 (blue circles) and disparity vectors (black arrow). During the calculation phase of the disparity vectors and the peaks (ϕ), the pixels along the image borders were set to zero to avoid errors in the processing operations around each pixel using a search window. Therefore, if a peak is located along the edge of the image, operations attempting to examine the surrounding pixels might fail or yield incorrect results due to the absence of data beyond the border. This is the reason for the missing particles in the graph

The hypothesis proposed by Sciacchitano et al.[72] posits that the distribution of the disparity vectors follows a Gaussian shape, as evidenced in the case study shown in Figure 3.35. The error is thus estimated by Sciacchitano et al.[72] by calculating the ratio $\boldsymbol{\sigma}/N$, with sigma being the standard deviation $\boldsymbol{\sigma} = \{\sigma_u, \sigma_v\}$. In order to account for bias errors (the mean of the disparity set may be non-zero), the function $\boldsymbol{\mu} = \{\mu_u, \mu_v\}$ is also introduced. Mathematically, taking into

account that brighter particle images have a larger contribution than dimmer ones, $\boldsymbol{\mu}$ and $\boldsymbol{\sigma}$ are computed as the weighted mean and weighted standard deviation of the disparity set [72]:

$$\mu = \frac{1}{N}\sum_{i=1}^{N} c_i d_i \qquad \sigma = \sqrt{\frac{\sum_{i=1}^{N} c_i \left(d_i - \mu\right)^2}{\sum_{i=1}^{N} c_i}}$$

where the weight is chosen equal to the square root of the particle image intensity product Π [72]

$$c_i = \sqrt{\Pi(x_i)} \quad \text{for } i = 1, 2, ...N$$

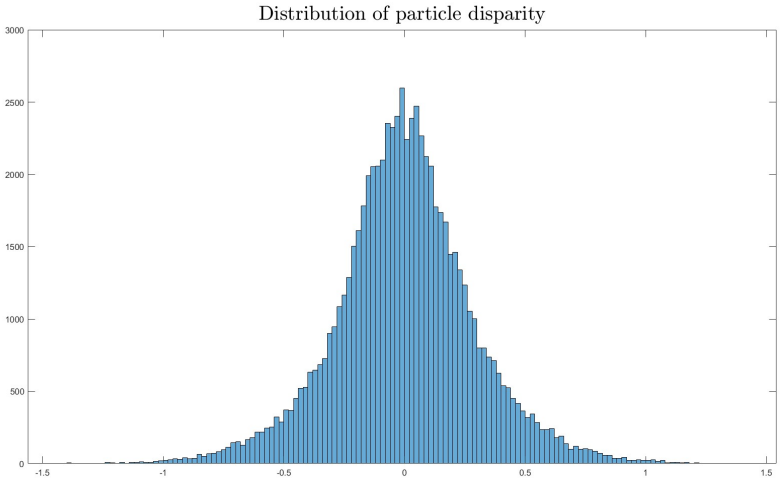

Figure 3.35: Distribution of the disparity vector in the case study

To sum up, the formula representing the immediate estimation of error, denoted as $\hat{\boldsymbol{\delta}}$, is defined as follows [72]:

$$\hat{\boldsymbol{\delta}} = \left\{\hat{\delta_u}, \hat{\delta_v}\right\} = \sqrt{\boldsymbol{\mu}^2 + \left(\frac{\boldsymbol{\sigma}}{\sqrt{N}}\right)^2} \tag{3.8}$$

within this context, $\hat{\boldsymbol{\delta}}$ symbolizes the evaluated magnitude of the true error $\boldsymbol{\delta}$ present in the velocity vector.

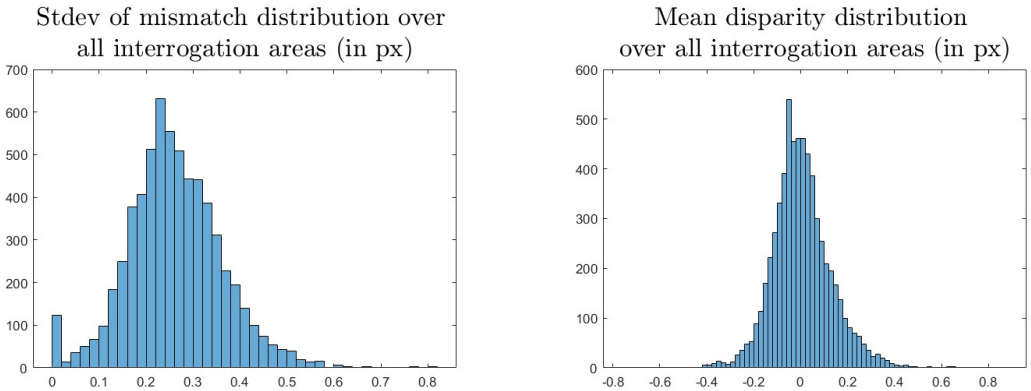

Figure 3.36: Evaluation of the factors $\boldsymbol{\sigma}$ and $\boldsymbol{\mu}$ for the following case study

To establish a confidence interval for assessing valid velocity vectors, a coverage factor k is introduced such that [72]:

$$U = k \cdot \delta$$

For small N (typically around 20), as is common in conventional PIV interrogation, a 95% confidence level is achieved with $k \approx 2.1$ [72].
In Figure 3.36, the assessments of the standard deviation $\boldsymbol{\sigma}$ and the mean of the disparity set $\boldsymbol{\mu}$ are presented for the case study analyzed using PIVlab. The error evaluation is presented in Figure 3.37 both as space-resolved form and as an estimation of the magnitude of the actual error.

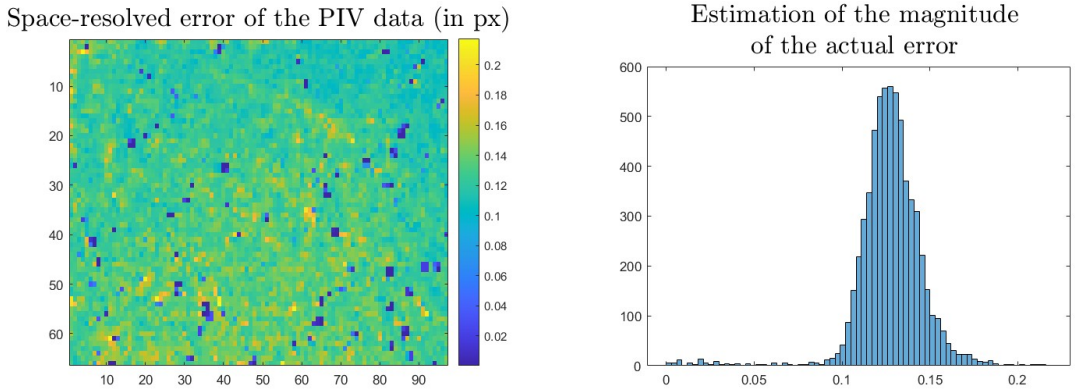

Figure 3.37: Error evaluation, as defined in Equation 3.8, for the current case study

Chapter 4

Results

In the following chapter, the results obtained from the conducted study will be presented. The analysis will begin with a validation of the measurement apparatus, with a focus on the flow within the test section and its behavior, to ensure consistency with the physical principles of the problem. Subsequently, the tests conducted on both smooth and rough plates will be discussed. This will include verification of the results against the DNS data provided by Moser et al.[39], as well as an analysis of the correlations identified between the solutions derived from the test rig data and those obtained from other experimental setups in the laboratory. Among these, the SRHT rig [118][124][115] will be considered for a comparison of the aerodynamic results with heat transfer data. Additionally, the QSSHT rig [111][108] will be used for transposing the obtained results, while maintaining fluid dynamic similarity, to actual test data on full-scale 1:1 objects.

4.1 Rig Validation - FULL FOV Test Smooth Plates

Analyses have been conducted from the outset to demonstrate the actual validity of the measurement system and compliance with the laws concerning the problem under examination. In particular, since there is a wall that forces the flow to orient itself in the direction of the duct's axis, this flow belongs to the category of "guided" flows. The physics of these flows has been extensively described in Section 2.5.1, from which the transition from laminar to turbulent flow has been established at $Re_{cr} = 2300$, according to the literature. In the case under examination, the lowest Reynolds number tested is around 6×10^3, characteristic of a turbulent flow behavior, which is also considered fully developed since the relationship $(L_h/D_h)_{turb} \geq 10$ is satisfied (the reader is referred to Section 2.5.1 for a more detailed description of the phenomenon).

Below is presented the output of the post-processing, performed with MATLAB, relating to a FULL FOV test, conducted at $Re = 2.30e + 04$. To ensure consistency with trends found in the literature, and working within a rectangular duct, the velocity profile has been compared with the modified power law developed by Salama [102] (the reader is referred to Section 2.5.1.3 for a detailed description of the phenomenon). Figure 4.2 shows the accurate fitting of the obtained profile with the theoretical one, with an error less than $\pm 2\%$ and not exceeding $\pm 0.1\%$ in the vicinity of the center of the duct.

The results are consistent with the phenomenological laws of the problem, with the maximum velocity occurring at the center of the duct, as expected from the family of guided flows. Moreover, the correct fitting with the theoretical parabolic law supports the affirmation that the measurement system can be considered correctly validated, thus allowing to proceed with tests related to the

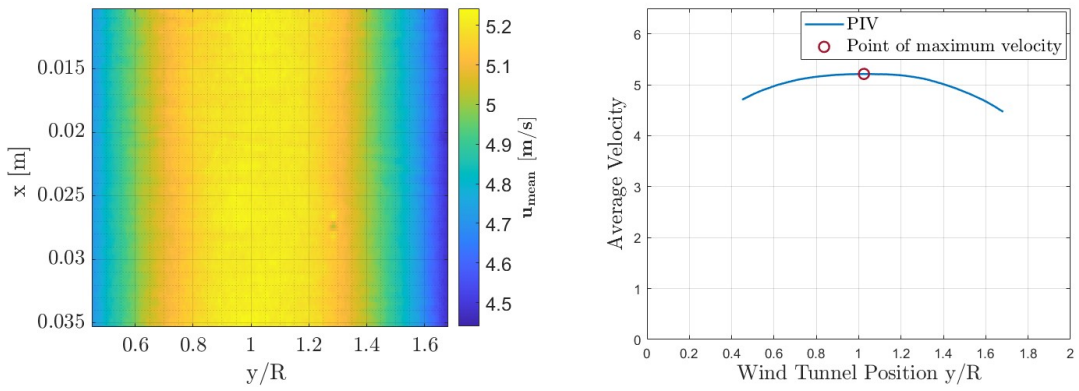

Figure 4.1: Time averaged velocity magnitude at the center-channel position and point of maximum velocity for smooth plates at $Re = 2.30e + 04$. The point $y/R = 1$ represents the center of the duct

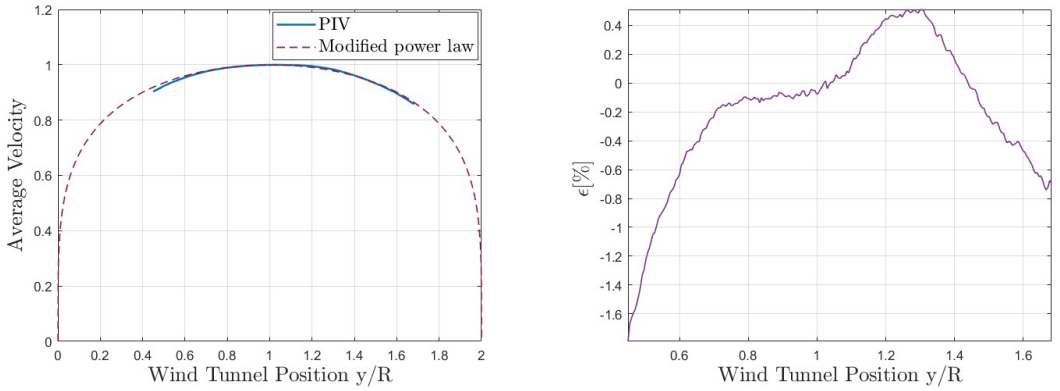

Figure 4.2: Velocity profile compared with the modified power law and resulting error [%]

visualization of the flow characteristics near the wall.

4.2 Boundary Layer Test

The need to evaluate the flow behavior in the immediate vicinity of the wall has led to the implementation of tests with a camera very close to the test section. A summary of the settings used is presented in Table 3.4. The first surfaces to be tested were the smooth plates. These were subjected to tests at different Reynolds numbers and at different camera distances from the TS. These surfaces also served the purpose of validating the accuracy of the data resulting from the PIV measurements, as well as verifying the results related to the normalized mean velocity profile in a turbulent boundary layer in semi-logarithmic coordinates compared to the trends found in the literature.

4.2.1 Smooth Plates

The time-averaged velocity magnitude from the smooth wall up to more than 50% of the channel height is shown in Figure 4.3; it can be observed that the no-slip wall condition is satisfied: the fluid particles in contact with the wall have zero velocity. Along the direction orthogonal to the wall, however, the fluid transitions from zero velocity to a velocity equal to that of an ideal fluid.

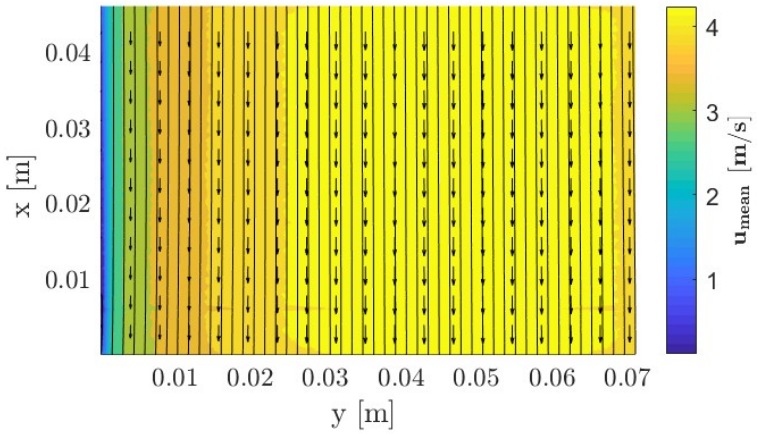

Figure 4.3: Time averaged velocity magnitude near the smooth wall at $Re = 2.48e + 04$. Visualization through streamlines for a illustration of the flow moving straight downward

The mean velocity profiles for the smooth-wall boundary layers in inner variables are shown in Figure 4.4. The experimental data related to the transposition of these results were obtained from tests conducted at $Re = 2.48e + 04$, using a four-pass multipass method with 50% overlap and final interrogation windows of 18×18 px.

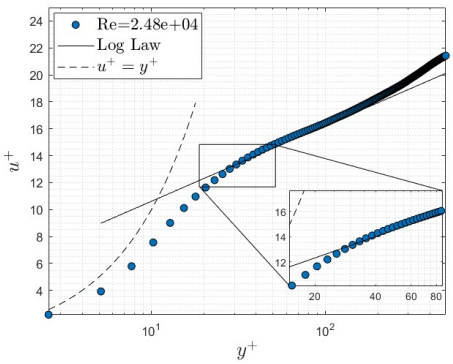

Friction velocity u_τ derived theoretically from Relation 3.3

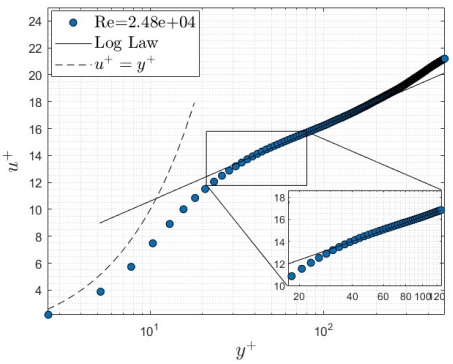

Friction velocity u_τ derived by Clauser Chart method

Figure 4.4: Log law plots at $Re = 2.48e + 04$ with smooth walls

Figure 4.4 shows both analysis methods used for determining the velocity law near the wall: the determination of the friction velocity using Relation 3.3, and the improvement of the log-law fitting using the Clauser chart method described in 3.2.9. Regarding this last method, once the skin friction factor C_f is derived, the evaluation of u_τ becomes straightforward in relation to Equation 3.6. The alignment of the experimental results with the theoretical log-law is improved by this procedure. To take a closer look at the near-wall region, it is observed that the fitting of data in the region defined by the viscous sublayer (with $y^+ \leq 5$) does not show a perfect collapse with the experimental data. This is due to the very small analysis region of approximately $y^+ \leq 5 \Rightarrow y = (3.607 \times 10{-}4)$ m for the case under study, where the interrogation window is of the same order of magnitude. Indeed, in the test in question, the pixel size is $(2.004 \times 10{-}5)$ m, the

50% overlap related to the last 18×18 pixel interrogation window implies a step of 9 px, that is $(1.803 \times 10{-}4)$ m. As a result, there are only about $2 - 3$ experimental points within the viscous layer, which is insufficient for an accurate evaluation of the layer dominated by viscous diffusion effects.

To achieve a better collapse of the viscous sublayer with experimental data, tests were conducted with smaller interrogation windows and at lower velocities, in accordance with Relationship 3.1. Figure 4.5 shows a comparison between tests performed at different Reynolds numbers. At lower velocities, and thus the ability to use smaller interrogation windows, the near-wall region is captured with greater accuracy in relation to the theoretical value, thanks to the collection of about 10 points in the viscous sublayer using interrogation windows of 12×12 pixels.

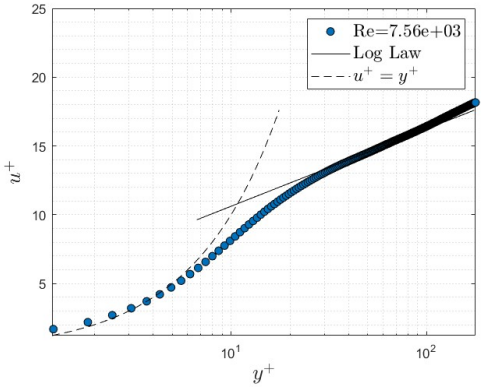

$Re = 7.56e + 03$ and 12×12 int. windows

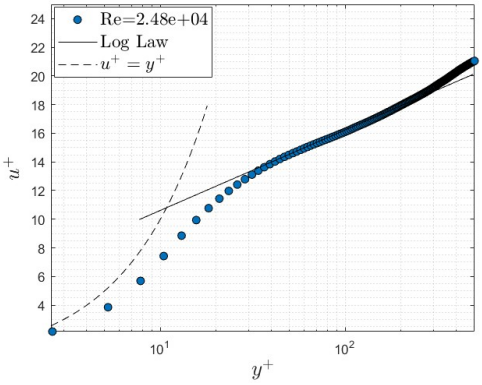

$Re = 2.48e + 04$ and 18×18 int. windows

Figure 4.5: Non-dimensional velocity profile in wall unit for different Re and different interrogation windows

The comparison of experimental data with the DNS numerical solutions implemented by Moser et al. [39] is shown in Figure 4.6 for three different Reynolds numbers.

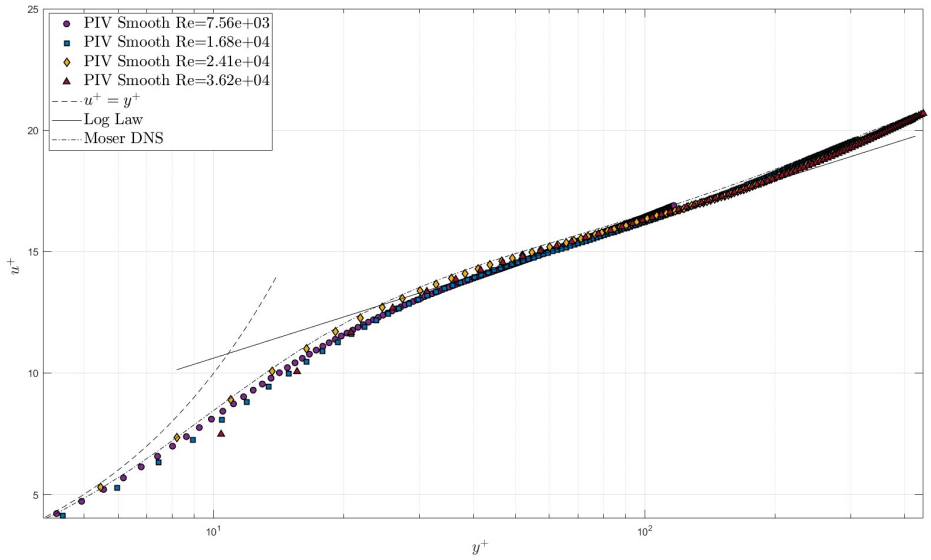

Figure 4.6: Dimensionless mean velocity profile u^+ as a function of the dimensionless wall distance y^+ for turbulent rectangular duct flow with Reynolds numbers between $7.56e + 03$ and $3.62e + 04$

The data from PIV tests reveal an almost complete alignment with the numerical data, with

only a slight deviation in the viscous region. This graph also highlights the universal nature of the inner region: the flow characteristics in this section, whether dominated by viscous diffusion (inner layer) or turbulent diffusion (log layer), do not depend on the geometry or the Reynolds number, which results in the experimental data tending to overlap despite varying test velocity conditions.

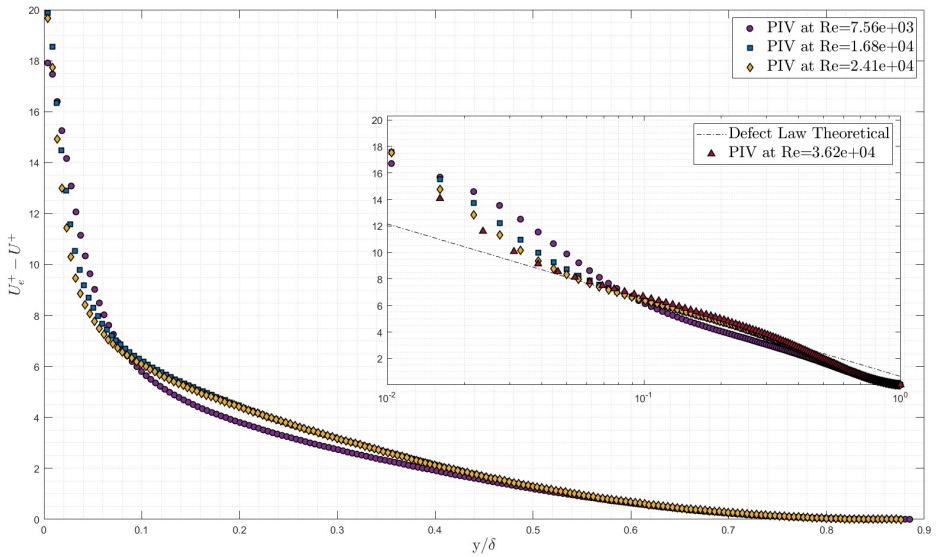

Figure 4.7: Mean velocity profiles in velocity-defect form for turbulent rectangular duct flow with Reynolds numbers between $7.56e+03$ and $3.62e+04$: inset in log-normal axes

The approach to the outer region, following the defect layer, occurs at approximately $y^+ > 800$. In this region, the velocity loses its universal characteristic, as it begins to depend on the geometry of the problem and the Reynolds number. As described in 2.5.1.4, the universal velocity-defect law exhibits a universal scaling behavior for the outer region, which, for a rectangular duct, is defined by Relation 2.7. The behavior of this law for the same Reynolds numbers used in the analysis of the wall law is shown in Figure 4.7. The settings used to conduct the tests and some pertinent results are shown in Table 4.1.

Volume flow l/s	Re -	$\overline{U}$ ms^{-1}	Piv int. windows [px]	u_τ no CCM ms^{-1}	u_τ CCM ms^{-1}	τ_w Pa
11	$7.56e+03$	1.179	12×12	0.0760	0.0773	0.0072
24.4	$1.68e+04$	2.614	18×18	0.152	0.149	0.0269
35.1	$2.41e+04$	3.761	24×24	0.209	0.212	0.0543
52.6	$3.62e+03$	5.636	26×26	0.299	0.301	0.109

Table 4.1: Settings used for the tests related to the smooth plates presented. The evaluation of u_τ was carried out using both Relation 3.3 and the Clauser Chart Method (CCM)

Finally, the results concerning Reynolds stresses, discussed in 2.4.2.1, are presented in Figure 4.8 and compared with the numerical results of Moser et al[39]. To characterize these values, the parameter Re_τ has been defined, evaluated through the friction velocity: $Re_\tau = (u_\tau D_h \rho)/\mu$. The terms considered for comparison with the DNS data are those involved in the transport in the j-direction of momentum per unit mass in the i-direction, $\langle\overline{u'u'}\rangle$, $\langle\overline{u'v'}\rangle$, $\langle\overline{v'v'}\rangle$, and have been divided by the square of the friction velocity (u_τ^2) in order to evaluate them in dimensionless form, and called $\langle\overline{u'u'}\rangle^+$, $\langle\overline{u'v'}\rangle^+$ and $\langle\overline{v'v'}\rangle^+$. These arise from the nonlinear advection terms in the Navier–Stokes equations and the energy equation [81].

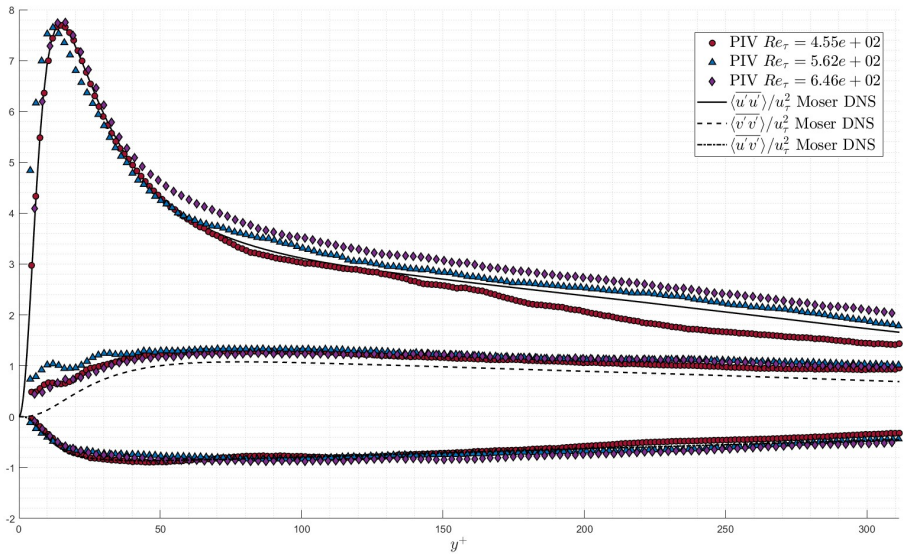

Figure 4.8: Normal Reynolds stresses for $Re_{\tau_{Moser}} = 5.87e+02$ and $Re_{\tau_{PIV}}$ between $4.55e+02$ and $6.46e+02$

In this case, the experimental data do not perfectly collapse onto the numerical trends, especially when approaching the outer layer and in relation to the term $\langle \overline{u'u'} \rangle^{+1}$. In any case, the deviations are not very significant and could be attributed to errors introduced during the calibration phase: this process is carried out using a ruler, so an error associated with the ruler's gradation of 0.5 mm must be taken into account, which could explain the imperfect data compaction.

From the various analyses, it has been demonstrated that the flow follows the expected universal scaling laws. Moreover, the verification of the data through comparison with results found in the literature indicates a properly operating measurement setup and a data evaluation process carried out correctly. This suggests that the behavior is correct and testing can proceed.

4.2.2 Rough Plates

In order to investigate the flow characteristics assumed in the presence of different rough surfaces, tests were conducted for all the available rough plates. Specifically, these examinations were limited to tests near the bed plate, and therefore tests under FULL FOV conditions were not performed. For further studies on this last type of examination, the reader is referred to the works of Pedreño Marin [121] and Tamagnini & Agostino [124].

The mean velocity profiles in inner variables for different roughness surfaces at $Re = 2.48e+04$ are shown in Figure 4.9. Contrary to what is observed with smooth walls, textured walls produce phenomena characterized by d and ΔU^+, which are shifts occurring perpendicular to the wall and alterations in the velocity profile within the logarithmic layer. These effects are termed the *zero-plane displacement* and the *roughness function*, respectively. The zero-plane displacement is understood as a hypothetical point of origin that symbolizes the level where the average drag force is operative, as outlined by Jackson [24]. Conversely, the roughness function quantifies the increase

[1] v is the spanwise component while u is the streamwise one, since the test section is positioned vertically. The reference system follows the $x - y$ convention, going from bottom to top and from left to right, respectively. As for the generation of normalized components in wall units, y^+ represents the wall-normal component, which in non-wall coordinates becomes y

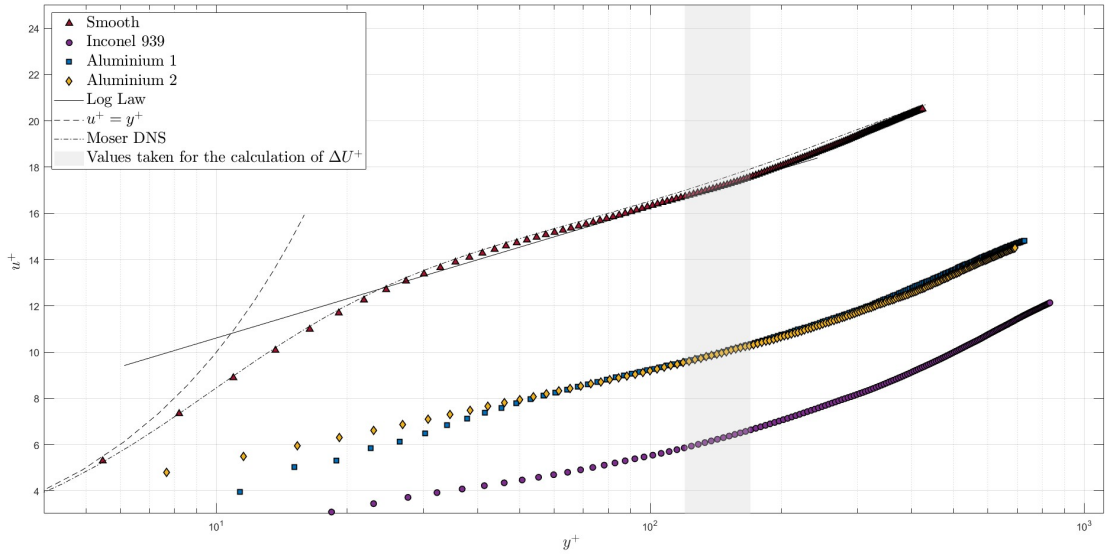

Figure 4.9: Inner scaling of the vertically averaged streamwise velocity profile for different rough surface, compared with the DNS Moser [39] turbulent boundary-layer profile for smooth surface, and with the experimental data for smooth plates from the current study. The value of the log-law slope κ and the smooth-wall intercept C used in the current investigation are 0.41 and 5, respectively. Considering the plate shown in Figure 3.28 as example, with the origin of the axes located in the bottom right corner, the tests reported in the graph pertain to the position $y = 0.045\,\text{m}$, $x = 0.120\,\text{m}$, with a thickness of the incident laser beam of $2e - 3\,\text{m}$ and a field of view of $0.022\,\text{m}$. The x and y axes correspond respectively to the larger and smaller dimensions of the plate

(if negative) or decrease (if positive) in momentum as a consequence of the wall's irregularities, as explained in 2.5.2. This dependence of ΔU^+ on surface texture is evident in Figure 4.9: Inconel 939 shows much more pronounced roughness compared to that highlighted on the two aluminum plates, causing a shift in the logarithmic velocity profile related to the first surface that is much more significant compared to the characteristic one of the last two. The values of the roughness functions are positive ($\Delta U^+ > 0$), indicating an increase in drag compared to the smooth case (for which $\Delta U^+ = 0$). This phenomenon is characteristic of most types of roughness in industrial settings, which develop within conduits due to wear, sedimentation or surface irregularities induced by additive manufacturing techniques. In contrast, examples of textures that can lead to an opposite effect are the riblets.

The assessment of the wall offset d, as will be presented in the following, is the result of an adaptation of the procedure described by Medjnoun et al.[100]. Specifically, the zero-plane displacement d is estimated using the wall law described in Equation 2.10, by modifying the parameter that defines the distance from the wall and subtracting the offset d. Thus, the relationship becomes:

$$u^+ = \frac{\overline{U}}{u_\tau} = \frac{1}{\kappa} \ln \left[(y - d) \frac{u_\tau}{\nu} \right] + C - \Delta U^+$$

By deriving this relationship with respect to y, the indicator function Ξ is obtained:

$$\Xi = (y^+ - d^+) \frac{du^+}{dy^+} = \frac{1}{\kappa} \tag{4.1}$$

For smooth wall, and therefore for $d = 0$, it can be easily demonstrated that the left-hand side (Ξ) and the right-hand side ($1/\kappa$) of Equation 4.1 are equivalent. By differentiating the classic

logarithmic law (Eq. 2.5) with respect to y^+, one obtains::

$$\frac{du^+}{dy^+} = \frac{1}{\kappa}\frac{1}{y^+}$$

Subsequently, substituting this result into Equation 4.1:

$$\Xi = \frac{1}{\kappa}$$

Equation 4.1 is traditionally used to determine the extent of the inertial sublayer as well as the logarithmic slope κ for smooth-wall flows, once the friction velocity u_τ is known (Österlund et al.[40]). Consequently, this means that if κ is assumed to be universal between smooth and rough walls, d should be only a function of the velocity gradient and the friction velocity [100].

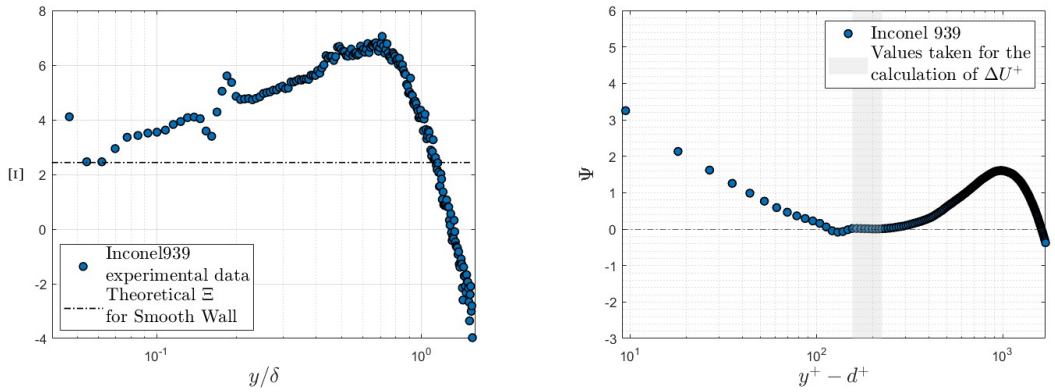

a b

Figure 4.10: (a) Indicator function Ξ; (b) Modified log-law function Ψ. Tests performed on Inconel 939 at $Re = 2.48e + 04$. The boundary-layer thickness δ was identified as the wall-normal distance at which the vertically-averaged streamwise velocity reached 99% of the free-stream speed $\overline{U}$ given by the volume flow

Since the friction velocity u_τ is calculated as described in Section 3.2.9, the zero-plane displacement is determined by minimizing the difference between the right and left terms of Equation 4.1: thus, by minimizing the difference between the function Ξ, resulting from the tests on rough plates, and the line defining the smooth wall case, the aim is to align the region where the flow is still close to the typical behavior of smooth walls. This will be the offset point, as roughness tends to alter the velocity distribution within the boundary layer, causing a shift of the logarithmic law with respect to the smooth wall case. The results of this process are shown in Figure 4.10a, as an example, for Inconel 939 at a $Re = 2.48e + 04$.

Once the zero-plane displacement is determined, the difference between the logarithmic velocity distribution and the measured inner-normalized velocity profiles is examined[100] to obtain:

$$\Psi = u^+ - \frac{1}{\kappa}\ln\left[(y^+ - d^+)\right] - C + \Delta U^+$$

In the grey-highlighted region of Figure 4.10b, the profiles of Ψ reach a plateau at zero for the appropriate values of ΔU^+. This region is also highlighted in Figure 4.9. This procedure was carried out to derive the values of d and ΔU^+ for all the rough surfaces tested. Table 4.2 presents some aerodynamic parameters, including the values of the zero-plane displacement in wall units and in meters for the three rough plates under examination at $Re = 2.48e + 04$. The tests for such evaluations were those conducted at the center of the plate, totaling 5 tests in order to assess the area defined by the median line in Figure 3.28. The value of d is not constant due to the

heterogeneity of the roughness.

Roughness texture	Re -	d^+ -	$d \times 10^{-3}$ [m]	ΔU^+ average	$Re_\tau \times 10^2$ -
Inconel 939	$2.48e+04$	$[76.43, 107.56]$	$[3.08, 4.33]$	10.77	16.32
Aluminium 1	$2.48e+04$	$[47.79, 74.39]$	$[2.32, 3.62]$	7.33	9.36
Aluminium 2	$2.48e+04$	$[45.51, 91.21]$	$[2.19, 4.39]$	7.24	9.73

Table 4.2: Aerodynamic parameters of the turbulent boundary-layer flow over the different multiscale rough surfaces. The value of d is referenced with respect to the bed-plate, which is the region where roughness start to evolve on the plate. This point is the origin of the wall-normal distance y, or y^+ in wall units

It is interesting to note that the profiles illustrated in Figure 4.9 exhibit a logarithmic region slope similar to that of the smooth wall, supporting the universal nature of the inner layer as stated in 4.2.1, even in the presence of different surface textures and, consequently, different geometries.

The results of the velocity defect profile assessment for smooth and rough surfaces at $Re = 2.48e+04$ are shown in Figure 4.11. A good collapse of data between the smooth case, Aluminium 1, and Aluminium 2 is observed, although it is not perfect. More pronounced differences are visible in comparison to Inconel 939. Such differences are not new in this field of study; indeed, while there is significant evidence supporting the validity of Townsend's wall similarity hypothesis in the presence of many different idealized roughness topographies, other studies have indicated a substantial modification of the outer layer in the presence of roughness. Jiménez[52] proposed a

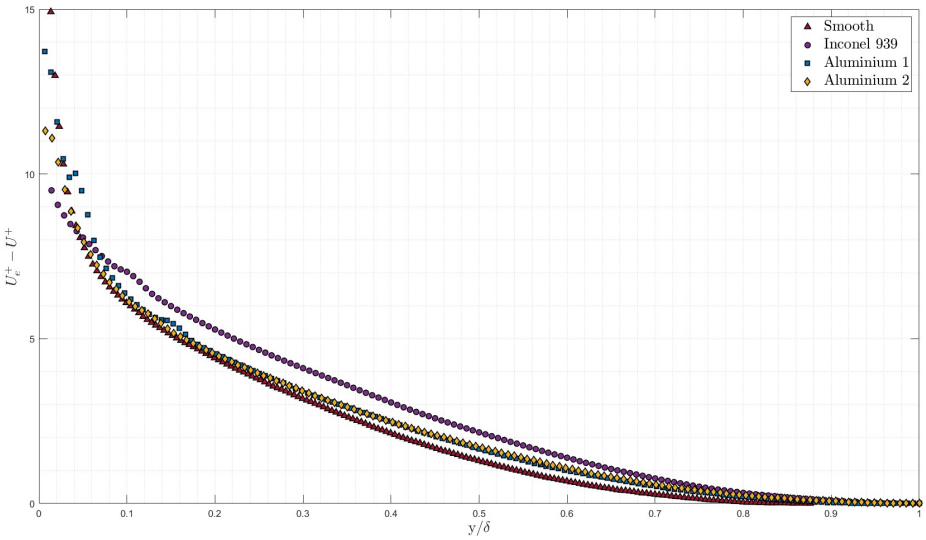

Figure 4.11: Mean velocity profiles in velocity-defect form for both smooth and rough walls

physical threshold as a condition criterion for the velocity profile to be self-similar in the outer layer ($k/\delta \leq 1/40$), describing the flow as similar to the flow over obstacles when the ratio of the boundary layer thickness to the actual roughness height (δ/k) exceeds 40. The values of this ratio for the three roughnesses are presented in Table 4.3. The value of k was determined by creating a topographic map, shown in Figure 4.12, of the various rough surfaces and calculating the average peak elevations in the PIV captured zone. For Inconel, the value of the parameter k/δ is significantly greater than $1/40$ ($\approx 1/15$), in agreement with Jiménez's analysis regarding the

failure of Townsend's wall similarity hypothesis for k/δ values greater than the defined threshold. For Aluminum 1 and Aluminum 2, the ratio does not deviate much from the limit ($= 0.025$); indeed, the profiles related to these two surfaces in the outer layer collapse perfectly with each other and are very similar to the smooth case. Moreover, the greater deviation noted for Inconel 939 could be related to a greater influence of roughness due to higher peaks and more pronounced roughness compared to the aluminium surfaces.

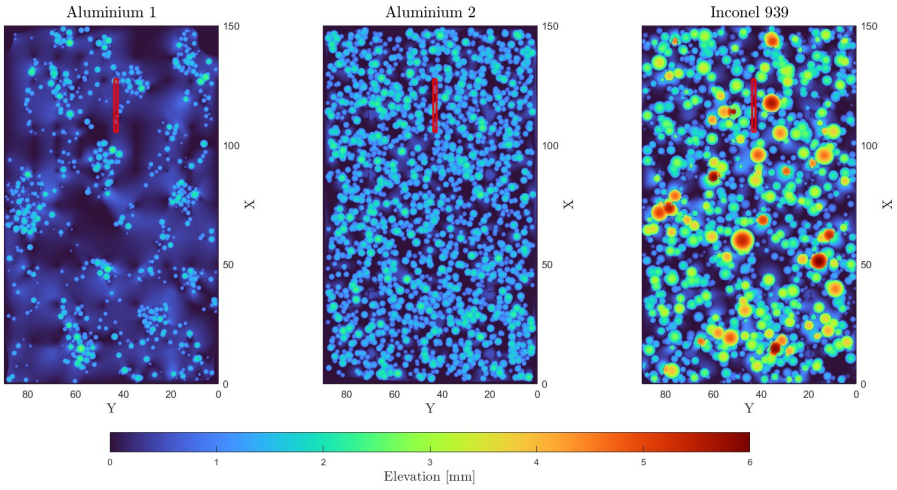

Figure 4.12: Topographic map for the three tested rough surfaces. The red rectangle represents the PIV captured area within which the parameter k is calculated

Roughness texture	Re -	$k \times 10^{-3}$ [m]	k^+ -	k/δ -
Inconel 939	$2.48e+04$	3.242	66.82	0.0669
Aluminium 1	$2.48e+04$	1.147	28.47	0.0230
Aluminium 2	$2.48e+04$	1.265	33.88	0.0267

Table 4.3: Experimental parameters for determining Jiménez's threshold. The non-dimensional roughness height k^+ is evaluated using the friction velocity and the kinematic viscosity

The Reynolds normal stress profiles, normalized by u_τ^2, for rough surfaces are presented in Figure 4.13 for the same Re_τ. Significant deviations are highlighted for all the Reynolds stress profiles. In particular, it is noted that for the normal stress perpendicular to the wall, $\langle\overline{v'v'}\rangle^+$, there is a marked decrease as the wall is approached. Moreover, for Aluminum 1 and Inconel 939, there is a region very close to the roughness elements where $\langle\overline{v'v'}\rangle^+$ is very high. The effect is certainly not confined to the roughness layer, as the distributions for the three surfaces are quite different for most of the layer. In the outer layer, the profiles related to Aluminum 1 and Aluminum 2 tend to converge, while the profile for Inconel 939 shows a decrease, thus indicating a decay in the wall-normal turbulence intensity. The data in the viscous sublayer (with $y/\delta < 0.06$) are too sparse to make assessments.

The Reynolds stress profiles in the streamwise component tend to become well-compacted fo the two aluminium surfaces, especially as one moves away from the wall; near the wall, there is a slight deviation in the data which could be due to the different nature of the irregularities. Inconel, on

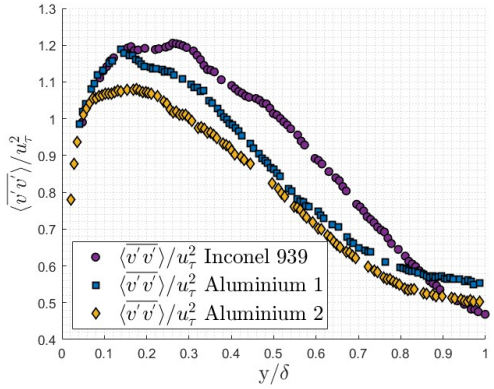

Wall-normal Reynolds normal stress profiles

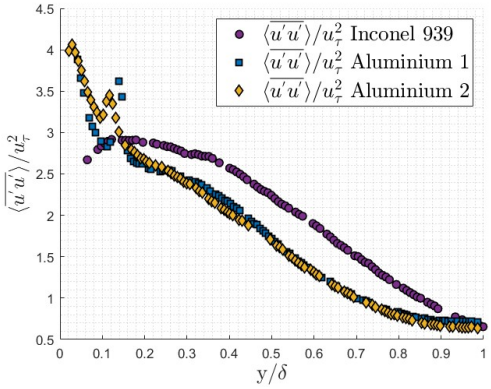

Streamwise Reynolds normal stress profiles

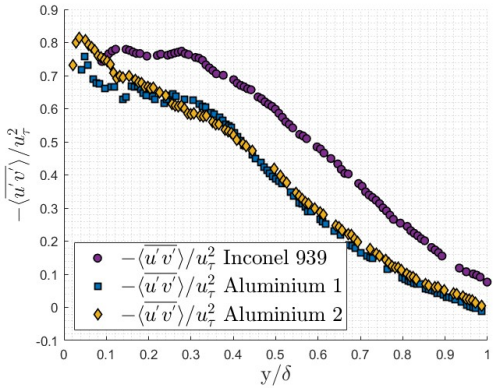

Reynolds shear stress profiles

Figure 4.13: Reynolds stress for the tested rough surfaces at $Re_\tau = 950$ ($u_\tau = 0.311$). The test section is vertical with the x-axis following the streamwise direction of the flow. Consequently, the streamwise component is u, while the wall-normal component is v

the other hand, exhibits significant deviations throughout the analysis region, representing greater velocity fluctuations compared to the other two surfaces away from the wall, and then tends to align with the other profiles as it approaches the center of the channel. Inconel also shows a reduction in the $\langle \overline{u'u'} \rangle^+$ factor near the wall, which could be due to the irregular nature of Inconel's roughness: the high heterogeneity of peaks and troughs might cause an early disruption of the coherent flow structures highlighted by the elongated vortices typical of turbulence in contexts with smooth or slightly rough surfaces.

Significant effects of the surface condition are also observed in the Reynolds shear stresses. The two aluminum plates once again tend to converge, while the profile for the Inconel deviates in terms of values even in the overlap region. The maximum value of $\langle \overline{u'v'} \rangle^+$ is found around $y/\delta = 0.08 - 0.12$, which is typical of confined turbulent flows, where the production of turbulence is at its maximum in the buffer layer region. The different behavior of Inconel 939 in the intermediate region might indicate an influence of the surface roughness on the turbulent structures and on the momentum transport, as roughness can enhance turbulent transport near the wall, leading to increased production of turbulent shear stress. It is plausible that the aluminum surfaces have a lesser effect on turbulence, resulting in lower values of $\langle \overline{u'v'} \rangle^+$.

The distribution map of Reynolds shear stress for the three roughened plates is depicted in Figure 4.14. For Inconel, there is a varied distribution of the factor $-\langle \overline{u'v'} \rangle^+$, which could indicate greater turbulent interaction. Aluminium 1, on the other hand, shows more uniform fields, suggest-

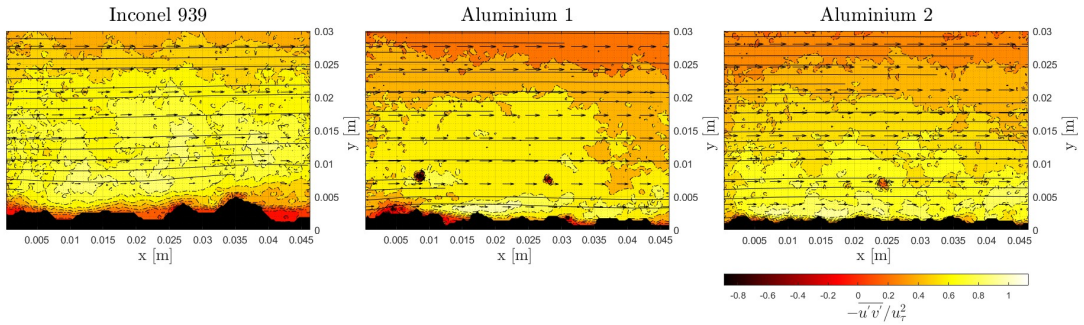

Figure 4.14: Contour maps of Reynolds shear stress for $Re_\tau = 950$ ($u_\tau = 0.311$)

ing a more stable and less turbulent flow. Aluminium 2 displays an intermediate behavior. These different patterns, and the results associated with them, appear to be consistent with Medjnoun et al.[100] statements: an increase in roughness complexity leads to a redistribution of shear stress across different scales, along with a variation in the recirculation bubble distribution. According to Medjnoun et al.[100], when roughness scales are added (as with Inconel), larger vortical structures break down into smaller eddies, leading to a redistribution of turbulence across scales. This is in line with the fields observed for Inconel, which suggest more intense turbulence and a more pronounced separation of the shear layer. The roughness scale distribution for Aluminium 1 is much less marked and compact; Aluminium 2, however, displays roughness scales that are similar with densely distributed irregularities, implying an intermediate behavior: there is not a varied pattern as seen with Inconel, but it is more intense than that of Aluminium 1.

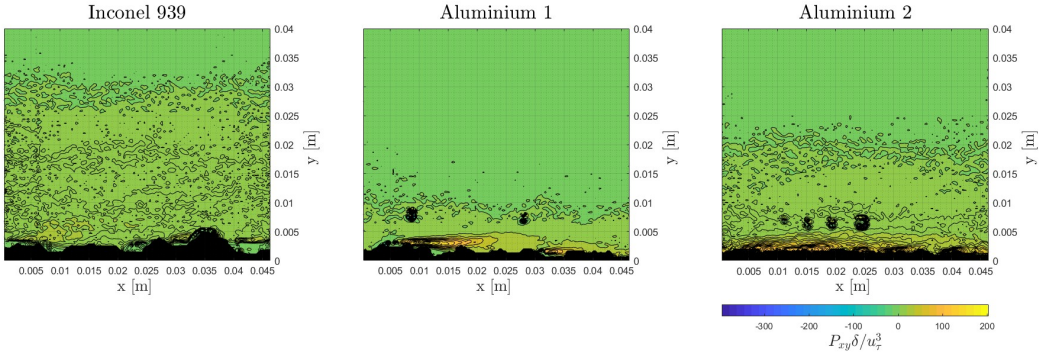

Figure 4.15: Turbulence production maps for $Re_\tau = 950$ ($u_\tau = 0.311$)

The turbulence production factor associated with the Reynolds shear stress, P_{xy} (where $P_{xy} = -\langle\overline{u'v'}\rangle dU/dy$), presented in the form of turbulence production maps, is illustrated in Figure 4.15 for the various rough surfaces. To obtain a normalized value of the factor P_{xy}, it has been multiplied by the boundary layer thickness δ, and divided by u_τ^3 to ensure consistency with the units of measurement. According to Medjnoun et al.[100], this map confirms the assumptions made earlier, as the areas where stronger shear layers are observed (Figure 4.14) are associated with regions of higher turbulence production. Of particular interest is what happens near the wall: in this region, indeed, the turbulence generated by the dense multiscale roughness structures present on Aluminium 2 is greater than that on the first aluminium surface and on Inconel. This could also explain the behavior of the Reynolds shear stresses $-\langle\overline{u'v'}\rangle^+$ shown in Figure 4.13c: it is noted that very close to the wall, Aluminium 2 exhibits a peak and generally higher values compared to the other two materials. This situation diminishes as one moves out of the inner layer ($y/\delta \gtrsim 0.2$),

where the high heterogeneity of Inconel tends to spread turbulence away from the wall more than the aluminium surfaces do, resulting in higher values of $-\langle\overline{u'v'}\rangle^+$. Indeed, it is clear that the influence of roughness on turbulence generation is confined up to about $y \approx 0.012\,\text{m}$ for Aluminium 1, $y \approx 0.025\,\text{m}$ for Aluminium 2 and $y \approx 0.03\,\text{m}$ for Inconel, thus decreasing as one approaches the center of the duct.

4.3 Correlations with SRHT Rig

The following analysis is based on the cross-correlation of the thermal results obtained from SRHT with respect to the aerodynamic considerations stemming from the analysis of flow behavior using the PIV technique. In particular, the flow patterns through various roughnesses will be studied graphically, in order to draw conclusions about the thermal behavior of different surfaces. Furthermore, the study will delve into the skin friction factor C_f. The value of the equivalent sand grain roughness k_s^+ for the different roughnesses will also be determined.

4.3.1 Flow Behavior Near Roughness

PIV analyses were performed in the same region where the trends and maps of Nusselt number on the three roughened plates were calculated. The settings used for the analysis are shown in Table 4.4. Pedreño Marin[121] and Brogliato[118] had hypothesized that the areas downstream of the roughness elements could lead to a decrease in the Nusselt number due to vortices or flow recirculation zones. Following this hypothesis, the thermal data resulting from the tests conducted with the SRHT were compared with the results from the PIV technology.

Re -	Laser power %	$\Delta t \times 10^{-3}$ [s]	$f - stop$ camera	Int. windows [px]	Field of view [cm]	Direction of the flow
$2.48e+04$	15	0.022	14	24×24	(1.3×2.2)	left $\rightarrow$ right

Table 4.4: PIV settings for correlation with SRHT rig across all three roughness surfaces

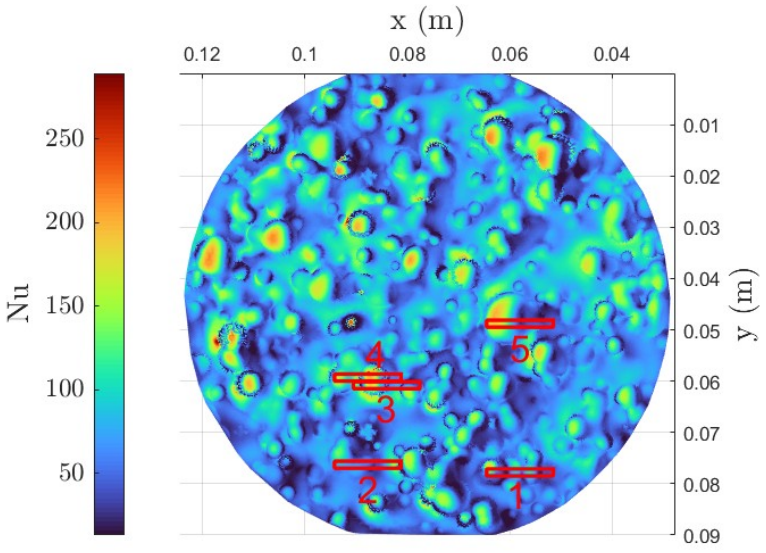

Figure 4.16: Nusselt map [127] for Inconel 939 at $Re = 2.48e+04$

The results in terms of Nusselt number maps for Inconel 939 are depicted in Figure 4.16, while the different roughness patterns and the corresponding flow behavior are illustrated in Figure 4.17.

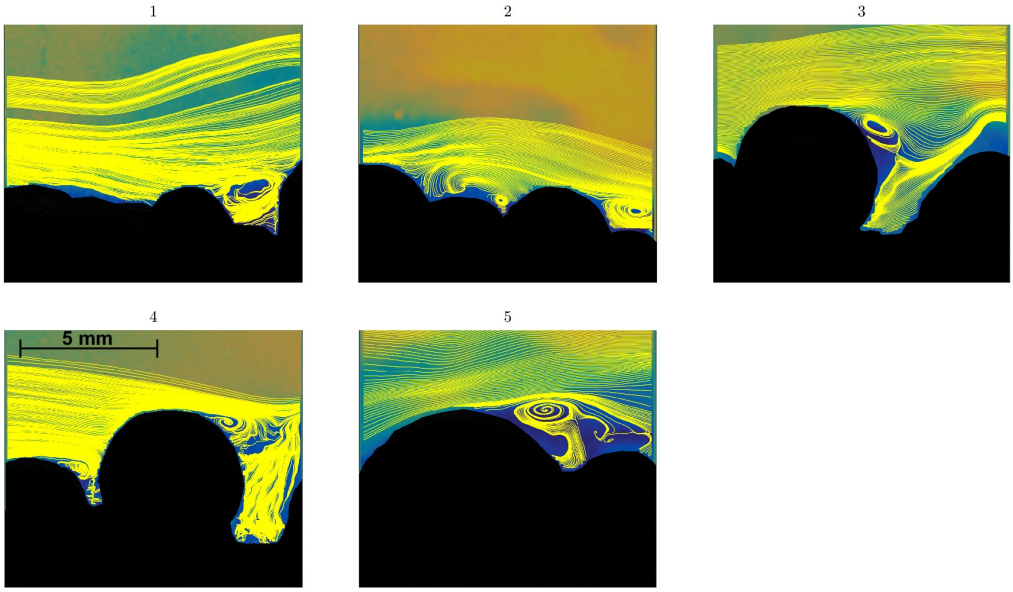

Figure 4.17: Flow behavior in the vicinity of Inconel surface roughness at $Re = 2.48e + 04$. The images have been cropped to display only the area of interest

Five different analysis areas were selected, categorized with increasing numbering, to reflect different characteristics of roughness: regions 1 and 2 exhibit a roughness pattern with a small trough followed by a more pronounced peak; spots 3 and 4 are chosen to capture the same texture in order to observe the flow behavior further downstream. This region is characterized by a large bubble that significantly impedes the flow and features a groove just downstream before the rise of the next peak. The fifth area identifies the largest bubble on the plate. These zones are also of interest regarding heat transfer: Figure 4.16 clearly shows that areas with an increase in the Nusselt number are associated with downstream decreases of this parameter behind the roughness. Comparing thermal data with the images from the PIV technique, it is evident that "air bearing" of flow form in recirculation zones, creating "impermeability zones" between the flow and the surface, which could be the cause of the low Nu values found behind the peaks. In areas where the current is impeded, on the other hand, the Nu value increases. Furthermore, in areas 3, 4, and 5, a phenomenon of vortex detachment downstream of the roughness areas is evident, which could contribute to the previously described phenomenon.

The thermal map of Aluminum 1 is shown in Figure 4.18, and the corresponding flow behavior is illustrated in Figure 4.19. As stated several times, Aluminum 1 features much less pronounced irregularities compared to Inconel. Moreover, the roughness is sparsely distributed across the plate, with peaks followed by very wide valleys. In spot 1 and region 3, the flow behavior is clearly distinguishable and is influenced by d-type and k-type roughness, respectively (see Figure 3.9 for reference). In the first case, the interchange of small roughness peaks and short valleys causes the flow to be "trapped" within the space between these two entities. Recirculation bubbles form within the valleys, causing the external flow to "glide over" them, as if it were not influenced by the height of the roughness. In the second case, however, the sequence of more extended peaks and valleys means that the recirculation bubble within the valley influences the external flow, pushing

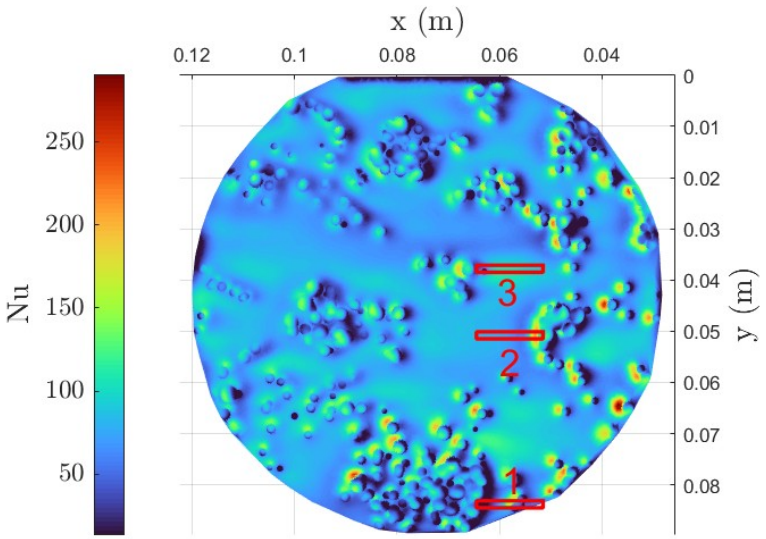

Figure 4.18: Nusselt map [127] for Aluminium 1 at $Re = 2.48e + 04$

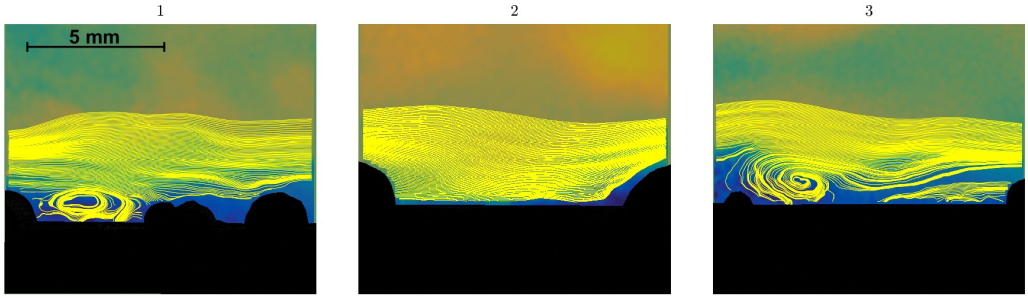

Figure 4.19: Flow behavior in the vicinity of Aluminum 1 surface roughness at $Re = 2.48e + 04$. The images have been cropped to display only the area of interest

the flow lines upward as it is about to exit the flat zone. In this case, the flow seems to be influenced by the height of the roughness. Region 2 has been selected to demonstrate that there is indeed a relationship between roughness and the increase of the Nusselt number: along the valley, the flow lines are straight, and the Nusselt number does not exhibit a high value, whereas at the exact point where the roughness is encountered, the thermal map shows an increase in heat transfer following the flow's impact with the peaks after the valley.

The thermal map of Aluminum 2 is shown in Figure 4.20, and the corresponding flow behavior is illustrated in Figure 4.21. The relationship between roughness and flow behavior in the case of Aluminum 2 is more complex. This is because, in this instance, the roughness features are densely packed on the plate, with varied roughness scales that are not significantly different from one another. Also, in line with previous observations about impingement zones, the thermal map indicates a relatively homogeneous distribution of the Nusselt number, without showing areas with very high Nu peaks. While there are zones where this parameter is higher, the value does not deviate much from the average. This graphical assertion is confirmed by PIV images, which indeed show straight flow lines over the roughness, as if the high density of the roughness did not allow the flow to establish itself within them, but only to develop above them. Areas where the rough pattern is more heterogeneous and allows for the presence of small valleys (spots 2 and 4) are more

prone to flow deviations, impact zones with the roughness, and therefore an increase in Nu (as noted in Figure 4.20 for regions 2 and 4). However, these spots are only sparsely present on the plate pertaining to Aluminum 2.

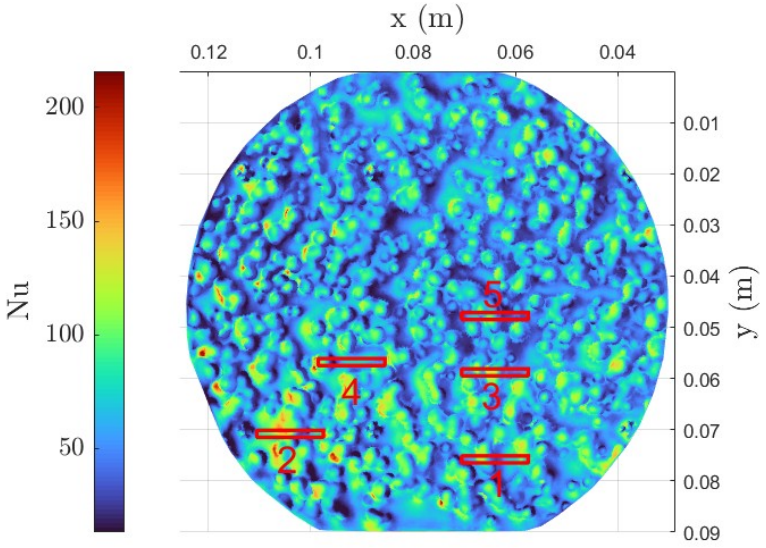

Figure 4.20: Nusselt map [127] for Aluminium 2 at $Re = 2.48e + 04$

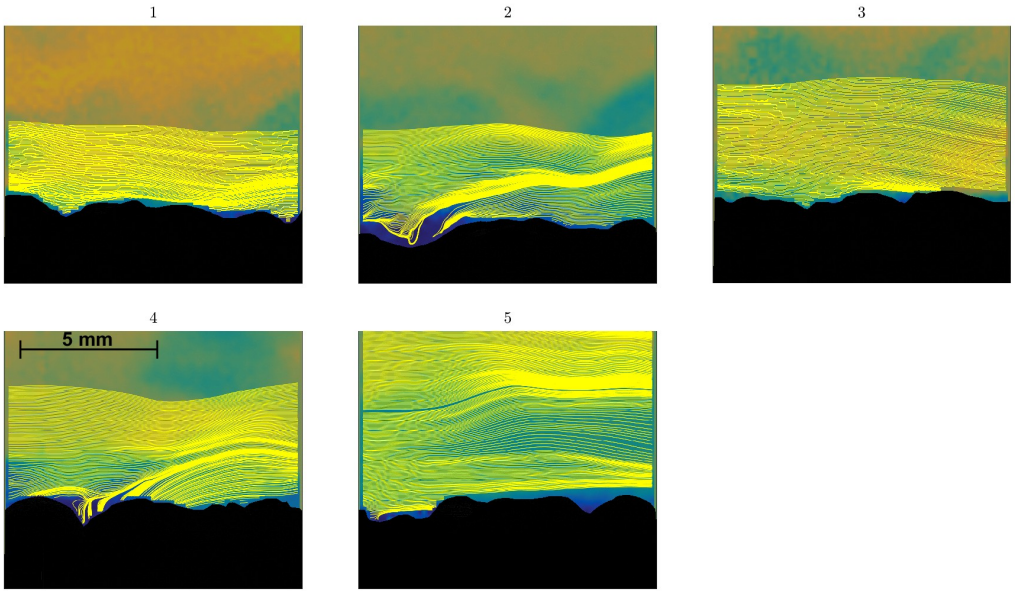

Figure 4.21: Flow behavior in the vicinity of Aluminum 2 surface roughness at $Re = 2.48e + 04$. The images have been cropped to display only the area of interest

4.3.2 Skin-Friction Coefficient Estimation

The continuation of the discussion aims at analyzing and estimating the skin-friction coefficient C_f for rough plates. Specifically, the region selected for analysis was deliberately chosen within the area covered by the SRHT rig for thermal purposes, in order to perform correlations at the end of the examination. Figure 4.22 shows the spot analyzed for the creation of the thermal map,

where the red rectangle indicates the PIV analysis area, measuring (50×1.36) mm. The choice of a more extensive analysis area was driven by the need to capture a pattern that would represent as accurately as possible the homogeneous configuration of the three roughness features.

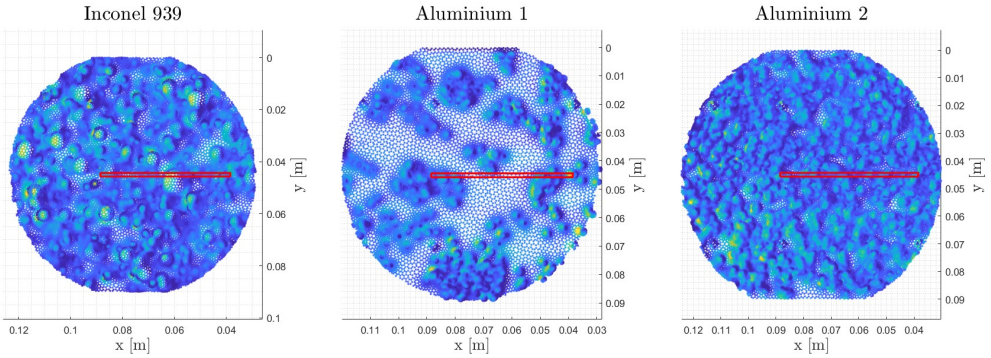

Figure 4.22: Analysis area of the SRHT rig [127]. These zones represent the final analysis window of the rig, where the flow is deemed to be fully developed. Highlighted in red is the PIV technique analysis area, measuring (50×1.36) mm. Tests conducted at $Re = 2.48e + 04$

The choice to calculate the skin-friction factor stems from the necessity to describe the response of the wall shear stress to the three multiscale rough surfaces investigated and also because a clear link to the Nusselt number becomes apparent following Relation 2.2.

The evaluation of the skin-friction factor used is derived from the nature of the roughness function ΔU^+, that is, the velocity shift in the log-layer between the smooth and rough cases [98]. Thus:

$$\Delta U^+ = U_S^+ - U_R^+ \tag{4.2}$$

The skin-friction factor is defined as

$$C_f = \frac{\tau_w}{\frac{1}{2}\rho\overline{U}^2}$$

Isolating the wall shear stress, one obtains:

$$\tau_w = \rho\overline{U}^2 \frac{C_f}{2}$$

Inserting this expression into the evaluation of u_τ (Relation 2.3), one arrives at:

$$u_\tau = \sqrt{\frac{\tau_w}{\rho}} = \sqrt{\frac{\rho\overline{U}^2}{\rho}\frac{C_f}{2}}$$

and furthermore inserting this expression into the evaluation of U^+ (Relation 2.4)

$$U^+ = \frac{\overline{U}}{u_\tau} = \frac{\overline{U}}{\overline{U}}\frac{1}{\sqrt{\frac{C_f}{2}}} = \sqrt{\frac{2}{C_f}}$$

Therefore, Relation 4.2 can be rewritten as:

$$\Delta U^+ = \left(\sqrt{\frac{2}{C_f}}\right)_S - \left(\sqrt{\frac{2}{C_f}}\right)_R \tag{4.3}$$

which results in a different form of estimating the roughness function, namely as the difference

between the skin-friction of the rough wall from that of a smooth wall at equivalent Reynolds or Re_τ [79].

In Equation 4.3, ΔU^+ and $(C_f)_S$ are known, so it's possible to extract $(C_f)_R$ by isolating it and obtaining:

$$(C_f)_R = \frac{2}{\left[\left(\sqrt{\frac{2}{C_f}}\right)_S - \Delta U^+\right]^2} \tag{4.4}$$

The results related to the evaluation of the skin-friction factor C_f for the smooth plate, derived using the CCM (3.2.9), are shown in Figure 4.23, compared with the experimental values obtained by Schultz & Flack[79]. The fit is excellent.

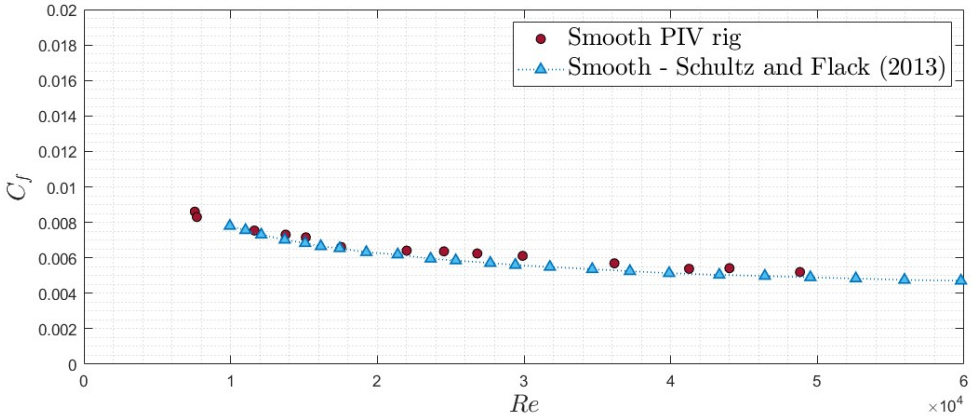

Figure 4.23: Skin-friction results for smooth surface. Results compared with the experimental values obtained by Schultz & Flack[79]

Subsequent tests were conducted at the same Reynolds numbers Re_τ to apply Equation 4.4 and obtain the skin-friction factor values for the three multiscale rough surfaces investigated. The results of these analyses are depicted in Figure 4.24.

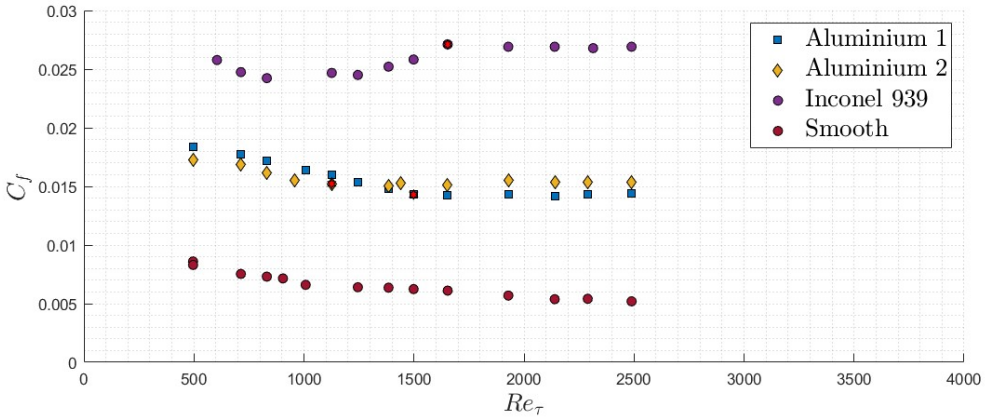

Figure 4.24: Skin-friction results for rough surface. The red stars highlight the skin-friction estimates corresponding to beginning of fully rough regime

As highlighted by previous research (see, for example, the studies by Medjnoun et al.[100]), the fully rough regime is characterized by the dominance of pressure-related drag forces over viscous ones. In the cases analyzed, for $Re_\tau \gtrsim 1600$, the viscous drag components tend to play a lesser role compared to the pressure-induced drag, which is enhanced due to the introduction of additional levels of roughness. This consideration becomes even stronger when analyzing the

Reynolds number for each rough plate associated with the Re_τ at which they reach a plateau of C_f (fully rough regime). This comparison is shown in Table 4.5. It is noted that the first plate to reach the fully rough condition is the one representing Aluminium 2, which could be due to the high density of the roughness causing various levels of irregularities that contribute more significantly to the pressure-induced drag. This concept is confirmed by the results pertaining to Aluminium 1. This material has the smallest roughness scales, hence a more extended contribution of the viscous drag components is expected, which, however, tend to diminish but at higher Reynolds numbers.

Roughness texture	Re_τ -	Re -
Inconel 939	1600	$1.67e+04$
Aluminium 1	1500	$1.77e+04$
Aluminium 2	1130	$1.25e+04$

Table 4.5: Values of Re_τ and Re required for the different roughnesses to reach the fully rough regime condition (related to the red stars highlighted in Figure 4.24)

Naturally, the magnitude of the skin-friction coefficient is significantly influenced by the nature of the roughness, as well as its size and extent: Inconel, displaying more pronounced peaks, exhibits a higher C_f, while the aluminum surfaces tend to settle on similar values.

The equivalent sandgrain roughness height k_s^+ can be deduced using the fully rough asymptote relation of Nikuradse[4] (Equation 2.12), so:

$$k_s^+ = e^{\kappa(\Delta U^+ - C + 8.5)}$$

The results obtained are tabulated in Table 4.6.

Roughness texture	Re -	k_s^+ -	$k_s \times 10^{-3}$ [m]	k_s/δ -	u_τ [ms^{-1}]
Inconel 939	$1.67e+04$	206.692	11.987	0.248	0.260
Aluminium 1	$1.77e+04$	50.598	3.342	0.0671	0.228
Aluminium 2	$1.25e+04$	56.993	5.249	0.111	0.164

Table 4.6: Values of k_s^+ and k_s for the three multiscale rough surfaces investigated

The value of k_s^+ for Inconel is approximately 200, significantly higher than the value established by Nikuradse[4] in 1933, which is $k_s^+ = 70$. The aluminum surfaces, on the other hand, are closer to this value, which might suggest that the irregularities on these surfaces are more close to the internal texture of the pipes studied by Nikuradse, marked by irregularities such as sand grains. Moreover, values of k_s are presented in Table 4.6 as a fraction of δ, and range between 6% and 24% of the boundary-layer thickness.

After deriving the aerodynamic parameters of the turbulent boundary-layer flow over the different multiscale rough surfaces, possible correlations with the SRHT rig were mapped. For a more accurate description of the methodology and the thermal results analysis, the reader is referred to Brogliato[118], Tamagnini & Agostino[124], and Wen[115]. The emphasis of the following work focuses on the cross-correlation between the average Nusselt number trends in the last analysis window of the SRHT rig and the friction coefficient C_f trends analyzed with the PIV technique for all the tested roughnesses. Specifically, to define this relationship, a particular behavior of the

aluminum surfaces was analyzed in the range $1.0e+04 < Re < 1.5e+04$. Figure 4.25 presents these trends related to the average Nusselt number.

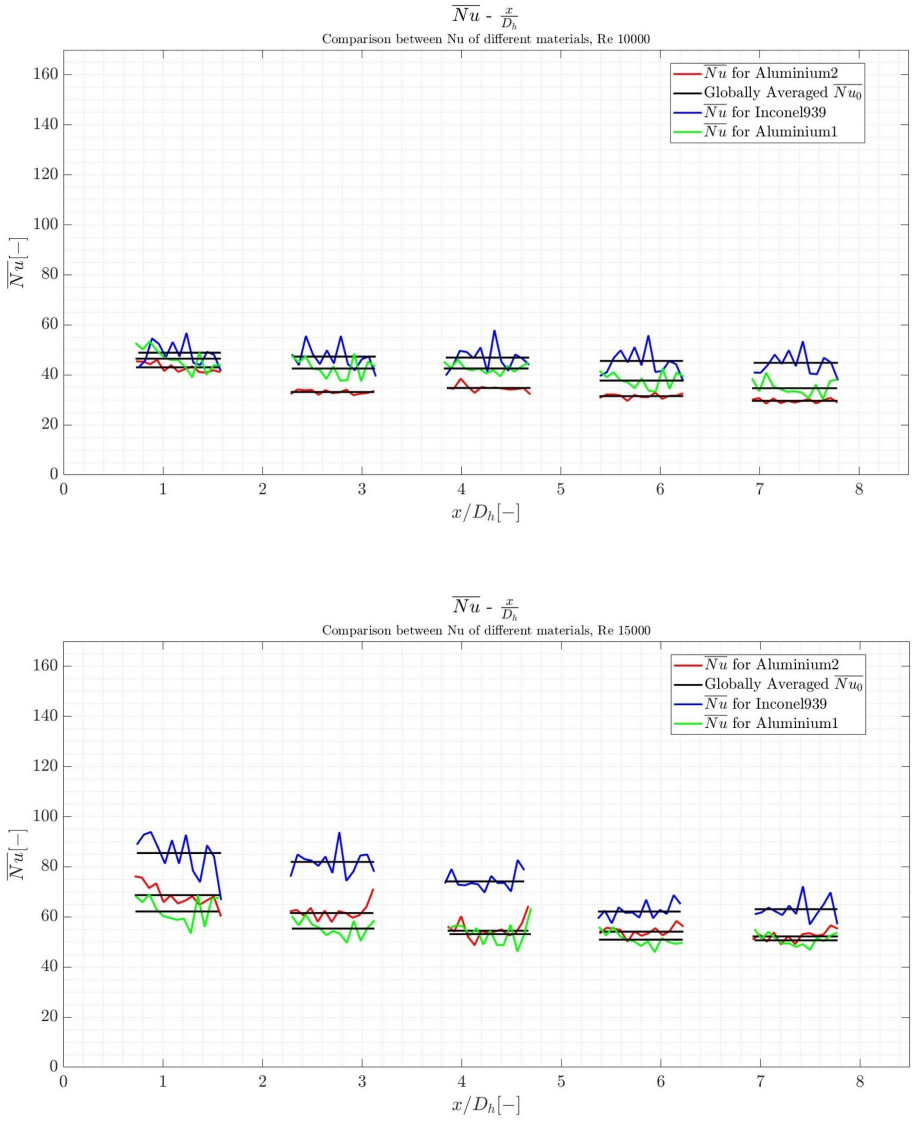

Figure 4.25: Three surfaces comparison for all $Re = 1.0e+04$ and $Re = 1.5e+04$ [124]

The last window (fully developed flow) indicates a reversal of the Nusselt number between Aluminium 1 and Aluminium 2 plates: at low Re values, the thermal behavior of Aluminium 2 is very close to that of the smooth plate (see also the discussion in Section 4.3.1 regarding the high roughness density and the flow lines passing over them), as if the boundary layer creates an "air bearing" that completely covers the irregularities, making the plate aerodynamically flat. This could affect the Nu due to the absence of impact zones between the flow and the surface. In this case, $\langle Nu_{AL1} \rangle > \langle Nu_{AL2} \rangle$, where the brackets $\langle\rangle$ indicate the average value. As Re increases, a reversal of this trend is observed; in fact, for $Re = 1.5e+04$ it is found that $\langle Nu_{AL1} \rangle < \langle Nu_{AL2} \rangle$. This could result from a decrease in the boundary layer thickness near the roughness at higher speeds, becoming smaller than the size of the irregularities, which would explain the increase in the Nusselt number due to the impact with the roughness.

This inversion was also observed following the evaluation of the friction coefficient C_f. Figure 4.26 presents the highlighted experimental results. It is noted that the zone where the inversion occurs is between a Reynolds number of $1.2e+04$ and $1.8e+04$, consistent with the thermal level observations. In this case as well, regarding the influence of the wall shear stress on the multiscale rough aluminium surfaces, the relationship $(C_f)_{AL1} > (C_f)_{AL2}$ for $Re < 1.2e+04$ and $(C_f)_{AL1} < (C_f)_{AL2}$ for $Re \gtrsim 1.5e+04$ persists, in analogy with the relative thermic case. This result highlights a close relationship between the aerodynamic behavior in terms of surface drag and the thermal information found for the rough plate, leading future studies and analyses to focus on a possible empirical relationship from this perspective. However, it is important to highlight that Gissi [127] pointed out a strong sensitivity of the SRHT tests to errors caused by Reynolds number fluctuations, making further investigations necessary to confirm this possible correlation.

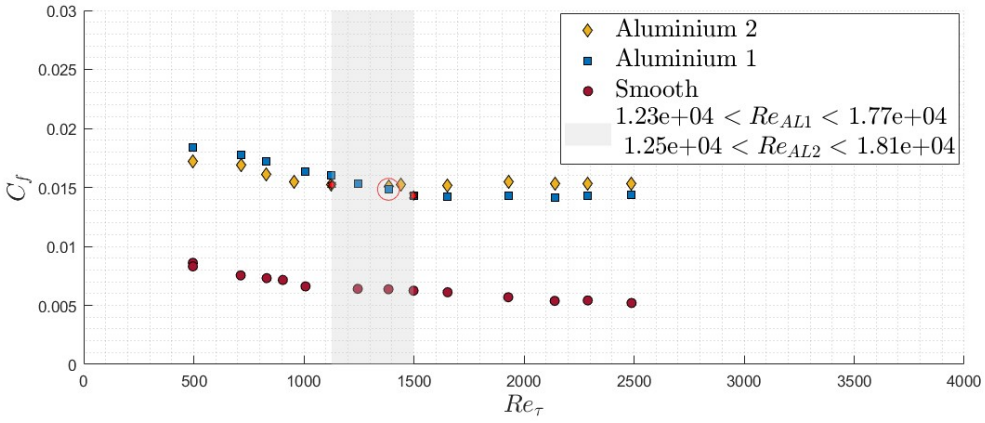

Figure 4.26: Skin-friction results for aluminium surface. The red stars highlight the skin-friction estimates corresponding to beginning of fully rough regime, while the red circle represents the inversion point found experimentally

4.4 Correlations with QSSHT Rig

The QSSHT rig is designated to evaluate the pressure drop and measuring the enhancement of the Nusselt number for various test objects. These test objects are 1:1 scale models of upscaled reproductions used for roughness analysis with PIV technique and SRHT rig. Such test objects replicate the cooling ducts of the turbine, featuring an inner channel and an outer coating of a different material. The use of additive manufacturing to produce these components introduces surface irregularities within these ducts, shown in Figure 4.27, from which various upscaled roughness plates related to each material are subsequently constructed as described in Section 3.2.2.

The following section will present the results related to the Darcy friction factor f obtained through PIV, and the respective extraction and processing methods. These data will be compared with the evaluations obtained from the QSSHT rig to perform analyses on the roughness parameters that most significantly impact the friction characteristics of the material.

4.4.1 Darcy Friction Factor Smooth

The Darcy friction factor is a dimensionless quantity used in the Darcy-Weisbach equation to describe friction losses in pipe flow as well as open-channel flow. It is also known as the Darcy-Weisbach friction factor, resistance coefficient, or simply the friction factor, and it is four times

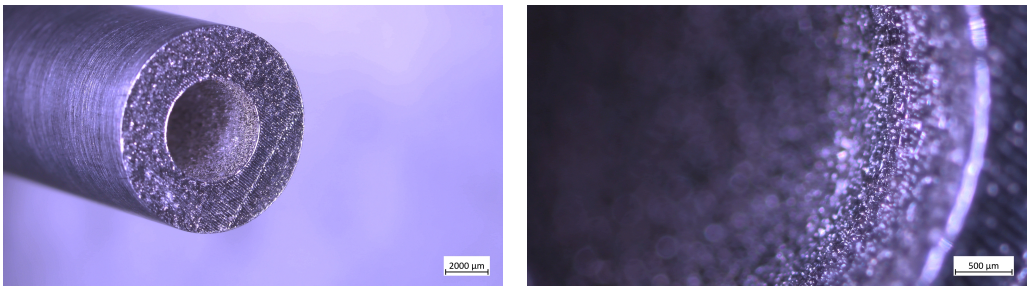

Figure 4.27: 1:1 scale Test object TO2501-1, made of Inconel 939, with an internal diameter of 5 mm and a length of 90 mm. Images obtained using a Zeiss Stemi 2000-C stereomicroscope with Zeiss Axiocam 208 color camera

larger than the Fanning friction factor, in accordance with Equation 2.9. Referencing this relationship, it can be stated that:

$$f = 4 \cdot C_f \tag{4.5}$$

Thus, once the skin-friction factor for smooth surfaces is obtained, the friction factor can be calculated. By using Relationship 4.5, evaluations related to f for smooth plates are obtained, as presented in Figure 4.28, comparing them with the results reported by Schultz & Flack[79] and with the theoretical values determined by the Colebrook-White equation (Equation 3.4).

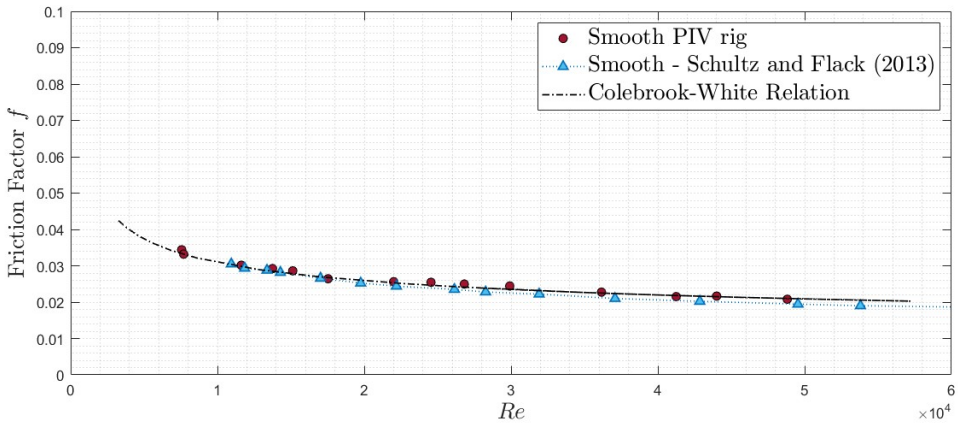

Figure 4.28: Darcy friction factor results for smooth surface

The experimental results tend to align optimally with the theoretical trend formulated by Colebrook. Having confirmed the consistency of the results with the literature, these data obtained using the PIV technique were compared with those derived from the QSSHT rig. The settings used for the PIV image acquisition vary: the Δt and the size of the interrogation windows change according to the Reynolds number, while the laser power and the f-stop are kept constant at values of 25% and 16, respectively. The other parameters have been determined by following the methodology described in section 3.2.4.1. The results and various comparisons with other measurement techniques are shown in Figure 4.29.

It is observed that the values obtained through PIV are already in a turbulent context, beyond the transition. This is due to the fact that with the available technology, it was not possible to reach Reynolds numbers low enough to be in laminar flow. Moreover, the results from the velocimetry rig align perfectly with the theoretical trend, as previously stated. The results related to the QSSHT

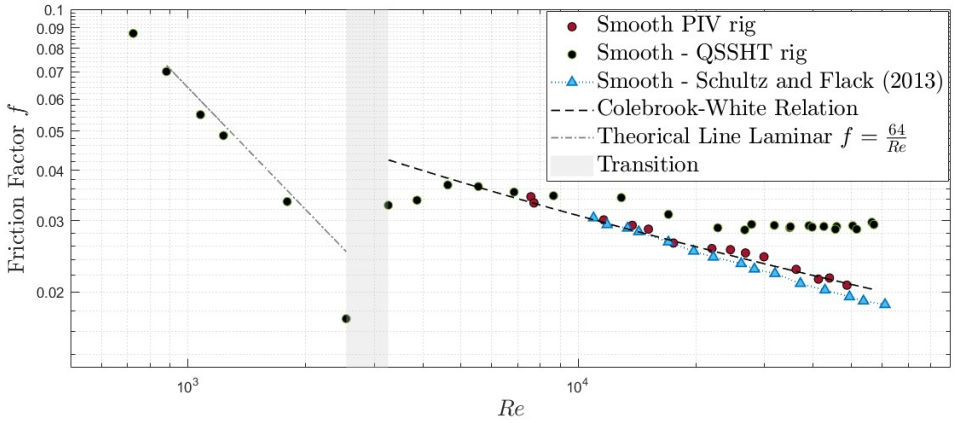

Figure 4.29: Darcy friction factor results for smooth surface compared with results from QSSHT rig in loglog plot

rig, on the other hand, tend to deviate from this curve, settling into the typical configuration of a fully rough regime. This is because the 1:1 scale test objects defined as smooth still exhibit surface irregularities, resulting in a relative roughness value ε/D_h much higher than what can be found in the PIV rig test section. Indeed, the upscale smooth plates turn out to be much smoother (since they were printed using SLA with Accura Xtreme Grey material), and notably, the value of ε/D_h results negligible compared to that of the QSSHT rig. Figure 4.30 provides a visualization of the irregularities present on the inner wall of the 1:1 scale smooth test objects and on the upscale smooth plate.

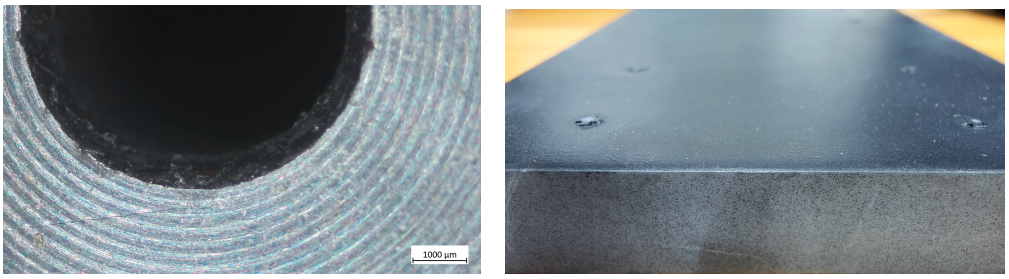

1:1 scale smooth test object

Upscale smooth plate

Figure 4.30: Zoomed-in image near the wall

4.4.2 Darcy Friction Factor Rough

It was desired to extend the previous discussions to rough plates as well, by adopting a different approach to ensure consistency with the physics of the problem. The skin-friction factor is a local factor dependent on the specific characteristics of the analyzed surface. Initially, this could impose limitations on the methodology for rough plates, as the PIV technique might not be able to resolve every point on the surface, or at least the extremely high number of required tests would make the analysis onerous and challenging. To confirm or refute this hypothesis, an analysis was conducted to define the variation of the skin-friction factor as a function of the analysis spot, captured with the PIV technique. From Equation 4.3, the dependence of ΔU^+ on the calculation of $(C_f)_R$ is evident, as it is the only term that varies in the equation since the skin-friction factor for smooth plates remains unchanged compared to the results shown in Figure 4.28.

A median line was thus drawn for all three types of multiscale roughness investigated, obtaining the profile of peaks and valleys along this curve. The aim is to perform PIV tests to acquire the aerodynamic parameters by analyzing this median spot, conducting a total of 5 tests moving along increasing X. The PIV settings used are listed in Table 4.7, while the profilometric evaluations are illustrated in Figure 4.31.

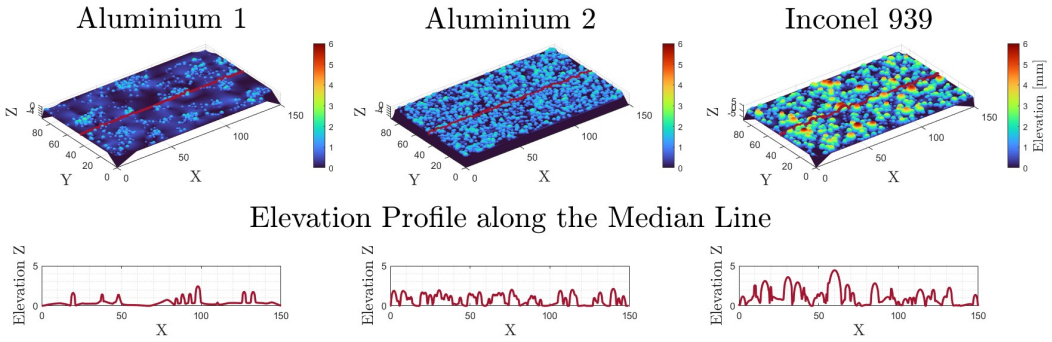

Figure 4.31: Median line along which PIV and profilometer tests were conducted for the various roughnesses along this curve

Re -	Laser power %	$\Delta t \times 10^{-3}$ [s]	$f - stop$ camera	Int. windows [px]	Field of view [cm]
$2.31e+04$	25	0.021	14	20×20	(3.0×5.1)
$2.48e+04$	25	0.022	14	22×22	(3.0×5.1)

Table 4.7: PIV settings for test along median line

The various evaluations of the skin-friction factor C_f and the ΔU^+ for all the rough plates analyzed are presented in the figures below.

During data processing, a parameter ζ was evaluated, which represents the normalized standard deviation with respect to the average value in percentage. As illustrated in Figures 4.32, 4.34, and 4.36, this parameter for all the multiscale roughnesses investigated and for both Reynolds numbers analyzed remains below 4% in the evaluation of C_f, and below 2% in the extrapolation of ΔU^+. This suggests that such parameters are not highly dependent on the measurement spot, therefore, the hypothesis of considering the Darcy friction factor as four times the skin-friction factor for rough surfaces represents a valid methodology and approximation. In any case, such errors will be taken into account in subsequent evaluations, using a possible error window characterized by the maximum error highlighted by the parameter ζ for every rough surface, which is within 2% and 4%.

Figure 4.38 shows the evaluations of the friction factor f for Inconel 939 and a comparison with theoretical data and that from the QSSHT test rig. The comparison was carried out with a test object of 1.25 mm diameter because the profilometry used to model the upscale plate related to the Inconel 939 material was obtained from this object. The shaded area represents the error zone defined by the parameter ζ previously evaluated. It is noted that the estimates of the friction factor tend to converge once the fully rough flow regime condition is reached. Before this zone, the data do not adhere, which could be due to design factors: although the fluid dynamic similarity requirement is met (the Reynolds numbers with which the tests were conducted for the two test

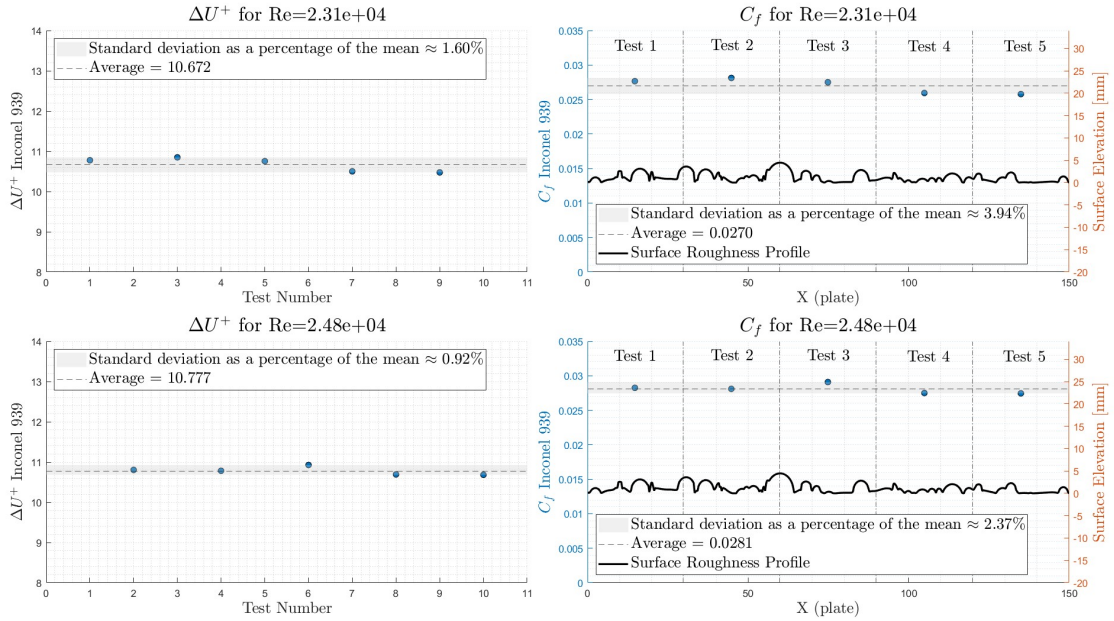

Figure 4.32: Evaluation of parameters C_f and ΔU^+ for Inconel 939 along the median line for a total of 5 tests

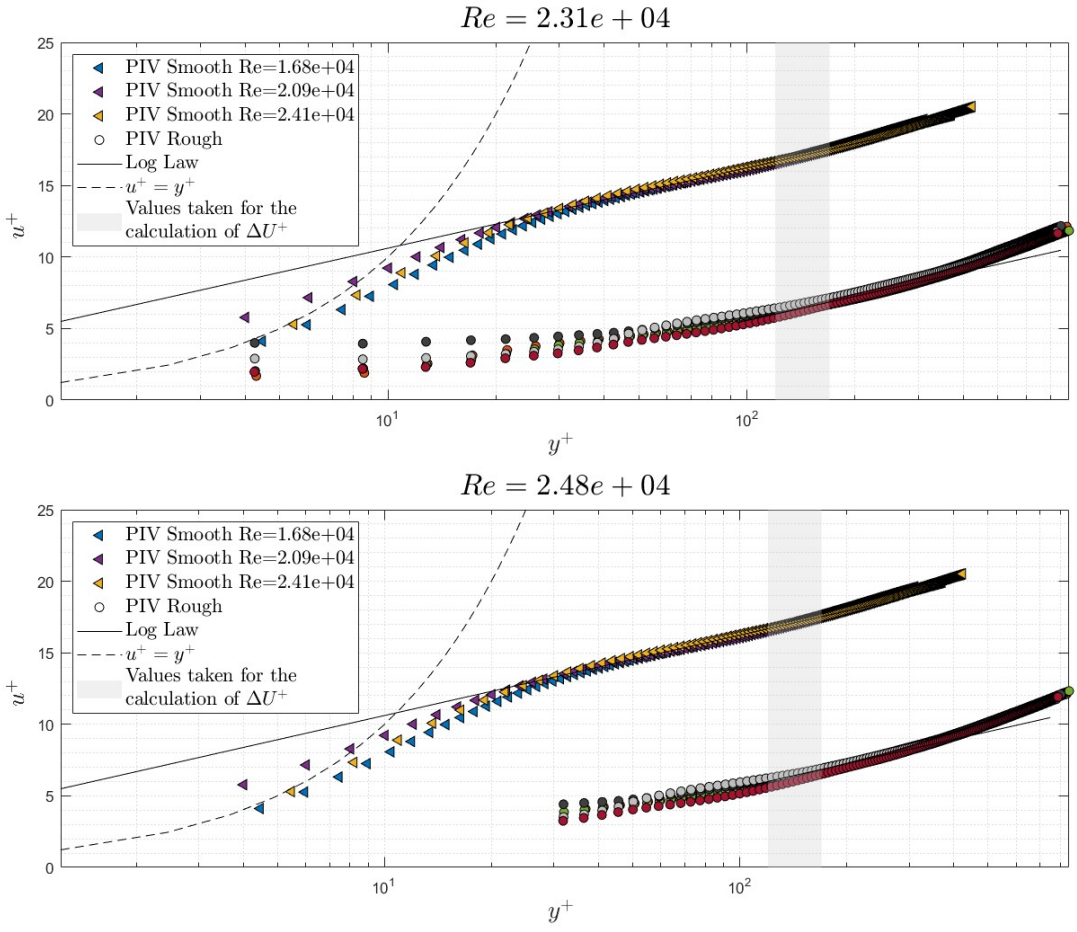

Figure 4.33: Near wall velocity profile Inconel 939 for $Re = 2.31e + 04$ and $Re = 2.48e + 04$

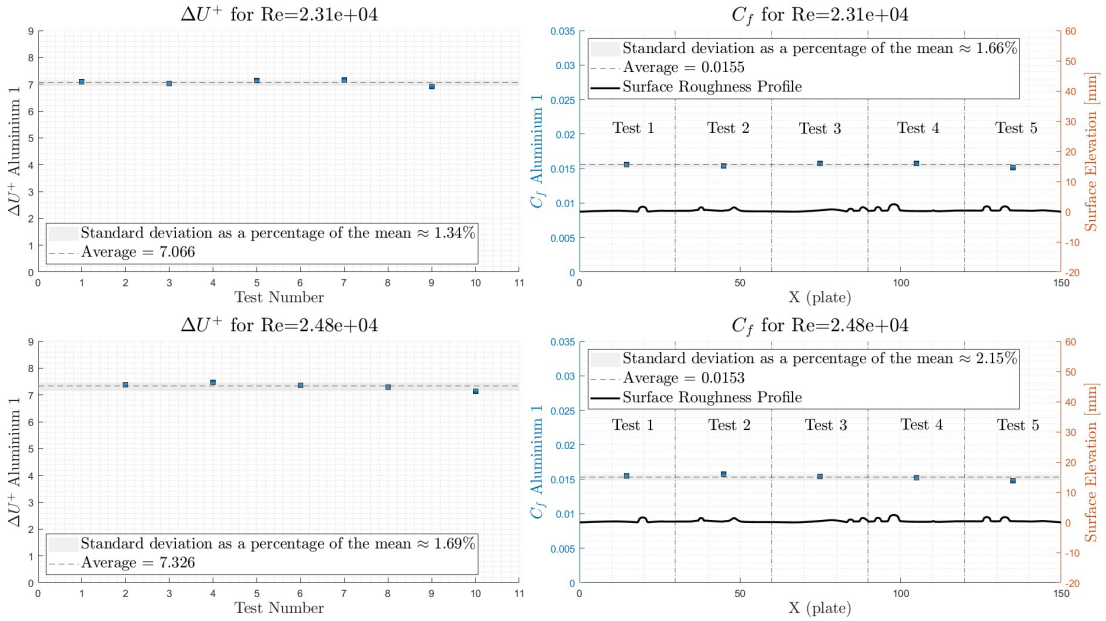

Figure 4.34: Evaluation of parameters C_f and ΔU^+ for Aluminium 1 along the median line for a total of 5 tests

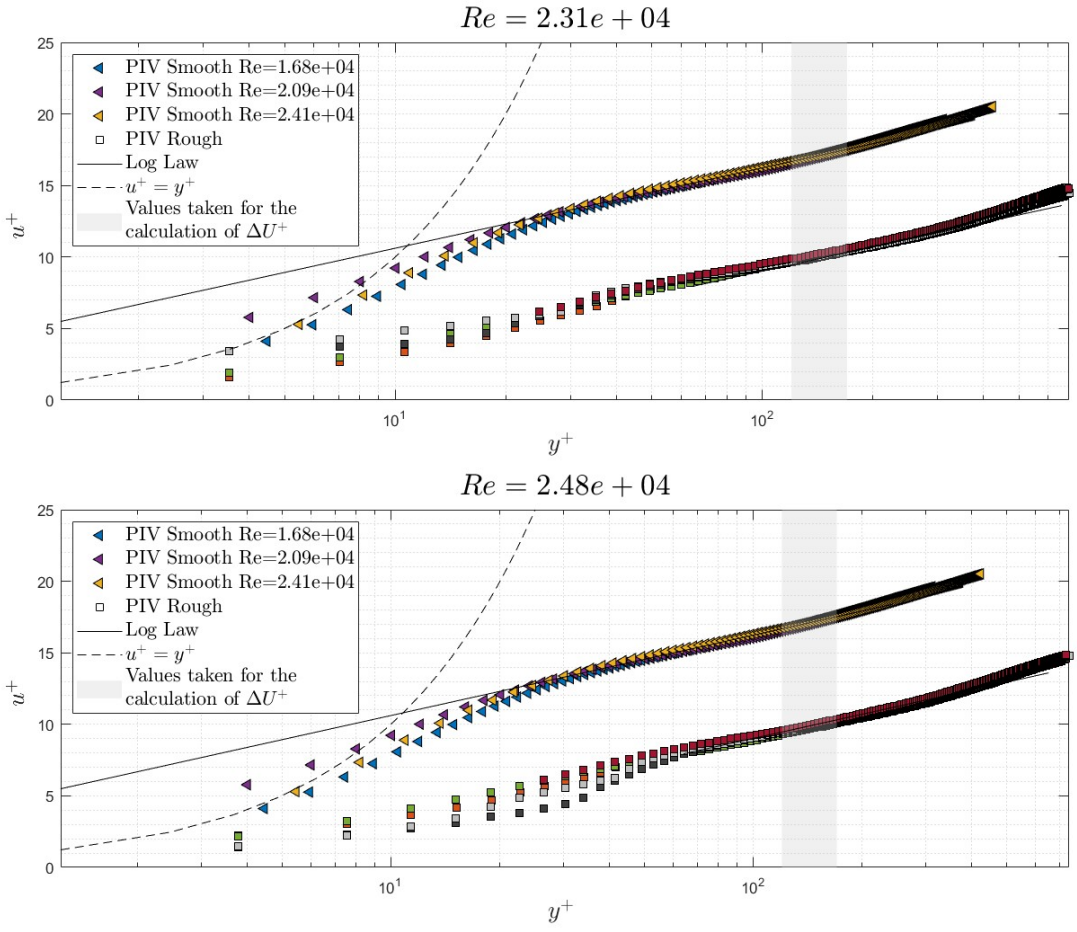

Figure 4.35: Near wall velocity profile Aluminium 1 for $Re = 2.31e + 04$ and $Re = 2.48e + 04$

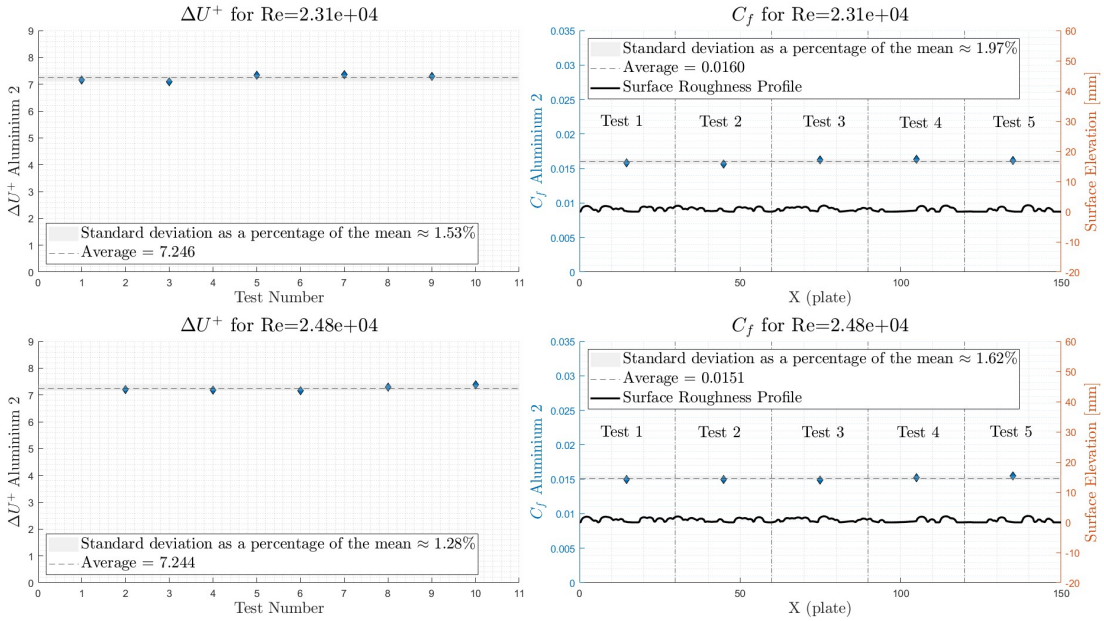

Figure 4.36: Evaluation of parameters C_f and ΔU^+ for Aluminium 2 along the median line for a total of 5 tests

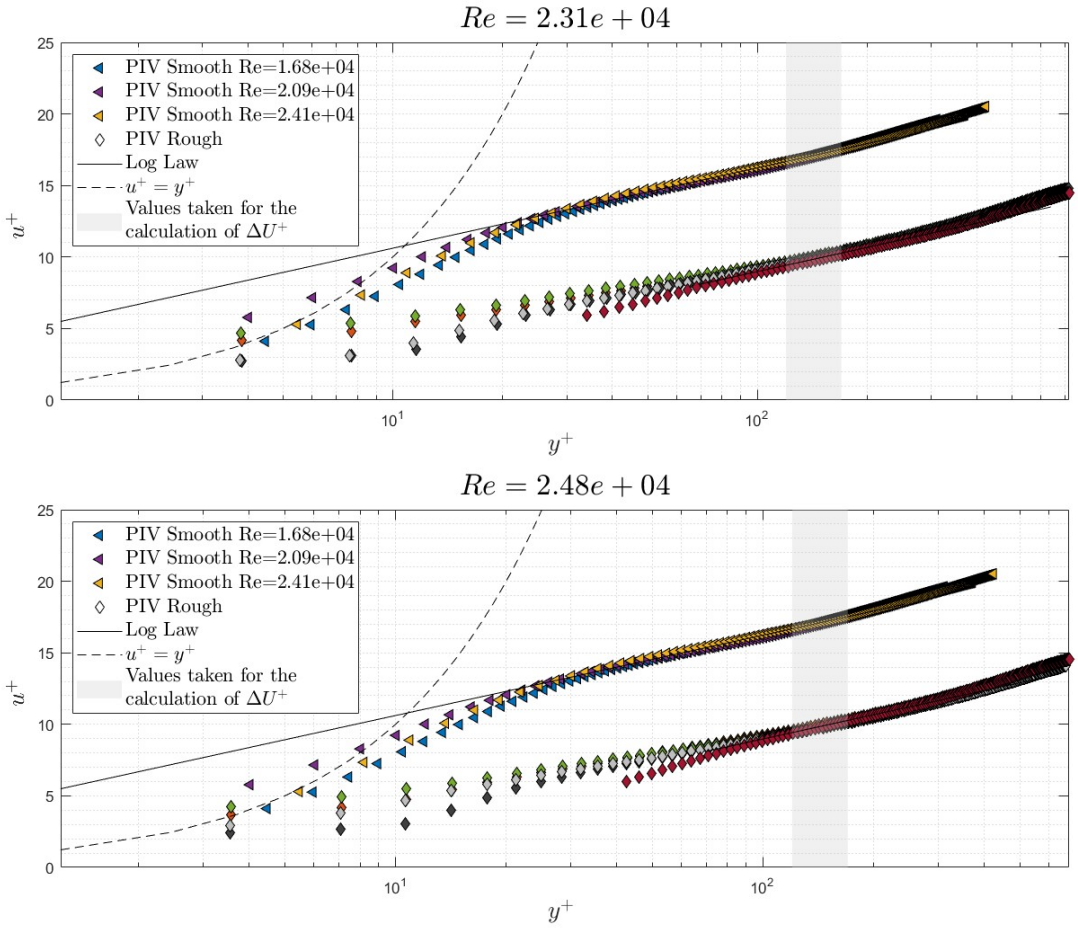

Figure 4.37: Near wall velocity profile Aluminium 2 for $Re = 2.31e + 04$ and $Re = 2.48e + 04$

rigs coincide, see Section 3.1.1), there are significant differences regarding the geometry of the two systems. Firstly, the QSSHT test rig features circular test objects, while the PIV system has a rectangular test section, which could create secondary flow zones at the corners of the test section, affecting the transition. Moreover, the transition could occur at two different spots, since the length of the two sections, relative to the diameter, does not match ($L_c/D_h = 72$ for the QSSHT and 11.40 for the PIV; the test object dimensions are 90 mm × 1.25 mm, whereas for the dimensions of the test section, see Table 3.1), which could lead to different transition zones. Additionally, the PIV analysis section shows one rough side and the other three smooth (the rough plates are positioned along only one side of the internal rectangular area), while the analysis on the QSSHT considers objects with the entire internal area being rough. Despite this, the results show a good fit in the area where the flow is fully rough, confirming the validity of the performed tests and the methodology employed to assess the skin friction factor C_f and the friction factor f.

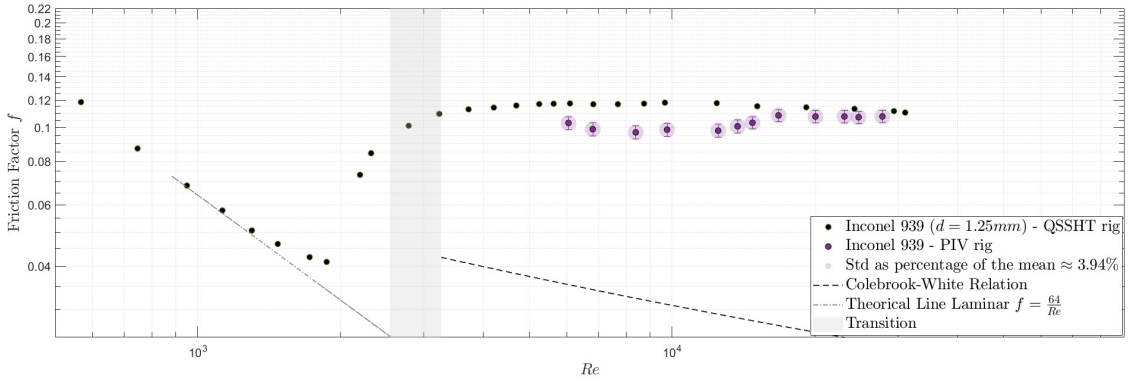

Figure 4.38: Moody diagram type chart related to the tests carried out on Inconel 939 using the PIV technique and the QSSHT rig. The highlighted area, also defined by the errorbar, shows the maximum measurement error determined by the parameter ζ

Figure 4.39 displays the results of the Darcy evaluation for the two aluminum surfaces compared with theoretical trends and assessments carried out using the QSSHT rig. The comparison was made using a test object in aluminum with an internal diameter of 1.5 mm, since it was from this that the characterizing parameters for the plates named Aluminium 1 and Aluminium 2 were derived. Brogliato [118] conducted an analysis and modeling of the two induced roughnesses, obtaining two different materials by optimizing different sets of roughness parameters: for Aluminium 1, the parameters R_a, R_q, and R_z were optimized, while Aluminium 2 resulted from the maximization, in comparison to the real case, of skewness R_{sk} and kurtosis R_{ku}. Table 3.2 illustrates this point, showing that the discrepancy in error level between the real parameters and those characterizing the modeled surfaces is minimized for the previously described sets.

The tests carried out to measure the roughness parameters were conducted using a Mitutoyo Surftest SJ-410 profilometer, sliding the profilometer along lines for the entire length of the test object. For this analysis, Brogliato [118] performed a total of 6 tests on different lines of 4 mm each. The outputs of such measurements are shown in Table 4.8. It is noted that the parameter with the greatest variation among the evaluation lines is the skewness (near 90%), which also indicates a significant deviation of the R_{sk} value compared to the actual value for Aluminium 1 (more than 800%).

This significant deviation in Aluminium 1 compared to the actual surface makes this artificial plate less accurate compared to the real material, as also confirmed by the results shown in Figure 4.39. The friction factor evaluations for Aluminium 2 are very close to those of the real test

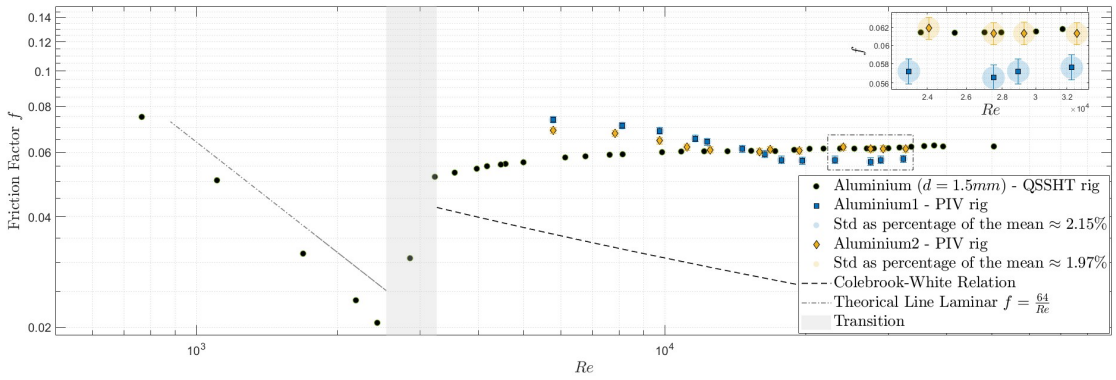

Figure 4.39: Moody diagram type chart related to the tests carried out on aluminium surfaces using the PIV technique and the QSSHT rig. The highlighted area, also defined by the errorbar, shows the maximum measurement error determined by the parameter ζ. In the top left insert, a zoom of the area surrounded by the rectangle

Test	R_a [μm]	R_q [μm]	R_z [μm]	R_p [μm]	R_v [μm]	R_{sk} -	R_{ku} -	R_t [μm]
1	6.344	7.897	37.881	20.636	17.244	-0.037	3.481	64.334
2	5.013	6.381	32.217	18.205	14.012	0.19	3.127	44.07
3	6.724	8.147	35.261	19.02	16.241	0.168	2.415	53.354
4	5.523	7.191	37.547	21.644	15.904	0.55	4.96	55.025
5	5.346	7.104	37.257	20.625	16.632	0.164	3.884	60.213
6	6.43	7.961	39.575	21.126	18.45	0.277	2.938	48.295
ERROR	11.73%	9.06%	7.00%	6.52%	9.01%	87.95%	25.49%	13.75%
MEAN	5.897	7.447	36.623	20.209	16.414	0.219	3.468	54.215

Table 4.8: Evaluation of roughness parameters on the real rough surface. Six tests were conducted to assess the parameters

object, whereas for Aluminium 1 there is a slight deviation of about 5% compared to the value derived from tests with the QSSHT rig. This highlights an intuitive result: the plates modeled by optimizing skewness and kurtosis, namely those related to Aluminium 2, more accurately replicate the actual aluminum test object. This is a direct extension of the parameters defined in Table 3.2, where the greater errors occur in the modeling of roughness for Aluminium 1, while for Aluminium 2 the deviations are more contained (larger errors in the range $[814; 67.27]\%$ in the comparison between the parameters of the real material and those of the artificial surface for Aluminium 1 versus $[66.7; 44.81]\%$ for Aluminium 2).

A more interesting result emerges from a quantitative assessment of these data. It has been ascertained that the 800% deviations related to R_{sk} for Aluminium 1 compared to the actual rough material are one of the main reasons causing a divergence in the friction factor data when compared with those from the real test object derived from the QSSHT rig. However, these deviations, as mentioned, are very small (around 5%) despite the large error in roughness parameters. Moreover, indirectly, the only parameter that shows congruence between Aluminium 1 and Aluminium 2 compared to the real case is R_z, where the error relative to the first surface is 0.8% (2.32 actual and 2.35 for the analogous rough surface), while for the second material it is around 7% (2.32 actual and 2.48 for the analogous rough surface), making this the only roughness parameter that changes insignificantly between the two roughness models and reality. All these considerations

might suggest that R_z is the parameter that most influences the behavior of the Darcy friction factor, while the other defined roughness parameters play a less impactful role. This is supported by the results in Figure 4.39, where the high errors in the parameters of Aluminium 1 do not significantly affect the deviation of the results from the real ones, where all roughness parameters are different except for R_z, which appears to be approximately the same. It is also interesting to observe the pattern of deviation in the results between Aluminium 1 and Aluminium 2 in the fully rough regime: the Darcy values for the first surface are lower than those for the second, consistent with the R_z values. Indeed, Aluminium 1 shows a lower R_z than that related to Aluminium 2, following the trend of the friction factor f profiles. Although this analysis is only hypothetical, it reflects well the experimental results obtained, suggesting the need for more plate models with a more varied set of roughness parameters to better analyze this dependence.

Further confirmation of the possible validity of this hypothesis comes from the analysis conducted by Pagani[108], a previous thesis student who worked on the QSSHT rig. von Kármán[5] established a correlation based on the experimental data extrapolated from Nikuradse[4] to link the pressure losses of a fully developed turbulent flow in a rough pipe to the relative roughness, obtaining the following relation:

$$f_{\text{von Kármán}} = \left(2\log_{10}\frac{3.7D_h}{\varepsilon}\right)^{-2} \tag{4.6}$$

which was subsequently expanded by Colebrook and White[8] to link the Darcy friction factor with the Reynolds number (a correlation generally used to represent the Moody chart). However, Pagani[108] noted very high relative roughness values for the tested test objects, higher than those highlighted by Nikuradse's data, also contravening the absence of experimental data for high values of ε/D_h. The analysis of test objects made of different materials through AM, such as Inconel 939, Haynes 282, and STAL15 (a single-crystal superalloy used in the first stage blades of industrial gas turbines), showed a deviation from von Kármán's correlation (also due to the lack of experimental data), leading to the definition of a new correlation, in the same mathematical form as Equation 4.6, using all experimentally obtained friction values:

$$f_{\text{Pagani/SiemensEnergy}} = \left(2.62\log_{10}\frac{0.89D_h}{R_z}\right)^{-2} \tag{4.7}$$

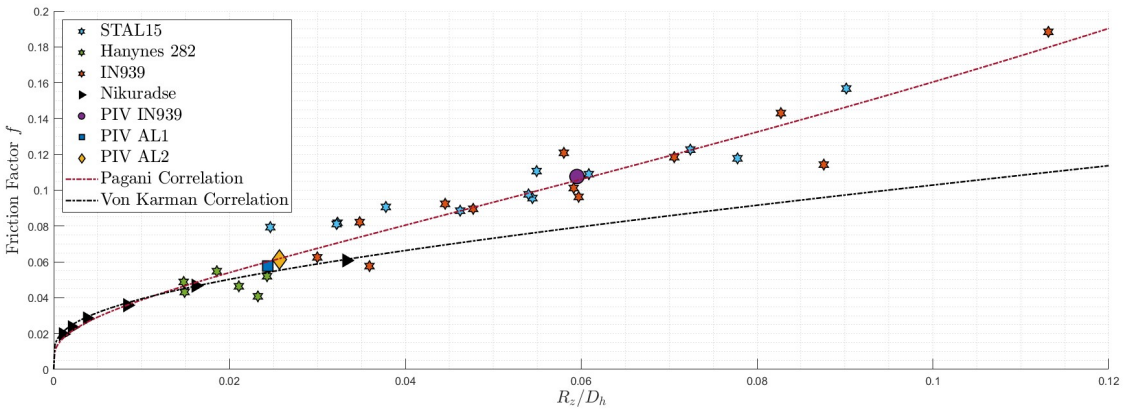

Figure 4.40: Fully turbulent Darcy friction factor correlation in a rough channel. The larger markers represent the friction factor data obtained through the analysis performed using PIV technique

It can be noted that samples with low relative roughness have Darcy turbulent friction factors comparable to those obtained by Nikuradse[4] almost a century ago, demonstrating the reliability of the work; moreover, Relation 4.7 has R_z as the sole relative roughness parameter, providing further confirmation to the analysis carried out before. The results obtained by Pagani[108] are shown in Figure 4.40, compared with the values extrapolated from Nikuradse[4] and von Kármán's correlation[5]. Also included in the figure are the Darcy values calculated with the previous analysis following the data collected using the PIV technique. The highlighted friction factor represents an average of the values in the context of a fully rough regime, just like the data collected by Pagani[108]. An excellent alignment of the experimental PIV values with the correlation related to the Darcy friction factor f found through the QSSHT rig is observed, functioning only on R_z as the roughness parameter:

$$f_{\text{Pagani/SiemensEnergy}} = f\left(\frac{D_h}{R_z}\right)$$

This could serve as additional evidence of the strong impact of R_z on the friction factor, while highlighting a very weak dependence on the other roughness parameters.

Chapter 5

Conclusions and Future Works

The results of this thesis work aim to evaluate the impact of roughness in turbine cooling ducts on flow behavior, friction coefficients, and thermal correlations. The various tests carried out have allowed for the creation of an extensive database, which will be valuable for future research. The impact of different Reynolds numbers was analyzed in relation to the thermal properties of the surfaces under equivalent flow conditions. A cross-correlation between friction coefficients and Nusselt numbers was observed by examining the trends of both and noting shared reversal points between the two profiles. Initial hypotheses concerning the impact of flow recirculation zones downstream of the roughness have been confirmed, revealing areas of low thermal transmission at these points, characterized by aerodynamically smooth regions. The increase in the Nusselt number in the areas of interaction between flow and roughness was also confirmed by PIV images. Comparisons with other rigs have led to the development of new assumptions on the effect of roughness parameters on friction coefficients, particularly the Darcy friction factor f. The consistency of the data obtained with the PIV technique on upscale artificial roughness plates compared to measurements on full-scale 1:1 test objects has shown a significant dependence of the friction coefficient on the roughness parameter R_z, with profile behavior that accurately reflects the existing relationship between the values of this parameter for the three different multiscale rough surfaces investigated. This has led to the proposition of a new hypothesis on the predominant influence of R_z on friction coefficients over other roughness parameters. The alignment of these data with the curve representing the empirical relationship of the friction coefficient as a function of R_z further confirms the plausibility of this thesis.

The research in question requires additional data to be validated or expanded. Therefore, future work could aim at creating new upscale artificial roughness plates with different sets of roughness parameters, so that the dependency under examination can be more thoroughly investigated. In addition, to improve the quality of PIV tests, a rhodamine-based paint could be used on the plates to prevent reflections: by equipping the camera with a specific band-pass filter, recording of reflected light, which is transformed from green to orange by the reflective paint, would be avoided. A new system for velocity measurement could also be implemented in the wind tunnel: manometric reading through external ambient pressure proves to be an ineffective method, as it does not allow for stability in the reading of mass flow. A Venturi tube or an orifice disk, implemented in one of the wind tunnel ducts, could represent an optimal solution. Moreover, since work is being conducted with a channel, direct measurement of wall shear stress τ_w by evaluating pressure drop, using static pressure taps on the test section, could help increase the overall accuracy of the results.

Appendix A

Turbine Cooling Method

Below is a summary overview of the most commonly used cooling techniques in the industrial sector, specifically relating to cooling methods for turbine blades. For further details on the subject, it is advisable to consult the references in the text, which are the main sources from which the following analysis has been drawn.

A1 Rib Turbulated Cooling

Earlier studies on cooling channels primarily focused on stationary conditions. A significant amount of experimental and numerical research [21][46][26][29] has been conducted on the effects of turbulator shapes and configurations on flow patterns and heat transfer distributions in single or multi-pass channels. Recently, Li et al. [96] investigated the flow structure inside a rotating channel fitted with 90-degree ribs using Particle Image Velocimetry. The majority of these studies have demonstrated that adjusting the configurations of ribs can improve overall heat transfer or reduce the pressure drop penalty within the cooling channel [105][60].

When the coolant passes over a rib oriented at 90 degrees to the mainstream flow, the flow near the channel wall separates. Following this separation, reattachment occurs, and the boundary layer reattaches to the channel wall. This reattached boundary layer, being thinner, results in increased heat transfer coefficients within the ribbed channel [60]. The secondary flow induced by the rib is illustrated in Figure A.1.

If V-shaped rib turbulators are used, four vortices are generated, as is evident in Figure A.1, where in the channel with angled ribs, two counter-rotating vortices are formed in the cross-section of the cooling passage. The additional set of counter-rotating vortices associated with the V-shaped ribs results in greater heat transfer enhancement in a channel with V-shaped ribs than in one with angled ribs. The ribs also create turbulent mixing in the areas of flow separation. With this additional mixing, heat is more effectively dissipated from the wall, thereby increasing heat transfer enhancement. Because the ribs disturb only the flow near the wall of the cooling channel, the pressure drop penalty imposed by the ribs is manageable [60].

A2 Impingement Cooling

Jet impingement cooling is often employed in the proximity of an airfoil's leading edge, an area that experiences intense thermal loads [60][57][105]. In this region, the increased thickness of the blade wall provides an ideal surface for the cooling jets to impact upon, facilitating effective temperature regulation. This technique may also be applied around the midsection of the vane. Developing an

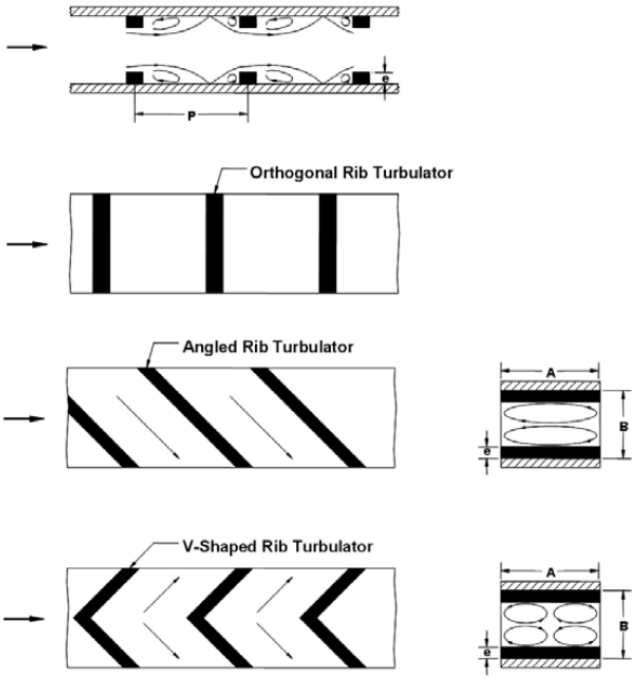

Figure A.1: A Typical Test Model for Studies of Turbulent Cooling with Rib-Induced Secondary Flow [60]

efficient cooling strategy involves an array of considerations, including the size and arrangement of jet holes, the geometry of the cooling channels, and the contour of the surface being targeted [60]. These factors collectively influence the distribution of the heat transfer coefficient. Jet impingement at the blade's mid-chord closely resembles the process on a flat surface. Nevertheless, the pronounced curvature at the vane's leading edge necessitates careful consideration when applying impingement cooling techniques in that area [60].

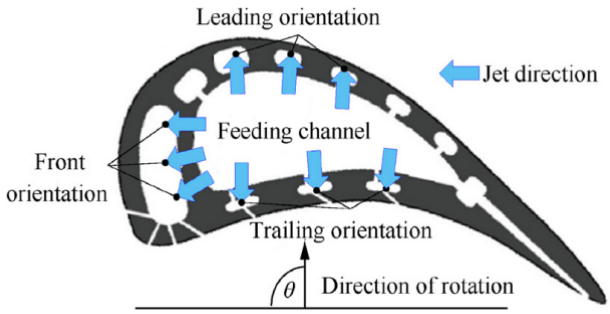

Figure A.2: Sketch of jet orientation relative to rotating axis [78]

In scenarios involving rotating jet impingement, the flow patterns of the jets are influenced by the Coriolis and centrifugal forces, which are dependent on the jet's orientation relative to the rotation axis. The study of rotating jet impingement identifies three primary orientations: the axial or front orientation (($\theta = 0$) degrees), the leading orientation (($\theta = 90$) degrees), and the trailing orientation (($\theta = -90$) degrees). These orientations are depicted in Figure A.2.

A3 Pin-Fin Cooling

Pin fins are predominantly utilized in the confined space of a turbine blade's trailing edge, where the constraints of manufacturing render the use of impingement and ribbed channels unfeasible [57]. The pin fins employed in turbine blade cooling typically exhibit a pin height-to-diameter ratio ranging from 0.5 to 4. The cooling mechanism in turbine pin-fin arrays involves a combination of heat transfer from the pins themselves and from the endwall of the channel [60][57].

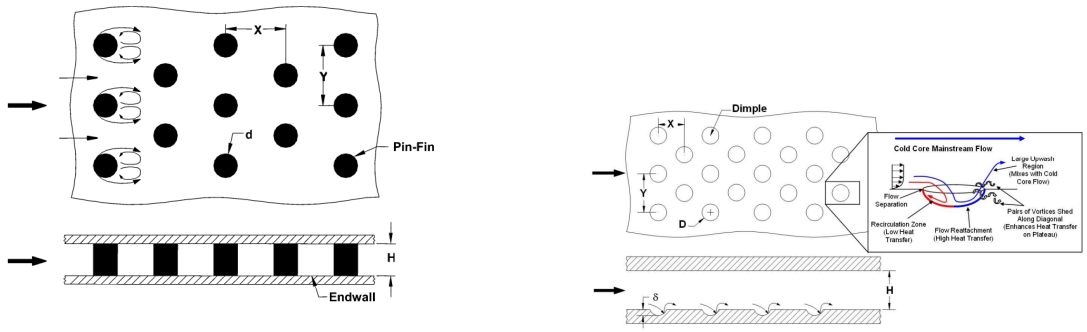

a b

Figure A.3: (a) Secondary flow induced by pin fins [57]; (b) Conceptual View of Dimple Induced Secondary Flow [60]

The flow dynamics around the pins in an array can be likened to the flow around an isolated cylinder. As the coolant moves past a pin, the flow detaches, resulting in wake formation on the downstream side of the pin [57]. Concurrently, a horseshoe-shaped vortex emerges just ahead of the pin's base, and the vortex wraps around the pins, as depicted in Figure A.3a. This horseshoe vortex creates additional mixing and thus enhanced heat transfer [57][60][105].

A4 Dimple/Protrusion Cooling

Dimple is a new cooling scheme that is firstly introduced by Schukin et al [37]. When compared to smooth channels, dimples offer a considerable increase in heat transfer with only a minimal penalty in pressure loss [105]. In recent years, dimples have been considered as an alternative to pin-fin cooling [60].
A typical test section used for dimple cooling studies is depicted in Figure A.3b, which also illustrates the secondary flow induced by the dimples. These concave dimples cause flow separation and reattachment, resulting in pairs of vortices. The regions of high heat transfer are found in the areas of flow reattachment on the flat surface immediately downstream of each dimple [57]. The heat transfer in a channel with dimples is typically 2 to 2.5 times greater than in a smooth channel, albeit with a pressure loss penalty that is 2 to 4 times higher than that of a smooth channel [60]. These performance metrics exhibit minimal dependence on the Reynolds number and the channel aspect ratio [60].

A5 Latticework cooling

Latticework duct, also recognized as a vortex-based cooling system or confined vortex network, is a cooling method that some Russian gas turbines have adopted. An illustration in Figure A.4 displays the gas turbine blade equipped with this grid-like cooling architecture. This configuration is characterized by a series of parallel ridges, where the ridges on one side make direct contact with

those on the opposite side. These ridges are arranged at a specific angle to one another, known as the intersecting angle. Figure A.4 also includes a depiction of the typical trajectory taken by the cooling air as it moves within the grid framework.

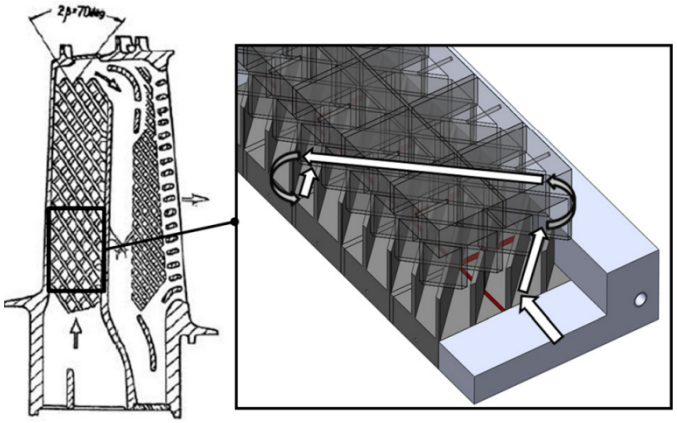

Figure A.4: Example of lattice cooled blade [30] and schematic of subchannel flow [77]

Carcasci et al.[77], Bunker et al.[50] and Gorelov et al.[30] have described the process by which the coolant is introduced into the grid structure, undergoes directional changes at designated points within the network, and impacts the beginning of the neighboring sub-channel. This sequence repeats itself throughout the coolant's passage until it exits the grid system.

The primary benefit of this type of cooling approach is the significant enhancement of heat transfer it offers, although it does come with a notably increased pressure drop, especially when compared to the conventional ribbed turbulators found in serpentine channels.

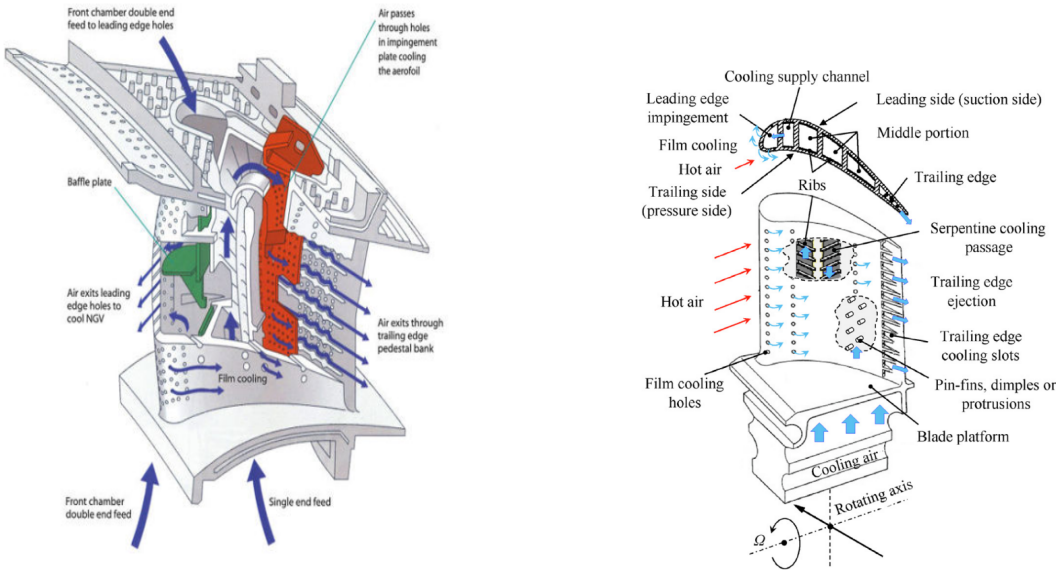

a b

Figure A.5: Gas turbine blade cooling schematic: (a) Path of the flow inside the blade [129]; (b) Typical techniques for turbine blade cooling [105]

A6 Film Cooling

Turbine blade film cooling has been studied since the early 1970s. Within the context of cooling systems for turbine blades that employ film cooling technology, as depicted in Figure A.5b, cooler air is directed from the interior of the blade to its exterior. This flow creates a barrier between the blade's surface and the hot gases passing by. The effectiveness of this film cooling method is largely influenced by several factors [57]: the relative strength of the coolant's flow compared to the hot gas stream (also known as the blowing ratio), the comparative temperatures of the coolant and the gas stream (or density ratio), the design of the cooling holes (encompassing dimensions, distribution, form, angle relative to the blade surface, and the number of rows), and their strategic placement on the blade (which could be at the leading or trailing edges, on the pressure or suction faces, along the endwall or at the blade tip). These factors must be assessed under conditions that mimic actual engine operations, which include variables like the Reynolds number, Mach number, turbulence from combustion processes, and the fluctuating wake flow. Typically, an increased momentum ratio translates to more effective film cooling, resulting in less heat being transferred to the turbine blade for a fixed temperature ratio. Conversely, a lower temperature ratio, implying cooler coolant, leads to improved cooling performance for a specific momentum ratio [57].

Appendix B

Dimensional Analysis

Dimensional analysis is based on the principle of *dimensional homogeneity*, which must be present when writing a mathematical relationship involving different dimensional physical quantities. This principle establishes that:

- The dimensional physical quantities appearing on both sides of the equation must be combined in such a way that the final structure yields the same dimension on the right side of the equation as the quantity that appears on the left side;
- In the dimensional equation with four quantities $X + Y + Z = W$, the quantities X, Y, Z and W must all have the same dimensions;
- The same equation can be expressed in a dimensionless form by dividing all terms by one of the quantities, for example W. In this form, the number of variables is reduced to three:

$$\frac{X}{W} + \frac{Y}{W} + \frac{Z}{W} = 1$$

It is also important to highlight that each dimensional physical quantity can be expressed through its respective fundamental quantities:

International System		**Technical** System	
Length	**L**	Length	**L**
Mass	**M**	Force	**F**
Time	**T**	Time	**T**

Table B.1: Comparison between International System and Technical System

In the International System, the dimensions of force, mass, and acceleration expressed through the fundamental units L, M, and T are as follows:

$$\begin{aligned} \text{Mass} \quad & [\text{m}] \rightarrow [M] \\ \text{Acceleration} \quad & [\text{a}] \rightarrow [L \cdot T^{-2}] \\ \text{Force} \quad & [\text{F}] \rightarrow [M \cdot L \cdot T^{-2}] \end{aligned}$$

In situations where a problem is affected by over three parameters, understanding the individual contributions of each becomes challenging. To streamline the analysis, it is advantageous to consolidate these parameters into dimensionless groups, reducing the total to just three core variables. For the purpose of creating these dimensionless units, the *Buckingham* $\pi - theorem$ [2] provides a practical approach.

B1 *Buckingham π − theorem*

The *Buckingham π − theorem* provides a framework for simplifying complex problems in physics. The theorem allows for the identification of dimensionless groups or dimensionless variables through the use of dimensional analysis, starting from the dimensional physical quantities that describe a physical phenomenon.

Suppose there are N dimensional physical quantities involved, denoted as

$$(Q_1, Q_2, Q_3, \ldots, Q_N)$$

Each of these quantities can be expressed through K fundamental physical quantities of the measurement system in use (for example, Length, Mass, Time, etc.).

The relationship that links the N physical quantities can be represented in the generic form:

$$f(Q_1, Q_2, Q_3, \ldots, Q_N) = 0$$

or alternatively:

$$Q_1 = F(Q_2, Q_3, \ldots, Q_{N-1}) \tag{B.1}$$

The proof of the *Buckingham π − theorem* will not be provided, but the fundamental steps will be illustrated, and the results will be applied to problems in fluid dynamics, with reference to the International System of units.

B1.1 Definition

The Buckingham Π theorem states that if N is the number of dimensional physical quantities and K is the number of fundamental quantities, then $N - K$ independent dimensionless groups, called Π groups, can be constructed. Through these groups, the previous dimensional relationship (B.1) can be expressed in a dimensionless form:

$$F(\Pi_1, \Pi_2, \Pi_3, \ldots, \Pi_{N-K}) = 0$$

The Π_i groups are derived from the dimensional physical quantities Q_i by appropriately combining them into groups of $K + 1$.

$$\begin{aligned}
\Pi_1 &= F_1(Q_1, Q_2, Q_3, \ldots, Q_K, Q_{K+1}) \\
\Pi_2 &= F_2(Q_1, Q_2, Q_3, \ldots, Q_K, Q_{K+2}) \\
&\vdots \\
\Pi_{N-K} &= F_{N-K}(Q_1, Q_2, Q_3, \ldots, Q_K, Q_{K+(N-K)})
\end{aligned}$$

The relationship in the previous form has led to a reduction in the number of variables in the study of the physical problem, going from N to $N - K$.

B1.2 Structure of the Generic Adimensional Group Π_i

Each dimensionless group Π_i is given by the product of dimensional physical quantities appropriately combined and raised to a suitable power. The determination of such products comes from dimensional analysis. To justify the theorem without going into the details of the proof, consider

the Equation B.2:

$$f(Q_1, Q_2, Q_3, \ldots, Q_N) = 0 \tag{B.2}$$

This relationship is expressed as the product of the dimensional physical quantities, each raised to its own exponent α_i. In other words, a monomial form is used:

$$[Q_1^{\alpha_1} \cdot Q_2^{\alpha_2} \cdot Q_3^{\alpha_3} \cdot \ldots \cdot Q_N^{\alpha_N}] = [0] \tag{B.3}$$

The exponents α_i are sought such that the dimension of the monomial relation becomes "null", or in other words, a dimensionless form. An "obvious" solution is $\alpha_1 = \alpha_2 = \ldots = \alpha_N = 0$.

Let M, L, T, ... be the K fundamental quantities through which the various dimensional physical quantities Q_i are expressed. For each quantity Q_i, it is given that:

$$\begin{aligned} Q_1 &= g_1(M, L, T, \ldots), \\ Q_2 &= g_2(M, L, T, \ldots), \\ &\vdots \\ Q_N &= g_N(M, L, T, \ldots). \end{aligned}$$

Substituting into Equation B.3, it is obtained:

$$[g_1(M, L, T, \ldots)^{\alpha_1} \cdot g_2(M, L, T, \ldots)^{\alpha_2} \cdot \ldots \cdot g_N(M, L, T, \ldots)^{\alpha_N}] = [0] \tag{B.4}$$

The equation will remain dimensionally null if the exponents α_i are selected appropriately. Under the International System, where the dimensional physical quantities Q_i are expressed solely through the three fundamental quantities: length (L), mass (M), and time (T), K is set to 3. However, K could be greater than 3 if a particular quantity is involved in the specific problem. Relation B.4 highlights the fact that each fundamental quantity (M, L, T) carries exponents derived from every function g_i. Consequently, for each fundamental quantity M, L, and T, an exponent that is a function of combinations of the various exponents $\alpha_1, \ldots, \alpha_N$ can be considered.

Based on this, a new relation in monomial form can be written where each fundamental quantity M, L, T has as its exponent a function $H_i(\alpha_1, \ldots, \alpha_N)$:

$$[M^{H_1(\alpha_1,\ldots,\alpha_N)} \cdot L^{H_2(\alpha_1,\ldots,\alpha_N)} \cdot T^{H_3(\alpha_1,\ldots,\alpha_N)}] = [0]$$

This relation is dimensionally satisfied (dimensionless) if the exponent functions H_i for each fundamental quantity are identically zero. Therefore, the following equalities need to be set:

$$\begin{aligned} H_1(\alpha_1, \alpha_2, \ldots, \alpha_N) &= 0, \\ H_2(\alpha_1, \alpha_2, \ldots, \alpha_N) &= 0, \\ H_3(\alpha_1, \alpha_2, \ldots, \alpha_N) &= 0. \end{aligned}$$

Only K relations for the functions H_i can be written, in this instance, only 3, corresponding to the number of fundamental quantities. The unknowns are denoted by N, representing the values of the exponents $\alpha_1, \ldots, \alpha_N$ that appear in Equation B.3. Since there are N unknowns and K equations with $K < N$, it is not possible to determine the value of all the unknowns due to indeterminacy. Only K values of α can be expressed in terms of the remaining $N - K$ values of α. This principle is utilized to determine the structure of each dimensionless group.

By expressing K unknowns α_K in terms of the remaining $N-K$ unknowns α_{N-K} and substituting these expressions into Relation B.3, the $N-K$ dimensionless groups Π_i are derived:

$$[Q_1^{\alpha_1} \cdot Q_2^{\alpha_2} \cdot Q_3^{\alpha_3} \cdot \ldots \cdot Q_N^{\alpha_N}] = [0]$$

Dimensional analysis is instrumental in pinpointing these groups, offering a systematic way to summarize or interrelate findings from experiments. However, this technique does not guarantee an accurate functional relationship [59], neither does it confirm the proper selection of all variables involved. In fields like fluid mechanics and heat transfer, numerous dimensionless numbers such as the Reynolds number, Nusselt number, and others have been initially determined through this method. These parameters form the cornerstone of many empirical correlations in scientific research. A list of the most commonly used dimensionless groups in fluid dynamics is shown in Table B.2.

Non-dimensional Number	**Definition**	**Physical Meaning**	**Typical Value**	**Interpretation**
Prandtl	$Pr = \frac{c_p \mu}{k_{tc}}$	momentum diffusivity / thermal diffusivity	≈ 1	Approximately the ratio of the velocity boundary layer thickness to the thermal layer thickness.
Schmidt	$Sc = \frac{\mu}{\rho D_2}$	momentum diffusivity / mass diffusivity	≈ 1	–
Lewis	$Le = \frac{Sc}{Pr} = \frac{k}{\rho c_p D_{12}}$	thermal diffusivity / mass diffusivity	≈ 1	Note that in some references $Le = \frac{Pr}{Sc}$
Stanton	$St = \frac{Nu}{Re \cdot Pr} = \frac{h}{\rho u C_p}$	heat transferred / fluid thermal capacity	$\ll 1$	Modified Nusselt number
Nusselt	$Nu = \frac{hL}{k_{tc}}$	total heat transfer / conductive heat transfer	$\gg 1$	Dimensionless temperature gradient at the surface
Damkohler	$Da = \frac{\tau_f}{\tau_c}$	fluid dynamic time scale / chemical reaction time scale	$\gg 1$	$Da \gg 1$ implies diffusion controlled combustion
Reynolds	$Re = \frac{\rho u L}{\mu}$	inertial force / viscous force	$\gg 1$	–

Table B.2: Commonly used dimensionless groups in fluid dynamics

The following are various examples to illustrate the operation and application of the method.

B1.3 Example 1. Aerodynamic resultant force F acting on an airfoil

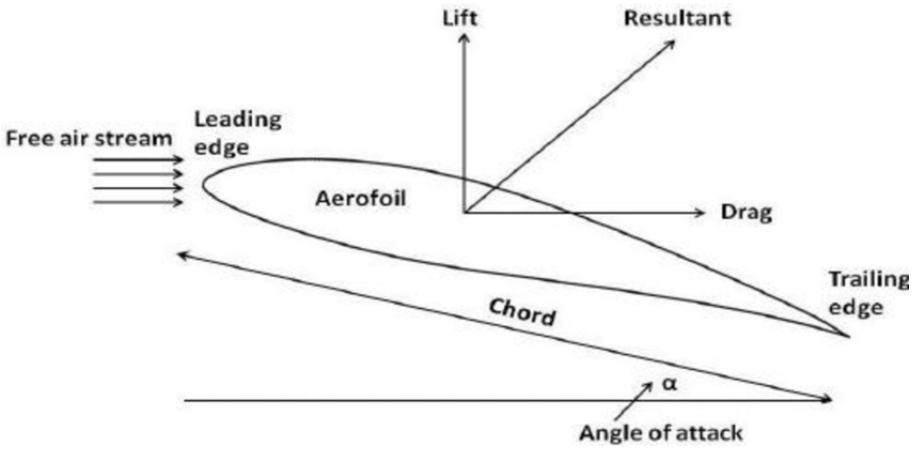

Figure B.1: Force vectors on an airfoil [101]

The aerodynamic resultant force F acting on a given airfoil profile (see Figure B.1) depends on

the previously mentioned dimensional physical quantities, namely:

- chord of the airfoil profile c
- velocity of the undisturbed flow V_∞
- angle of attack α
- properties of the fluid ρ_∞, μ_∞
- speed of sound $a_\infty = \sqrt{\gamma \cdot R/M \cdot T_\infty}$

In the problem, the geometry of the profile is given and considered as a fixed parameter. Furthermore, the angle of attack of the profile is also fixed and thus considered a given parameter. Therefore, geometry and angle of attack are excluded from the analysis when searching for dimensionless groups.

The functional relation can be represented as:

$$f(F, V_\infty, \rho_\infty, \mu_\infty, a_\infty, c) = 0$$

With $N = 6$ and $K = 3$, the number of dimensionless groups Π_i that can be determined is:

$$N - K = 6 - 3 = 3$$

$N - K$ corresponds to the number of independent equations that can be written for the three fundamental quantities.

The monomial relation for the force F takes the already introduced form:

$$[F^{\alpha_1} \cdot V_\infty^{\alpha_2} \cdot \rho_\infty^{\alpha_3} \cdot \mu_\infty^{\alpha_4} \cdot a_\infty^{\alpha_5} \cdot c^{\alpha_6}] = [0]$$

The dimensions of the individual dimensional physical quantities are expressed in terms of the fundamental quantities M, L, T, leading to:

$$\left[(M \cdot L \cdot T^{-2})^{\alpha_1} \cdot (L \cdot T^{-1})^{\alpha_2} \cdot (M \cdot L^{-3})^{\alpha_3} \cdot (M \cdot L^{-1} \cdot T^{-1})^{\alpha_4} \cdot (L \cdot T^{-1})^{\alpha_5} \cdot (L)^{\alpha_6}\right] = [0]$$

For each fundamental quantity, the corresponding exponent function is written as

$$\left[M^{(\alpha_1+\alpha_3+\alpha_4)} \cdot L^{(\alpha_1+\alpha_2-3\alpha_3-\alpha_4+\alpha_5+\alpha_6)} \cdot T^{(-2\alpha_1-\alpha_2-\alpha_4-\alpha_5)}\right] = [0]$$

To ensure that the dimension on the left-hand side is zero, as prescribed by the right-hand side of the relation, the three exponent functions must be null:

$$\begin{aligned} \alpha_1 + \alpha_3 + \alpha_4 &= 0, \\ \alpha_1 + \alpha_2 - 3\alpha_3 - \alpha_4 + \alpha_5 + \alpha_6 &= 0, \\ -2\alpha_1 - \alpha_2 - \alpha_4 - \alpha_5 &= 0 \end{aligned}$$

Three arbitrary unknowns α_i can be expressed in terms of the remaining three. Historically, α_2, α_3, α_6 have been expressed in terms of α_1, α_4, α_5:

$$\begin{aligned} \alpha_2 &= -2\alpha_1 - \alpha_4 - \alpha_5, \\ \alpha_3 &= -\alpha_1 - \alpha_4, \\ \alpha_6 &= -2\alpha_1 - \alpha_4 \end{aligned}$$

Rewriting the relation for the force F with the exponents obtained in this manner yields:

$$[F^{\alpha_1} \cdot V_\infty^{\alpha_2} \cdot \rho_\infty^{\alpha_3} \cdot \mu_\infty^{\alpha_4} \cdot a_\infty^{\alpha_5} \cdot c^{\alpha_6}] = [0]$$

$\Rightarrow$

$$\left[F^{\alpha_1} \cdot V_\infty^{(-2\alpha_1-\alpha_4-\alpha_5)} \cdot \rho_\infty^{(-\alpha_1-\alpha_4)} \cdot \mu_\infty^{\alpha_4} \cdot a_\infty^{\alpha_5} \cdot c^{(-2\alpha_1-\alpha_4)}\right] = [0]$$

The different dimensional quantities with the same exponent α_i are grouped together:

$$\left[\left(\frac{F}{V_\infty^2 \cdot \rho_\infty}\right)^{\alpha_1} \cdot \left(\frac{\mu_\infty}{V_\infty \cdot c}\right)^{\alpha_4} \cdot \left(\frac{a_\infty}{V_\infty}\right)^{\alpha_5}\right] = [0]$$

The assigned values to the three unknowns α_1, α_4, and α_5 are arbitrary and have historically been considered to be:

$$\begin{aligned}\alpha_1 &= 1,\\ \alpha_4 &= -1,\\ \alpha_5 &= -1\end{aligned}$$

The three groups: Π_1, Π_2, and Π_3 are thus defined as follows:

- The force coefficient: $\Pi_1 = C_F = \frac{F}{\rho_\infty V_\infty^2 c^2}$,
- The Reynolds number: $\Pi_2 = Re_\infty = \frac{V_\infty c}{\mu_\infty}$,
- The Mach number: $\Pi_3 = M_\infty = \frac{V_\infty}{a_\infty}$

If one wishes to write the monomial expression for the force F, it is obtained as

$$F = C_F \cdot \rho_\infty \cdot V_\infty^2 \cdot c^2$$

B1.4 Example 2. Conversion of the energy equation into its dimensionless form

The equation is expressed as

$$u\frac{\partial T}{\partial x} + v\frac{\partial T}{\partial y} = \alpha\frac{\partial^2 T}{\partial y^2}$$

Dimensional quantities such as u, v, T, x, and y are replaced by dimensionless quantities defined as follows:

$$\begin{aligned} u^* &= \frac{u}{u_\infty}, \qquad & v^* &= \frac{v}{u_\infty},\\ x^* &= \frac{x}{L}, \qquad & y^* &= \frac{y}{L},\end{aligned}$$

$$T^* = \frac{T - T_s}{T_\infty - T_s}$$

Therefore, the terms transform as follows:

$$u\frac{\partial T}{\partial x} = \frac{u_\infty u^*}{L(T_\infty - T_s)}\frac{\partial T^*}{\partial x^*},$$
$$v\frac{\partial T}{\partial y} = \frac{v_\infty v^*}{L(T_\infty - T_s)}\frac{\partial T^*}{\partial y^*},$$
$$\alpha\frac{\partial^2 T}{\partial y^2} = \frac{k}{\rho c_p L^2}\cdot\frac{1}{(T_\infty - T_s)}\frac{\partial^2 T^*}{\partial y^{*2}}$$

Substituting the dimensionless terms and simplifying by canceling common terms, and multiplying and dividing the right-hand side by μ, the equation becomes:

$$u^*\frac{\partial T^*}{\partial x^*} + v^*\frac{\partial T^*}{\partial y^*} = \frac{k\mu}{\mu\rho c_p u_\infty L}\frac{\partial^2 T^*}{\partial y^{*2}}$$

This simplifies to

$$u^*\frac{\partial T^*}{\partial x^*} + v^*\frac{\partial T^*}{\partial y^*} = \frac{1}{\mathrm{Re}_L\cdot\mathrm{Pr}}\frac{\partial^2 T^*}{\partial y^{*2}} \tag{B.5}$$

as indicated by Equation B.5, demonstrating that all terms are dimensionless.

Appendix C

Turbulence Scales and Energy Cascade

In the analysis of fluid flows, turbulence is often encountered. There is no definitive description of turbulent flow, yet it exhibits several identifying features, such as irregularity, diffusivity, association with large Reynolds numbers, three-dimensionality, dissipation, and adherence to the continuum model, as detailed in the publications of experts such as Pope [41]. In the analysis of the *energy cascade process*, the dissipative nature of turbulent flows constitutes the central element of the phenomenon.

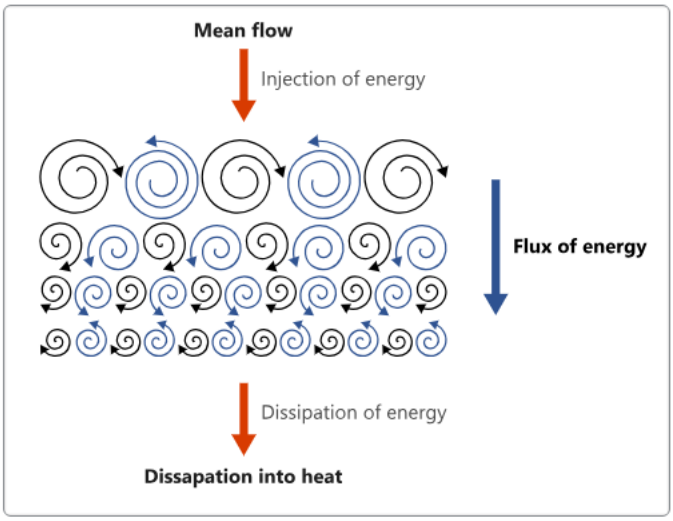

Figure C.1: Energy Cascade [128]

The dissipative characteristic of turbulent flows implies that the kinetic energy contained within the smaller, dissipative eddies is transformed into thermal energy. These smaller eddies receive kinetic energy from slightly larger eddies. In turn, these larger eddies gain their energy from even larger eddies, and so on [94]. The largest eddies extract their energy from the mean flow. This process of energy transfer from the largest turbulent scales (eddies) down to the smallest is termed the cascade process, as shown in Figure C.1.

C1 Turbulent scales

In the context of turbulent flow, the largest scales correspond to the size of the flow's geometry, such as the thickness of the boundary layer, characterized by a length scale ℓ_0 and a velocity scale v_0. These scales draw kinetic energy from the mean flow, which operates on a time scale similar to that of the large scales; mathematically, this can be expressed as the inverse of the characteristic time $t_0 \approx \ell_0/v_0$ [94].

The large scales are not isolated; they transfer part of their kinetic energy to somewhat smaller scales through interaction. This transfer is part of a cascade process that systematically conveys kinetic energy from the largest to the smallest scales within the flow. At these minute scales, viscous forces become significant, causing the kinetic energy to be converted into thermal energy through dissipation.

While the predominant direction of kinetic energy transfer is from larger to smaller scales, there are instances where the transfer can momentarily reverse, channeling energy from the smaller back to the larger scales [94]. The rate of energy dissipation, represented by ε (with units of m^2/s^3), is linked to both the kinematic viscosity ν and the square of the velocity gradient fluctuations. Although frictional forces are present across all scales, they are most pronounced within the smallest eddies. In practice, some dissipation occurs at every scale, but it is commonly accepted that the bulk of the energy input into the large scales is ultimately dissipated at the smallest scales.

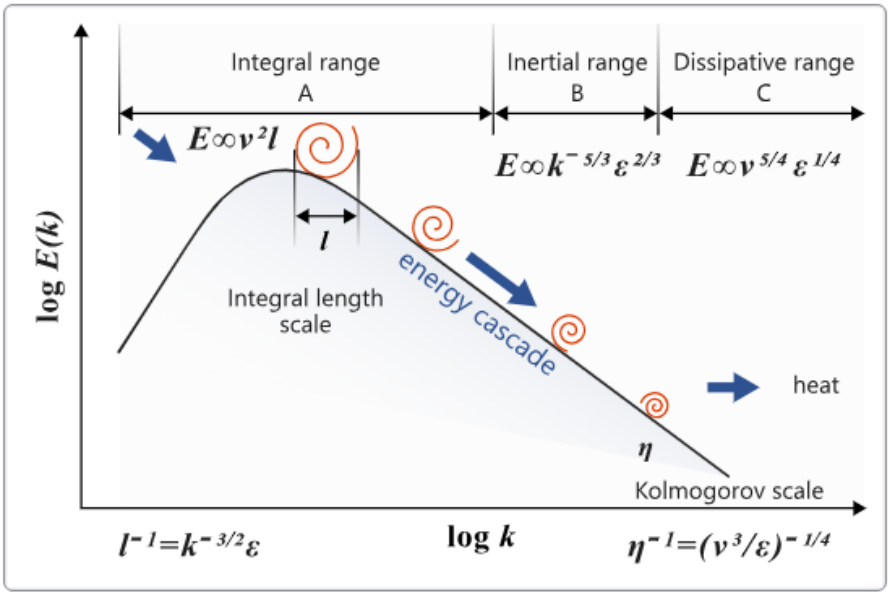

Figure C.2: Schematic Representation of Turbulence Energy Spectrum [128]

To clarify the concept of turbulence scales, one can refer to Figure C.2. This figure illustrates a characteristic energy spectrum E associated with turbulent flows, depicted in terms of wave number space κ. Turbulent flows display a wide array of eddy sizes, making the energy spectrum a useful framework for classifying eddies according to their scale [128]. From this classification, three main scales are identified: the *integral length scale*, the *Taylor microscale*, and the *Kolmogorov length scale*.

C1.1 Integral Length Scale

The integral length scale corresponds to the largest eddies within the energy spectrum. These structures are the primary carriers of energy, exhibiting a high degree of anisotropy and engaging

in energy production through their interaction with the mean flow. The size of eddies in this integral range is highly influenced by the specific conditions of the flow and is typically on the order of the flow's characteristic length, such as the hydraulic diameter [128]. The energy spectrum for these large eddies is generally proportional to the square of the velocity times the length scale $E \propto \nu^2 l$. The integral length scale is mathematically expressed as $l = k^{3/2}/\varepsilon$, with corresponding time scales $t = k/\varepsilon$ and a velocity scale $v = \sqrt{k}$ [128].

C1.2 Taylor Microscale

The Taylor microscale represents a mid-size scale within the energy spectrum, positioned between the largest and smallest eddies. Within the inertial subrange, the kinetic energy transitions from larger to smaller eddies through the energy cascade mechanism. This subrange is characterized by vortex stretching, which amplifies the rotational velocity of the eddies while reducing their cross-sectional radius [128]. Through dimensional analysis [94], the energy spectrum E, wave number κ, and energy dissipation rate ε can be related by the following expression:

$$E = \kappa^a \varepsilon^b \quad \text{with dimensions} \quad [\mathrm{m}^3/\mathrm{s}^2] = [1/\mathrm{m}]^a [\mathrm{m}^2/\mathrm{s}^3]^b$$

For dimensional consistency, two conditions must be satisfied, corresponding to the dimensions of meters [m] and seconds [s]:

$$\begin{aligned} 3 &= -a + 2b \\ -2 &= -3b \end{aligned}$$

Solving for a and b yields $b = \frac{2}{3}$ and $a = -\frac{5}{3}$. Substituting these values into the equation for the energy spectrum gives:

$$E(\kappa) = C_K \varepsilon^{\frac{2}{3}} \kappa^{-\frac{5}{3}}$$

where C_K represents the Kolmogorov constant, approximately 1.5. This leads to the *Kolmogorov spectrum law*, or the "$-5/3$ *law*", which states that for fully turbulent flows (high Reynolds number), the energy spectrum will exhibit a $\kappa^{-5/3}$ decay in the inertial subrange [94].

C1.3 Kolmogorov Scales

The *Kolmogorov scaling law* [11] of turbulences has been considered the most important theoretical breakthrough in the last century. This framework plays a crucial role in the examination and interpretation of turbulent phenomena across various disciplines, including meteorology, physics, chemistry, biology, and engineering [94].

The scale identified by Kolmogorov represents the smallest size of turbulent eddies. At this level, the turbulent structures are rendered isotropic, as the intensive action of viscosity neutralizes any anisotropy inherited from larger-scale eddies [128]. In this zone, the kinetic energy cascading from larger eddies is ultimately transformed into thermal energy. The characteristic length scale of this dissipative range is postulated to be dependent on both the kinematic viscosity, denoted as ν, and the rate at which energy is dissipated per unit mass, symbolized by ε.

Given the assumption above, it is possible to characterize the velocity scale v_η, length scale ℓ_η, and time scale τ_η with respect to ν and ε through the use of dimensional analysis. The expression is formulated as:

$$v_\eta = \nu^a \varepsilon^b$$

where the dimension of velocity is $[m/s]$. Matching these to the dimensions of ν ($[\mathrm{m}^2/\mathrm{s}]$) and ε ($[\mathrm{m}^2/\mathrm{s}^3]$), one must ensure dimensional consistency, resulting in two equations [94]:

For the dimension of meters [m]:

$$1 = 2a + 2b$$

For the dimension of seconds [s]:

$$-1 = -a - 3b$$

Upon solving these equations, the values of a and b are determined to be $\frac{1}{4}$. Consequently, the equations for ℓ_η and τ_η are derived as follows:

$$v_\eta = (\nu\varepsilon)^{\frac{1}{4}} \tag{C.1}$$

$$\ell_\eta = \left(\frac{\nu^3}{\varepsilon}\right)^{\frac{1}{4}} \tag{C.2}$$

$$\tau_\eta = \left(\frac{\nu}{\varepsilon}\right)^{\frac{1}{2}} \tag{C.3}$$

Where Equation C.2 and C.3 are called Kolmogorov length and velocity scales of viscous eddies [51]. It follows from the respective definitions that the ratio between the largest and smallest scales in the flow is given by

$$\frac{L}{\eta} = Re^{\frac{3}{4}} \tag{C.4}$$

This implies that increasing the Reynolds number does not reduce the rate of energy dissipation, but rather extends the range of scales through which the energy must cascade before it reaches the dissipative limit [51].

Appendix D

Gamma Distribution

This section examines the specific probability distribution functions that are utilized in the sphere generation method referenced in Section 3.2.2.

D1 Implementing Gamma Distribution for Modeling Diameter Distribution

The gamma distribution is characterized by a shape parameter k and a scale parameter θ. A random variable X that follows this distribution is denoted as $X \sim \Gamma(k, \theta)$. The probability density function (pdf) for the gamma distribution is given by:

$$f(x; k, \theta) = \frac{x^{k-1} e^{-\frac{x}{\theta}}}{\theta^k \Gamma(k)}$$

where $x > 0$ and $k, \theta > 0$. The Gamma function $\Gamma(k)$ is defined through the integral:

$$\Gamma(k) = \int_0^\infty t^{k-1} e^{-t}\, dt$$

Statistical parameters such as the mean μ and variance σ^2 of the gamma distribution are derived from the shape and scale parameters by the relations:

$$\mu = k\theta,$$
$$\sigma^2 = k\theta^2$$

For the purpose of modeling the diameter distribution utilizing the gamma distribution, the relationship between the surface roughness parameters and the distribution parameters must be established. According to Wen [115], the relationship is defined as:

$$\mu = 3.5\, R_{a_{\mathrm{up}}},$$
$$\sigma = R_{q_{\mathrm{up}}}$$

This relationship is determined through a heuristic approach [115], employing trial-and-error to align the surface roughness parameters from an analog surface with those obtained from up-scaled measurements. While a direct relationship between the two sets of parameters is elusive due to the random distribution of the spheres, it is postulated that a certain relationship exists.

Bibliography

[1] Osborne Reynolds. "An Experimental Investigation of the Circumstances Which Determine Whether the Motion of Water Shall Be Direct or Sinuous, and of the Law of Resistance in Parallel Channels". In: *Philosophical Transactions of the Royal Society of London* 174 (1883), pp. 935–982. URL: http://dx.doi.org/10.1098/rstl.1883.0029.

[2] E. Buckingham. "On Physically Similar Systems; Illustrations of the Use of Dimensional Equations". In: *Phys. Rev.* 4 (4 Oct. 1914), pp. 345–376. DOI: 10.1103/PhysRev.4.345. URL: https://link.aps.org/doi/10.1103/PhysRev.4.345.

[3] Wilhelm Nusselt. "The fundamental law of heat transfer Natural and forced convection]". In: *Geeundheits-Iwenieur,* 38.42 and 43 (1915), 477-482 and 490–496.

[4] J Nikuradse. "Stromungsgesetz in rauhren rohren". In: *Tech. Rep. 361, VDI-Forschungsheft, July/August* (1933).

[5] T. VON KÁRMÁN. "Mechanische Ähnlichkeit und Turbulenz." In: *In Proceedings of the Third International Congr. Applied Mechanics* (1933), pp. 85–105.

[6] Thomas H. Chilton and Allan P. Colburn. "Mass Transfer (Absorption) Coefficients Prediction from Data on Heat Transfer and Fluid Friction". In: *Industrial & Engineering Chemistry* 26 (1934), pp. 1183–1187. URL: https://api.semanticscholar.org/CorpusID:95352901.

[7] Hermann Schlichting. "Experimentelle Untersuchungen zum Rauhigkeitsproblem". In: *Ingenieur-Archiv* 7 (1936), pp. 1–34. URL: https://api.semanticscholar.org/CorpusID:122277243.

[8] C. F. Colebrook, C. M. White, and Geoffrey Ingram Taylor. "Experiments with fluid friction in roughened pipes". In: *Proceedings of the Royal Society of London. Series A - Mathematical and Physical Sciences* 161.906 (1937), pp. 367–381. DOI: 10.1098/rspa.1937.0150. eprint: https://royalsocietypublishing.org/doi/pdf/10.1098/rspa.1937.0150. URL: https://royalsocietypublishing.org/doi/abs/10.1098/rspa.1937.0150.

[9] J Nikuradse. "Laws of flows in rough pipes". In: *Technical Memorandum 1292, NACA, Washington, April* (1937).

[10] MILLIKAN C B. "A critical discussion of turbulent flow in channels and circular tubes". In: *Proc. 5th Int. Congress on Applied Mechanics (Cambridge, MA, 1938)* (1939), pp. 386–392. URL: https://cir.nii.ac.jp/crid/1571698600956910848.

[11] Andrey Nikolaevich Kolmogorov. "Dissipation of Energy in Locally Isotropic Turbulence". In: *Akademiia Nauk SSSR Doklady* 32 (Apr. 1941), p. 16.

[12] FRANCIS H. CLAUSER. "Turbulent Boundary Layers in Adverse Pressure Gradients". In: *Journal of the Aeronautical Sciences* 21.2 (1954), pp. 91–108. DOI: 10.2514/8.2938. eprint: https://doi.org/10.2514/8.2938. URL: https://doi.org/10.2514/8.2938.

[13] Francis R. Hama. "Boundary Layer characteristics for smooth and rough surfaces". In: 1954. URL: https://api.semanticscholar.org/CorpusID:198669151.

[14] Donald Coles. "The law of the wake in the turbulent boundary layer". In: *Journal of Fluid Mechanics* 1.2 (1956), pp. 191–226. DOI: 10.1017/S0022112056000135.

[15] D.F. Dipprey and R.H. Sabersky. "Heat and momentum transfer in smooth and rough tubes at various prandtl numbers". In: *International Journal of Heat and Mass Transfer* 6.5 (1963), pp. 329–353. ISSN: 0017-9310. DOI: https://doi.org/10.1016/0017-9310(63)90097-8. URL: https://www.sciencedirect.com/science/article/pii/0017931063900978.

[16] Allan P. Colburn. "A method of correlating forced convection heat-transfer data and a comparison with fluid friction". In: *International Journal of Heat and Mass Transfer* 7.12 (1964), pp. 1359–1384. ISSN: 0017-9310. DOI: https://doi.org/10.1016/0017-9310(64)90125-5. URL: https://www.sciencedirect.com/science/article/pii/0017931064901255.

[17] A. E. Perry, W. H. Schofield, and P. N. Joubert. "Rough wall turbulent boundary layers". In: *Journal of Fluid Mechanics* 37.2 (1969), pp. 383–413. DOI: 10.1017/S0022112069000619.

[18] Boris Sergeevich Petukhov. "Heat Transfer and Friction in Turbulent Pipe Flow with Variable Physical Properties". In: *Advances in heat transfer* 6 (1970), pp. 503–564. URL: https://api.semanticscholar.org/CorpusID:123990589.

[19] Jr. R. Dirling. "A method for computing roughwall heat transfer rates on reentry nosetips". In: 1973. URL: https://api.semanticscholar.org/CorpusID:123468431.

[20] A. Townsend. "The Structure of Turbulent Shear Flow". In: *Cambridge Monographs on Mechanics and Applied Mathematics, Cambridge University Press, second edn.* (1976).

[21] J.C. Han, L.R. Glicksman, and W.M. Rohsenow. "An investigation of heat transfer and friction for rib-roughened surfaces". In: *International Journal of Heat and Mass Transfer* 21.8 (1978), pp. 1143–1156. ISSN: 0017-9310. DOI: https://doi.org/10.1016/0017-9310(78)90113-8. URL: https://www.sciencedirect.com/science/article/pii/0017931078901138.

[22] M. M. Pimenta, R. J. Moffat, and W. M. Kays. "The Structure of a Boundary Layer on a Rough Wall with Blowing and Heat Transfer". In: *Journal of Heat Transfer* 101.2 (May 1979), pp. 193–198. ISSN: 0022-1481. DOI: 10.1115/1.3450945. eprint: https://asmedigitalcollection.asme.org/heattransfer/article-pdf/101/2/193/5744403/193_1.pdf. URL: https://doi.org/10.1115/1.3450945.

[23] Hermann Schlichting. *Boundary-layer theory*. McGraw-Hill series in mechanical engineering. McGraw-Hill, 1979. ISBN: 9780070553347, 0070553343.

[24] P. S. Jackson. "On the displacement height in the logarithmic velocity profile". In: *Journal of Fluid Mechanics* 111 (1981), pp. 15–25. DOI: 10.1017/S0022112081002279.

[25] H. W. Coleman, B. K. Hodge, and R. P. Taylor. "A Re-Evaluation of Schlichting's Surface Roughness Experiment". In: *Journal of Fluids Engineering* 106.1 (Mar. 1984), pp. 60–65. ISSN: 0098-2202. DOI: 10.1115/1.3242406. eprint: https://asmedigitalcollection.asme.org/fluidsengineering/article-pdf/106/1/60/5711368/60_1.pdf. URL: https://doi.org/10.1115/1.3242406.

[26] J. C. Han, J. S. Park, and C. K. Lei. "Heat Transfer Enhancement in Channels With Turbulence Promoters". In: *Journal of Engineering for Gas Turbines and Power* 107.3 (July 1985), pp. 628–635.

[27] P. M. Ligrani and R. J. Moffat. "Thermal boundary layers on a rough surface downstream of steps in wall temperature". In: *Boundary-Layer Meteorology* 31.2 (Feb. 1985), pp. 127–147. DOI: 10.1007/BF00121174.

[28] K. L. Lim A. E. Perry and S. M. Henbest. "An experimental study of the mrbulence stmcture in smooth- and rough-wall boundary layers". In: *J. FluidMech.* 177 (1987), pp. 437–466.

[29] J.C. Han and J.S. Park. "Developing heat transfer in rectangular channels with rib turbulators". In: *International Journal of Heat and Mass Transfer* 31.1 (1988), pp. 183–195. ISSN: 0017-9310. DOI: https://doi.org/10.1016/0017-9310(88)90235-9. URL: https://www.sciencedirect.com/science/article/pii/0017931088902359.

[30] V. A. Gorelov, M. M. Goikhenberg, and V. A. Malkov, eds. *The investigation of heat transfer in cooled blades of gas turbines.* July 1990.

[31] Ronald Adrian. "Particle-Imaging Techniques For Experimental Fluid-Mechanics". In: *Annual Review of Fluid Mechanics* 23 (Jan. 1991), pp. 261–304. DOI: 10.1146/annurev.fluid.23.1.261.

[32] M.H. Hosni, Hugh W. Coleman, and Robert P. Taylor. "Measurements and calculations of rough-wall heat transfer in the turbulent boundary layer". In: *International Journal of Heat and Mass Transfer* 34.4 (1991), pp. 1067–1082. ISSN: 0017-9310. DOI: https://doi.org/10.1016/0017-9310(91)90017-9. URL: https://www.sciencedirect.com/science/article/pii/0017931091900179.

[33] M. R. Raupach, Robert Anthony Antonia, and Sundara Rajagopalan. "Rough-Wall Turbulent Boundary Layers". In: *Applied Mechanics Reviews* 44 (1991), pp. 1–25. URL: https://api.semanticscholar.org/CorpusID:120811506.

[34] M. Samimy and S. K. Lele. "Motion of particles with inertia in a compressible free shear layer". In: *Physics of Fluids A: Fluid Dynamics* 3.8 (Aug. 1991), pp. 1915–1923. ISSN: 0899-8213. DOI: 10.1063/1.857921. eprint: https://pubs.aip.org/aip/pof/article-pdf/3/8/1915/12387330/1915_1_online.pdf. URL: https://doi.org/10.1063/1.857921.

[35] D. Goldstein, R. Handler, and L. Sirovich. "Modeling a No-Slip Flow Boundary with an External Force Field". In: *Journal of Computational Physics* 105.2 (1993), pp. 354–366. ISSN: 0021-9991. DOI: https://doi.org/10.1006/jcph.1993.1081. URL: https://www.sciencedirect.com/science/article/pii/S0021999183710818.

[36] M.H. Hosni et al. "Roughness element shape effects on heat transfer and skin friction in rough-wall turbulent boundary layers". In: *International Journal of Heat and Mass Transfer* 36.1 (1993), pp. 147–153. ISSN: 0017-9310. DOI: https://doi.org/10.1016/0017-9310(93)80074-5. URL: https://www.sciencedirect.com/science/article/pii/0017931093800745.

[37] *Study and Application of Hemispheric Cavities for Surface Heat Transfer Augmentation.* Vol. Volume 4: Heat Transfer; Electric Power; Industrial and Cogeneration. Turbo Expo: Power for Land, Sea, and Air. June 1995, V004T09A034. DOI: 10.1115/95-GT-059. eprint: https://asmedigitalcollection.asme.org/GT/proceedings-pdf/GT1995/78811/V004T09A034/2406522/v004t09a034-95-gt-059.pdf. URL: https://doi.org/10.1115/95-GT-059.

[38] Warren M. Rohsenow, James P. Hartnett, and Young I. Cho. *Handbook of Heat Transfer.* eng. 1st ed. New York, NY: McGraw-Hill Education, 1998. ISBN: 9780070535558.

[39] Robert D. Moser, John Kim, and Nagi N. Mansour. "Direct numerical simulation of turbulent channel flow up to Reτ=590". In: *Physics of Fluids* 11.4 (Apr. 1999), pp. 943–945. ISSN: 1070-6631. DOI: 10.1063/1.869966. eprint: https://pubs.aip.org/aip/pof/article-pdf/11/4/943/19098956/943_1_online.pdf. URL: https://doi.org/10.1063/1.869966.

[40] Jens M. Österlund et al. "A note on the overlap region in turbulent boundary layers". In: *Physics of Fluids* 12.1 (Jan. 2000), pp. 1–4. ISSN: 1070-6631. DOI: 10.1063/1.870250. eprint: https://pubs.aip.org/aip/pof/article-pdf/12/1/1/19060457/1_1_online.pdf. URL: https://doi.org/10.1063/1.870250.

[41] Stephen B. Pope. *Turbulent Flows*. Cambridge University Press, 2000.

[42] Shinji Nakagawa and Thomas J. Hanratty. "Particle image velocimetry measurements of flow over a wavy wall". In: *Physics of Fluids* 13.11 (Nov. 2001), pp. 3504–3507. DOI: 10.1063/1.1399291. URL: https://doi.org/10.1063/1.1399291.

[43] E.S. Gadelmawla et al. "Roughness parameters". In: *Journal of Materials Processing Technology* 123.1 (2002), pp. 133–145. ISSN: 0924-0136. DOI: https://doi.org/10.1016/S0924-0136(02)00060-2. URL: https://www.sciencedirect.com/science/article/pii/S0924013602000602.

[44] Jennifer van Rij, B. Belnap, and Phillip Ligrani. "Analysis and Experiments on Three-Dimensional, Irregular Surface Roughness". In: *Journal of Fluids Engineering* 124 (Sept. 2002), p. 671. DOI: 10.1115/1.1486222.

[45] Robert Boyle. "Measurements and Predictions of Surface Roughness Effects on Turbine Vane Aerodynamics". In: 6 (Jan. 2003). DOI: 10.1115/GT2003-38580.

[46] P.R. Chandra, C.R. Alexander, and J.C. Han. "Heat transfer and friction behaviors in rectangular channels with varying number of ribbed walls". In: *International Journal of Heat and Mass Transfer* 46.3 (2003), pp. 481–495. ISSN: 0017-9310. DOI: https://doi.org/10.1016/S0017-9310(02)00297-1. URL: https://www.sciencedirect.com/science/article/pii/S0017931002002971.

[47] Michael Schultz et al. "Three Models to Relate Detachment of Low Form Fouling at Laboratory and Ship Scale". In: *Biofouling* 19 Suppl (May 2003), pp. 17–26. DOI: 10.1080/0892701031000089516.

[48] A. Zwebek and P. Pilidis. "Degradation Effects on Combined Cycle Power Plant Performance—Part I: Gas Turbine Cycle Component Degradation Effects". In: *Journal of Engineering for Gas Turbines and Power-transactions of The Asme - J ENG GAS TURB POWER-T ASME* 125 (July 2003). DOI: 10.1115/1.1519271.

[49] A. Zwebek and P. Pilidis. "Degradation Effects on Combined Cycle Power Plant Performance—Part II: Steam Turbine Cycle Component Degradation Effects". In: *Journal of Engineering for Gas Turbines and Power-transactions of The Asme - J ENG GAS TURB POWER-T ASME* 125 (July 2003). DOI: 10.1115/1.1519272.

[50] Ronald Bunker. "Latticework (Vortex) Cooling Effectiveness: Part 1 — Stationary Channel Experiments". In: vol. 3. Jan. 2004. DOI: 10.1115/GT2004-54157.

[51] Javier Jiménez. "The Contributions of A. N. Kolmogorov to the theory of turbulence". In: *Arbor : Ciencia, Pensamiento y Cultura* 178 (Aug. 2004). DOI: 10.3989/arbor.2004.i704.550.

[52] Javier Jiménez. "Turbulent Flows Over Rough Wall". In: *Annu. Rev. Fluid Mech* 36 (Jan. 2004), pp. 173–96. DOI: 10.1146/annurev.fluid.36.050802.122103.

[53] John Kim. "Rough-Wall Turbulent Boundary Layers". In: *CALIFORNIA UNIV LOS ANGELES DEPT OF MECHANICAL AND AEROSPACE ENGINEERING* (2004).

[54] Michael Schultz. "Frictional Resistance of Antifouling Coating Systems". In: *Journal of Fluids Engineering-transactions of The Asme - J FLUID ENG* 126 (Nov. 2004). DOI: 10.1115/1.1845552.

[55] Karen Flack, Michael Schultz, and Thomas Shapiro. "Experimental support for Towsend's Reynolds number similarity hypothesis on rough walls". In: *Physics of Fluids* 17 (Jan. 2005). DOI: 10.1063/1.1843135.

[56] Bernhard Weigand William Morrow Kays Michael E. Crawford. *Convective Heat and Mass Transfer*. McGraw-Hill series in mechanical engineering. McGraw-Hill, 2005. ISBN: 9780071238298.

[57] Je-Chin Han. "Turbine Blade Cooling Studies at Texas A&M University: 1980-2004". In: *Journal of Thermophysics and Heat Transfer* 20.2 (2006), pp. 161–187. DOI: 10.2514/1.15403. eprint: https://doi.org/10.2514/1.15403. URL: https://doi.org/10.2514/1.15403.

[58] FRANK P. INCROPERA et al. *Fundamentals of heat and mass transfer*. eng. 6th ed. New York: John Wiley and Sons, 2006. ISBN: 978-0471457282.

[59] C. P. Kothandaraman. *Fundamentals of heat and mass transfer*. eng. Rev. 3rd ed. New Delhi: New Age International P Ltd., Publishers, 2006. ISBN: 1-282-07420-2.

[60] Lesley Mae Wright. "Enhanced Internal Cooling of Turbine Blades and Vanes". In: 2006. URL: https://api.semanticscholar.org/CorpusID:53482872.

[61] IAN P. CASTRO. "Rough-wall boundary layers: mean flow universality". In: *Journal of Fluid Mechanics* 585 (2007), pp. 469–485. DOI: 10.1017/S0022112007006921.

[62] TOMOAKI IKEDA and Paul Durbin. "Direct simulations of a rough-wall channel flow". In: *Journal of Fluid Mechanics* 571 (Jan. 2007), pp. 235–263. DOI: 10.1017/S002211200600334X.

[63] Seung-Hyun Lee. "Direct numerical simulation of the turbulent boundary layer over a rod-roughened wall". In: *Journal of Fluid Mechanics* 584 (Aug. 2007), pp. 125–146. DOI: 10.1017/S0022112007006465.

[64] Yanbo wu and Kenneth Christensen. "Outer-layer similarity in the presence of a practical rough-wall topography". In: *Physics of Fluids - PHYS FLUIDS* 19 (Aug. 2007). DOI: 10.1063/1.2741256.

[65] Fulvio Scarano. "AE4-180 Experimental Aerodynamics". In: *Delft University of Technology course notes* (2008).

[66] Albert Betz, ed. *Ergebnisse der Aerodynamischen Versuchsanstalt zu Göttingen - IV. Lieferung*. Vol. 007. Göttinger Klassiker der Strömungsmechanik. Göttingen: Universitätsverlag Göttingen, 2009. DOI: 10.17875/gup2009-104.

[67] Jiarong Hong, Joseph Katz, and Michael Schultz. "High Resolution PIV Measurement near a Rough Wall in an Optically Index-matched Facility". In: *8TH INTERNATIONAL SYMPOSIUM ON PARTICLE IMAGE VELOCIMETRY - PIV09* (Aug. 2009). URL: https://flair.monash.edu.au/intranet/proceedings/piv2009/Site/AA2_Wall-bounded_Shear_Flows_1_files/PIV09-0064.pdf.

[68] Jeffrey Bons. "A Review of Surface Roughness Effects in Gas Turbines". In: *Journal of Turbomachinery-transactions of The Asme - J TURBOMACH-T ASME* 132 (Apr. 2010). DOI: 10.1115/1.3066315.

[69] Karen A. Flack and Michael P. Schultz. "Review of Hydraulic Roughness Scales in the Fully Rough Regime". In: *Journal of Fluids Engineering* 132.4 (Apr. 2010), p. 041203. ISSN: 0098-2202. DOI: 10.1115/1.4001492. eprint: https://asmedigitalcollection.asme.org/fluidsengineering/article-pdf/132/4/041203/5516817/041203_1.pdf. URL: https://doi.org/10.1115/1.4001492.

[70] Mohammad Amir and Ian Castro. "Turbulence in rough-wall boundary layers: Universality issues". In: *Experiments in Fluids* 51 (Aug. 2011), pp. 313–326. DOI: 10.1007/s00348-011-1049-7.

[71] Jiarong Hong, Joseph Katz, and Michael Schultz. "Near-wall turbulence statistics and flow structures over 3D roughness in a turbulent channel flow". In: *Journal of Fluid Mechanics - J FLUID MECH* 667 (Jan. 2011), pp. 1–37. DOI: 10.1017/S0022112010003988.

[72] Andrea Sciacchitano, Bernhard Wieneke, and Fulvio Scarano. "PIV uncertainty quantification by image matching". In: *Measurement Science and Technology* 24.4 (Mar. 2013), p. 045302. DOI: 10.1088/0957-0233/24/4/045302. URL: https://dx.doi.org/10.1088/0957-0233/24/4/045302.

[73] Specialist Committee on Detailed Flow Measurement Techniques of the 27th ITTC. "GUIDELINE ON BEST PRACTICES FOR THE APPLICATION OF PIV/SPIV IN TOWING TANKS AND CAVITATION TUNNELS". In: *International Towing Tank Conference* (Jan. 2014). eprint: https://www.ittc.info/media/7991/75-02-01-04.pdf.

[74] William Thielicke. "The flapping flight of birds: Analysis and application". English. PhD thesis. University of Groningen, 2014. ISBN: 978-90-367-7241-9.

[75] Michael A. Boles Yunus A. Çengel. *Thermodynamics: An Engineering Approach. 8th ed.* McGraw-Hill Education. McGraw-Hill, 2014. ISBN: 9780073398174.

[76] B. Aupoix. "Improved heat transfer predictions on rough surfaces". In: *International Journal of Heat and Fluid Flow* 56 (2015), pp. 160–171. ISSN: 0142-727X. DOI: https://doi.org/10.1016/j.ijheatfluidflow.2015.07.007. URL: https://www.sciencedirect.com/science/article/pii/S0142727X15000892.

[77] Carlo Carcasci et al. "Heat Transfer and Pressure Drop Measurements on Rotating Matrix Cooling Geometries for Airfoil Trailing Edges". In: June 2015, V05AT11A011. DOI: 10.1115/GT2015-42594.

[78] Haiyong Liu, Cunliang Liu, and Wenming Wu. "Numerical investigation on the flow structures in a narrow confined channel with staggered jet array arrangement". In: *Chinese Journal of Aeronautics* 28.6 (2015), pp. 1616–1628. ISSN: 1000-9361. DOI: https://doi.org/10.1016/j.cja.2015.08.017. URL: https://www.sciencedirect.com/science/article/pii/S1000936115001831.

[79] Karen Flack et al. "Skin-friction behavior in the transitionally-rough regime". In: *International Journal of Heat and Fluid Flow* 61 (June 2016), pp. 21–30. DOI: 10.1016/j.ijheatfluidflow.2016.05.008.

[80] Liubov Magerramova, Boris Vasilyev, and Vladimir Kinzburskiy. "Novel Designs of Turbine Blades for Additive Manufacturing". In: June 2016, V05CT18A001. DOI: 10.1115/GT2016-56084.

[81] FTM Nieuwstadt (†), Bendiks Jan Boersma, and Jerry Westerweel. *Turbulence: Introduction to Theory and Applications of Turbulent Flows*. English. Springer, 2016. ISBN: 978-3-319-31597-3. DOI: 10.1007/978-3-319-31599-7.

[82] Tommaso Fiorini. "Turbulent Pipe Flow - High Resolution Measurements in CICLoPE". PhD thesis. alma, Maggio 2017. URL: http://amsdottorato.unibo.it/8158/.

[83] R.J. Goldstein. *Fluid mechanics measurements, second edition*. Jan. 2017, pp. 1–712. ISBN: 9780203755723. DOI: 10.1201/9780203755723.

[84] Robin Andersson et al. "Characterization of Flow Structures Induced by Highly Rough Surface Using Particle Image Velocimetry, Proper Orthogonal Decomposition and Velocity Correlations". In: *Engineering* 10 (Jan. 2018), pp. 399–416. DOI: 10.4236/eng.2018.107028.

[85] Wentao Fu et al. "Streamlined frameworks for advancing metal based additive manufacturing technologies". In: *Journal of the Global Power and Propulsion Society* 2 (2018), pp. 317–328. DOI: 10.22261/QJLS4L. URL: https://doi.org/10.22261/QJLS4L.

[86] Spencer Onuh. "Additive Manufacturing Technology Development: A Trajectory Towards Industrial Revolution". In: *American Journal of Mechanical and Industrial Engineering* 3 (Dec. 2018), p. 80. DOI: 10.11648/j.ajmie.20180305.12.

[87] Mr. Prakash Santosh Patil. "Recent Studies in Internal Cooling of gas turbine blade : a Review". In: 2018. URL: https://api.semanticscholar.org/CorpusID:139084285.

[88] Markus Raffel et al. *Particle Image Velocimetry: A Practical Guide*. English. 3rd. Springer, 2018. ISBN: 978-3-319-68851-0. DOI: 10.1007/978-3-319-68852-7.

[89] *INDUSTRIALIZATION AND CURRENT FIELD EXPERIENCE OF ADDITIVELY MANUFACTURED GAS TURBINE COMPONENTS*. Vol. The Future of Gas Turbine Technology 9th International Gas Turbine Conference, Brussels, Belgium. Oct. 2018. eprint: https://etn.global/wp-content/uploads/IGTC18_Proceedings/Papers/47.%20Siemens%20-%20Vladimir%20Navrotsky.pdf.

[90] Chen Zhang, Sandijs Vasilevskis, and Bartosz Kozlowski. *Particle Image Velocimetry: User Guide*. English. DCE Technical reports 237. Denmark: Department of Civil Engineering, Aalborg University, 2018.

[91] ASME B46.1. *Surface Texture (Surface Roughness, Waviness, and Lay)*. The American Society of Mechanical Engineers, 2019, p. 144. ISBN: 9780791873250.

[92] Samantha Taylor, Eric Christopher Forrest, and Bradley Howell Jared. "Investigating Applicability of Surface Roughness Parameters in Describing the Metallic Additive Manufacturing Process." In: (Aug. 2019). URL: https://www.osti.gov/biblio/1641526.

[93] Bruno Chanetz et al. "Experimental Aerodynamics, An Introductory Guide". In: (Jan. 2020). DOI: 10.1007/978-3-030-35562-3.

[94] Lars Davidson. "Fluid mechanics, turbulent flow and turbulence modeling". In: 2020. URL: https://api.semanticscholar.org/CorpusID:219810565.

[95] Olivier Léon, Philippe Reulet, and Francois Chedevergne. "Aerodynamic and heat transfer effects of distributed hemispherical roughness elements inducing step changes in a turbulent boundary layer". In: *International Journal of Heat and Fluid Flow* 85 (Aug. 2020), p. 108672. DOI: 10.1016/j.ijheatfluidflow.2020.108672.

[96] Haiwang Li et al. "Experimental investigation of turbulent flow in a rotating straight channel with continuous ribs". In: *Physics of Fluids* 32.1 (Jan. 2020), p. 015114. ISSN: 1070-6631. DOI: 10.1063/1.5131223. eprint: https://pubs.aip.org/aip/pof/article-pdf/doi/10.1063/1.5131223/15803924/015114_1_online.pdf. URL: https://doi.org/10.1063/1.5131223.

[97] Dong-Gyu Ahn. "Directed Energy Deposition (DED) Process: State of the Art". In: *Int. J. of Precis. Eng. and Manuf.-Green Tech. 8* 140 (Feb. 2021), pp. 703–742. DOI: 10.1007/s40684-020-00302-7.

[98] Daniel Chung et al. "Predicting the Drag of Rough Surfaces". In: *Annual Review of Fluid Mechanics* 53 (Jan. 2021), pp. 439–471. DOI: 10.1146/annurev-fluid-062520-115127.

[99] Mohammadreza Kadivar, David Tormey, and Gerard Mcgranaghan. "A review on turbulent flow over rough surfaces: Fundamentals and theories". In: *International Journal of Thermofluids* 10 (Mar. 2021), p. 100077. DOI: 10.1016/j.ijft.2021.100077.

[100] T. Medjnoun et al. "Turbulent boundary-layer flow over regular multiscale roughness". In: *Journal of Fluid Mechanics* 917 (2021), A1. DOI: 10.1017/jfm.2021.228.

[101] Krishna Munuswamy et al. "Analysis of various NACA airfoil and fabrication of wind tunnel to test the scaled-down model of an airfoil". In: *IOP Conference Series: Materials Science and Engineering* 1130 (Apr. 2021), p. 012021. DOI: 10.1088/1757-899X/1130/1/012021.

[102] Amgad Salama. "Velocity Profile Representation for Fully Developed Turbulent Flows in Pipes: A Modified Power Law". In: *Fluids* 6.10 (2021). ISSN: 2311-5521. DOI: 10.3390/fluids6100369. URL: https://www.mdpi.com/2311-5521/6/10/369.

[103] William Thielicke and René Sonntag. "Particle Image Velocimetry for MATLAB: Accuracy and enhanced algorithms in PIVlab". In: *Journal of Open Research Software* (May 2021). DOI: 10.5334/jors.334.

[104] T.T. Wohlers et al. *Wohlers Report 2021: 3D Printing and Additive Manufacturing Global State of the Industry*. Wohlers Associates, 2021. ISBN: 9780991333271. URL: https://books.google.it/books?id=vGJszgEACAAJ.

[105] Kirttayoth Yeranee and Yu Rao. "A review of recent studies on rotating internal cooling for gas turbine blades". In: *Chinese Journal of Aeronautics* 34 (Jan. 2021), pp. 85–113. DOI: 10.1016/j.cja.2020.12.035.

[106] Samia Adil and Ismail Lazoglu. "A review on additive manufacturing of carbon fiber-reinforced polymers: Current methods, materials, mechanical properties, applications and challenges". In: *Journal of Applied Polymer Science* 140 (Dec. 2022). DOI: 10.1002/app.53476.

[107] Amanda Björnram and Klara Ljunggren. "Characterization of Additively Manufactured Surfaces of Cooling Channels". In: *MA thesis. Linköping University* (2022).

[108] Riccardo Pagani. "Experimental Analysis of the Thermal and Hydraulic Performance in Straight and Complex Additively Manufactured Mini-Channels". In: *MA thesis. Polytechnic University of Milan* (2022).

[109] International Organization for Standardization. *Geometric Product Specifications (GPS) - Surface Texture: Profile Method - Terms, Definitions, and Surface Texture Parameters*. ISO 21920-2:2021, 2022, p. 78.

[110] Taspia Shawkat Chowdhury et al. "A critical review on gas turbine cooling performance and failure analysis of turbine blades". In: *International Journal of Thermofluids* 18 (2023), p. 100329. ISSN: 2666-2027. DOI: https://doi.org/10.1016/j.ijft.2023.100329. URL: https://www.sciencedirect.com/science/article/pii/S2666202723000484.

[111] Venturi Cora. "Investigation of Thermal Performance of AM Channels and the Influence of the Printing Angle". In: *Politecnico di Torino* (2023).

[112] Patrick Lehmann. "Investigation of the local heat transfer characteristics on additively manufactured surfaces using infrared thermography". In: *Technical Universitu of Munich* (2023).

[113] *Development and Validation Under Engine Operation Environment of Addtively Manufactured Hot Turbine Parts*. Vol. Volume 13C: Turbomachinery — Deposition, Erosion, Fouling, and Icing; Design Methods and CFD Modeling for Turbomachinery; Ducts, Noise, and Component Interactions. Turbo Expo: Power for Land, Sea, and Air. June 2023, V13CT32A037. DOI: 10.1115/GT2023-103771. eprint: https://asmedigitalcollection.asme.org/GT/proceedings-pdf/GT2023/87103/V13CT32A037/7045887/v13ct32a037-gt2023-103771.pdf. URL: https://doi.org/10.1115/GT2023-103771.

[114] Shuji Tanigawa et al. "Development of metal AM technology for gas turbine components". In: *Journal of the Global Power and Propulsion Society* July (2023), pp. 49–65. DOI: 10.33737/jgpps/163429. URL: https://doi.org/10.33737/jgpps/163429.

[115] Kabin Wen. "Investigation of Roughness Effects on Heat Transfer of Upscaled Additively Manufactured Channels in the Turbulent Region Using Infrared Thermography". In: *KTH ROYAL INSTITUTE OF TECHNOLOGY* (2023).

[116] Liang Xu et al. "Development Trend of Cooling Technology for Turbine Blades at Super-High Temperature of above 2000 K". In: *Energies* 16.2 (2023). ISSN: 1996-1073. DOI: 10.3390/en16020668. URL: https://www.mdpi.com/1996-1073/16/2/668.

[117] Wagih Abu Rowin et al. "Accurately predicting turbulent heat transfer over rough walls: a review of measurement equipment and methods". In: *Experiments in Fluids* 65 (May 2024). DOI: 10.1007/s00348-024-03812-1.

[118] Alberto Brogliato. "Investigation of the Effect of Additive Manufacturing Induced Surface Roughness on Local Heat Transfer Properties Using IR Thermography". In: *Politecnico di Torino* (2024).

[119] Aaron Brugnera. "Experimental investigation of heat transfer in additive manufactured channels with different Prandtl". In: *Politecnico di Torino* (2024).

[120] Siemens Energy. *SGT-800 gas turbine*. Optional note. 2024. URL: https://siemens-energy.com/global/en/home/products-services/product/sgt-800.html#Emissions-tab-5 (visited on 12/14/2024).

[121] Ambrosio Pedreño Marin. "PIV flow measurements for heat transfer characterization in upscaled AM surface roughness". In: *Delft University of Technology* (2024).

[122] Fraser O'Neill and Ali Mehmanparast. "A review of additive manufacturing capabilities for potential application in offshore renewable energy structures". In: *Forces in Mechanics* 14 (2024), p. 100255. ISSN: 2666-3597. DOI: https://doi.org/10.1016/j.finmec.2024.100255. URL: https://www.sciencedirect.com/science/article/pii/S2666359724000015.

[123] Shamim Pourrahimi and Lucas Hof. "On the Post-Processing of Complex Additive Manufactured Metallic Parts: A Review". In: *Advanced Engineering Materials* 26 (Apr. 2024). DOI: 10.1002/adem.202301511.

[124] Carlotta Tamagnini and Francesca Agostino. "Thermo-fluid dynamic characterization of an additive manufacturedrough channel and development of an experimental PIV apparatus". In: *Politecnico di Milano* (2024).

[125] A. Cengel Yunus and J. Ghajar Afshin. *Heat and mass transfer: Fundamentals and applications*. eng. 5th ed. New York, NY: McGraw-Hill Professional, 2024. ISBN: 9780073398181.

[126] Longfei Zhou et al. "Additive Manufacturing: A Comprehensive Review". In: *Sensors* 24.9 (2024). ISSN: 1424-8220. DOI: 10.3390/s24092668. URL: https://www.mdpi.com/1424-8220/24/9/2668.

[127] Fabio Gissi. "Infrared Thermography-Based Heat Transfer Analysis and Thermal Boundary Layer Evaluation on Upscaled Models of Additively Manufactured Rough Surfaces". In: *Politecnico di Torino* (2025).

[128] Altair AcuSolve. *Turbulence Scales and Energy Cascade*. URL: https://2021.help.altair.com/2021/hwsolvers/acusolve/topics/chapter_heads/turbulence_intro_c.htm (visited on 01/01/2025).

[129] Oxford Thermofluids Institute. *Turbine Cooling Group*. Optional note. URL: https://oti.eng.ox.ac.uk/research/research-groups/turbine-cooling-group/ (visited on 12/18/2024).